SPECTROSCOPY OF NEUTRON-UNBOUND FLUORINE

by

Gregory Arthur Christian

A DISSERTATION

Submitted
to Michigan State University
in partial fulfillment of the requirements
for the degree of

DOCTOR OF PHILOSOPHY

PHYSICS

2011

ABSTRACT

SPECTROSCOPY OF NEUTRON-UNBOUND FLUORINE

by

Gregory Arthur Christian

Neutron-unbound states in ^{27}F and ^{28}F have been measured using the technique of invariant mass spectroscopy, with the unbound states populated from nucleon knock out reactions, ^{29}Ne(^{9}Be, X). Neutrons resulting from the decay of unbound states were detected in the Modular Neutron Array (MoNA), which recorded their positions and times of flight. Residual charged fragments were deflected by the dipole Sweeper magnet and passed through a series of charged particle detectors that provided position, energy loss, and total kinetic energy measurements. The charged particle measurements were sufficient for isotope separation and identification as well as reconstruction of momentum vectors at the target. In addition to the neutron and charged particle detectors, a CsI(Na) array (CAESAR) surrounded the target, allowing a unique determination of the decay path of the unbound states.

In ^{27}F, a resonance was observed to decay to the ground state of ^{26}F with 380 ± 60 keV relative energy, corresponding to an excited level in ^{27}F at 2500 ± 220 keV. The ^{28}F relative energy spectrum indicates the presence of multiple, unresolved resonances; however, it was possible to determine the location of the ground state resonance as 210^{+50}_{-60} keV above the ground state of ^{27}F. This translates to a ^{28}F binding energy of 186.47 ± 0.20 MeV.

Comparison of the ^{28}F binding energy to USDA/USDB shell model predictions provides insight into the role of intruder configurations in the ground state structure of ^{28}F and the low-Z limit of the "island of inversion" around $N = 20$. The USDA/USDB calculations are in good agreement with the present measurement, in sharp contrast to other neutron rich, $N = 19$ nuclei (^{29}Ne, ^{30}Na, and ^{31}Mg). This proves that configurations lying outside of the *sd* model space are not necessary to obtain a good description of the ground state binding energy of ^{28}F and suggests that ^{28}F does not exhibit inverted single particle structure in its ground state.

ACKNOWLEDGEMENTS

As with any project, a large number of people have made contributions to the work presented in this dissertation, and each one of them deserves recognition and thanks. First, I thank my guidance committee members—Artemis Spyrou, Michael Thoennessen, Alex Brown, Carl Schmidt, Carlo Piermarocchi, and Hendrik Schatz—for their time and effort in reviewing my work. In particular, Michael and Artemis have both served as top-notch academic advisors at various points in my time as a graduate student, giving useful insight, advice, assistance, and motivation.

A number of people made direct contributions to the experiment and its analysis, including the entire MoNA Collaboration, the NSCL Gamma Group, and NSCL operations and design staff. I will single a few of them out, and I hope I do not miss anyone. Nathan Frank wrote the original experiment proposal and was a close collaborator during the preparation, running, and ongoing analysis. The MoNA graduate students—Michelle Mosby, Shea Mosby, Jenna Smith, Jesse Snyder, and Michael Strongman—were all expert shift-takers during the run. In particular, Jesse took every night shift, which I think we all appreciated. Thomas Baumann and Paul DeYoung designed the electronics logic for the timestamp setup, without which the experiment would not have run. Alexandra Gade, Geoff Grinyer, and Dirk Weisshaar provided much assistance in the assembly and running of CAESAR, and Alissa Wersal, NSCL REU student, performed much of the hard labor necessary for CAESAR calibration and analysis. Daniel Bazin kept the Sweeper magnet and its associated detectors tuned and running throughout the experiment, and Craig Snow and Renan Fontus put a lot of work into designing and assembling a magnetic shield for CAESAR. On the theory side, Angelo Signoracci provided the matrix elements and binding energy corrections for the IOI shell model calculations.

For each person who made direct contributions to this work, there are many more who contributed indirectly. First among these are my parents, Paul and Jane, who have always provided support and encouragement. All of my extended family and friends at various stages in life have

contributed in some way, but they are too numerous to list individually. I should also thank my teachers at all levels of education, in particular the late Owen Pool, my first physics teacher, and John Wood, who introduced me to nuclear physics. I am also grateful to everyone in the NSCL and the MSU Department of Physics and Astronomy for creating an environment that is, by and large, a pleasure to work in as a graduate student. There are plenty of horror stories out there regarding graduate student life, but I have found little of this to be true in my time at MSU and the NSCL. Along these lines, I am very grateful that I was able to take a two year break from my graduate studies and be allowed to return and pick up right where I left off, with no negative impact to my progress.

Finally, I must acknowledge the funding agency which made this work possible, the National Science Foundation, under grants PHY-05-55488, PHY-05-55439, PHY-06-51627, and PHY-06-06007.

TABLE OF CONTENTS

LIST OF TABLES

LIST OF FIGURES

Chapter 1

INTRODUCTION

The fundamental question of nuclear structure is a simple one: what happens when protons and neutrons are combined to form a compound system? Despite its seemingly simple nature, the atomic nucleus is a varied and complex object. Construction of a complete and accurate model of all nuclei would require a detailed understanding of the strong nuclear force as well as the ability to exactly solve an $n-$body quantum mechanical problem. At present, neither of these is tractable, but it is nevertheless possible to construct models which reproduce a variety of experimental observations relevant to nuclear structure. One of the most successful models used to describe the structure of light to medium mass nuclei is the "shell model," which treats nuclei as collections of independent nucleons (protons and neutrons) moving in a mean field.

Beginning in 1933, W. Elsasser noted that certain "magic" numbers of protons and neutrons result in enhanced nuclear stability [2]. This led to the development of the shell model, in which nuclei are modeled as systems of non-interacting nucleons sitting in a potential well. Initially, this idea was disregarded as it was not believed that strong inter-nucleon fores could average to form such a well. Moreover, little experimental data was available to support such a hypothesis [3]. Over a decade later, M. Goeppert-Mayer revisited the nuclear shell model with the benefit of a large number of experimental data, noting the particular stability of nuclei at proton or neutron numbers 8, 20, 50, 82 and 126 [4]. However, using simple potential wells to construct the mean field, it was only possible to reproduce gaps at numbers 8 and 20, so the independent particle model of the nucleus continued to be disregarded [3].

The major breakthrough for the shell model came in 1949, when Mayer and the group of Haxel, Suess, and Jensen independently demonstrated that large shell gaps at 8, 20, 28, 50, 82 and 126 are reproduced theoretically in a mean field model by adding a spin-orbit term to a harmonic oscillator potential [5, 6]. The energy spacings resulting from such a potential are illustrated in

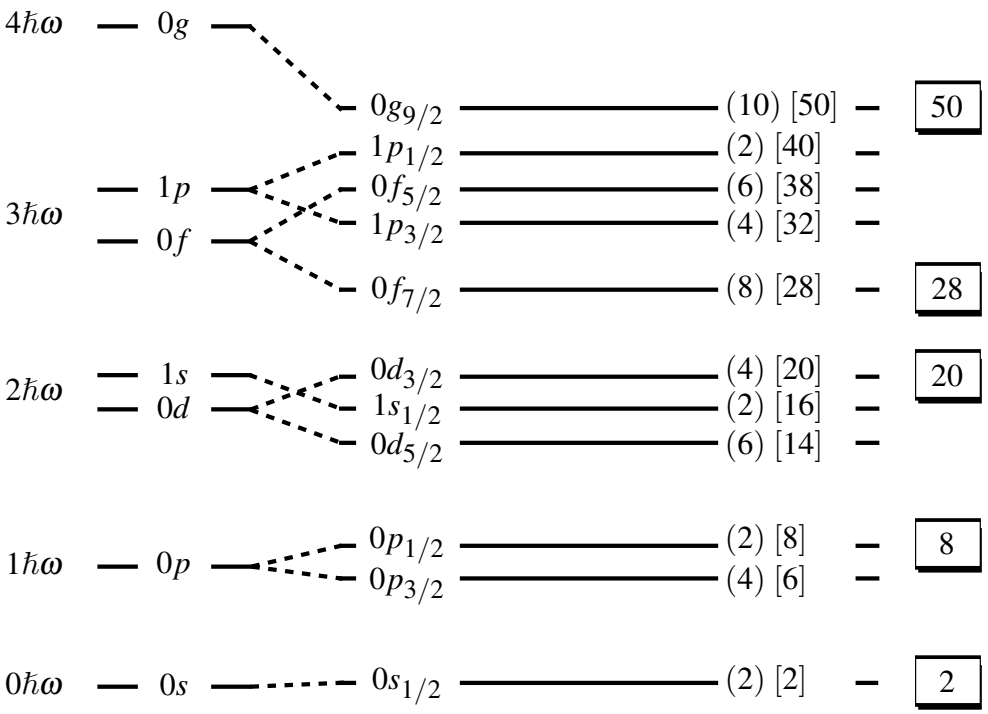

Figure 1.1: Level spacings in the nuclear shell model (up to number 50), from a harmonic oscillator potential that includes a spin-orbit term [1].

Fig. 1.1[1]. Later refinements were made to the shell model, including the use of a more realistic Woods-Saxon potential [7], but for stable nuclei the basic picture is similar to that of Fig. 1.1.

Early studies involving nuclei away from stability indicated a breakdown in the large shell gap at $N = 20$ [8–11]. The loss of magicity at $N = 20$ and at other magic numbers has since been demonstrated in a wide variety of experiments, and a great amount of experimental and theoretical effort has been put forth to understand the evolution of nuclear shell structure when going from stable nuclei to those with large neutron to proton ratio. In the present work, these efforts are continued through the study of neutron-unbound states in ^{27}F and ^{28}F, circled on a nuclear chart in Fig. 1.2. These nuclei lie close to the traditional magic number $N = 20$ and are some of the most neutron rich $N \sim 20$ systems presently available for experimental study.

[1]Throughout this document, the shell labeling scheme of Fig. 1.1, beginning with $n = 0$, is used. Other sources may use a scheme that begins with $n = 1$, but the distinction is typically clear from context.

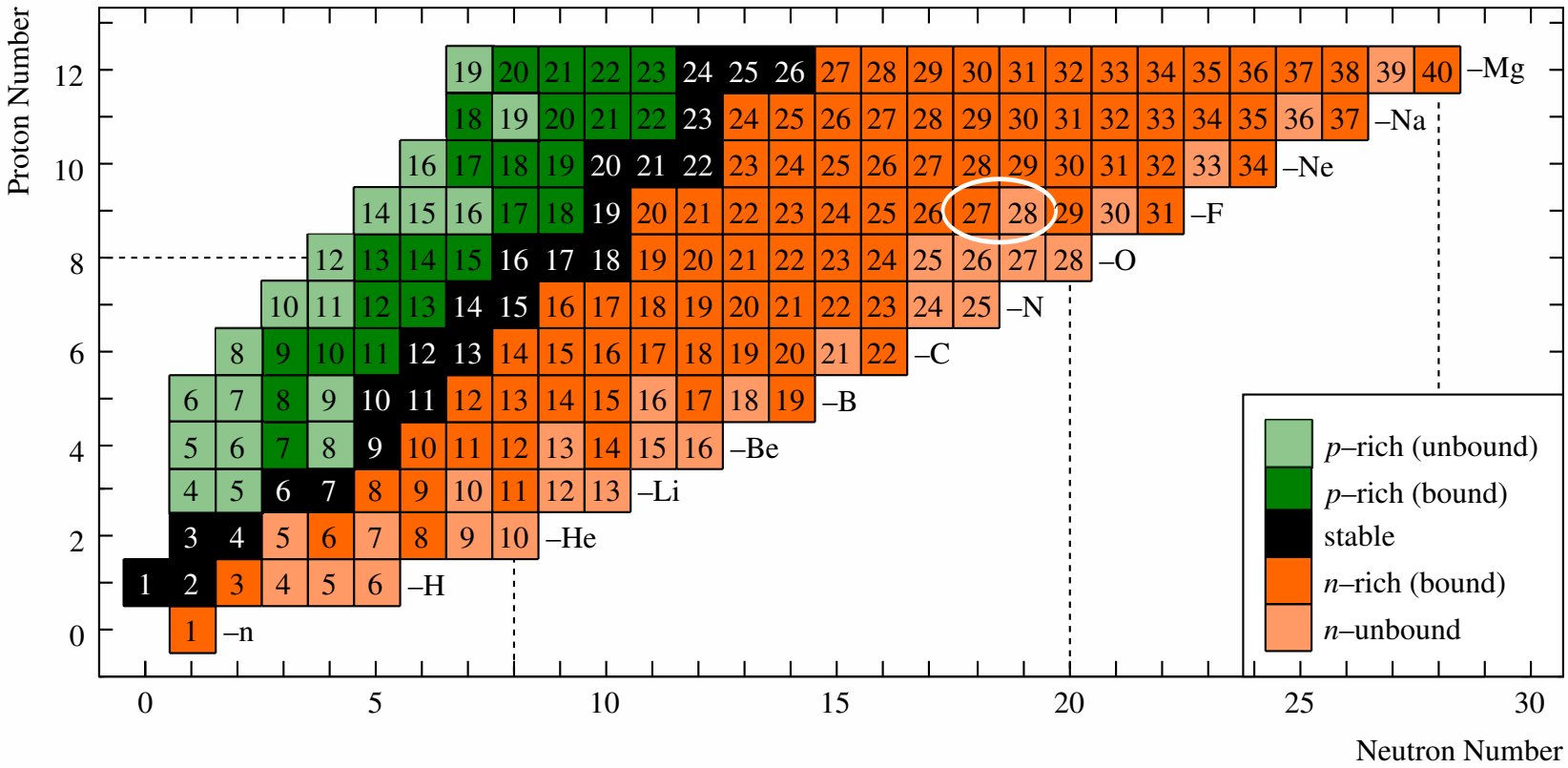

Figure 1.2: The nuclear chart up to $Z = 12$. The white circle indicates the fluorine isotopes under investigation in the present work. For interpretation of the references to color in this and all other figures, the reader is referred to the electronic version of this dissertation.

Chapter 2

MOTIVATION AND THEORY

2.1 Evolution of Nuclear Shell Structure

Since the earliest studies indicating a change in shell structure for neutron rich nuclei [8–11], a wide variety of data have been collected to support this hypothesis. The first indications came in Ref. [8], in which mass measurements of sodium ($Z = 11$) isotopes, ranging from ^{26}Na to ^{31}Na, were reported. The sodiums were produced in reactions of a 24 GeV proton beam on a thick Uranium target, with the reaction products separated and their masses measured in a single-stage magnetic spectrometer at CERN [13]. The authors found that the heavier isotopes ^{31,32}Na were significantly more bound than predicted by theoretical calculations using a closed $N = 20$ shell. This deviation is shown in Fig. 2.1, adapted from the original article. The masses of these isotopes could only be reproduced theoretically if neutrons were allowed to be promoted from the $0d_{3/2}$ to the $0f_{7/2}$ level, a configuration which was not in line with previous assumptions of a closed $N = 20$ shell.

Extending the mass measurements of [8] to include other isotopes in the $N = 20$ region, one can see clear evidence for quenching of the $N = 20$ shell gap by plotting two-neutron separation energies as a function of mass number, as is done for isotopes of neon ($Z = 10$) through calcium ($Z = 20$) in Fig. 2.2. A significant decrease in two neutron separation energy is expected to follow a large shell gap since nuclei below the gap will be much more tightly bound than those above it. As shown in the figure, a large decrease in separation energy is present for stable and nearly stable isotopes (aluminum through calcium, $13 \leq Z \leq 20$). This decrease becomes diminished for the neutron rich isotopes of magnesium, sodium and neon ($Z = 12,\ 11,\ 10$).

Further confirmation of $N = 20$ shell gap quenching comes from consideration of the 2^+ first excited state energies of even-even nuclei in the $N \sim 20$ region. For nuclei with a closed $N = 20$ neutron shell, reaching the 2^+ configuration requires the promotion of neutrons across the large

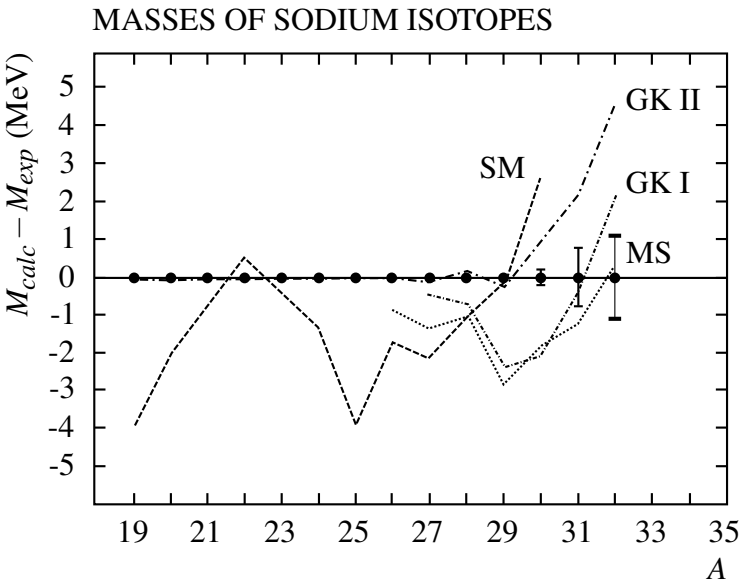

Figure 2.1: Difference between measured and calculated sodium ($Z = 11$) masses, adapted from Ref. [8]. A high value of $M_{calc} - M_{exp}$ indicates stronger binding than predicted by theory, as is the case for ^{31,32}Na.

shell gap. This requirement leads to a high-lying 2^+ first excited state, on the order of 2 MeV or more. On the other hand, if the gap is quenched, the next available level is lower, resulting in a decreased 2^+ excitation energy. Fig. 2.3 shows the 2^+ first excited state energies of even-even $N = 20$ isotones from neon ($Z = 10$) through calcium ($Z = 20$). As expected, the 2^+ energy is large for the nuclei with $Z \geq 14$, but it drops dramatically to less than 1 MeV for neon and magnesium, indicating a quenching of the $N = 20$ gap.

In addition to masses and excited state energies, a number of other data have been collected to indicate the onset of deformation for neutron rich $N \sim 20$ nuclei. Deformation in nuclei is the result of collective modes, and its presence indicates the lack of a strong shell closure. Some of the experimental signatures of deformation include $B(E2)$ values for the transition from the 2^+ first excited state to the 0^+ ground state (for even-even nuclei); charge radii; and electromagnetic moments. A detailed overview of previous measurements of these observables is not relevant in the present work; however, a concise summary can be found in Ref. [20].

Prompted by the experimental discoveries outlined above, theoretical models were adjusted to

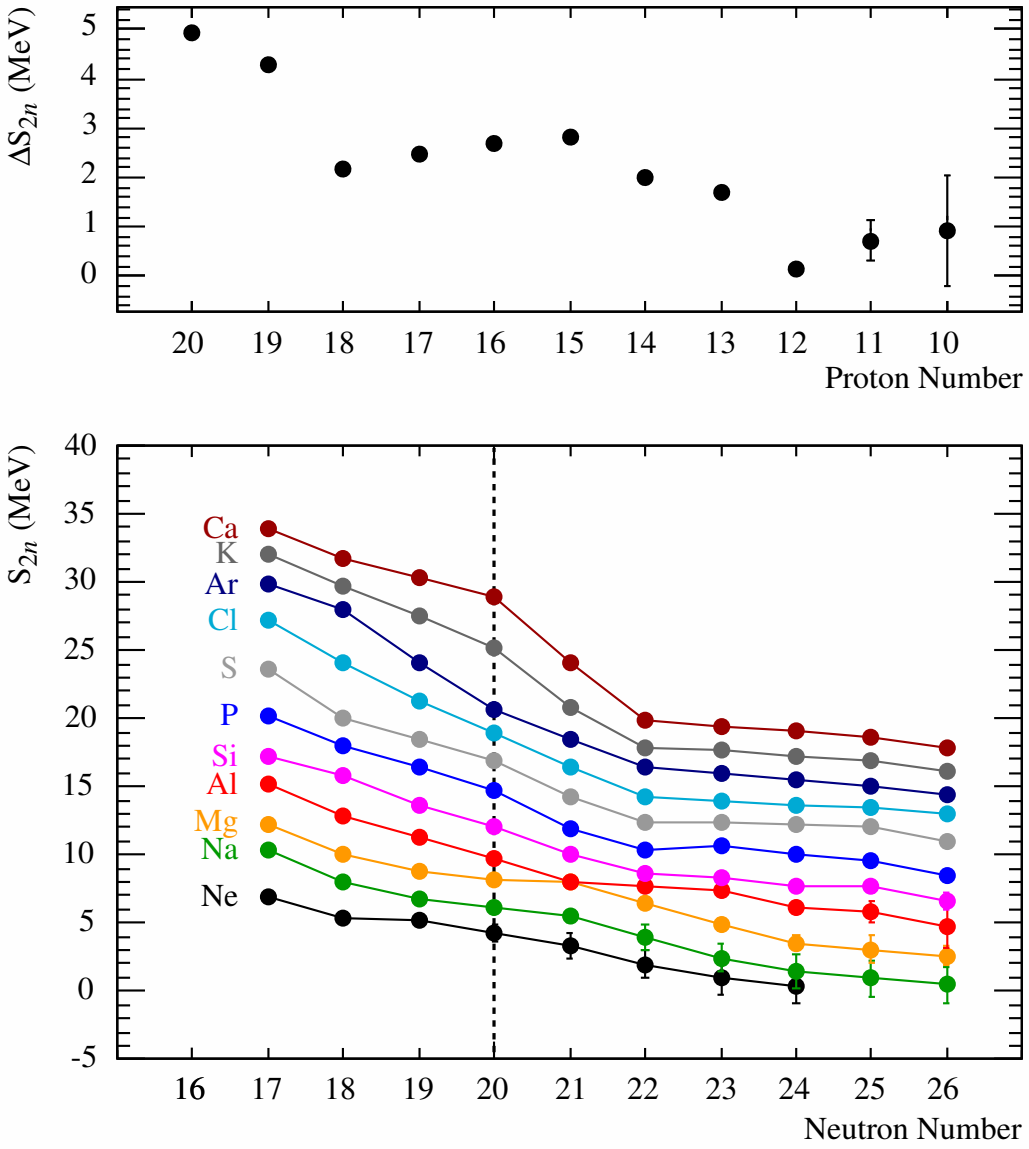

Figure 2.2: Two neutron separation energies for isotopes of neon ($Z = 10$) through calcium ($Z = 20$). The most neutron rich isotopes of Mg, Na and Ne do not demonstrate a dramatic drop in separation energy at $N = 20$, indicating a quenching of the shell gap. The top panel is a plot of the difference in two neutron separation energy between $N = 21$ and $N = 20$ as a function of proton number. S_{2n} values are calculated from Ref. [12].

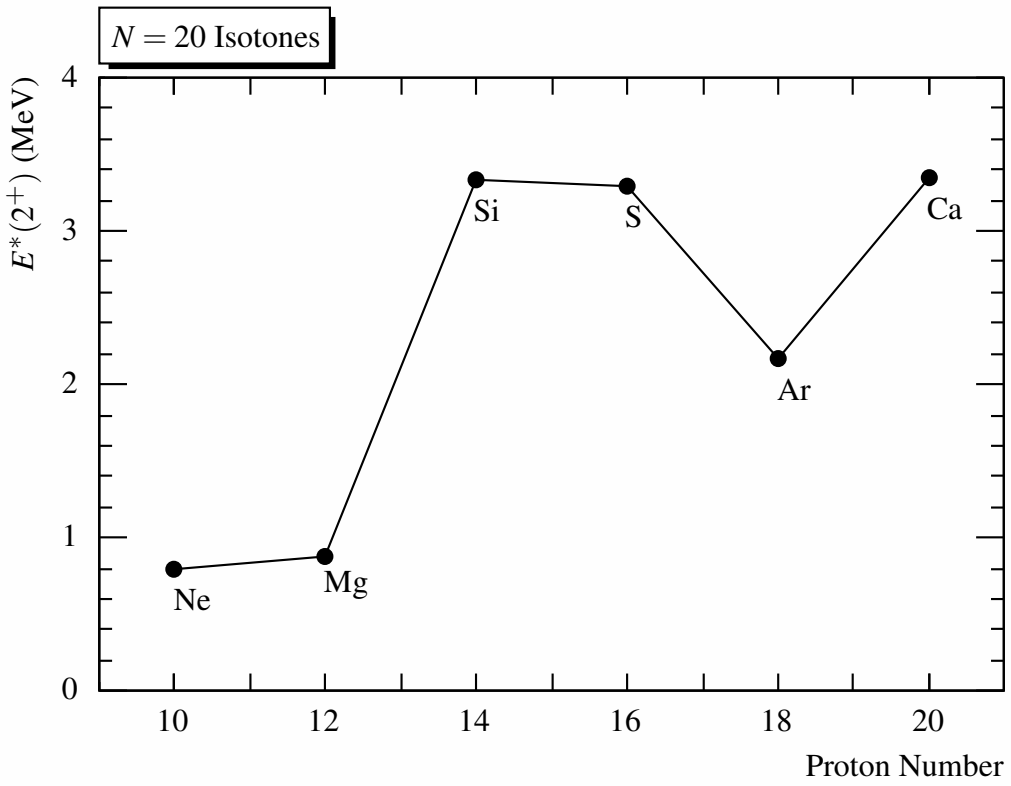

Figure 2.3: 2^+ first excited state energies for even-even $N = 20$ isotones, $10 \leq Z \leq 20$. The excited state energy drops suddenly to below 1 MeV for $Z \leq 12$, indicating a quenching of the $N = 20$ shell gap. The 2^+ energy for neon is taken from Refs. [14, 15]; all others are taken from the appropriate Nuclear Data Sheets [16–19].

better reproduce the anomalies observed for neutron rich nuclei around $N = 20$. One important adjustment is the extension of the shell model space to include neutron pf shell components, although in the interest of conserving computing power the models were—and often still are—truncated to include only a subset of pf shell. Further truncations include the allowance of only certain modes of excitation—for example, allowing a maximum of only two or four neutrons to be promoted into pf levels.[1]

Another major adjustment made to shell models was the development of effective interactions which more accurately reproduce single particle energies for cross-shell nuclei. A widely used interaction is the SDPF-M interaction [22], which consists of three parts. The first part, for the

[1] Such excitations also leave neutron holes in the *sd* shell and are often referred to as "multi-particle, multi-hole" (or np-nh) excitations.

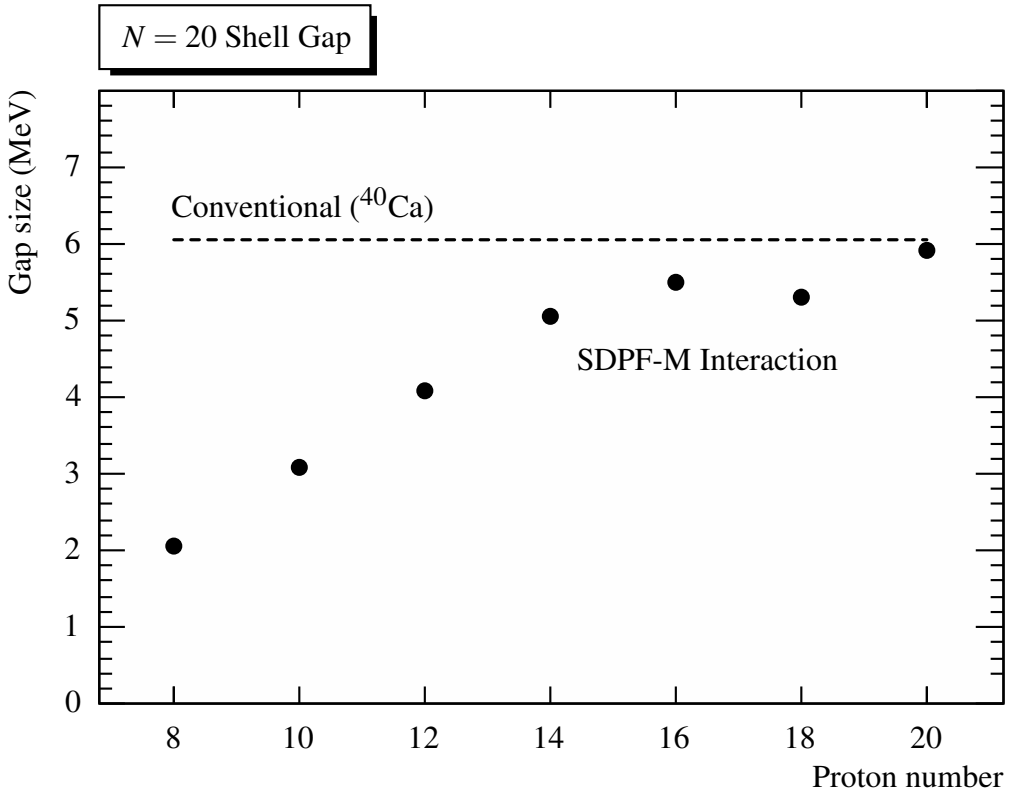

Figure 2.4: $N = 20$ shell gap for even-Z elements, $Z \leq 8 \leq 20$, calculated using the SDPF-M interaction. The gap size is large (~ 6 MeV) for calcium ($Z = 20$) and remains fairly constant from $Z = 18$ to $Z = 14$. Below that, the gap size begins to diminish rapidly, reaching a value of ~ 2 MeV for oxygen ($Z = 8$). Adapted from Ref. [21].

sd shell, is basically the Universal SD (USD) interaction [23], which consists of two-body matrix elements (TBME) that have been fit to reproduce experimental data on stable *sd* shell nuclei. The second component, relevant to the *pf* shell, is the Kuo-Brown (KB) interaction [24]. The KB interaction is obtained from the renormalized *G*-matrix, which is based on realistic nucleon-nucleon scattering. The final part, pertaining to the *sd*-*pf* cross-shell region, was originally developed in Ref. [25]. It begins with Millener-Kurath (MK) interaction [26] and adjusts the TBME $\langle 0f_{7/2}0d_{3/2} \mid V \mid 0f_{7/2}0d_{3/2}\rangle_{JT}$, J = 2-5 and T = 0-1. These TBME have all been scaled by a factor $A^{-0.3}$, similar to what is done for the USD interaction. As demonstrated in Fig. 2.4, the SDPF-M interaction reproduces the quenching of the $N = 20$ shell gap for neutron rich nuclei. The figure is a plot of the $N = 20$ gap size for even-Z elements from oxygen ($Z = 8$) to calcium

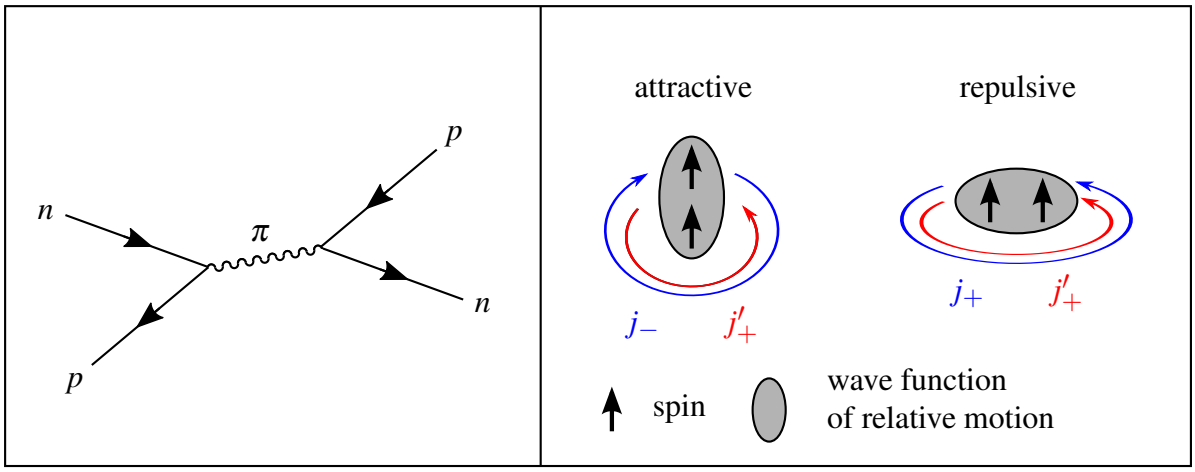

Figure 2.5: Left panel: Feynman diagram of the tensor force, resulting from one-pion exchange between a proton and a neutron [27]. Right panel: Diagram of the collision of a spin-flip nucleon pair $\{j_-,\ j'_+\}$ (left) and a non spin-flip pair $\{j_+,\ j'_+\}$ (right). In the spin-flip case, the wave function of relative motion is aligned parallel to the collision direction, resulting in an attractive interaction, while in the non spin-flip case the wave function of relative motion is aligned perpendicular to the collision direction, resulting in a repulsive interaction [27].

$(Z = 20)$. The predicted gap size is large for calcium, around 6 MeV, and stays fairly constant for nuclei with $Z = 18,\ 16,\ 14$. Below $Z = 14$, the gap size steadily decreases, reaching a value of around 2 MeV for oxygen $(Z = 8)$.

2.2 Theoretical Explanation

Changes in nuclear shell structure are driven by the tensor component of the effective nucleon-nucleon interaction [27–29]. This force is the result of one-pion exchange between nucleons, as illustrated in the Feynman diagram in the left panel of Fig. 2.5. Between protons and neutrons, the tensor force can be either attractive or repulsive, depending on the orbital and total angular momenta of the particles. If the orbital angular momenta of the proton and neutron are denoted by ℓ and ℓ', respectively, the total angular momenta will be $j_\pm = \ell \pm 1/2$ and $j'_\pm = \ell' \pm 1/2$. In the case of "spin-flip" partners $\{j_\pm,\ j'_\mp\}$, the tensor force is attractive. This is illustrated for nucleons with j_- and j'_+ in the right panel of Fig. 2.5. The two colliding nucleons have a high relative momentum, causing the spatial wave function of relative motion to be narrowly distributed

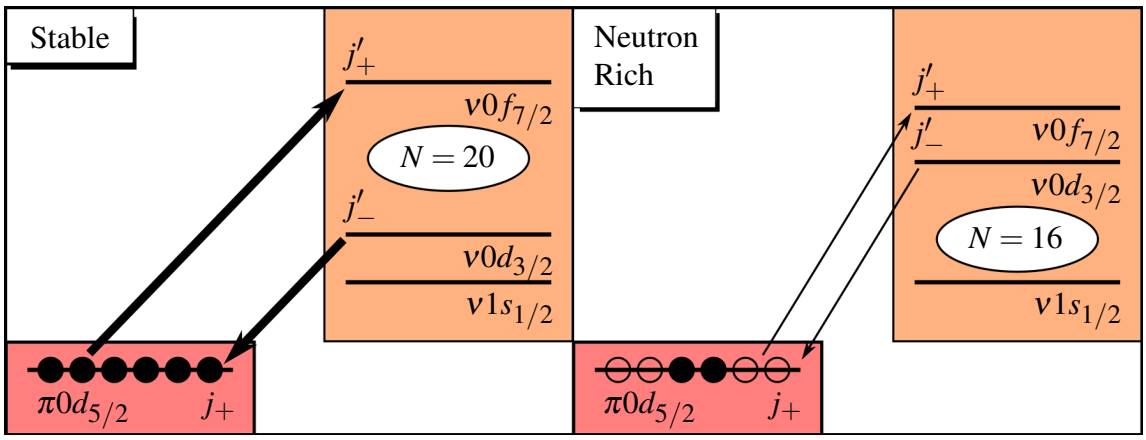

Figure 2.6: Schematic illustrating the role of the tensor force in driving changes in nuclear shell structure. Thick arrows represent a strong interaction and thin arrows a weak one. In the case of stable nuclei near $N = 20$ (left panel), there is a strong tensor force attraction between $0d_{3/2}$ neutrons and $0d_{5/2}$ protons, as well as a strong repulsion between $0f_{7/2}$ neutrons and $0d_{5/2}$ protons. These interactions lower the $0\nu d_{3/2}$ and raise the $\nu 0f_{7/2}$, resulting in a large gap at $N = 20$. In contrast, neutron rich nuclei near $N = 20$ (right panel) have a deficiency in $0d_{5/2}$ protons, weakening the attraction to $0\nu d_{3/2}$ and the repulsion to $\nu 0f_{7/2}$. This causes the $0\nu d_{3/2}$ to lie close to the $0\nu f_{7/2}$, reducing the gap at $N = 20$ and creating a large gap at $N = 16$ [27].

in the direction of the collision. This results in an attractive tensor force, analogous to the case of a deuteron. In the opposite case of $\{j_\pm,\ j'_\pm\}$, illustrated for $\{j_+,\ j'_+\}$ in the right panel of Fig. 2.5, the wave function of relative motion is stretched perpendicular to the direction of the collision, resulting in repulsion. Thus the tensor force is attractive for proton-neutron pairs with $\{j_\pm,\ j_\mp\}$ and repulsive for pairs with $\{j_\pm,\ j_\pm\}$.

The role of the tensor force in driving changes in nuclear shell structure is illustrated in Fig. 2.6. In stable nuclei near $N = 20$, the proton $0d_{5/2}$ level (j_+) is full or nearly filled. The result is a strong tensor force attraction to $0d_{3/2}$ neutrons (j'_-), as well as a strong tensor force repulsion to $0f_{7/2}$ neutrons (j'_+). These interactions serve to raise the $\nu 0f_{7/2}$ and lower the $\nu 0d_{3/2}$, producing a large shell gap at $N = 20$. In contrast, neutron rich nuclei near $N = 20$ are deficient in $0d_{5/2}$ protons. This weakens both the $\pi 0d_{5/2}$-$\nu 0d_{3/2}$ attraction and the $\pi 0d_{5/2}$-$\nu 0f_{7/2}$ repulsion, resulting in a raising of the $\nu 0d_{3/2}$ and a lowering of the $\nu 0f_{7/2}$ relative to stable nuclei. In this configuration, $\nu 0d_{3/2}$ and $\nu 0f_{7/2}$ are close in energy, quenching the large gap at $N = 20$. Furthermore, the $\nu 0d_{3/2}$ is raised in energy relative to the $\nu 1s_{1/2}$, forming a large gap at $N = 16$.

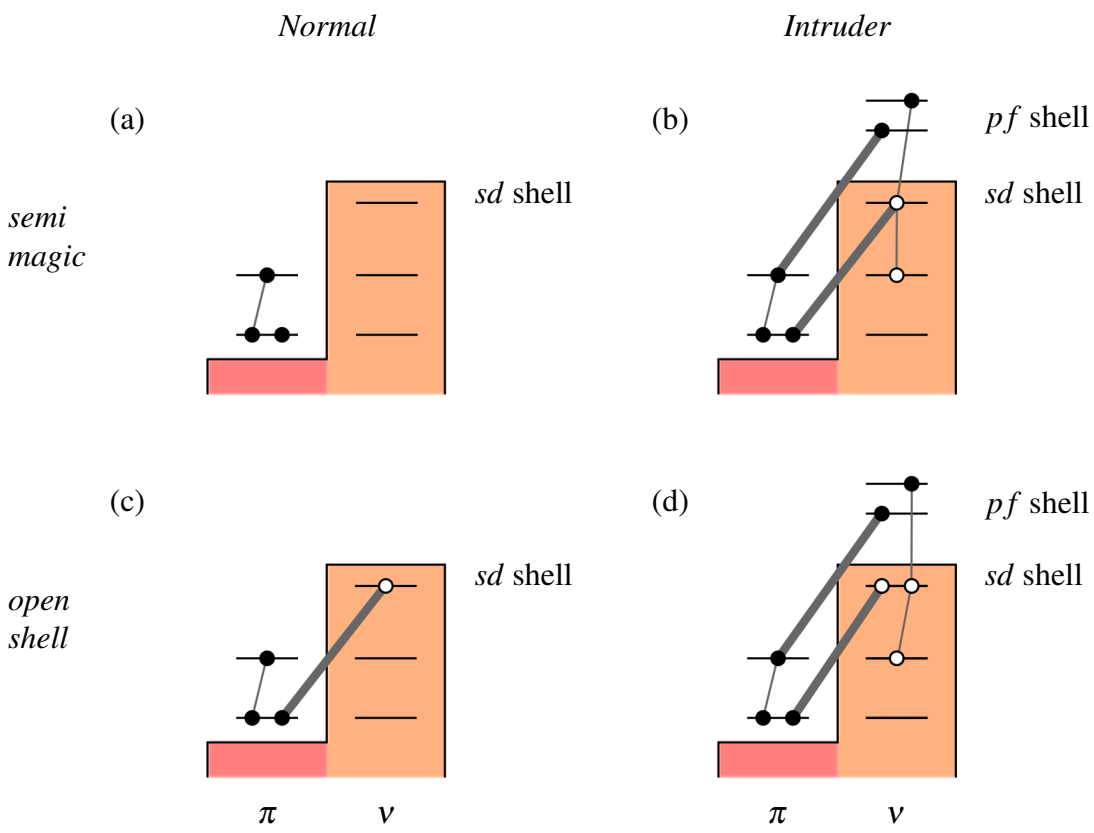

Figure 2.7: Sources of correlation energy. Thick grey lines represent a strong correlation; thin grey lines a weak one. The top panels [(a) and (b)] demonstrate the case of nuclei with closed neutron shells, while the bottom panels [(c) and (d)] show nuclei without a closed shell. In both cases, the intruder configurations [(b) and (d)] produce a stronger correlation energy, with the greatest energy gain coming from the configuration in (b) [30].

2.3 Correlation Energy

Reduction of the shell gap at $N = 20$ greatly enhances the contribution of neutron multi-particle, multi-hole (np-nh) excitations across the $0d_{3/2}$-$0f_{7/2}$ gap. Such arrangements are often referred to as "intruder configurations," the idea being that the pf shell component is intruding on the more conventional sd shell arrangement. As pointed out in 1987 by Poves and Retamosa [31], intruder configurations can result in enhanced binding due to correlation interactions between nucleons. Correlation interactions include the proton-neutron quadrupole interaction and pairing between like nucleons [32], with the binding gain of proton-neutron interactions being much greater than that of n-n or p-p pairing [30]. If the binding energy to be gained from correlation interactions is

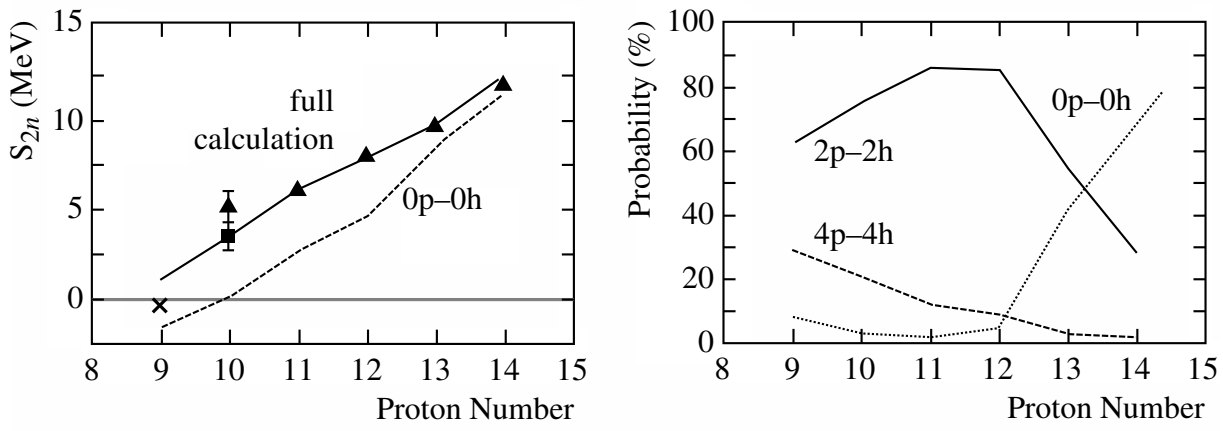

Figure 2.8: Left panel: Two neutron separation energy as a function of proton number, for $N = 20$ isotones, $9 \leq Z \leq 14$. The dashed line is a shell model calculation truncated to $0p$-$0h$, while the solid line is the same calculation without truncations. The triangle markers are experimental data, with the square marker being a more recent datum for ^{30}Ne [33]. The cross at ^{29}F is the result of a $2p$-$2h$ calculation which incorrectly predicts an unbound ^{29}F. Right panel: Occupation probabilities of $0p$-$0h$ (dotted line), $2p$-$2h$ (solid line), and $4p$-$4h$ (dashed line) configurations. Figure adapted from Ref. [34].

similar to that which is lost by exciting the nucleons into the pf shell, intruder configurations will play a significant role in the low-lying structure of the nucleus in question.

Fig. 2.7, adapted from Ref. [30], schematically illustrates the role of correlations in nuclei with normal [panels (a) and (c)] and intruder [panels (b) and (d)] configurations. In the case of a normal configuration in a semi-magic (closed $N = 20$ neutron shell, open proton shell) nucleus, the energy to be gained from correlations is small, limited to pairing interactions between protons. In contrast, for *intruder* configurations in semi-magic nuclei a large amount of energy is gained from correlations between protons and pf shell neutrons as well as protons and sd shell neutron holes. Similarly, there is an energy gain due to correlations when considering normal versus intruder configurations in open shell (no $N = 20$ magic closure) nuclei; however, the energy gain is smaller as the normal configuration already receives a significant amount of correlation energy from interactions between protons and sd shell neutron holes.

2.4 The Neutron Dripline

Perhaps one of the simplest and yet most intriguing problems of nuclear structure is that of existence: to determine which nuclear systems are bound, energetically able to exist as compound objects, and which ones are not. For neutron rich nuclei, this problems manifests itself as understanding the location of the neutron dripline, the line beyond which it is not possible to add more neutrons and still maintain a bound system. One of the most striking features of the neutron dripline is its abrupt shift towards neutron rich nuclei when transitioning from oxygen to fluorine. As shown in Fig. 2.9, adding a single proton to oxygen allows for the binding of at least six more neutrons (although ^{33}F is likely unbound, this has not yet been experimentally verified [35]).

The reason for this abrupt shift in the fluorine dripline was explored theoretically by Utsuno, Otsuka, Mizusaki, and Honma [34] with large-scale shell model calculations done using the Monte Carlo Shell Model (MCSM) [36]. The authors argue that quenching of the $N = 20$ shell gap allows for significant mixing between normal ($0p$-$0h$), intruder ($2p$-$2h$), and higher intruder ($4p$-$4h$) configurations, with the intruder configurations serving to increase the binding energy of the heaviest fluorines. In their calculations, ^{29}F is only predicted to be bound when $4p$-$4h$ and higher excitations are included, as shown in the left panel of Fig. 2.8. The calculations further reveal that the contribution of $4p$-$4h$ excitations to the ground state of ^{29}F is nearly 30% (right panel of Fig. 2.8). However, even the inclusion of high intruder configurations is not enough to bind ^{31}F. Regarding this point, the authors note that it is possible to bind ^{31}F by lowering the energy of the neutron $0p_{3/2}$ by 350 keV. They argue that a lowered $\nu 0p_{3/2}$ could result from a neutron halo or halo-like structure.

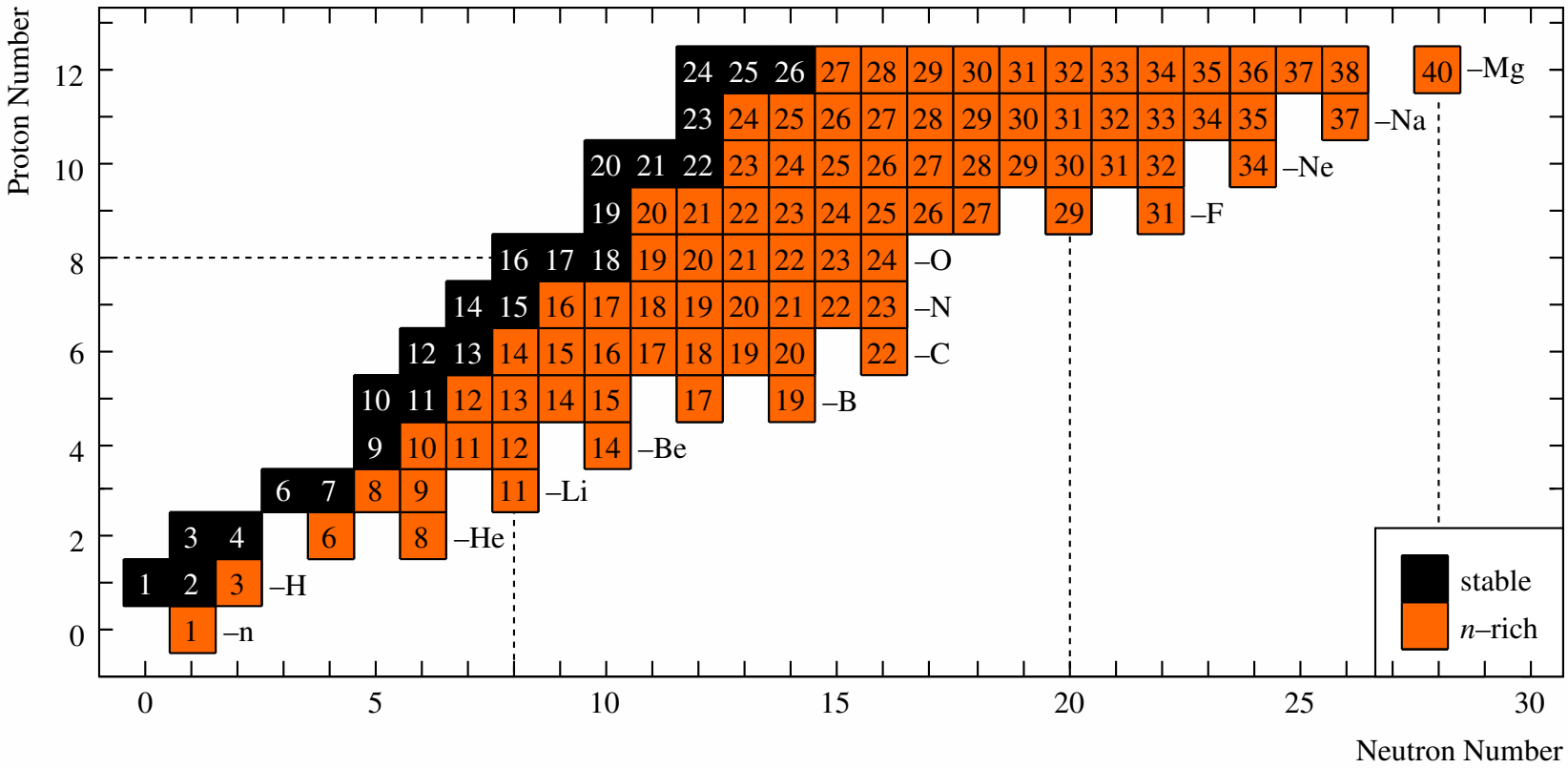

Figure 2.9: Chart of stable and bound neutron rich nuclei up to $Z = 12$. Note the abrupt shift in the neutron dripline between oxygen $(Z = 8)$ and fluorine $(Z = 9)$.

2.5 Previous Experiments

A simple yet important test of theoretical predictions is that of determining which nuclei are bound and which nuclei are not. As outlined in the previous section, theoretical reproduction of the fluorine neutron dripline is a difficult and enlightening problem—one which cannot be fully solved without *ad hoc* additions to the calculations. Experimentally, the neutron dripline around fluorine and oxygen has been explored a number of times [37–43], and it was determined in Ref. [37] that the fluorine dripline extends at least to ^{31}F. This experiment, performed at RIKEN, impinged a 94.1 AMeV beam of ^{40}Ar on a 690 mg/cm^2 tantalum target, separating reaction products in the RIPS fragment separator [44]. As shown in Fig. 2.10, eight counts of ^{31}F were observed in the experiment, confirming its bound nature. No events were observed for oxygens with $A \geq 26$, and the authors argue that ^{26,27,28}O are unbound based on their non-observation and interpolation of observed yields for other isotopes.

Another useful test of theory is the determination of excited state energies. By tuning shell model calculations to reproduce observed energies, one can better understand the makeup of the nuclei in question. In 2004, Elekes *et al.* [45] measured bound excited states in ^{25,26,27}F using the reactions ^{1}H(^{27}F, ^{25,26,27}Fγ) and measuring de-excitation gamma-rays in an array of 146 NaI(Tl) detectors surrounding the target. The observed (confidence level $\geq 2\sigma$) gamma transitions are shown in Fig. 2.11 along with *sd* shell model predictions; they are also summarized in Table 2.1. The authors note that the 727 keV transition in ^{25}F and the 681 keV transition in ^{26}F are reasonably well reproduced by *sd* shell model predictions which place the respective excited levels at 911 keV ($J^\pi = 1/2^+$) and 681 keV ($J^\pi = 2^+$). However, the *sd* calculations fail to reproduce the energies of the higher excited states in ^{25,26}F. Furthermore, they fail to reproduce the energies of either of the observed transitions in ^{27}F, regardless of whether the transitions are placed in parallel or in cascade. In all cases, the observations are significantly lower in energy than the *sd* shell model predictions.

The authors of [45] continue by presenting the results of a ^{27}F shell model calculation in the full $sdpf$ model space. This calculation predicts the first excited state to be a $1/2^+$ at 1.1 MeV.

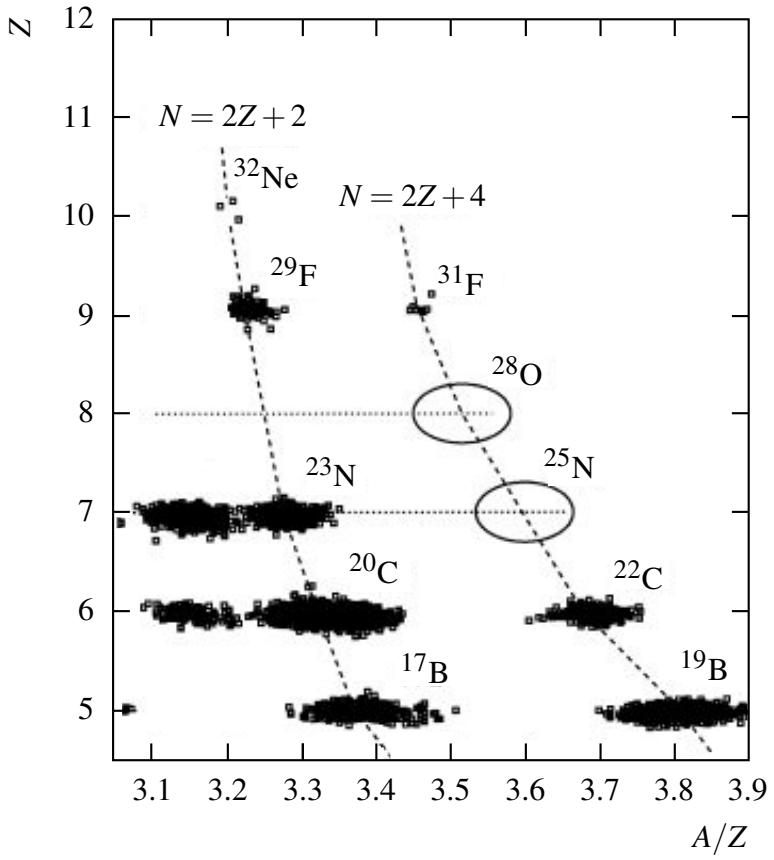

Figure 2.10: Particle identification plot from the reaction of ^{40}Ar at 94.1 AMeV on a tantalum target. Eight events of ^{31}F were observed in the experiment, while no events were observed for ^{26}O or ^{28}O. Figure adapted from Ref. [37].

Although still $\sim$ 300 keV higher than experiment, the lowering of the $1/2^+$ energy to better agree with experiment indicates that the inclusion of cross-shell excitations is necessary for a complete description of neutron rich fluorines. The authors also speculate that the 504 keV transition observed in ^{27}F is from the decay of $1/2^-$ intruder state arising from simultaneous and correlated proton-neutron excitations across the $Z = 8$ and $N = 20$ shell closures. They do not present any calculations to support this assertion.

Recently, a measurement of unbound excited states in ^{25,26}F was performed using the MoNA-Sweeper setup of the present work [46]. Unbound excited states in ^{25,26}F were populated using proton knockout (^{25}F) and charge exchange (^{26}F) reactions on a ^{26}Ne beam. A resonance in ^{25}F

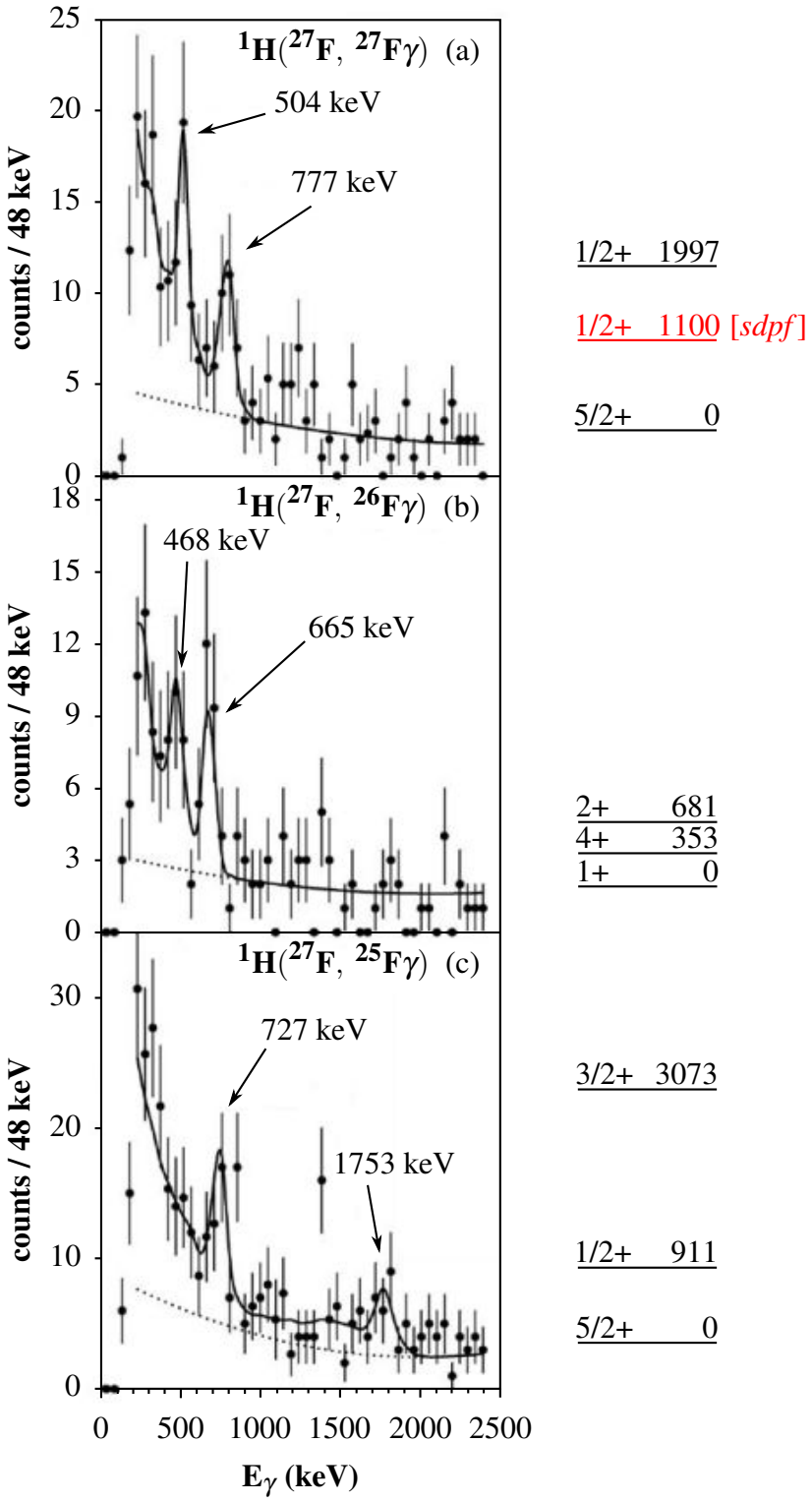

Figure 2.11: Gamma decay spectra of bound excited states in ^{27,26,25}F, along with *sd* shell model predictions on the right of the figure. For ^{27}F, the $1/2^+$ excited state prediction from a calculation done in the full *sdpf* model space is also included in red. Adapted from Ref. [45].

Table 2.1: Bound state gamma transitions observed in [45].

Nucleus	*Peak Position (keV)*
^{25}F	727(22)
	1753(53)
^{26}F	468(17)
	665(12)
^{27}F	504(15)
	777(19)

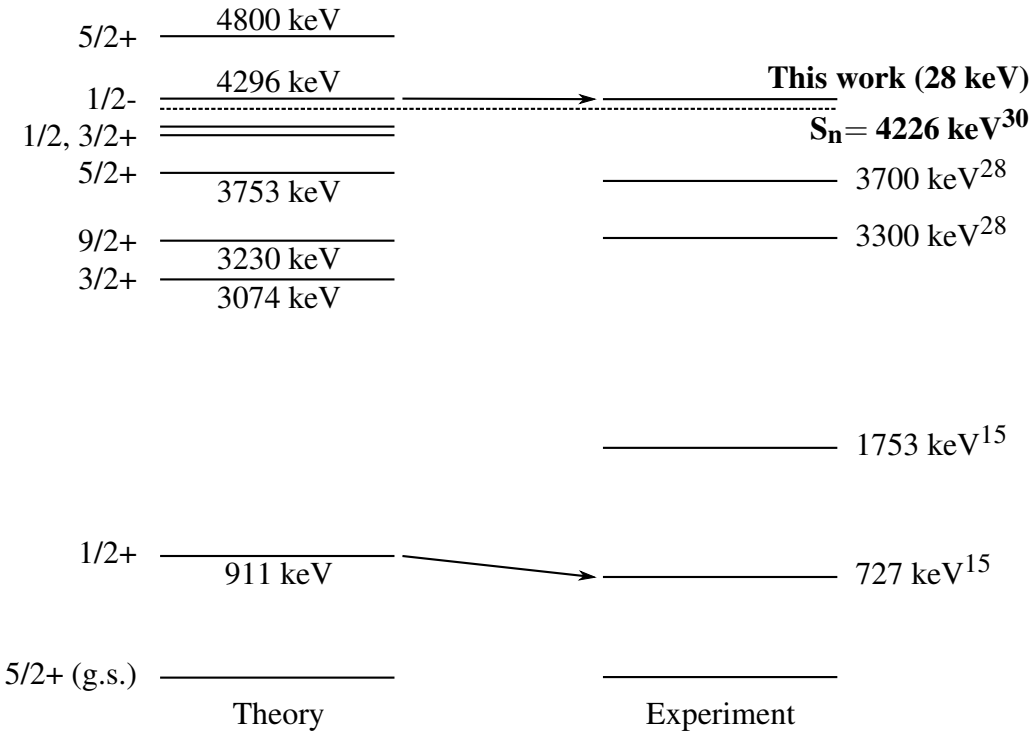

Figure 2.12: Comparison of experimental and theoretical levels for ^{25}F from Ref. [46]. The superscripts next to the experimental level energies denote references numbers within [46], and the measurement of [46] is labeled "this work" in the figure.

was observed with $28\,(4)$ keV decay energy, corresponding to an excited level at $4254\,(112)$ keV. The authors also claim to observe a resonance in ^{26}F with decay energy 206^{+36}_{-35} keV; such a resonance would correspond to an excited level in ^{26}F at $1007\,(119)$ keV. The ^{25}F result is compared to shell model calculations that allow for $2p$-$2h$ neutron excitations across the sd-pf shell gap, as well as proton excitations between the p and sd shell. The calculations predict a $1/2^-$ excited state at 4296 keV in ^{25}F. If this is indeed the resonant state observed in the experiment, then the calculations would be in excellent agreement. Based on calculated spectroscopic overlap with the ground state of ^{26}Ne, the authors argue that their observed resonance is likely the $1/2^-$. If they are correct, it would indicate that a shell model including neutron $2p$-$2h$ and proton p-sd excitations is sufficient to describe the level structure of ^{25}F, at least up to and around the one-neutron separation energy. No comparison to theory is made for the ^{26}F resonance as experimental resolution and background contributions make the interpretation of this decay spectrum extremely difficult.

The role of pf shell configurations in the binding of ^{29,31}F can also be investigated by measuring properties of neighboring elements in the same mass region as the heavy fluorines. Along these lines, measurements of two-proton knockout cross sections to excited states in ^{30}Ne have recently been performed with the goal of understanding the contribution of intruder configurations to the structure of ^{30}Ne and the implications for the binding of ^{29,31}F [14]. In this work, a beam of ^{32}Mg was impinged on a beryllium target, with reaction products separated and identified in the S800 spectrometer [47] and gammas collected in an array of 32 segmented germanium detectors. Two transitions were observed in coincidence with ^{30}Ne: a strong one at $792(4)$ keV and a weaker one at $1443(11)$ keV, as shown in Fig. 2.13. The 792 keV transition was also measured in Ref. [15] with far lower statistics. The authors of [14] place their observed transitions in cascade, assigning the lower transition to the 2^+ first excited state in ^{30}Ne and the higher transition to the 4^+ second excited state at 2235 keV. The authors then compare their measured excited state energies to three separate shell model calculations: one in the sd shell only; another including $2p$-$2h$ cross-shell excitations; and the final one, done in the MCSM, including mixed $0p$-$0h$, $2p$-$2h$, and $4p$-$4h$ configurations. As with ^{27}F, the sd shell calculation greatly overpredicts the first excited

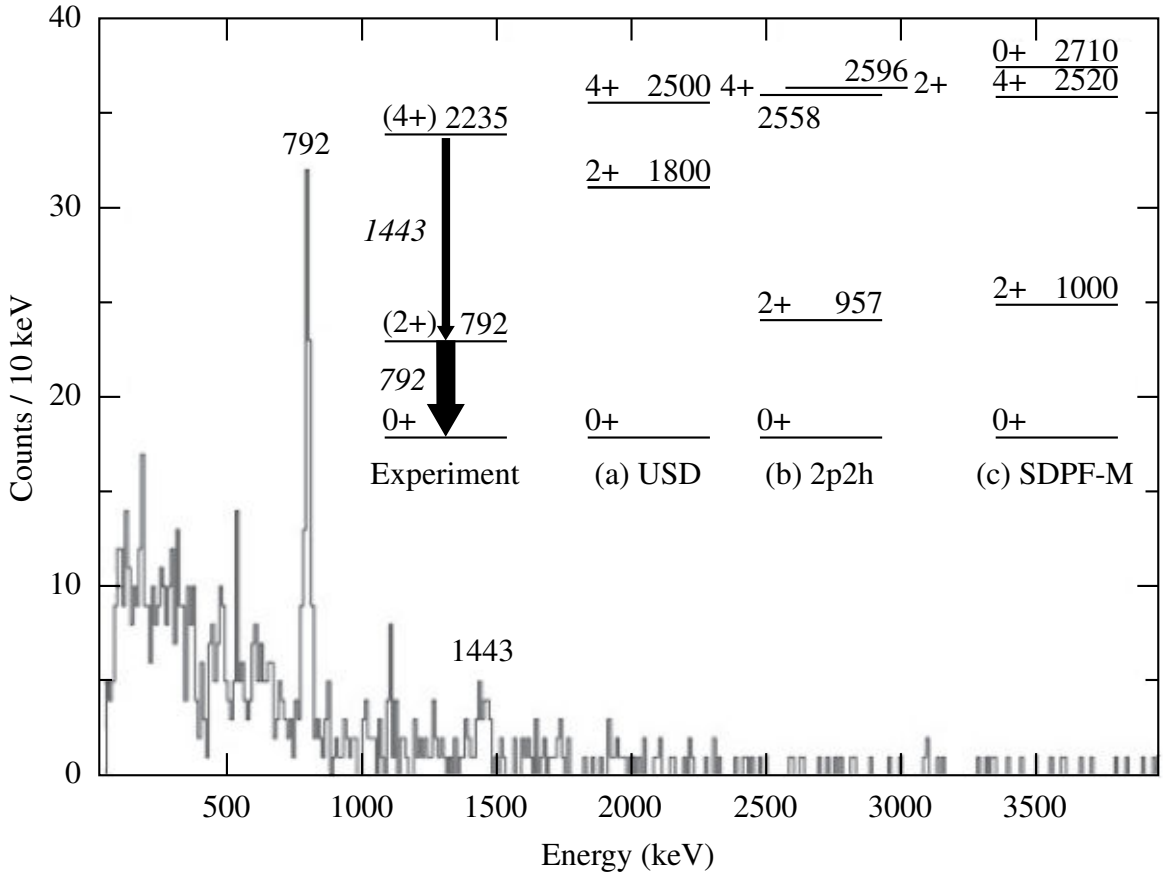

Figure 2.13: ^{30}Ne gamma de-excitation spectrum from Ref. [14]. Experimental level assignments and a variety of theoretical predictions are also included.

state energy, placing it $\sim$ 1 MeV too high at 1800 keV. The $2p$-$2h$ and MCSM calculations are closer to experiment, lowering the energy to 957 keV and 1000 keV, respectively.

Following the discussion of excited state energies, the authors of [14] discuss their results for two-proton knockout cross sections from ^{32}Mg to the 0^+, 2^+, and 4^+ states in ^{30}Ne. In all cases, their results are smaller than the $2p$-$2h$ and MCSM predictions by a factor of four or greater (the *sd* shell model predicts even higher cross sections). The authors argue that the mismatch between theory and experiment is the result of ^{30}Ne having a large $4p$-$4h$ component ($\sim$ 50% in the ground state), resulting in a smaller than predicted overlap with ^{32}Mg, whose ground state was measured to have $2p$-$2h$ components at a level of 90% or greater [48]. This mismatch is not accounted for in the shell models, resulting in the overprediction of $2p$ knockout cross sections. The authors speculate

that extending the $sdpf$ shell model space to include the $0f_{5/2}$ and $1p_{1/2}$ levels—as opposed including only the lower lying $0f_{7/2}$ and $1p_{3/2}$ as presently done—could predict a greater $4p$-$4h$ composition of ^{30}Ne (and also of ^{29,31}F). They also explore the possibility that dripline effects such as weak binding can increase the $4p$-$4h$ occupation of ^{30}Ne. Weak binding allows the wave function for a low-ℓ orbital to significantly extend beyond the average nuclear radius. This causes the level energy to be less sensitive to changes in radius (mass number), altering the density of states near the Fermi surface and causing multi-particle, multi-hole configurations to be favored. Shell models are not able to account for these changes due to their use of harmonic oscillator wave functions. The authors simulate these effects by performing an *ad hoc* lowering of the $0f_{7/2}$ and $1p_{3/2}$ energies by 800 keV and making shell model calculations. The calculations predict the ^{30}Ne ground state to be 49% $4p$-$4h$, in agreement with the authors' observation. The $4p$-$4h$ components of the ground states of ^{29}F and ^{31}F are predicted to be 51% and 36%, respectively. This lowering of the $0f_{7/2}$ and $1p_{3/2}$ energies is similar to the 350 keV lowering of the $1p_{3/2}$ in Ref. [34], which allows for a prediction of bound ^{31}F.

The present work deals with neutron decay spectroscopy performed on unbound states in ^{27}F and ^{28}F. In particular, measurements of the ground state binding energy of ^{28}F and the excitation energy of a neutron-unbound excited state in ^{27}F are presented and interpreted via comparison with shell model predictions. These measurements provide experimental data in a region where very little is known, and they will help to improve upon the current understanding of the evolution of nuclear structure in neutron rich nuclei.

Chapter 3

EXPERIMENTAL TECHNIQUE

3.1 Invariant Mass Spectroscopy

The neutron-unbound states under investigation in this work decay primarily through neutron emission, a process which happens on a very short timescale ($\sim 10^{-21}$ s). The decay products are the emitted neutron, n, and the residual charged fragment, f, as illustrated in Fig. 3.1. The decay energy of the de-excitation is calculated using the technique of invariant mass spectroscopy. This technique is derived from the conservation of relativistic four-momentum,

$$\mathbf{P} = (E,\ \vec{p}\,), \tag{3.1}$$

where $\mathbf{P}$ is the relativistic four-momentum of the particle in question; E is its total energy; and $\vec{p}$ is its Euclidean momentum vector.[1] Conservation of $\mathbf{P}$ can be expressed as

$$\mathbf{P}_i = \mathbf{P}_f + \mathbf{P}_n, \tag{3.2}$$

where the subscripts i, f, and n refer to the initial nucleus, residual nucleus and emitted neutron, respectively.

Squaring both sides of Eq. (3.2) yields

$$\mathbf{P}_i^2 = \left(\mathbf{P}_f + \mathbf{P}_n\right)^2 \equiv W^2, \tag{3.3}$$

where W is defined to be the invariant mass of the system, a constant. In Euclidian terms, this is expressed as

$$W^2 = \left(E_f + E_n\right)^2 - \|\mathbf{p}_f + \mathbf{p}_n\|^2 \tag{3.4}$$

$$= m_f^2 + m_n^2 + 2\left(E_f E_n - \mathbf{p}_f \cdot \mathbf{p}_n\right). \tag{3.5}$$

[1] Here we use natural units, $c \equiv 1$.

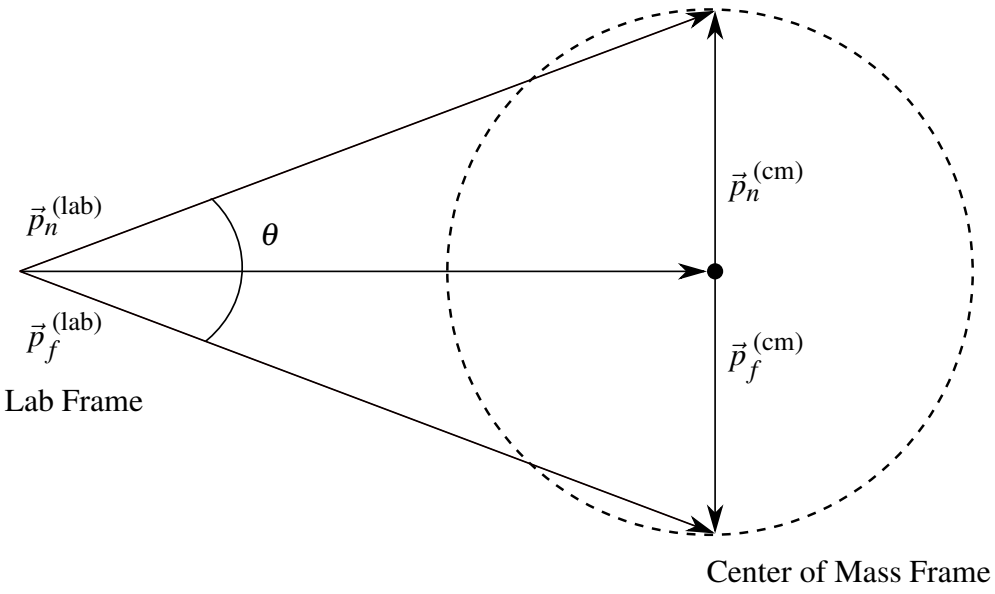

Figure 3.1: Decay of an unbound state via neutron emission.

Taking the square root of Eq. (3.5) and expanding the momentum dot product gives an expression for W :

$$W = \sqrt{m_f^2 + m_n^2 + 2\left(E_f E_n - p_f p_n \cos\theta\right)}, \tag{3.6}$$

where θ is the opening angle between the fragment and the neutron in the lab frame. Finally, subtracting the masses of the decay products results in an expression for the decay energy:

$$E_{\mathrm{decay}} = \sqrt{m_f^2 + m_n^2 + 2\left(E_f E_n - p_f p_n \cos\theta\right)} - m_f - m_n. \tag{3.7}$$

In order to make a measurement of the decay energy, as expressed in Eq. (3.7), it is necessary to measure the energy and angle of each decay product as it leaves the reaction target. The way in which these quantities are calculated will be explained in Section 4.3.

One limitation of invariant mass spectroscopy is that it is only able to measure the difference in energy between the initial unbound state and the state to which it decays. In some cases, this

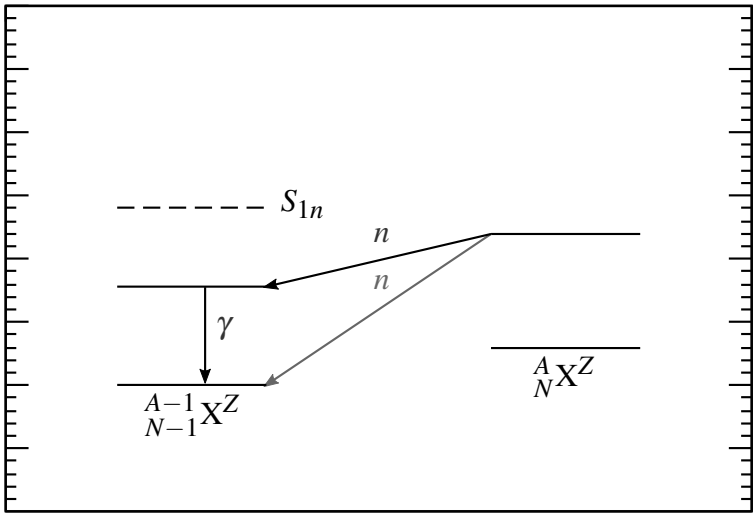

Figure 3.2: Illustration of the two possible decay processes of an unbound state which lies higher in energy than a bound excited state of the daughter. The state can either decay through direct neutron emission to the ground state of the daughter (grey arrow) or by neutron emission to an excited state in the daughter and subsequent gamma emission (black arrows).

causes an ambiguity in the absolute placement of the level in question. In particular, if the daughter nucleus has bound excited states, the unbound state has the option to neutron decay by one of two processes, as illustrated in Fig. 3.2. The first is direct neutron emission to the ground state of the daughter, and the second is a two step process: the unbound state first neutron decays to a bound excited state of the daughter which then de-excites by gamma emission. It is possible to distinguish between the two processes experimentally by measuring de-excitation $\gamma-$rays in coincidence with the neutron and the charged fragment, and this is the approach taken in the present work.

3.2 Beam Production

The reaction used to populate unbound states in ^{28}F is single proton knockout on a ^{29}Ne beam, while excited states in ^{27}F are likely populated in a two step process, starting with proton knockout to a highly excited state in ^{28}F. This highly excited state then decays into the unbound state of ^{27}F for which the breakup is observed. It is also plausible that unbound excited states in ^{27}F are populated by direct $1p$-$1n$ knockout. The desired beam nucleus, ^{29}Ne, is $\beta-$unstable ($t_{1/2} \simeq 15$ ms

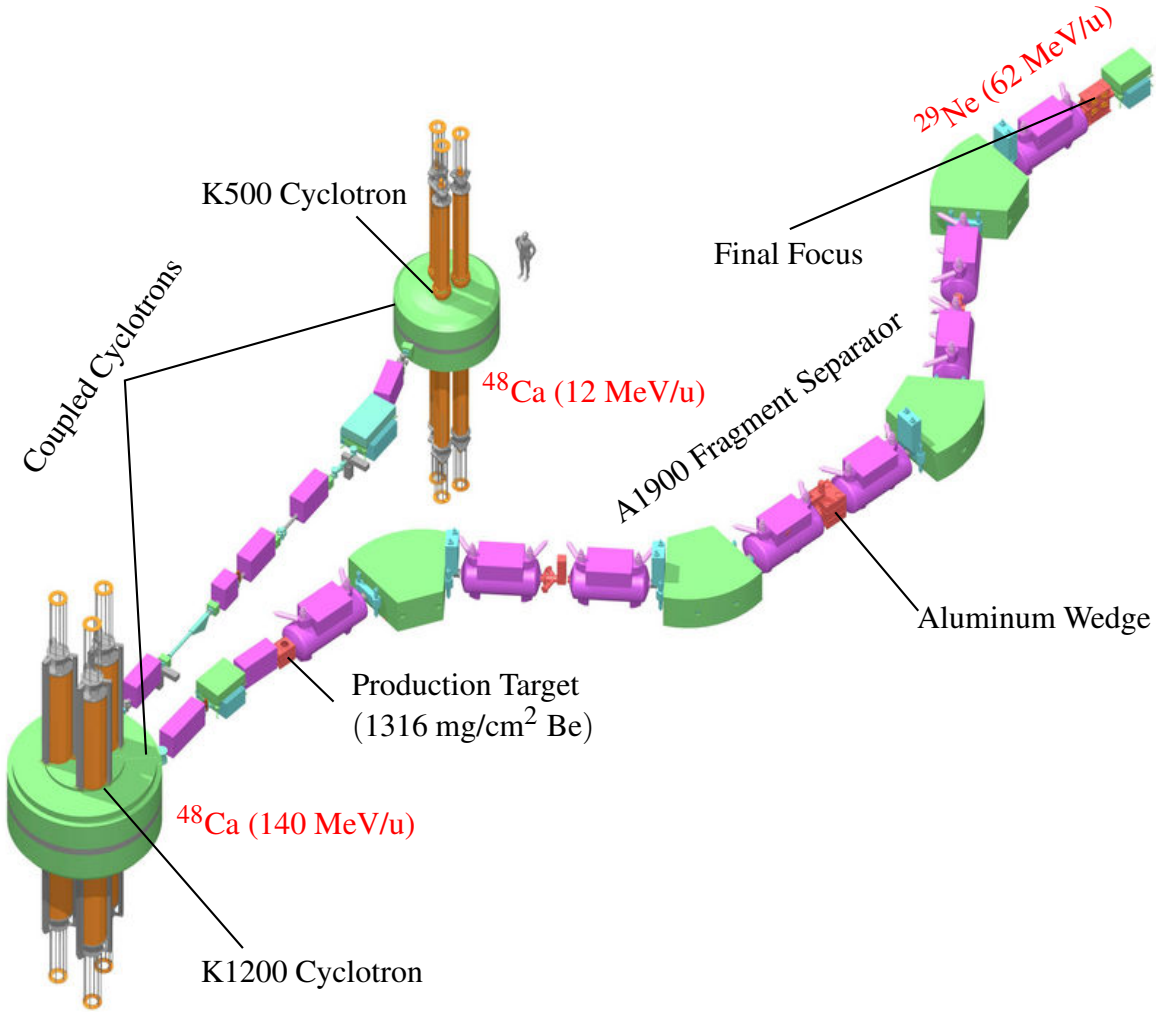

Figure 3.3: Beam production.

[49]), so it cannot be accelerated directly; instead the method of fast fragmentation [50] is used for beam production.

A diagram of the beam production mechanism is shown in Fig. 3.3. A beam of stable ^{48}Ca is first accelerated to an energy of 140 MeV/u in the NSCL coupled K500 and K1200 cyclotrons [51], exiting the K1200 fully ionized. It is then impinged on a beryllium target with a thickness of 1316 mg/cm^2. The beam undergoes fragmentation and other reactions in the target, producing a wide variety of nuclear species. These reaction products pass through the A1900 fragment separator [52] which selects ^{29}Ne fragments based on magnetic rigidity, $B\rho = \mathbf{p}/q$. The selection is

accomplished by tuning the four dipole magnets of the A1900 to the expected rigidities of the ^{29}Ne reaction products, with the final dipole being at 3.469 Tm. An achromatic aluminum wedge is also included after the second dipole to selectively disperse reaction products and improve separation. This wedge also has the undesired effect of creating tertiary reaction products which can have the same magnetic rigidity as the desired ^{29}Ne. Finally, slits are located at the intermediate focal plane, allowing the user to tune the total momentum acceptance of the device. Since the expected production rate of ^{29}Ne fragments is low, the slits are opened to a full momentum acceptance of 3.93%. The final energy of the ^{29}Ne beam delivered to the experimental vault is 61.9 ± 4.7 MeV/u.

Since the A1900 is only able to make selections based on $B\rho$, it is not possible to obtain a pure beam of ^{29}Ne. Isotopes of other elements will end up with roughly the same rigidity after passing through the device, and, as mentioned before, tertiary reaction products created in the wedge can also compose a portion of the beam. The A/Z of these contaminants is different from that of the beam, causing their velocity to also differ. As a result, the contaminants can be separated in off-line analysis as explained in Section 4.2.1.

3.3 Experimental Setup

A diagram of the experimental setup is shown in Fig. 3.4. After exiting the A1900, the beam is passed through a pair of plastic timing scintillators which provide a measurement of its time of flight. It also passes through a pair of position sensitive Cathode Readout Drift Chambers (CRDCs), which allow a calculation of its incoming position and angle. After the second CRDC, the beam is focused by a quadrupole triplet magnet onto the reaction target, which is made of ^{9}Be and is 288 mg/cm^2 in thickness.

After undergoing reactions in the Be target, there are up to three types of particles which need to be measured: charged fragments, neutrons and gammas. Gammas are recorded in the CAEsium-iodide ARray (CAESAR) [53], an array of 182 CsI(Na) crystals that surrounds the target and measures the gamma energies. Neutrons continue to travel at close to beam velocity and are recorded in the Modular Neutron Array (MoNA) [54, 55] which is located at zero degrees

behind the target and measures the neutrons' positions and times of flight. Charged fragments also continue to travel at close to beam velocity but are deflected away from zero degrees by the Sweeper magnet [56], a dipole. After deflection, the charged particles are passed through a series of detectors whose measurements make it possible to identify their nuclear species and to reconstruct their four-momenta at the target. Further details regarding the operation of these experimental systems are presented in the following subsections.

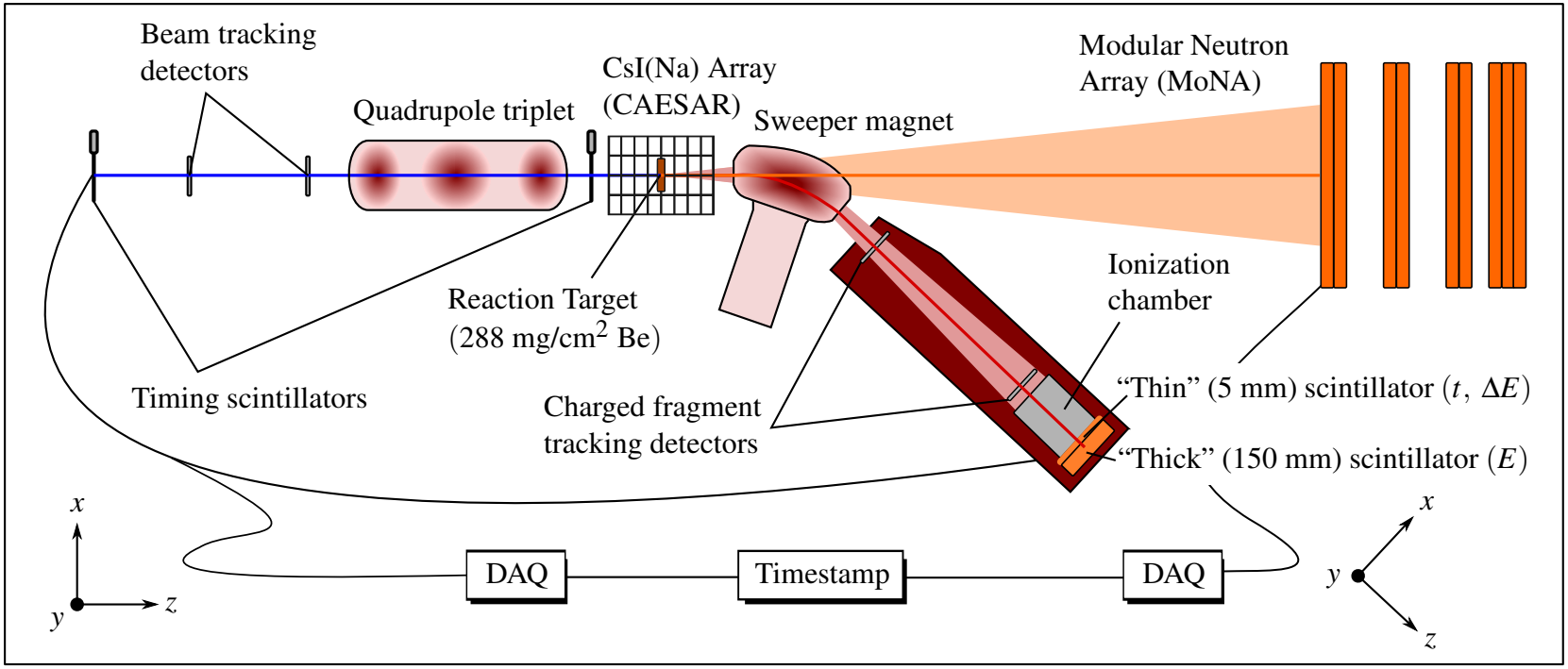

Figure 3.4: Experimental setup.

3.3.1 Beam Detectors

As mentioned, the time of flight of the beam is measured in a pair of plastic scintillators. The first is located at the focal plane of the A1900, and the second is located 44.3 cm upstream of the reaction target, resulting in a total flight path of 10.44 m. When a charged particle passes through one of the plastic scintillators, it creates electron-hole pairs which recombine, emitting photons. These photons are collected in a photo-multiplier tube (PMT) that is optically coupled to the plastic. The PMT serves to amplify the luminous signal and convert it to an electrical signal that can be recorded. The detection process happens on a fast timescale, allowing a time measurement with good resolution (< 1 ns). The scintillator located at the A1900 focal plane is 1008 μm thick, while the one close to the reaction target is 254 μm. Each scintillator is made of Bicron BC-404 material ($H_{10}C_9$) [57] and is coupled to a single PMT. In addition to the timing scintillators, a time measurement is also taken from the cyclotron radio-frequency (RF) signal.

The emittance of the incoming beam particles is measured with a pair of position sensitive CRDCs. A dramatization of the operation of a CRDC is shown in Fig. 3.5. Each detector is filled with a gas mixture of 80% CF_4 and 10% iso-butane at a pressure of 50 Torr. When charged particles pass through the gas, they ionize some of its molecules, releasing electrons. These electrons are subjected to a -250 V drift voltage, causing them to travel in the non-dispersive[2] direction towards an anode wire which collects the charge. The anode wire is held at a potential of $+1100$ V. Located near the anode wire are 64 aluminum pads with a 2.54 mm pitch, and the charge collected on the anode wire in turn induces a charge on these pads. Additionally, a Frisch Grid is used to remove any dependence of the pulse amplitude on where the charged fragment hits the gas.

The position of the charged fragment in the dispersive direction is determined from the distribution of the charge on the aluminum pads. The charge collected on each pad is plotted as a function of pad number, and the centroid is determined by fitting with a Gaussian. This centroid can be converted from pad space to position space by a linear transformation, using the pad pitch

[2]Through this document, the dispersive plane will be referred to as x and the non-dispersive plane as y. z refers to the beam axis.

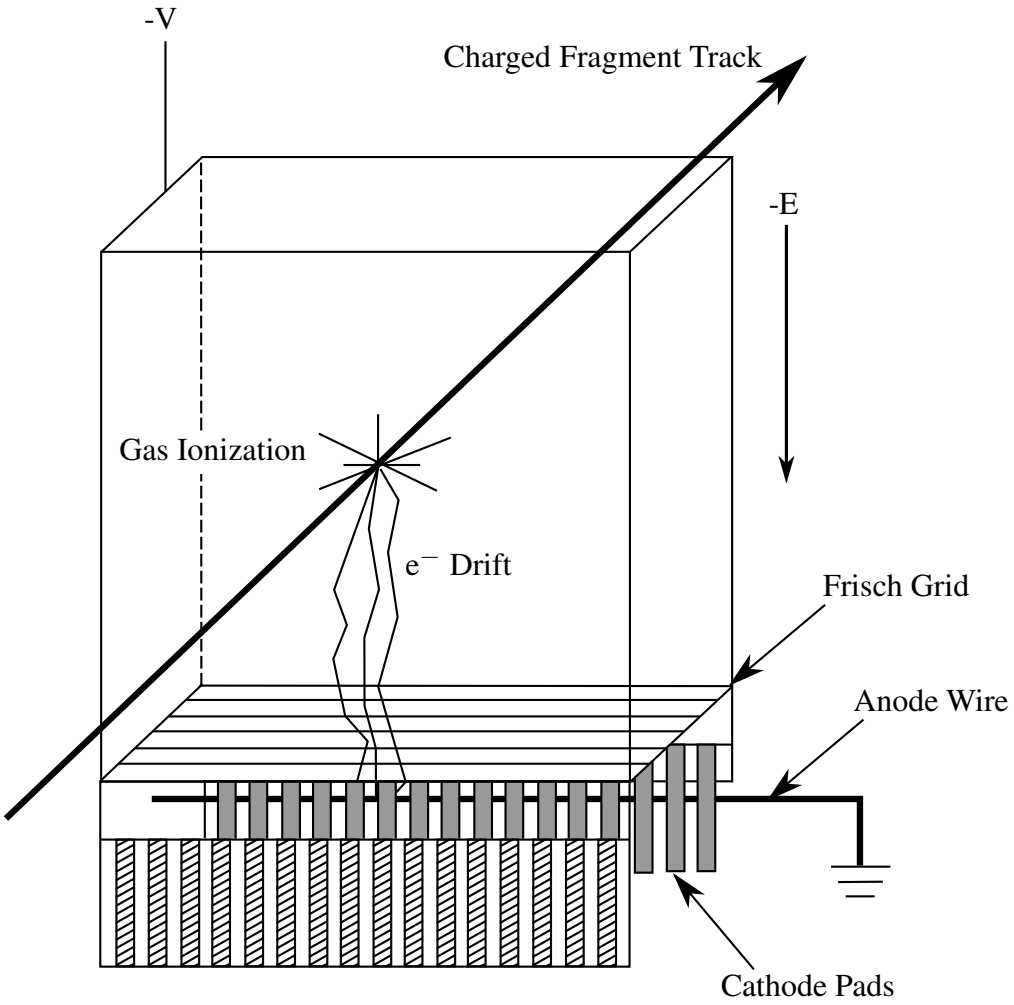

Figure 3.5: Dramatized view of the operation of a CRDC. Charged fragments interact in the gas, releasing electrons. The electrons are subjected to a drift voltage in the non-dispersive direction and are collected on the anode wire, in turn causing an induced charge to form on a series of aluminum pads. Position in the dispersive direction is determined by the charge distribution on the pads, while position in the non-dispersive direction is determined from the drift time of the electrons.

of 2.54 mm as the slope. The offset is determined from data taken when a tungsten mask, with holes drilled at known locations, shadows the detector. In the non-dispersive direction, the fragment position is determined from the time it takes the electrons to drift from the interaction point to the anode wire. The drift time is converted to absolute position using data taken with the tungsten mask in place.

Located after the beam tracking CRDCs is a quadrupole triplet magnet which serves to focus the beam particles onto the target. The field of this magnet is mapped, allowing the position and angle on the reaction target to be calculated from the position measurements of the beam tracking CRDCs. The outer quadrupole magnets have an effective length of 22.8 cm, while the inner quad has an effective length of 41.6 cm. Each quad is separated by a free drift of 22.8 cm. The optics of the triplet are tuned to produce a beam-spot which is narrow in angle and wide in position. Such a parallel beam is desired, as it improves the transmission of reaction products through the Sweeper.

3.3.2 Sweeper

The Sweeper magnet is a dipole with a bending angle of 43° and a radius of 1 meter. It has a large vertical gap of 14 cm to allow neutrons to pass on to MoNA uninhibited. Its maximum rigidity is 4 Tm, and for the present experiment it was set to a rigidity of 3.3065 Tm. This setting was chosen because it optimizes the transmission of ^{27}F reaction products.

Following the Sweeper is a pair of position sensitive CRDC detectors. The operation of these CRDCs is identical to that of the beam tracking CRDCs, as explained in Section 3.3.1. However, the specifications of the detectors are different. Each detector measures 30×30 cm^2 and has 128 pads (2.54 mm pitch) in the dispersive direction. The gas pressure for each detector is 50 torr, while the anode and drift voltages are set at $+950$ V and -800 V, respectively.

Following the downstream CRDC is an ionization chamber. It serves to measure energy loss, which is useful for element identification as explained in Section 4.2.3. Similar to the CRDCs, the ionization chamber is gas-filled, here the gas being a mixture of 90% argon and 10% methane at 300 torr. Charged particles traveling through the gas release electrons which travel via a -800 V

Table 3.1: List of charged particle detectors and their names. Detectors are listed in order from furthest upstream to furthest downstream.

Detector Name	*Detector Type*
RF	Time Measurement
A1900 Scintillator	Timing Scintillator
TCRDC1	Cathode Readout Drift Chamber
TCRDC2	Cathode Readout Drift Chamber
Target Scintillator	Timing Scintillator
CRDC1	Cathode Readout Drift Chamber
CRDC2	Cathode Readout Drift Chamber
Ion Chamber	Ionization Chamber
Thin Scintillator	Timing/Energy Loss Scintillator
Thick Scintillator	Total Kinetic Energy Scintillator

drift voltage to sixteen charge collection pads held at +1100 V. The total amount of charge collected on the pads is summed to give a measurement of energy deposited in the gas.

Downstream of the ionization chamber are two plastic (BC-404) scintillators. These detectors operate in the same way as the timing scintillators described in Section 3.3.1. Due to their larger area of 40×40 cm^2, the scintillators are coupled to four PMTs, with each PMT being located near a corner of the detector. The upstream scintillator is 0.5 cm in thickness, and its primary purpose is to measure the time of flight of the charged fragments. Additionally, the charge deposited in the detector can be used as an energy loss measurement, complimenting that of the ionization chamber. The downstream scintillator is 15 cm thick and stops the beam. Thus the charge collected in the detector gives an indication of the total kinetic energy of the fragment.

For ease of reference, each charged particle detector in the setup is given a unique name. These are listed in Table 3.1. Furthermore, each of the four PMTs in the thick and thin scintillators is given a numeric designation, outlined in Table 3.2. The point at which reaction products are narrowest in dispersive position is referred to as the "focal plane" or "focus," despite not being a true focus in the ion-optical sense. Similarly, the chamber housing all of the detectors which are downstream of the Sweeper is called the "focal plane box."

Table 3.2: Numeric designations for the PMTs in the thin and thick scintillators.

Number	*PMT Location*
0	Upper-Left
1	Lower-Left
2	Upper-Right
3	Lower-Right

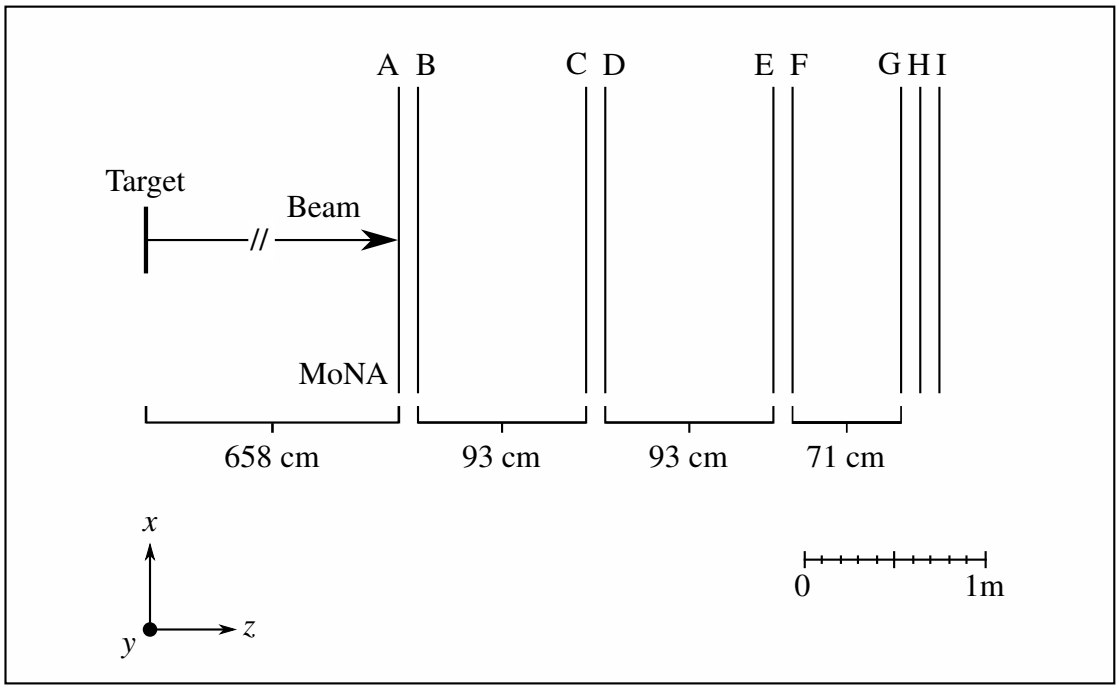

Figure 3.6: Location of MoNA detectors. Each wall is sixteen bars tall in the vertical (y) direction, and the center of each wall in the vertical direction is equal to the beam height. The black lines in the figure indicate the central position in z of the corresponding MoNA bar.

3.3.3 MoNA

MoNA is an array of 144 organic plastic scintillator bars, each bar being made of BC-408 material, which has an H:C ratio of 1.104 [57]. The bars measure $200 \times 10 \times 10$ cm^3 and are coupled through light guides to a PMT on either end. Due to the modular design of the detector, it can be arranged in a number of different configurations. In the present experiment, the array was arranged in nine walls, each 16 detectors high. Each wall is labeled with a letter from A–I, with wall A being the most upstream. Within a wall, the bars are labeled numerically from 0—15, with bar 0 being closest to the floor. The walls are arranged into four groups: the first three are two walls deep,

while the final one is three walls deep. Within a group, the detectors are placed flush against one another. The spacing between groups and overall distance from the reaction target are indicated in Fig. 3.6.

Since neutrons lack electrical charge, they cannot directly excite atoms in the MoNA bars to release scintillation light. Instead the neutrons interact via the strong interaction with protons in the hydrocarbon. When a neutron strikes a proton directly, it knocks the proton out of the lattice. This recoil proton can then generate scintillation light in a process similar to the one described in Section 3.3.1. This light is then collected in the PMTs and converted into electrical signals. The anode signal is sent to a constant fraction discriminator (CFD), where the exact time of the pulse is determined from the signal shape. The output of the CFD is fed into a time to digital converter (TDC), which, along with a common stop signal from the target scintillator, measures the time of flight of the neutron. The dynode signal is fed into a charge to digital converter (QDC), which measures the signal size, giving an indication of the amount of energy deposited in the plastic. The light deposition signal is calibrated into units of MeV-electron equivalent (MeVee), as explained in Section 4.1.2.3.

3.3.4 CAESAR

CAESAR is an array of 192 CsI(Na) crystals, situated in ten rings which surround the target. The rings are labeled A–J, with A being the most upstream. An outline of the detector arrangement is shown in Fig. 3.7. The crystals in the four outer rings have dimensions of $3 \times 3 \times 3$ in^3, while those in the inner rings have dimensions of $2 \times 2 \times 4$ in^3. The outermost rings each hold ten crystals, and their neighbors each hold fourteen. The remaining inner rings contain 24 crystals each. The crystals are encased in an aluminum housing 1 mm in thickness to shield them from water, and the 1.5 mm gap between the crystal and the aluminum is filled with reflective material. Each crystal is coupled to a PMT for collection of scintillation light. As PMTs rely on the flow of free electrons to operate, their operation is highly sensitive to the presence of magnetic fields. The Sweeper magnet produces large fringe fields, on the order of hundreds of Gauss, so a steel magnetic shield was

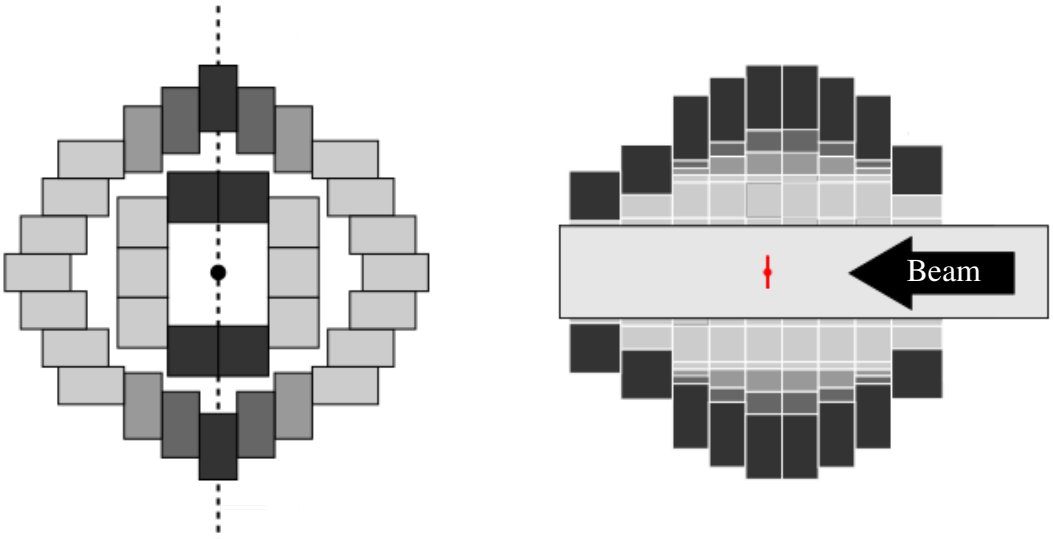

Figure 3.7: Arrangement of CAESAR crystals. The left panel shows a cross-sectional view perpendicular to the beam axis of an outer and an inner ring. The right panel shows a cross sectional view parallel to the beam axis of the nine rings used in the experiment. Figure taken from Ref. [53].

constructed and placed between the Sweeper and CAESAR.

Due to space limitations, only nine of the ten rings were used in the present experiment; the ring selected for omission was the one most upstream of the target. This ring was chosen because the Lorentz boost causes $\gamma-$ray emission to be forward focused. In its full configuration, the efficiency of CAESAR for $\gamma-$rays with $v/c = 0.3$ is approximately 30%, and its in-beam resolution is approximately 10% [53].

As CsI(Na) is an inorganic material, the process for producing scintillation light differs from that of organic plastic scintillators discussed previously. When a $\gamma-$ray enters the crystal, it can excite an electron from the valence band into a higher energy band where it is able to drift through the material. When the drifting electron encounters an impurity in the crystal (here a sodium atom), it ionizes it. The hole created in this ionized atom can then be filled by another electron, releasing a photon [58]. CsI(Na) is well suited for gamma detection, as it has good stopping power for $\gamma-$rays, as well as good intrinsic energy resolution.

Table 3.3: Logic signals sent between the Sweeper and MoNA subsystems and the Level 3 XLM. A valid time signal is one which surpasses the CFD threshold.

Logic Signal	*Description*
Sweeper Trigger	Valid time signal in the thin scintillator upper-left PMT.
MoNA Trigger	Valid time signal in *any* MoNA PMT.
MoNA Valid	Valid time signal in at least two PMTs on the same bar.
System Trigger	Coincidence condition satisfied in Level 3.
Busy	The system in question is working to process event data.

3.3.5 Electronics and Data Acquisition

Data from MoNA and from Sweeper/CAESAR were recorded on separate data acquisition (DAQ) machines. Each event was tagged with a unique 64-bit number, and data from the two systems were merged off-line before being analyzed. This is referred to as running in "timestamp mode," although the event tags are not timestamps in the strict sense as the clock generating them does not run continuously. The experiment was set up to require coincidences between the Sweeper and MoNA, and CAESAR was essentially a passive add on to the Sweeper system, not factoring into the trigger logic.

The trigger logic was handled by programmable Xilinx Logic Modules (XLMs), grouped into three levels depending on their function. "Level 1" and "Level 2" deal with the determination of whether or not an event in MoNA is valid, with a valid event defined to be one for which—at a minimum—each PMT on a single bar produces a valid time signal in its respective CFD. "Level 3" deals with the trigger conditions, involving both the Sweeper and MoNA, necessary for an event to be deemed a coincidence. Level 3 also contains a clock which runs whenever it is not busy processing an event; the signal from this clock serves as the unique event tag. In this section, the trigger logic specific to the timestamp setup is detailed as this mode of operation is unique to the present experiment. The logic and electronics of the individual subsystems are identical to previous experiments, and their details can be found in Refs. [53, 59–61].

Fig. 3.8 outlines the coincidence trigger logic. The two subsystems, Sweeper and MoNA, run independently but only record events when they are told to do so by the Level 3 XLM. A number

of signals are sent back and forth between Level 3 and the subsystems, and a description of each signal is given in Table 3.3. When an event triggers the Sweeper subsystem, it sends a trigger signal and a busy signal to Level 3. Receiving the busy signal from the Sweeper causes Level 3 to also go busy, stopping the clock. In parallel, if an event triggers MoNA, it sends a trigger and busy signal to Level 3 as well as a "valid" signal if at least two PMTs in the same bar have fired.

Upon receiving a trigger signal from the Sweeper, Level 3 opens a coincidence gate of 35 ns, waiting for a valid signal from MoNA. If it receives one, it sends a "system trigger" signal to each subsystem, telling them to go ahead and process the event. It also sends a clock signal to scaler modules that are part of each subsystem's data acquisition. Once the subsystems have finished processing, their busy signals to Level 3 cease, readying the system for the next event.

If Level 3 fails to receive a valid signal from MoNA before the coincidence gate closes, it will never send a system trigger signal to the Sweeper. Failing to receive the system trigger from Level 3, the Sweeper fast clears itself and ceases its busy signal to Level 3.

In the case of an event in MoNA that is not coincident with one in the Sweeper, MoNA will send, at a minimum, trigger and busy signals to Level 3. This causes Level 3 to go busy and reject signals from the Sweeper. Without a signal from the Sweeper, the coincidence gate is never opened and thus Level 3 cannot produce a system trigger. As it will not receive a system trigger signal from Level 3, MoNA fast clears itself and stops sending a busy signal to Level 3.

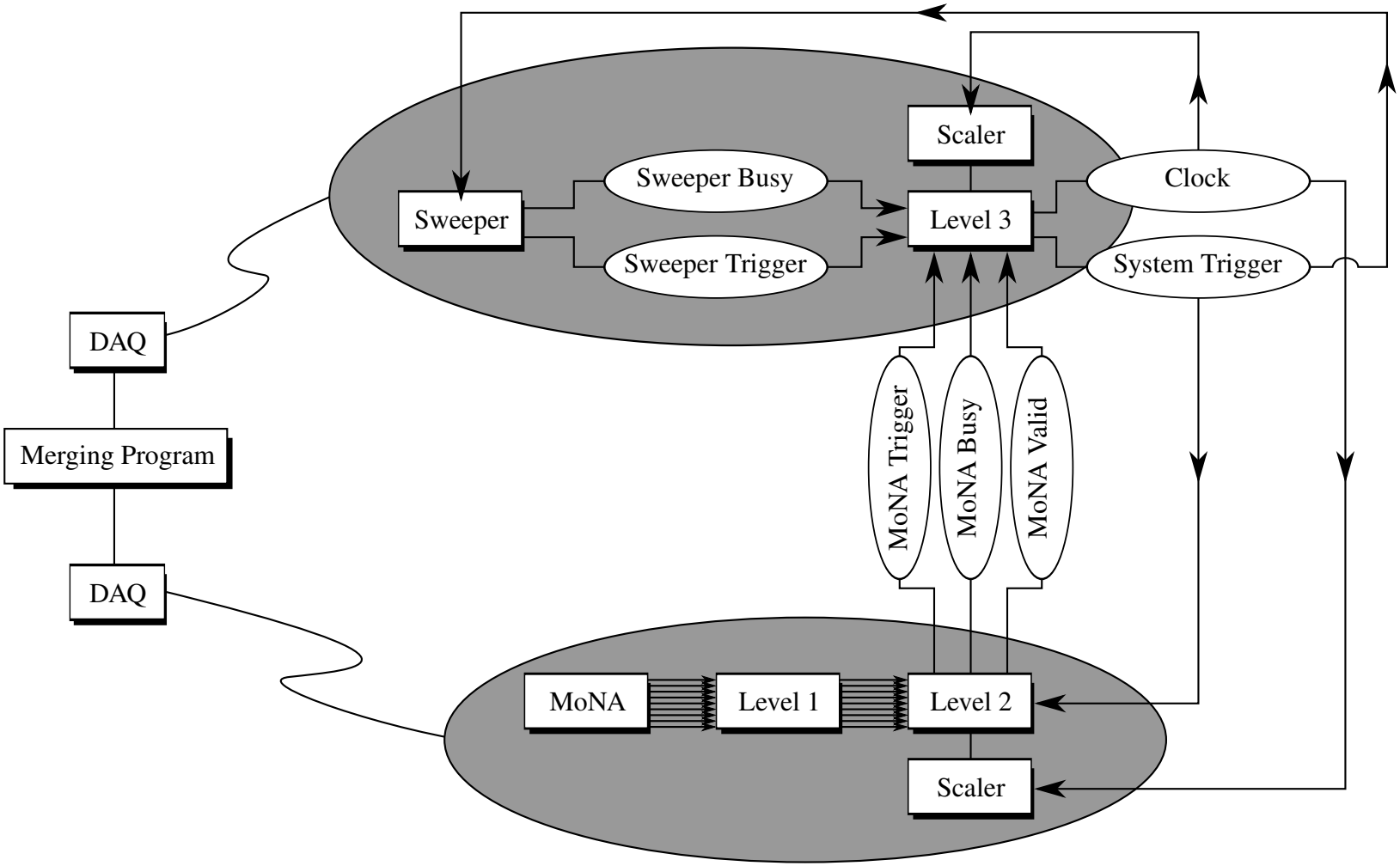

Figure 3.8: Diagram of the timestamp trigger logic.

Chapter 4

DATA ANALYSIS

4.1 Calibration and Corrections

4.1.1 Sweeper

4.1.1.1 Timing Detectors

Each of the timing scintillators in the Sweeper setup records the time of the interaction as a channel number in its corresponding TDC. The channel number is then multiplied by a slope of $+0.1$ ns/ch to convert into physical units (nanoseconds). This slope is taken simply from the full range of each TDC divided by the total number of channels. The time measurement also includes a 20 ns jitter, introduced by the use of Field-Programmable Gate Array (FPGA) delays. To remove the jitter, the nanosecond time value of the upper-left PMT in the thin scintillator is subtracted from the nanosecond time value of each individual PMT. For example, the calibrated time signal of the target scintillator is

$$t_{\text{target}}^{(\text{cal})} = \left(t_{\text{target}}^{(\text{raw})} \cdot 0.1\right) - \left(t_{\text{thin\_lu}}^{(\text{raw})} \cdot 0.1\right). \tag{4.1}$$

It should be noted that the signals are only subtracted after applying the 0.1 ns/ch slope, to account for any situation where the slope of the thin left-up TDC might be different from that of other TDCs in the system. Fig. 4.1 shows a sample timing spectrum before and after jitter subtraction.

After jitter subtraction, each time signal is given an offset to place it at the correct point in absolute time, with $t = 0$ defined to be the time at which the beam passes through the target. The offsets are determined by considering a run in which the target is removed and the Sweeper is tuned to match the rigidity of the incoming beam. In this case, the velocity of beam particles is known and can be used to calculate the appropriate time offsets. Once the fully calibrated (including offsets) time signal has been determined, time of flight between various detectors is calculated

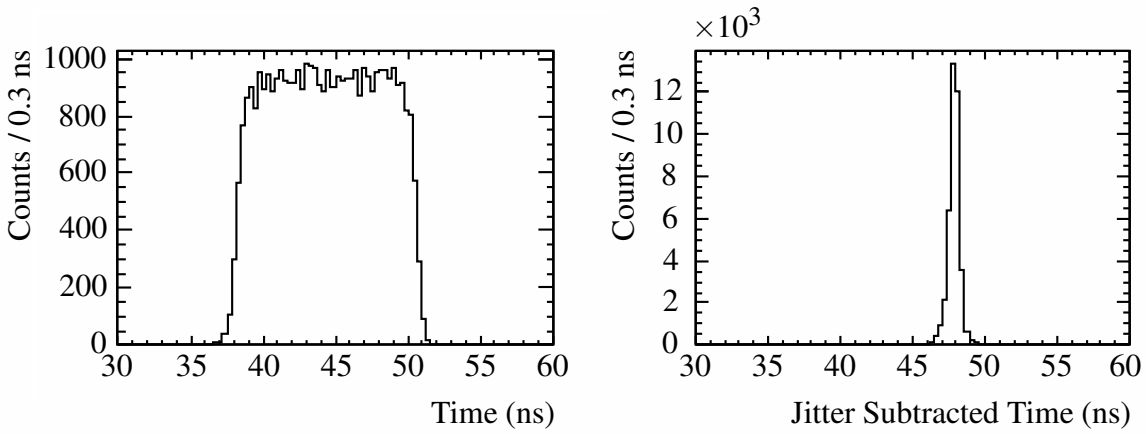

Figure 4.1: Example calibrated timing spectra before (left panel) and after (right panel) jitter subtraction.

by subtracting the calibrated time signal of the upstream detector from that of the downstream detector. In the case of the thin scintillator, the average signal of all four PMTs is used for time of flight calculations. For example, the time of flight from the target scintillator to the thin scintillator is calculated as

$$\mathrm{ToF}_{\mathrm{target}\to\mathrm{thin}} = \frac{t^{(0)}_{\mathrm{thin}} + t^{(1)}_{\mathrm{thin}} + t^{(2)}_{\mathrm{thin}} + t^{(3)}_{\mathrm{thin}}}{4} - t_{\mathrm{target}}, \tag{4.2}$$

where t refers to a calibrated time value, and the numeric superscripts refer to the corresponding PMT in the thin scintillator, as introduced in Table 3.2.

At two points during the experiment, the voltages on the thin and thick scintillators tripped due to fluctuations in the vacuum level of the Sweeper focal plane box. In order to protect the PMTs from sparking, their high voltage controllers were equipped with a safeguard that caused them to turn off if the vacuum level became too low. Although the PMT voltages were returned to their previous settings after the trips, the changes caused a noticeable shift in the time measurement of the thin scintillator PMTs. To account for this, the offset values of the thin scintillator PMTs were modified after each trip. The offset values were changed such that the central time of unreacted beam particles remains constant throughout the experiment.

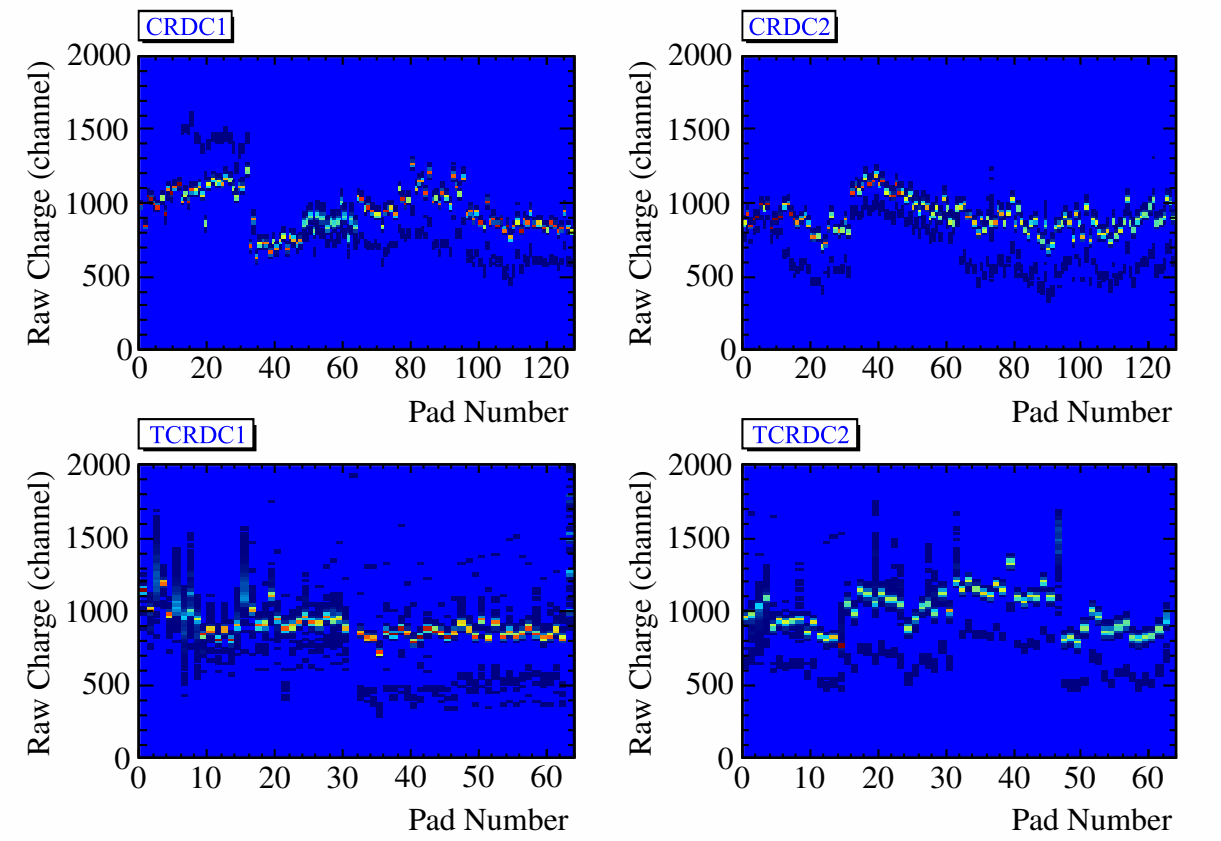

Figure 4.2: Pedestals for each of the CRDC detectors. Color represents the number of counts per bin.

4.1.1.2 CRDCs

As explained in Section 3.3.1, CRDC position in the x direction is calculated from the distribution of charge on the pads. Before doing this, the raw charge values are pedestal suppressed and gain matched. Pedestal suppression is done using data taken while no signal was present in the CRDCs. The signals on each CRDC pad are summarized in Fig. 4.2, and an example histogram of the signal on a single pad is shown in Fig. 4.3. To determine pedestal values, a histogram of the signal on each pad is fit with a Gaussian. Since the histogram shape is skewed slightly, each bin is given equal weight in the fit[1], which puts the Gaussian centroid at a value close to the true centroid of the histogram. This centroid is then divided by the number of samples recorded during the runs (eight in each case) to determine the pedestal offset for the pad in question. In the analysis, the pedestal

[1] Throughout the document, such a fit is referred to as "unweighted."

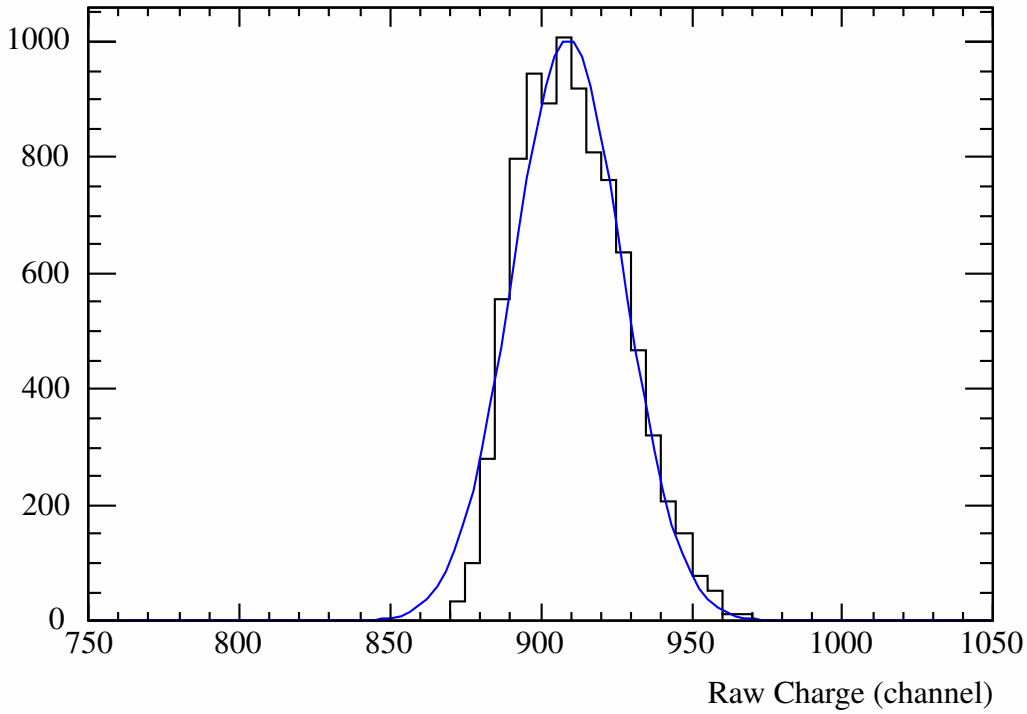

Figure 4.3: Example histogram of the signal on a single pad in a CRDC pedestal run. The blue curve is the result of an unweighted Gaussian fit and is used to calculate the pedestal value.

offset is subtracted from each sample before proceeding with further calculations.

After pedestal suppression, the CRDCs are gain matched to account for differences in charge collection or amplification between pads. Gain matching is done by considering a run where unreacted beam is swept across the focal plane[2]. This illuminates every pad in the active area of all four CRDCs and ensures that the signal size on all pads should be the same. Instead of applying a simple linear slope, a more active technique is used for gain matching since the necessary amplification factor varies with absolute signal size. The procedure used to gain match the CRDC detectors is as follows:

1. For each pad, make a two dimensional plot of charge on the pad versus Δ, where Δ is the distance of the pad in question from the pad registering maximum charge for that event. Such

[2]Hence referred to as a "sweep run."

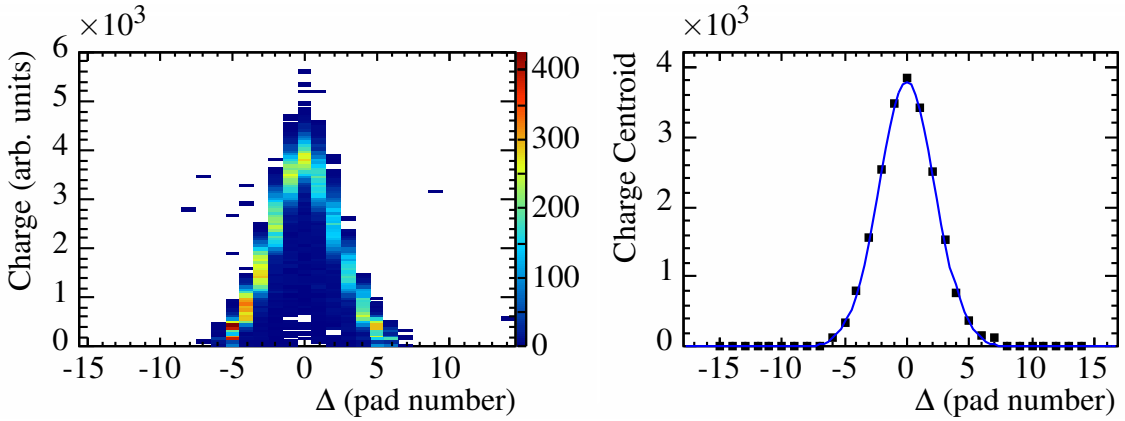

Figure 4.4: Example of the plots used in the gain matching procedure. The left panel is a two dimensional histogram of charge on the pad versus Δ, while the right panel shows the Gaussian centroids of the y axis projection of each x axis bin in the plot on the left. The curve in the right panel is the result of an unweighted fit to the data points, with the fit function a Gaussian centered at zero.

a plot is shown in the left panel of Fig. 4.4.

2. For each bin along the x axis, fit the y axis projection with a Gaussian. Similar to the pedestals, the fit should be unweighted to account for skew.

3. Plot each of the centroids from Step 2 versus Δ. Fit (unweighted) this plot with a Gaussian centered at zero. An example is shown in the right panel of Fig. 4.4.

4. Choose a reference pad near the center of the detector and match the signal sizes of all other pads to it by applying the following transformation:

$$q'_j = q_j \left(\frac{f_{ref}(\Delta)}{f_j(\Delta)} \right), \tag{4.3}$$

where q' and q denote the gain matched and non-gain matched signals, respectively; $_j$ denotes the pad being gain matched; $_{ref}$ denotes the reference pad; and f is the Gaussian function determined from the fits in Step 3.

The procedure outlined above is applied to each pad in the active area of all four CRDC detectors. For the focal plane CRDCs, the reference pad is chosen to be pad 60, while for the beam tracking CRDCs, the reference pad is number 50.

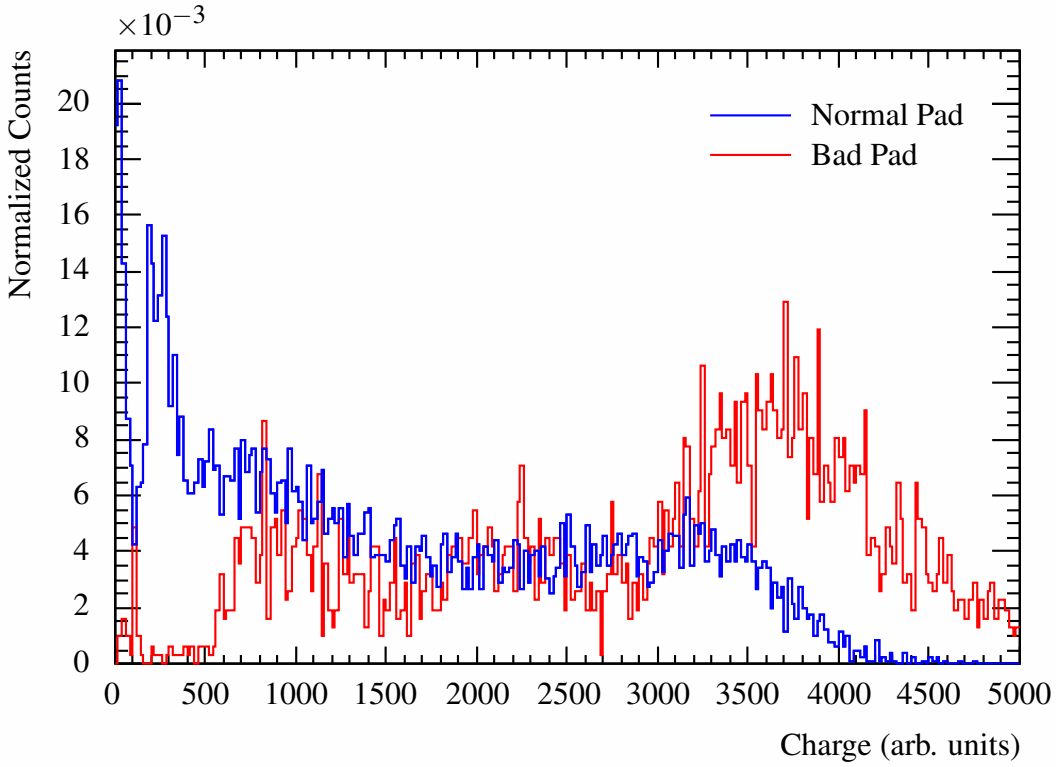

Figure 4.5: Difference in signal shape between a bad pad (red histogram) and a normal one (blue histogram). The bad pad in this figure is pad 24 of CRDC2, while the normal pad is number 60 in CRDC2.

Certain pads in each of the CRDCs display pathological features and need to be rejected in the analysis. Most often these pads are overly sensitive to electronic noise, causing them to display a signal which does not reflect the real amount of charge deposited on the pad. To determine which pads are bad, the charge signal of each pad in a sweep run is examined. Those pads displaying unusual charge distributions are labeled as bad pads and ignored in further analysis. This procedure is subjective, but as demonstrated in Fig. 4.5, the difference in signal shape between a bad pad and a normal one is fairly obvious. Table 4.1 lists the bad pads for each detector.

Once the pads in each CRDC have been pedestal suppressed and gain matched and all bad pads have been determined, it is possible to use the charge distribution on the pads to calculate the x position at which the charged particle hit the detector. The method for calculating the interaction position in pad space is to fit a plot of charge versus pad number with a Gaussian. The Gaussian

Table 4.1: List of the bad pads for each CRDC detector. Pads are labeled sequentially, starting with zero.

Detector	*Bad Pads*
CRDC1	66
CRDC2	24, 89, 105, 126
TCRDC1	30, 31, 58, 59, 63
TCRDC2	14, 21, 62, 63

centroid is then taken as the pad space interaction position. The fitting is done event-by-event using the GNU Scientific Library (GSL) [62] implementation of the Levenberg–Marquardt minimization algorithm [63, 64]. Starting values for the minimization are taken from the results of a center of gravity fit, and each data point in the fit is weighted equally. It should be noted that for events in the center of a detector, the difference in centroid values between a Gaussian fit and a center of gravity fit is negligible. However, for events near the edge where the full charge versus pad distribution is clipped, the Gaussian fit does a significantly better job of finding the true centroid. This effect is demonstrated in Fig. 4.6, which shows example charge versus pad distributions in the center and near the edge of CRDC2, as well as in Fig. 4.7, which is a scatter-plot of gravity centroids versus Gaussian centroids. The two values agree well until the edge of the detector is approached, at which point they begin to diverge.

To convert the position in pad space to one in real space, a simple linear transformation is used. The same is true for conversion of drift time to position in the y direction. In the x direction, the slope is taken simply from the pad pitch: ± 2.54 mm/pad, with the sign of the slope depending on the orientation of the detector. To determine the x offset and the y slope and offset, a tungsten mask with holes drilled at known locations inserted into the beam line, shadowing the detector. A sample masked position distribution for CRDC1 is shown in Fig. 4.8. By determining the centroid of the holes in time versus pad space and comparing with their known locations, the correct linear factors can be determined. During the experiment, the mask drive for CRDC2 was malfunctioning, causing the mask to only be inserted partially. As the drive operates in the y direction, the x offset value was not affected by this malfunction. Likewise, the y slope could still be determined using

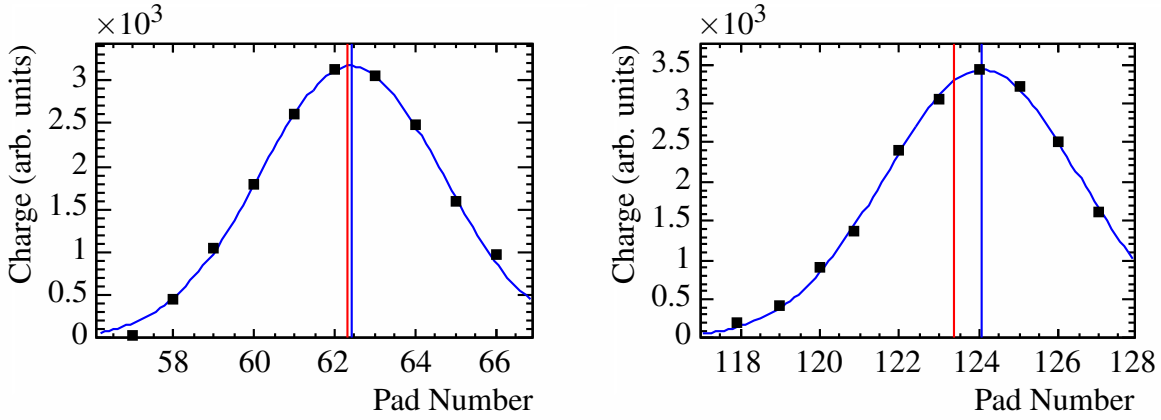

Figure 4.6: Charge distributions for an event near the middle of CRDC2 (left panel) and one near the edge (right panel). The blue curve is a Gaussian fit to the data points, and the blue vertical line is the centroid of that fit. The red vertical line is the centroid of a gravity fit to the points. The Gaussian and gravity centroids are nearly the same in the case of events near the middle, but on the edge the gravity fit is skewed towards lower pad number.

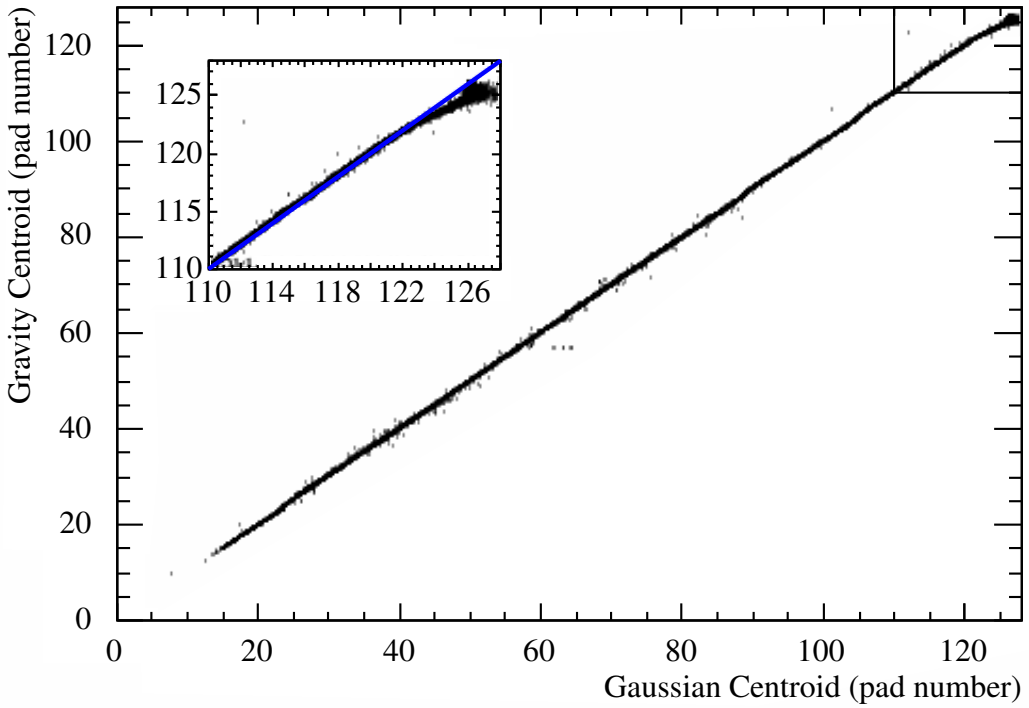

Figure 4.7: Gaussian versus gravity centroids for CRDC2. The two fits disagree near the edge of the detector, with the gravity fit skewed lower.

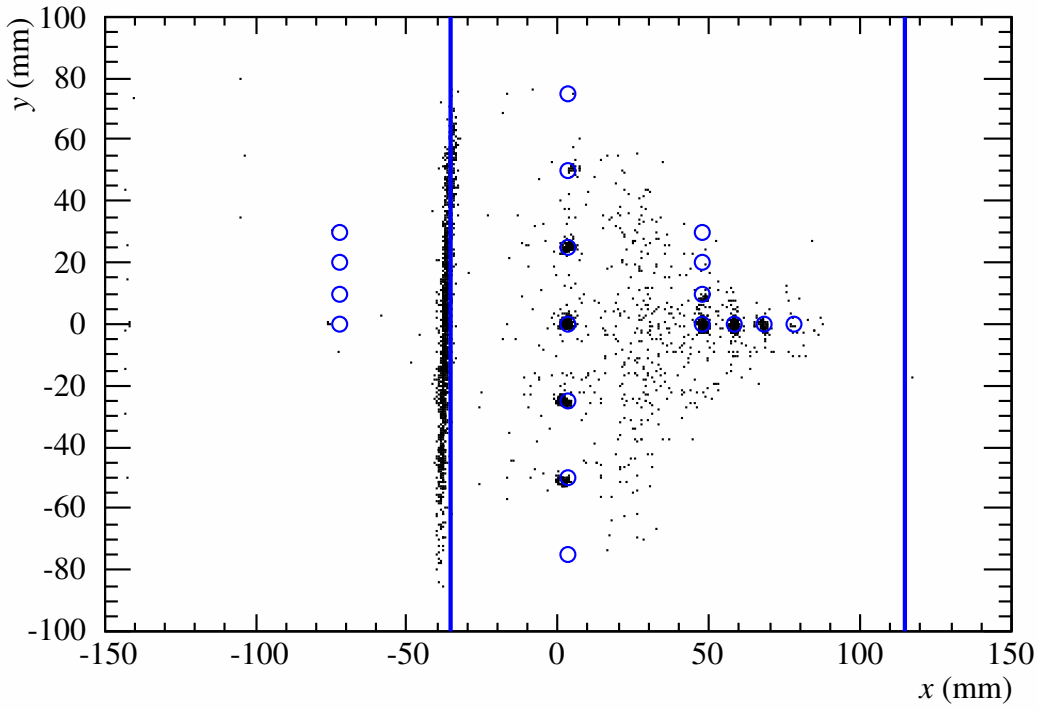

Figure 4.8: Example of calibrated position in both planes for CRDC1, with the tungsten mask in place. The blue open circles denote the position of the mask holes, and the blue vertical lines denote the position of slits cut into the mask.

the mask, as the spacing between holes remains identical. However, since the absolute position of the mask holes in the y direction was not known, the mask could not be used to determine the y offset. Instead, a beam of ^{25}Ne was sent down the focal plane, centered, with the vertical position of the beam defined to be $y \equiv 0$. The y offset for CRDC2 is then set from the location of the beam centroid.

Due to the possibility of detector drift, mask runs were taken approximately once per day during the experiment. The changes in the calibration parameters are shown in Fig. 4.9. As any drifts are fairly small, the calibration parameters are simply updated after each mask run to reflect their new values.

A further issue related to CRDCs is the poor performance of TCRDC2. As shown in Fig. 4.10, the x position tends to cluster around certain pads, creating the "spike" features seen in the plot.

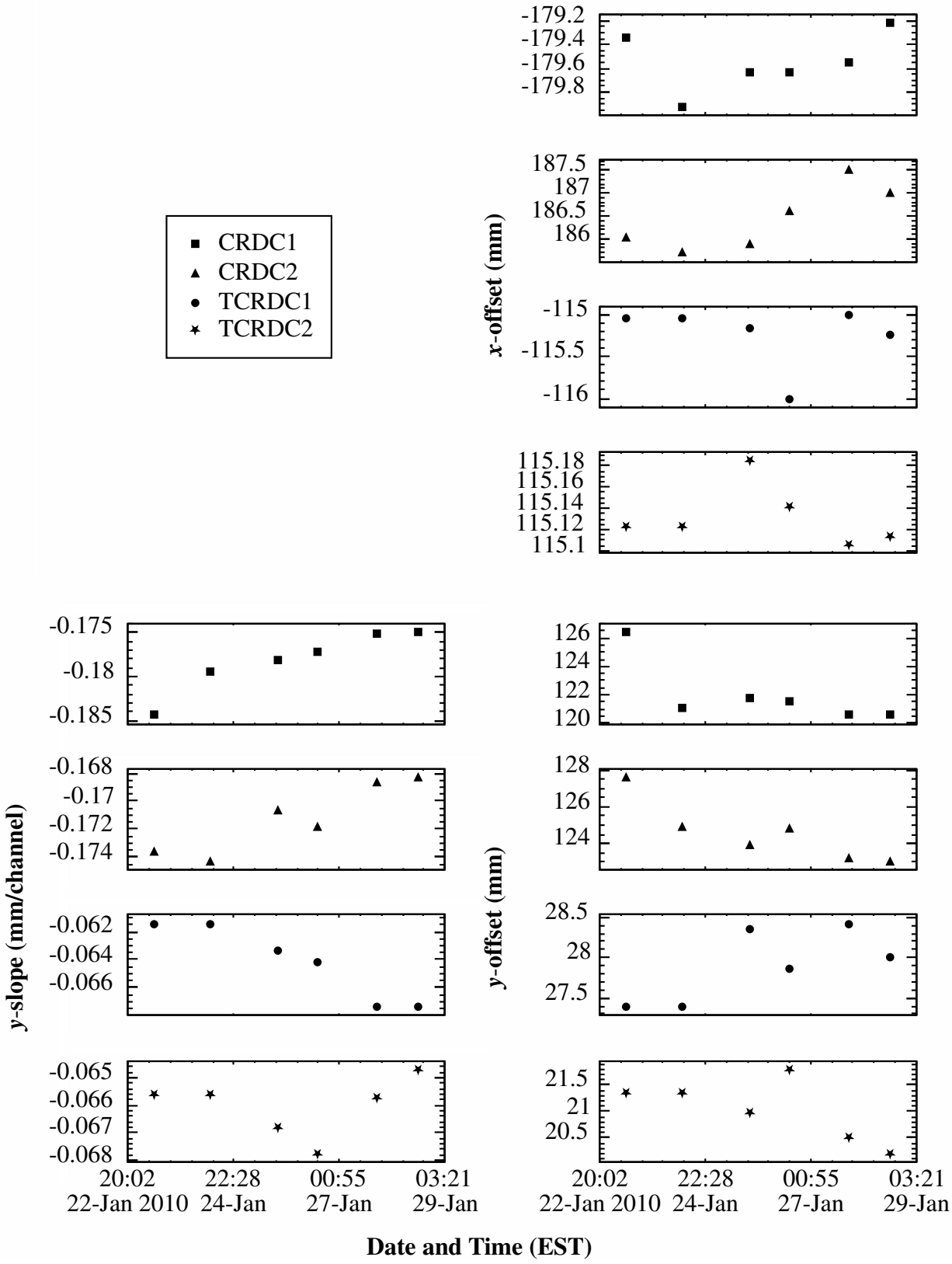

Figure 4.9: Drift of CRDC calibration parameters.

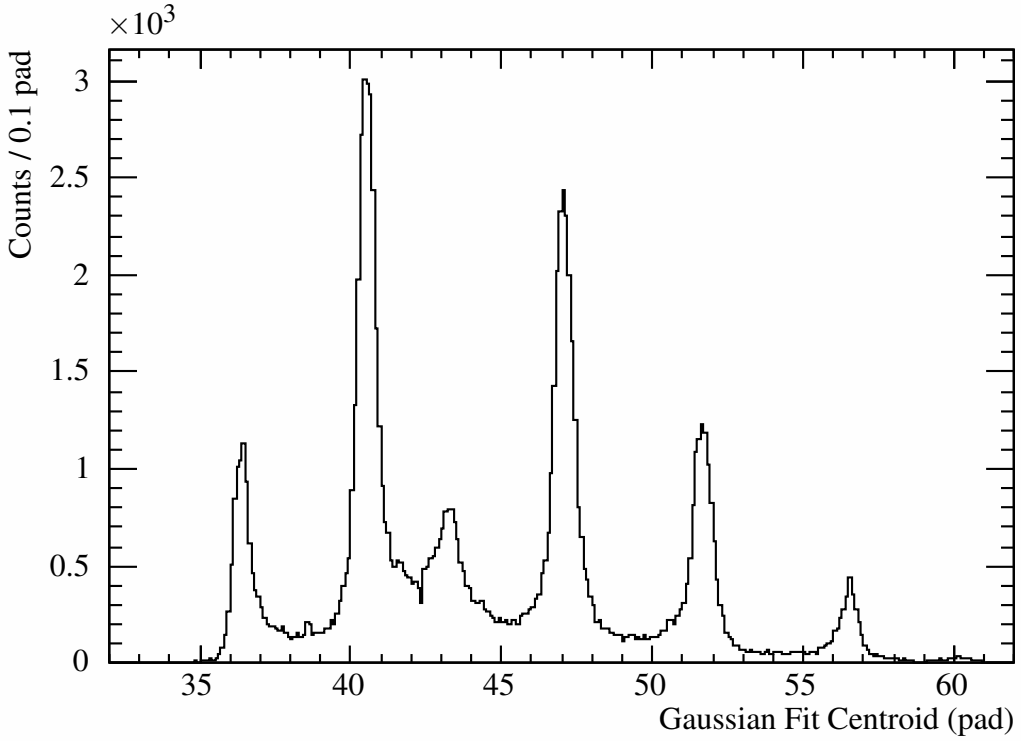

Figure 4.10: Gaussian centroids in pad space for TCRDC2.

This is the result of inhomogeneities in the drift field that cause electrons to be preferentially attracted to specific points on the anode wire. The spikes are not physical and are a result of detector malfunction; hence the x position measurement of TCRDC2 is not used event-by-event in the analysis. Instead, a plot of TCRDC2 x position versus TCRDC1 x position, as shown in Fig. 4.11, is used to determine a linear correlation between the two parameters,

$$x_2 = 1.162 \cdot x_1. \tag{4.4}$$

Such a correlation is expected based on the optics of the A1900. In the final analysis, the x position of beam particles at TCRDC2 is calculated simply from this linear function. Due to the small angular spread of the incoming beam, the influence of using this technique on the overall resolution is fairly minor.

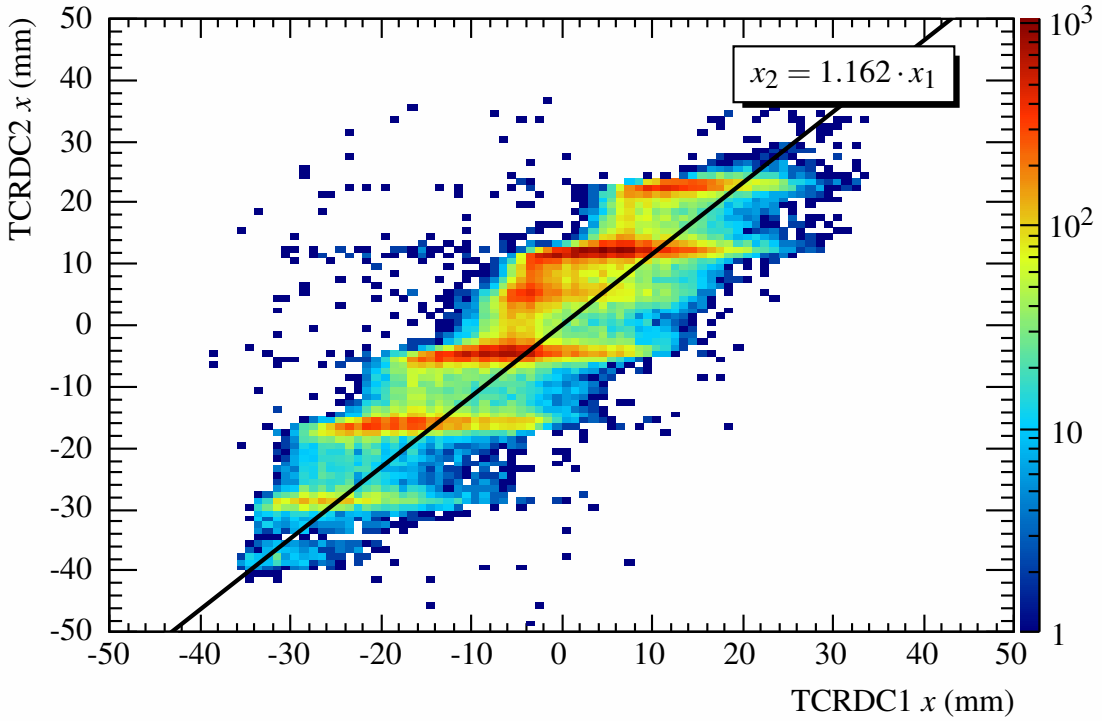

Figure 4.11: Plot of TCRDC2 x position versus TCRDC1 x position. The plot is used to determine a correlation of $x_2 = 1.162 \cdot x_1$, shown by the black line in the figure. The position at TCRDC2 determined by this correlation is what is used in the final analysis.

Table 4.2: Slope values for each pad on the ion chamber. Pad zero was malfunctioning and is excluded from the analysis.

Pad	*Slope*		
0	n/a	8	1.034799
1	1.218959	9	0.979036
2	0.941313	10	0.809853
3	0.864580	11	0.817919
4	0.925724	12	0.853119
5	0.725158	13	0.928206
6	0.971480	14	0.850262
7	0.852719	15	0.836822

4.1.1.3 Ion Chamber

Similar to the CRDCs, the pads on the ion chamber must be gain matched to account for differences in signal collection and amplification. The gain matching is done by multiplying each pad's signal by a slope factor, with the factors determined from a run where a beam of ^{25}Ne is centered in the focal plane. Since each pad should measure the same amount of energy loss, the slopes are set such that the signals match. Slope factors for each pad are listed in Table 4.2. The most upstream pad (pad zero) was malfunctioning during the experiment, so it is excluded from the analysis. After gain matching, the signals from the fifteen working pads are averaged to form an energy loss parameter.

As shown in Fig. 4.12, there is a dependence of the average ion chamber signal on both x and y position in CRDC2. The figure is generated from a sweep run with unreacted beam, so the energy loss should be uniform. To correct for this dependence, the plot of ΔE versus x is first fit[3] with a second order polynomial; the result of the fit is

$$f(x) = 399.762 - 0.0583744 \cdot x - 0.0008205 \cdot x^2, \tag{4.5}$$

and the ΔE signal is corrected as follows:

$$\Delta E_{\text{xcorr}} = 399.762 \cdot \frac{\Delta E}{f(x)}. \tag{4.6}$$

From here, ΔE_{xcorr} is plotted against CRDC2 y position and fit with a first order polynomial:

$$f(y) = 399.551 - 0.305093 \cdot y. \tag{4.7}$$

The same method is used to correct for the $y-$dependence:

$$\Delta E_{\text{xycorr}} = 399.551 \cdot \frac{\Delta E_{\text{xcorr}}}{f(y)}. \tag{4.8}$$

[3]The procedure used for fitting the two dimensional histogram is as follows: 1) Fit (unweighted) the y axis projection of each x axis bin with a Gaussian. 2) Plot the Gaussian centroids versus the x axis bin centers and fit this plot with the desired function. Unless otherwise noted, this is always the method used to fit two dimensional histograms.

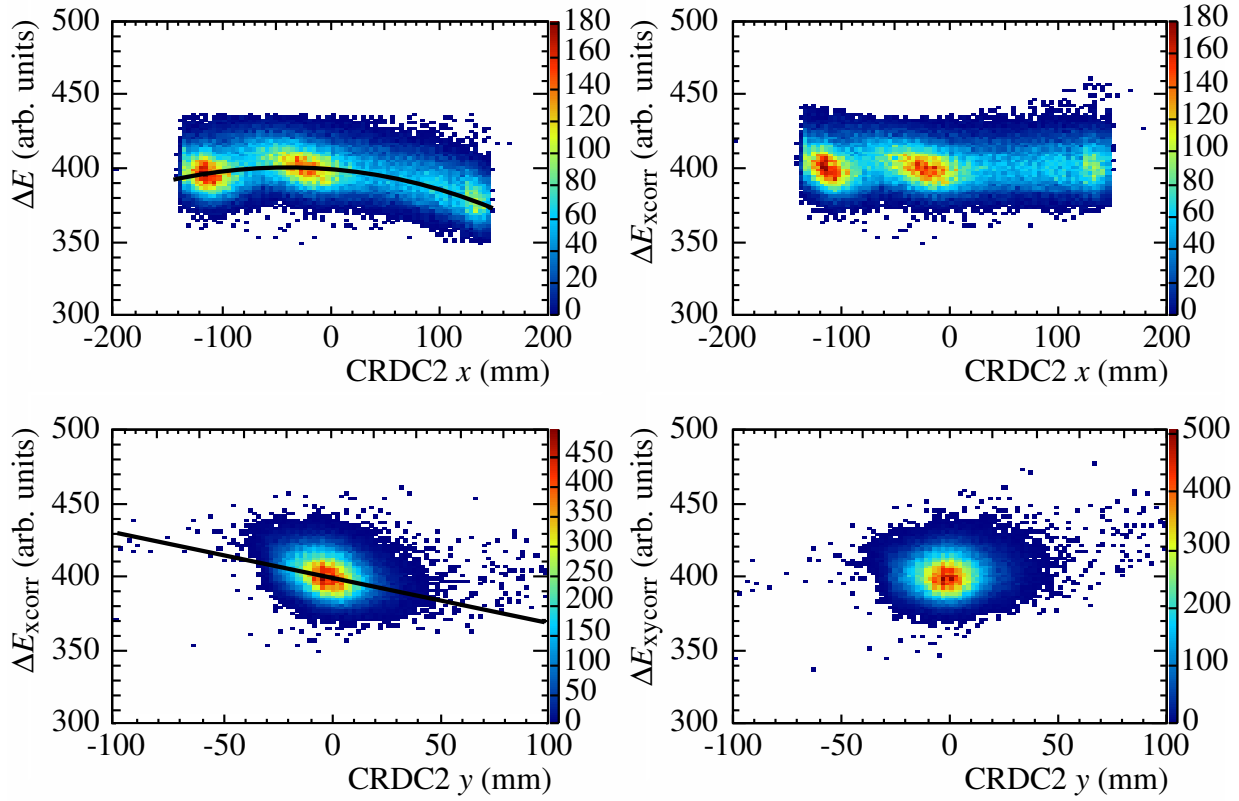

Figure 4.12: Upper left: Ion chamber ΔE signal versus CRDC2 x position; the black curve is a 3rd order polynomial fit used to correct for the dependence of ΔE on x. Upper right: Result of the $x-$correction: the dependence of ΔE on x is removed. Lower Left: $x-$corrected ΔE versus CRDC2 y position; the black curve is a linear fit used to correct for the dependence of ΔE_{xcorr} on y. Lower right: Final position corrected ion chamber ΔE versus CRDC2 y position.

4.1.1.4 Scintillator Energies

The calibration procedures for the thin scintillator ΔE and thick scintillator E signals are identical. First each of the four PMTs is gain matched using data from a sweep run, with the requirement that $|\, x_{\text{scint}} | < 10$ mm and $|\, y_{\text{scint}} | < 10$ mm, where x_{scint} and y_{scint} are the vertical and horizontal positions on the scintillator, calculated using ray tracing and the CRDC position measurements. It is necessary to use only events that hit near the center of the scintillator as this ensures that light attenuation is equal for all PMTs. Because the detector trip mentioned in Section 4.1.1.1 significantly impacts the energy signal of the scintillators, two sets of gain factors were determined: one for before the trip and one for after, with the gain factors set such that signal size is equal

Table 4.3: Slope values for thin and thick scintillator energy signals.

PMT	*Slope Pre-Trip*	*Slope Post-Trip*
Thin 0	1.136	2.167
Thin 1	1.158	2.174
Thin 2	1.360	2.437
Thin 3	1.073	2.169
Thick 0	2.860	4.771
Thick 1	1.438	4.888
Thick 2	2.483	3.272
Thick 3	2.155	3.174

throughout the experiment. Table 4.3 list the gain factors for each scintillator PMT.

After gain matching, a total energy signal for the detector is calculated as follows:

$$e_{\text{top}} = \frac{e_0 + e_2}{2}, \tag{4.9}$$

$$e_{\text{bottom}} = \frac{e_1 + e_3}{2}, \tag{4.10}$$

and

$$e_{\text{total}} = \frac{\sqrt{e_{\text{top}}^2 + e_{\text{bottom}}^2}}{2}. \tag{4.11}$$

As the ΔE and E_{total} signals are used only to determine relative differences between the various reaction products present in the focal plane, an absolute energy calibration is not needed. Hence the scintillator energy signals are left in arbitrary units.

The scintillator energy measurements, as calculated from Eqs. 4.9–4.11, have a dependence on the position at which the particle hits the scintillator. The reason is light attenuation: particles striking near an edge of the detector will produce a stronger signal in PMTs near that edge than in those on the opposite side, as the scintillation light becomes diminished when it traverses the plastic. This effect is corrected for empirically in the same way as the ion chamber, described in Section 4.1.1.3. The correction functions for the thin scintillator are:

$$f_{\text{corr}}^{(\text{thin})}(x) = 710.805 + 0.295609 \cdot x - 6.28603 \times 10^{-3} \cdot x^2 - 2.22623 \times 10^{-5} \cdot x^3 \tag{4.12}$$

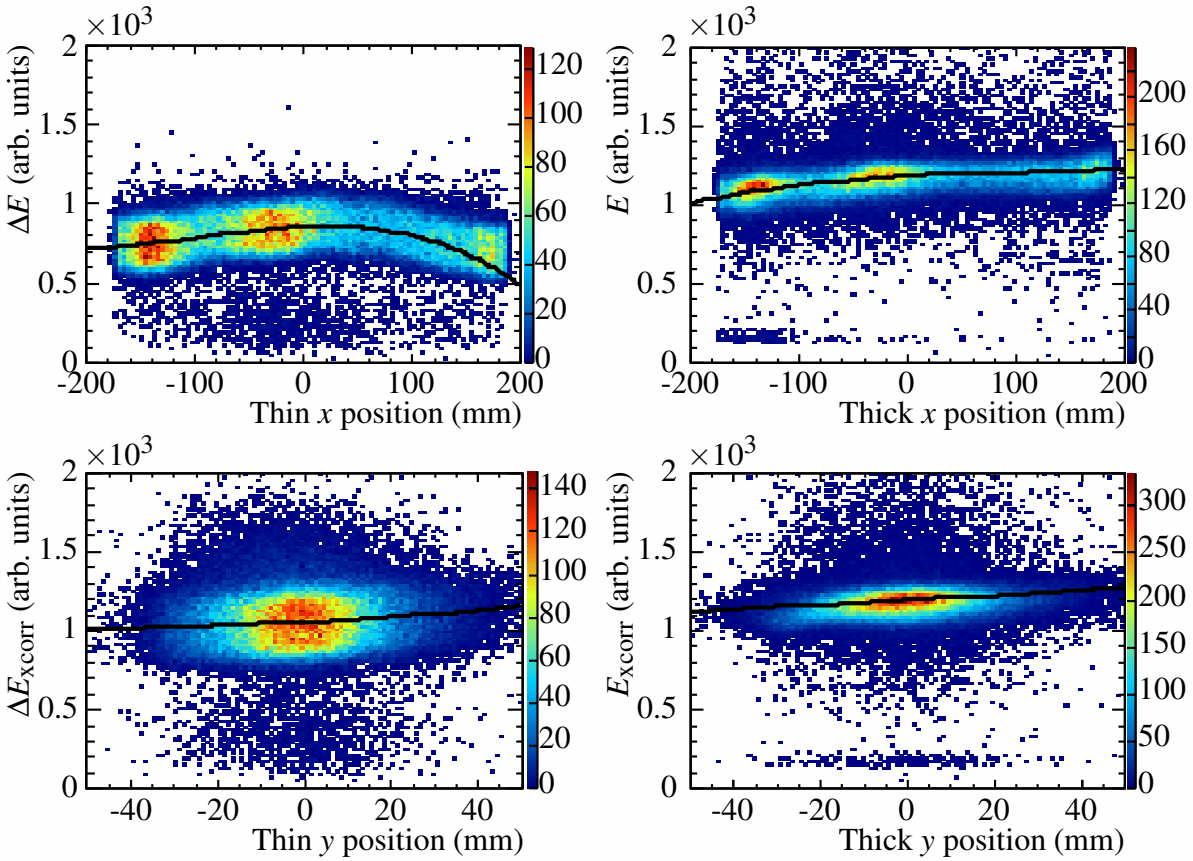

Figure 4.13: Position correction of the thin and thick scintillator energy signals. Top left: thin scintillator ΔE vs. x position, with a third order polynomial fit. Bottom left: thin scintillator ΔE (corrected for x dependence) vs. y position, with a second order polynomial fit. Top right: thick scintillator E_{total} vs. x position, with a third order polynomial fit. Bottom right: thick scintillator Etotal (corrected for x dependence) vs. y position, with a first order polynomial fit.

and

$$f_{\text{corr}}^{(\text{thin})}(y) = 1001 + 1.362 \cdot y + 0.01158 \cdot y^2, \tag{4.13}$$

while the correction functions for the thick scintillator are:

$$f_{\text{corr}}^{(\text{thick})}(x) = 1346.74 + 1346.74 \cdot x - 1.61185 \times 10^{-3} \cdot x^2 + 4.09761 \times 10^{-6} \cdot x^3 \tag{4.14}$$

and

$$f_{\text{corr}}^{(\text{thick})}(y) = 999 + 1.166 \cdot y. \tag{4.15}$$

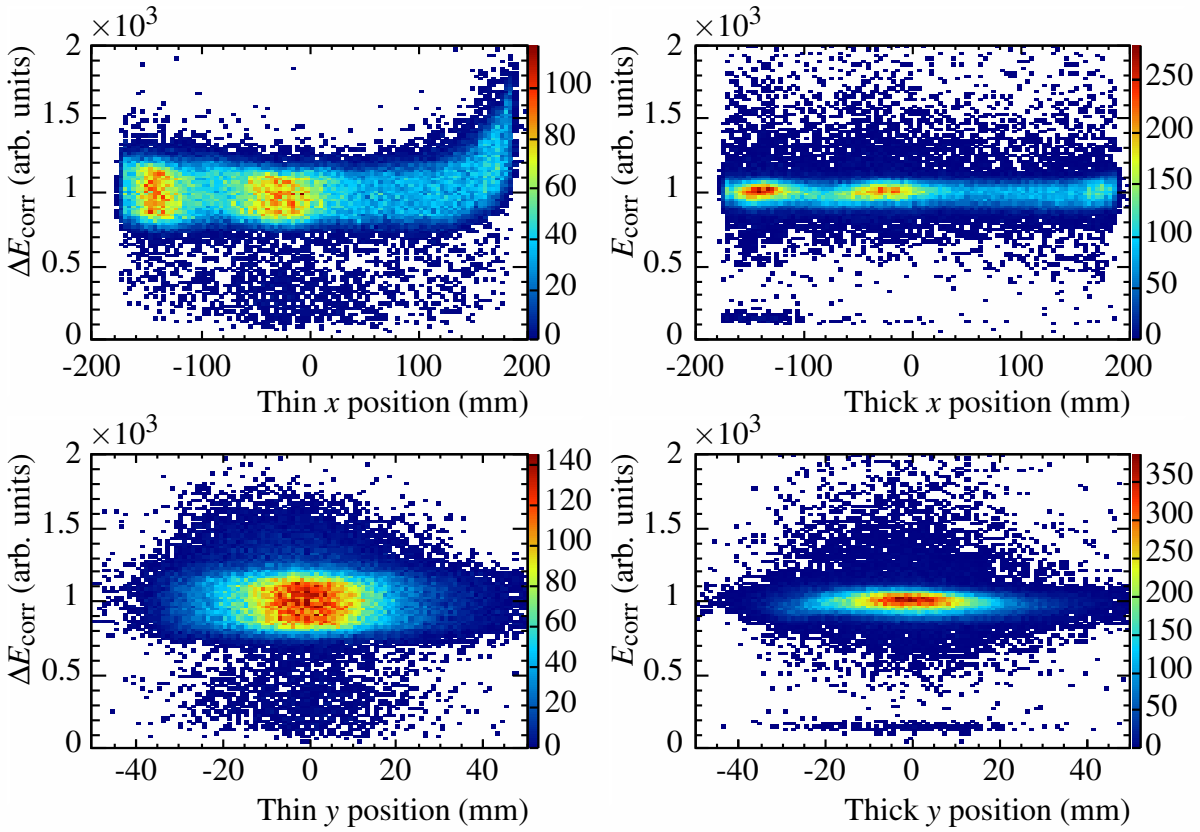

Figure 4.14: Results of the position correction of the thin and thick scintillator energy signals. The panels correspond to those of Fig. 4.13, displaying the final position corrected energy signals. As seen in the upper-left panel, the correction for thin ΔE could be improved by the use of a higher order polynomial; however this signal is not used in any of the final analysis cuts, so the correction is adequate as is.

The results of the position correction are shown in Fig. 4.14. It should be noted that the x position correction to thin ΔE signal produces a sharp kink at large positive x position. The reason is that a third order polynomial cannot describe the shape of ΔE versus x across the entire face of the scintillator. This can be seen in the upper-left panel of Fig. 4.13 where the fit curve fails to reproduce the histogram shape at large positive x. The correction could be improved by using a higher order polynomial; however, since the thin ΔE signal is only used for intermediate analysis checks and not in any of the final cuts or calculations, the third order correction presented here is sufficient.

As seen in Fig. 4.15, both the thin and thick scintillator energy signals drift throughout the

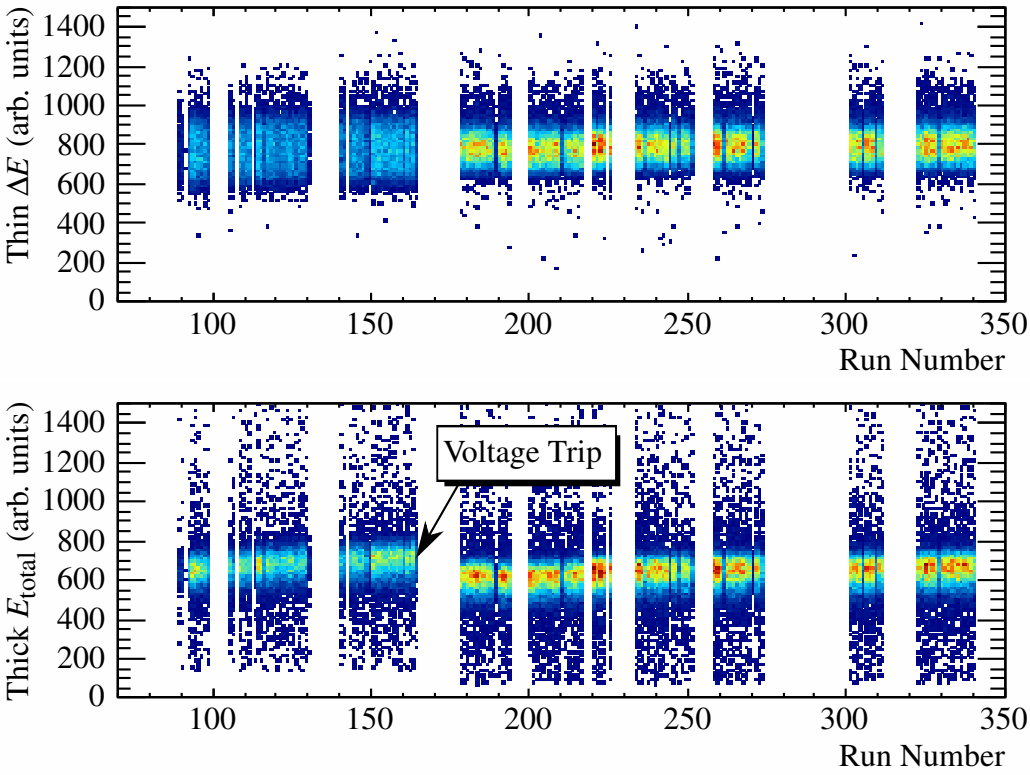

Figure 4.15: Thin (top panel) and thick (bottom panel) scintillator energies for ^{29}Ne unreacted beam in production runs. Gaps along the x axis correspond to non-production runs taken at various intervals during the experiment. The drift seen in the figure is corrected by setting Gaussian centroid of each run's ^{29}Ne energy signal to be constant throughout the experiment.

experiment. The events in the figure are from production runs, gated on ^{29}Ne unreacted beam particles that make it into the focal plane (gaps along the x axis correspond to calibration and other non-production runs). The ΔE and E_{total} measurements should be constant, so the observed drift is corrected run-by-run. The ΔE and E_{total} measurements, gated on ^{29}Ne, are fit (unweighted) with a Gaussian, and the corrected energy is calculated such that the centroids are constant:

$$E_{\text{runcorr}} = \frac{E_0}{E_c}, \tag{4.16}$$

where E_0 is an arbitrarily chosen value (1200 for thin ΔE and 500 for thick E_{total}), and E_c is the centroid of the Gaussian fit. Each run is approximately one hour in length, and the drift within a run is negligible.

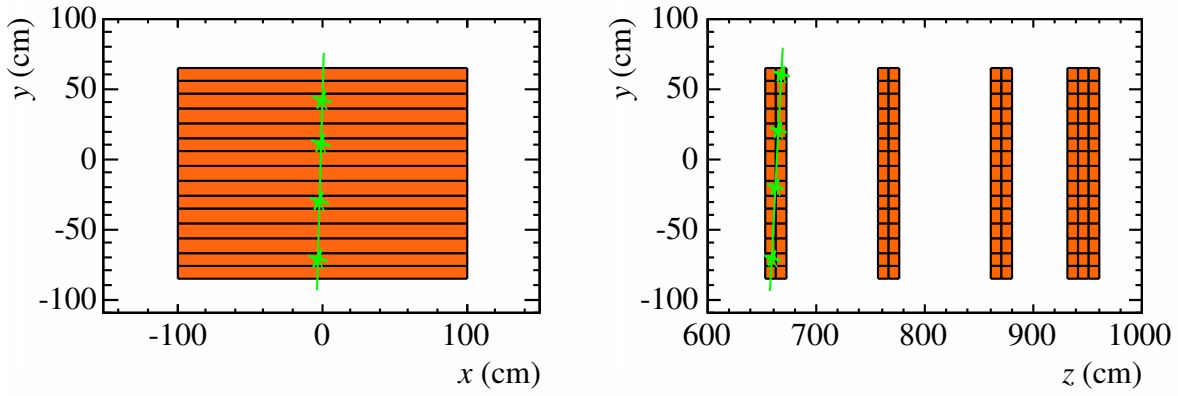

Figure 4.16: Example of the two types of muon tracks used in calculating independent time offsets for MoNA. The left panel illustrates a nearly vertical track, used to determine the time offsets within a single wall. The right panel shows an example of a diagonal track used to calculate offsets between walls.

4.1.2 MoNA

4.1.2.1 Time Calibrations

MoNA TDCs signals are calibrated with a linear slope and offset, and from there, the signals on each end of a bar are averaged to give a time of flight measurement. The slope of each TDC is determined using a time calibrator which sends a signal to the modules at a regular frequency of 40 ns^{-1}. For each TDC, the slope is determined as such:

$$m = \frac{40\ \text{ns}}{\Delta_{ch}}, \tag{4.17}$$

where Δ_{ch} is the average spacing between pulses in channel number. Slopes measured in a previous MoNA-Sweeper experiment were used, as the MoNA TDCs remained identical between the two runs.

Timing offsets are divided into two parts: a global offset for the entire array and individual offsets of each TDC relative to the others. The individual time offsets are determined using muons produced by the interaction of cosmic rays with the Earth's upper atmosphere. The muons travel to earth and pass through the detector, often interacting multiple times. They travel at a known

velocity close to the speed of light, 29.8 cm/ns, so by selecting for specific tracks through the detector, the time offset of each bar relative to the others can be determined. To calculate time offsets within a given wall, muon tracks which are nearly vertical are selected, as illustrated in the left panel of Fig. 4.16. The expected travel time between two bars in the same wall is then:

$$t = n \cdot \frac{10.27 \text{ cm}}{29.8 \text{ cm/ns}}, \tag{4.18}$$

where n is the number of bars between the two, and 10.27 cm is the nominal vertical distance between the center of two bars. Appropriate time offsets are determined by comparison of measured times with the expected time of Eq. (4.18). Time offsets between walls are determined similarly, except using diagonal tracks, as illustrated in the right panel of Fig. 4.16. All offsets are set relative to bar A8, which is at beam height and in the front wall of MoNA. Offsets within the front wall are calculated directly relative to bar A8, using vertical tracks. From here, offsets are propagated from wall to wall using diagonal tracks.

The global offset is calculated from the time of flight of $\gamma-$rays made at the target during production runs. The flight time of gammas to the front and center of MoNA is

$$\text{ToF}_\gamma = x_{\text{a8}}/c \tag{4.19}$$

where $x_{\text{a8}} = 658$ cm is the distance to the center of the front wall of MoNA (the center of bar A8), and c is the speed of light. Fig. 4.17 is a histogram of the time of flight to the center of the front wall of MoNA, with the prompt γ peak clearly identified and separated from prompt neutrons. To increase statistics, the entire front wall of MoNA is used for determining the global offset, with the time of flight scaled to account for each bar's distance from the target. Furthermore, when setting the timing offset a number of cuts are used to enhance the presence of target gammas: hit multiplicity must be equal to one; charge deposited must be less than 6 MeVee; and the absolute value of the interaction position in MoNA must be less than 30 cm in both the x and y planes.

Despite the use of constant fraction discriminators, there is a walk present in the MoNA timing at low signal size. This is demonstrated in Fig. 4.18, which shows a plot of time of flight for prompt

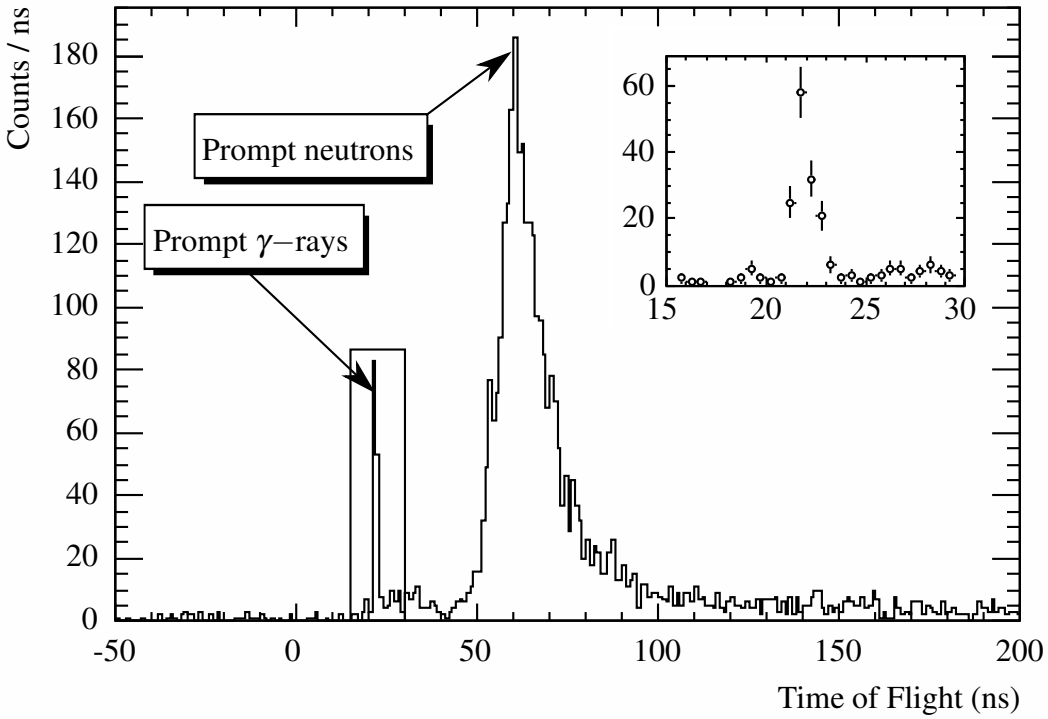

Figure 4.17: Time of flight to the center of the front wall of MoNA. The events in the figure are collected during production runs. The prompt γ peak used to set the global timing offset is clearly identifiable and separated from prompt neutrons. The plot includes a number of cuts, which are listed in the main text.

gammas versus energy deposited in MoNA. As seen in the figure, there is a clear dependence of time of flight on deposited energy. The function indicated in the figure,

$$f(q) = 23.5531 - 2.56625e^{-0.62272/q}, \tag{4.20}$$

is a fit to the histogram, with the functional form taken from Ref. [65].

In order to appropriately use the prompt γ−ray measurements to set the global MoNA timing offset, a correction must be made to account for the the CFD walk. Additionally, the walk correction must be included in the final neutron analysis in order to have an accurate measurement of neutron energy. An attempt was made to do the correction using Eq. (4.20), but the range of deposited energies probed by the γ peak is too small for this to be sufficient. Higher deposited energies can be reached, however, by considering runs in which MoNA records cosmic rays in

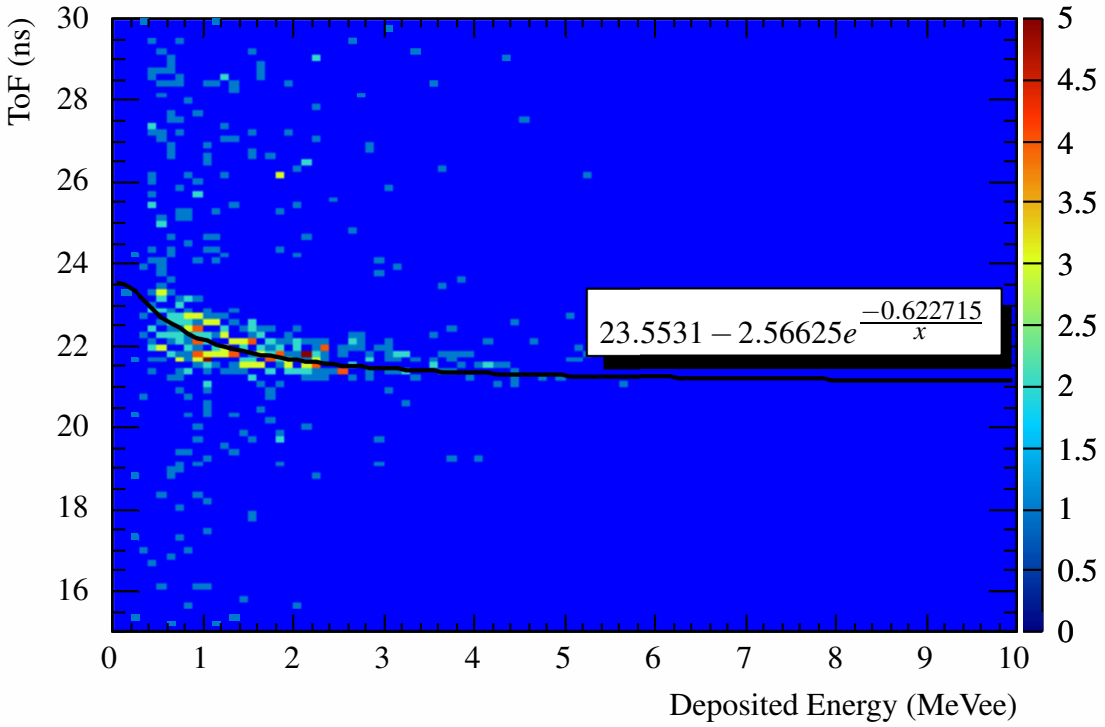

Figure 4.18: Time of flight to the front face of MoNA versus deposited energy, for prompt gammas. The plot includes cuts similar to those used in generating Fig. 4.17. The dependence of time of flight on deposited energy, as indicated in the figure, demonstrates the presence of walk for low signal size. The function in the figure is partially used for walk corrections, as explained in the text.

standalone mode, with the trigger being the first PMT in the array to fire. When run in this mode, a plot of the average time signal for a given bar versus the absolute value of x position, as shown in the inset of Fig. 4.19, represents the mean time it takes light to travel from the interaction point to each PMT. By applying a linear correction to the average time, one obtains a time measurement which should be constant. This time is plotted against deposited energy in the main panel of Fig. 4.19, and this histogram can then be fit and used to correct the walk. The fit function used is this case is:

$$f(q) = 229.4 + \frac{2.861}{q}, \tag{4.21}$$

with the functional form taken from Ref. [66]. As seen in Fig. 4.19, this function blows up at low deposited charge, making it a poor choice for walk correction in that region. Instead, a

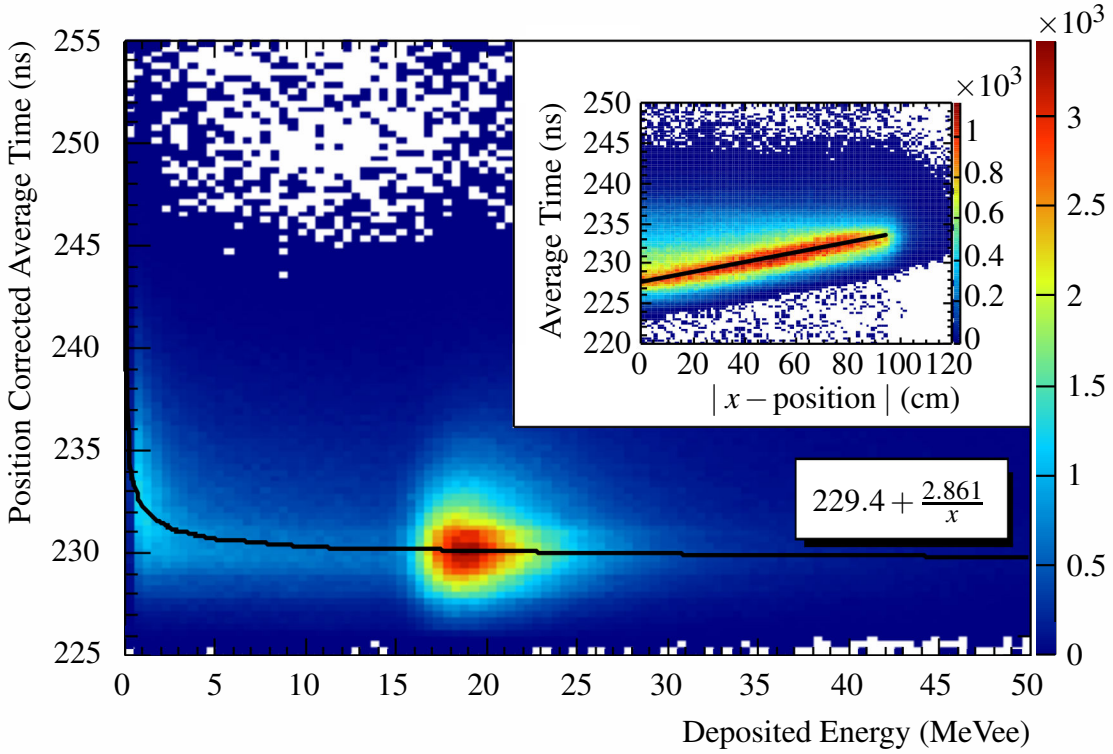

Figure 4.19: Inset: mean time vs. absolute value of x position for cosmic-ray data collected in standalone mode, where the trigger is the first PMT to fire. The time axis on the inset is determined by the mean travel time of light from the interaction point to the PMTs. If this parameter is corrected for the x position, using the line drawn on the inset, then a theoretically constant ToF is obtained. Plotting this constant ToF versus deposited energy reveals walk, as shown in the main panel of the figure. The function drawn in the main panel is used for walk correction of production data at high deposited charge, as explained in the text.

piecewise function is used to do the walk correction, with Eq. (4.20) used when $q \leq 1.8$ MeVee and Eq. (4.21) used otherwise. The transition point of 1.8 MeVee is taken from the crossing point of the two functions, as shown in Fig. 4.20. The final form of the walk corrected time of flight is then

$$t_{\text{corr}} = t - \begin{cases} \left(-2.56625e^{-0.62272/q} + 1.6531\right) & : \; q < 1.8 \\ \left(\frac{2.861}{q} - 1.761\right) & : \; q \geq 1.8. \end{cases} \tag{4.22}$$

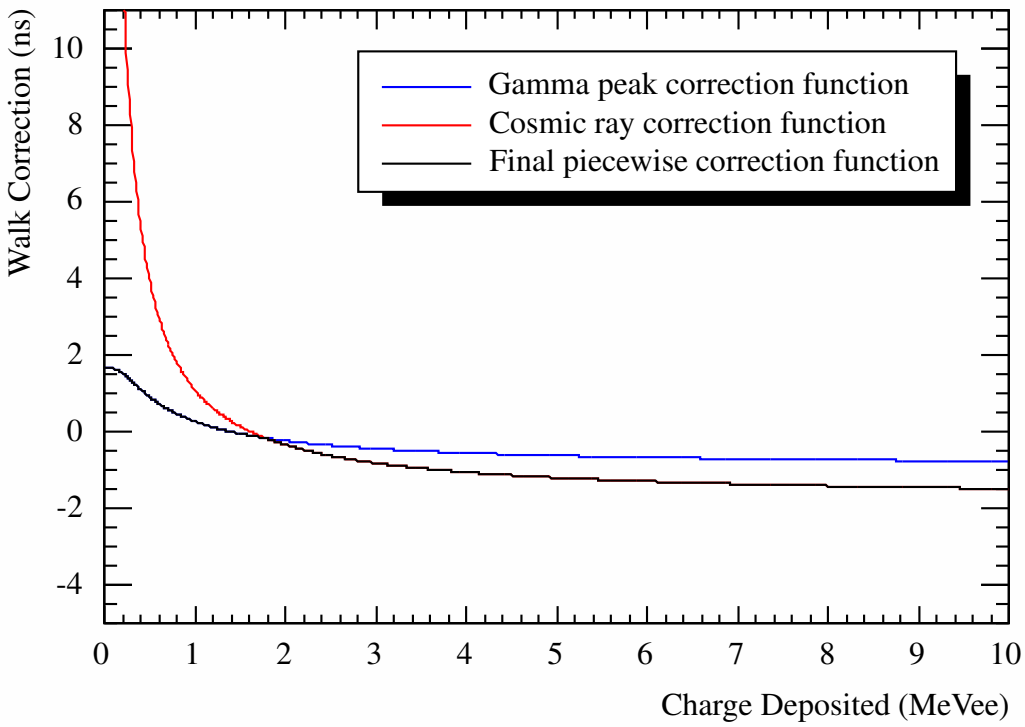

Figure 4.20: Walk correction functions. The blue curve is from a fit of time of flight vs. deposited energy, as shown in Fig. 4.18, while the red curve is from a fit of position-corrected time vs. deposited energy for cosmic ray data, shown in Fig. 4.19. The black curve is the final walk correction function, using the γ peak correction function (blue curve) below the crossing point ($q = 1.8$ MeVee) and the cosmic correction function (red curve) above. Note that the y axis in this figure represents the actual correction applied to the time of flight, which is the reason for the offset difference between the curves in this figure and those of Figs. 4.18–4.19.

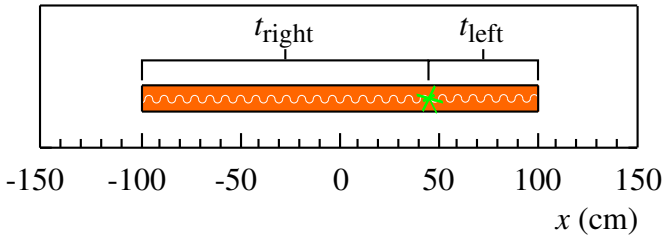

Figure 4.21: Illustration of MoNA x position measurement: the time it takes scintillation light to travel to each PMT is directly related to the distance from the PMT. By taking the time difference between the signals on the left and right PMTs, the x position in MoNA can be calculated.

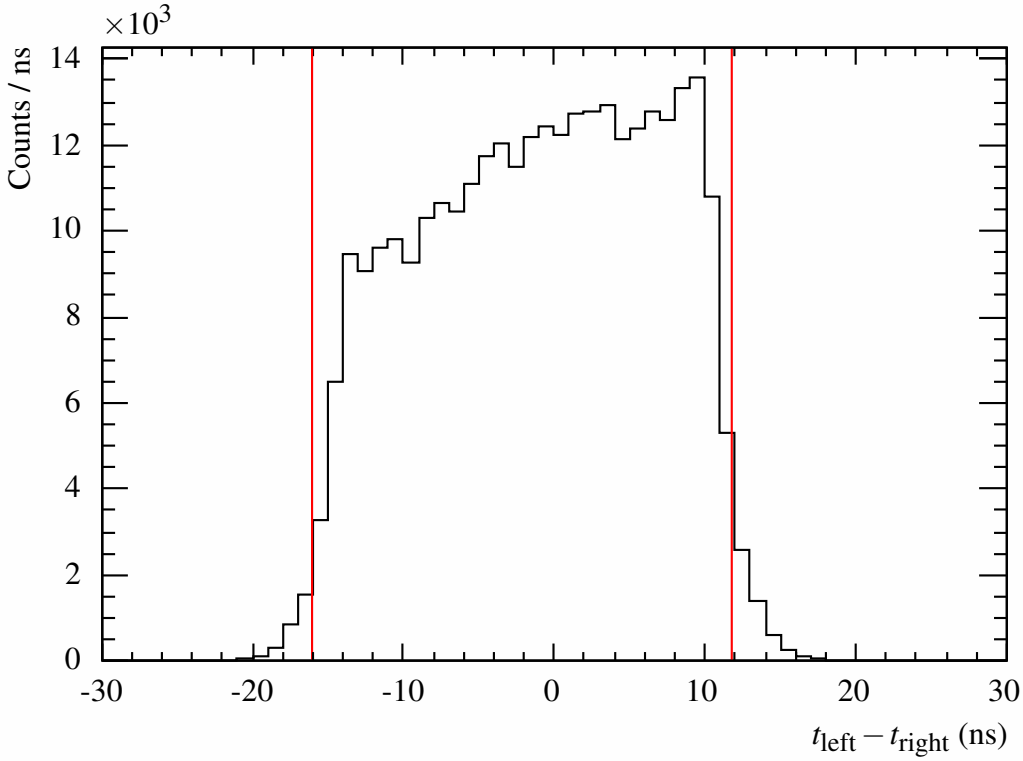

Figure 4.22: Example time difference spectrum for a single MoNA bar in a cosmic ray run. The $\frac{1}{3} \cdot max$ crossing points, indicated by the red vertical lines in the figure, are defined to be the edges of the bar in time space; these points are used to determine the slope and offset of Eq. (4.23). The asymmetry in the distribution is the result of the right side of MoNA being closer to the vault wall, thus receiving a larger flux of room γ-rays.

4.1.2.2 Position Calibrations

In order to accurately calculate neutron energy, as well as the angle of neutrons as they leave the target, the interaction position of a neutron within MoNA needs to be known. In the y and z planes, calculation of the interaction position is straightforward: it is simply taken to be at the center of the bar in which the neutron interacts. In the x direction, the interaction position is determined from the time difference between the left and right PMT signals. The time difference is directly related to the x interaction point since it is the result of scintillation light traveling a larger distance to one PMT versus the other, illustrated in Fig. 4.21. The time difference is related to the interaction position via a linear calibration:

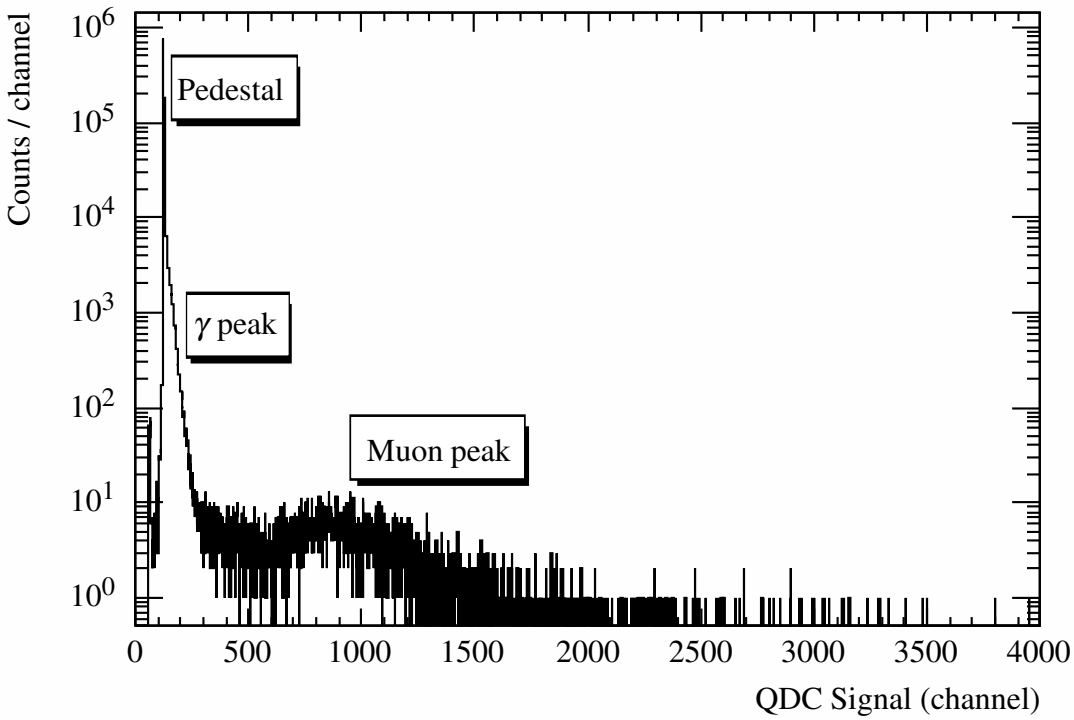

Figure 4.23: Example raw QDC spectrum for a single MoNA PMT. The pedestal and muon peak are indicated in the figure, along with the peak associated with room $\gamma-$rays interacting in MoNA. After adjusting voltages to place the muon bump of every PMT close to channel 800, a linear calibration is applied to move the pedestal to zero and the Gaussian centroid of the muon bump to 20.5 MeVee.

$$x = m \cdot \left(t_{\text{left}} - t_{\text{right}}\right) + b. \tag{4.23}$$

The slope m and offset b are determined from cosmic ray data: muons interacting near the edge of a bar are used to find its ends in time space, and these two points are sufficient to determine the linear factors. The edge of a bar in time space is defined to be at 1/3 of the maximum height of a histogram of time difference measurements, based on GEANT3 [67] simulations. Fig. 4.22 shows an example time difference spectrum, with the edges of the bar indicated.

Table 4.4: List of gamma sources used for CAESAR calibration. Energies are taken from Refs. [68–72].

Source	*Gamma Energies (keV)*
^{133}Ba	356
^{137}Cs	662
^{22}Na	1275
^{88}Y	898, 1836
^{56}Co	517, 846, 1771, 2034, 2598, 3272

4.1.2.3 Energy Calibrations

To account for differences in light collection and amplification, the PMTs in MoNA must be gain matched. This is done using cosmic ray muons, which deposit an average energy of 20.5 MeVee into a MoNA bar. The gain matching is done in two steps. The first step is to adjust the bias voltages on the the PMTs until their signals are approximately equal. Fig. 4.23 shows an example histogram of the raw QDC signal for a single PMT; the bump at around channel 800 is from muons interacting in MoNA. For each PMT, this bump is fit with a Gaussian, and the voltage on the PMT is adjusted to move the peak value close to 800. This procedure is iterated until the muon peak centroid of every PMT is within a few ($\sim$ 5 or less) channels of 800.

After adjusting the voltages to approximately line up the muon peaks, a software correction is applied to exactly match the peak locations. This is done in an automated routine which finds the location of the pedestal indicated in Fig. 4.23, as well as the Gaussian centroid of the muon bump. A linear slope and offset are then applied to place the pedestal at zero and the centroid of the muon bump at 20.5 MeVee.

4.1.3 CAESAR

The CAESAR crystals are calibrated using a variety of standard $\gamma-$ray check sources, listed in Table 4.4. Prior to beginning the experiment, the gain on each CAESAR photo-tube was adjusted to roughly align the peaks from the ^{88}Y source. Post experiment, a series of runs were taken with each source at the target location. For each of the gamma transitions listed in Table 4.4, the

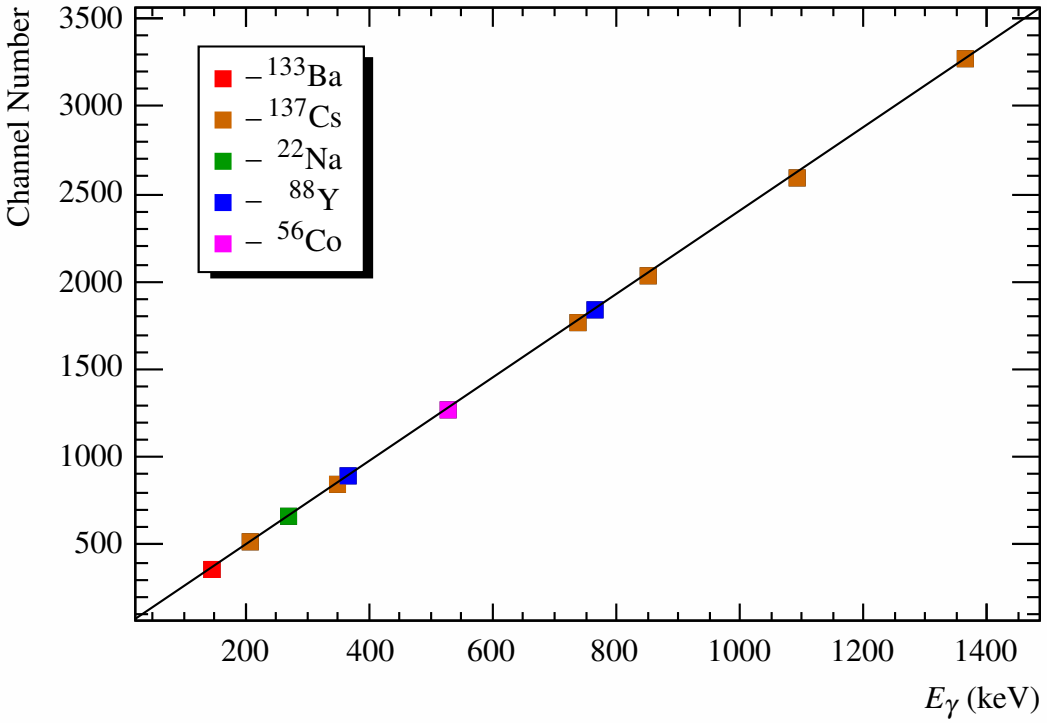

Figure 4.24: Example source calibrations for a single CAESAR crystal (J5). The solid black line is a linear fit to the data points ($R^2 = 0.999933$). All other crystals are similarly well described by a linear fit, so in the final analysis the calibration is done using the two ^{88}Y gamma lines at 898 keV and 1836 keV.

peak values in channel number were determined and plotted as a function of the known transition energy. This was done separately for each crystal in the array. As demonstrated in Fig. 4.24, the response is well described by a linear fit.

Since the response of CAESAR photo-tubes is influenced by the Sweeper's fringe fields, the calibration needs to be updated any time the Sweeper's current setting is changed, as hysteresis effects could potentially change the fringe field, in turn altering the calibration. During the experiment, approximately ten minutes of data were collected from the ^{88}Y source any time the Sweeper current was changed. Since the response function of CAESAR crystals is linear, the two data points from the ^{88}Y source $\left(E_\gamma = 898 \text{ keV and } E_\gamma = 1836 \text{ keV}\right)$ are used to set the calibration:

$$E = m \cdot ch + b, \tag{4.24}$$

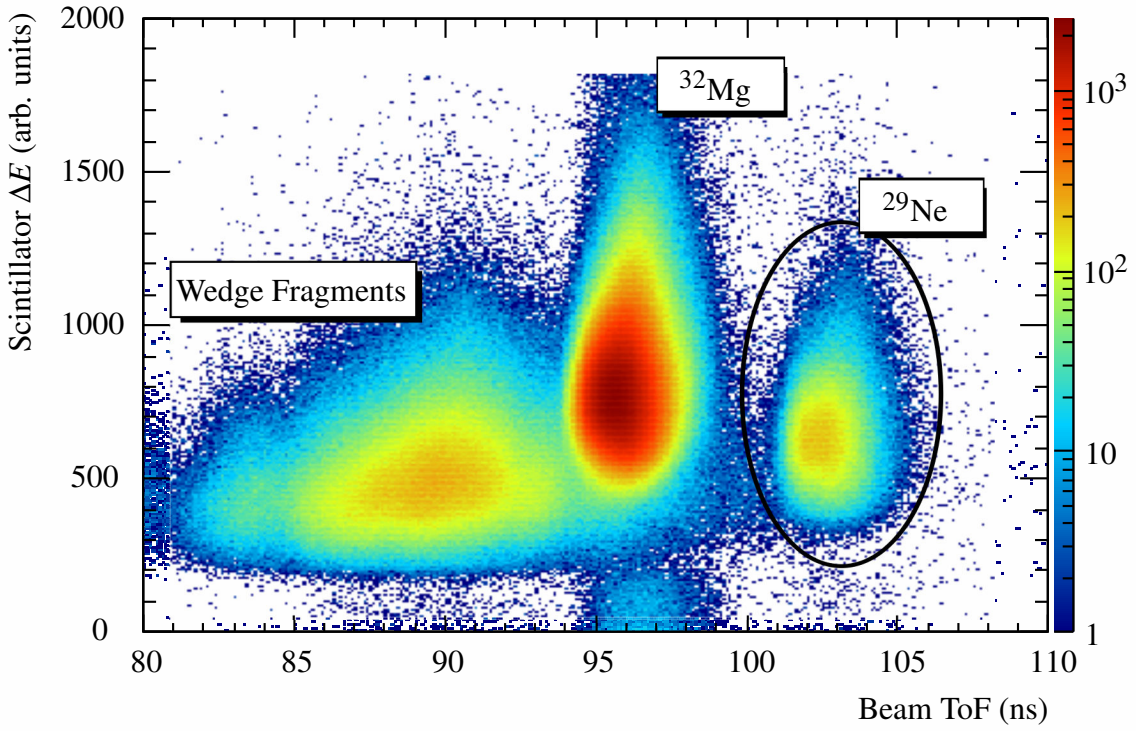

Figure 4.25: Beam components, including ^{29}Ne gate.

where *ch* is channel number, and *m* and *b* are determined from a linear fit of channel number versus energy for the two ^{88}Y transitions. The fit parameters are re-calculated after every ^{88}Y source run, with the updated parameters applied to the next block of production data.

4.2 Event Selection

In the course of the experiment, far more events are recorded than those of interest. This section[4] details the cuts used to select the events which are the result of the decay processes of interest: $^{28}\mathrm{F} \rightarrow {}^{27}\mathrm{F} + n$ and $^{27}\mathrm{F}^{*} \rightarrow {}^{26}\mathrm{F} + n$.

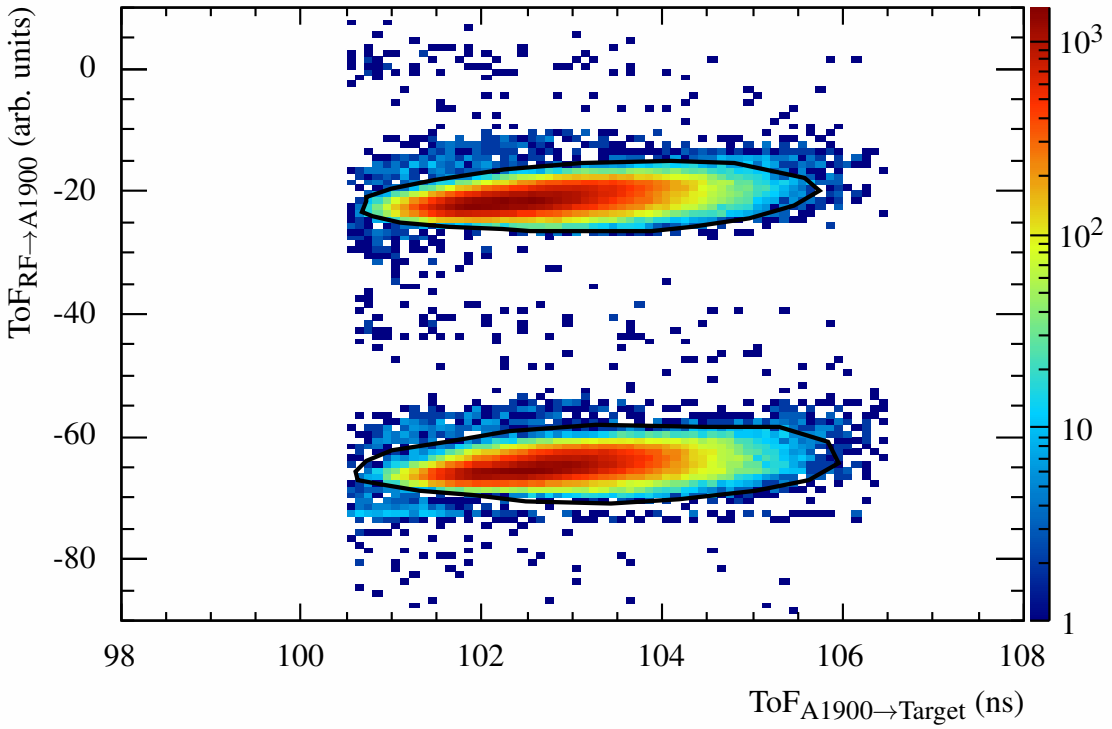

Figure 4.26: Flight time from the K1200 cyclotron (measured by the cyclotron RF) to the A1900 scintillator versus flight time from the A1900 scintillator to the target scintillator. The double peaking in ToF$_{RF\rightarrow A1900}$ is due to wraparound of the RF. By selecting only events which are linearly correlated in these two parameters, the contribution of wedge fragments to the beam is reduced. These selections are indicated by the black contours in the figure, with the final cut being an OR of the two gates.

4.2.1 Beam Identification

As mentioned in Section 3.2, the incoming beam is made up of a number of different nuclear species. The ^{29}Ne beam particles are selected from measurements of energy loss in the target scintillator and time of flight from the A1900 scintillator to the target scintillator. Fig. 4.25 shows a histogram of these two parameters, with the ^{29}Ne events circled. The overall contribution of ^{29}Ne to the beam is approximately one percent, with the remainder primarily composed of ^{32}Mg, as well as a variety isotopes created by reactions in the aluminum wedge.

[4]Cuts pertaining to inverse reconstruction of tracks through the Sweeper magnet will be presented in Section 4.3.1.1, after that subject has been properly introduced.

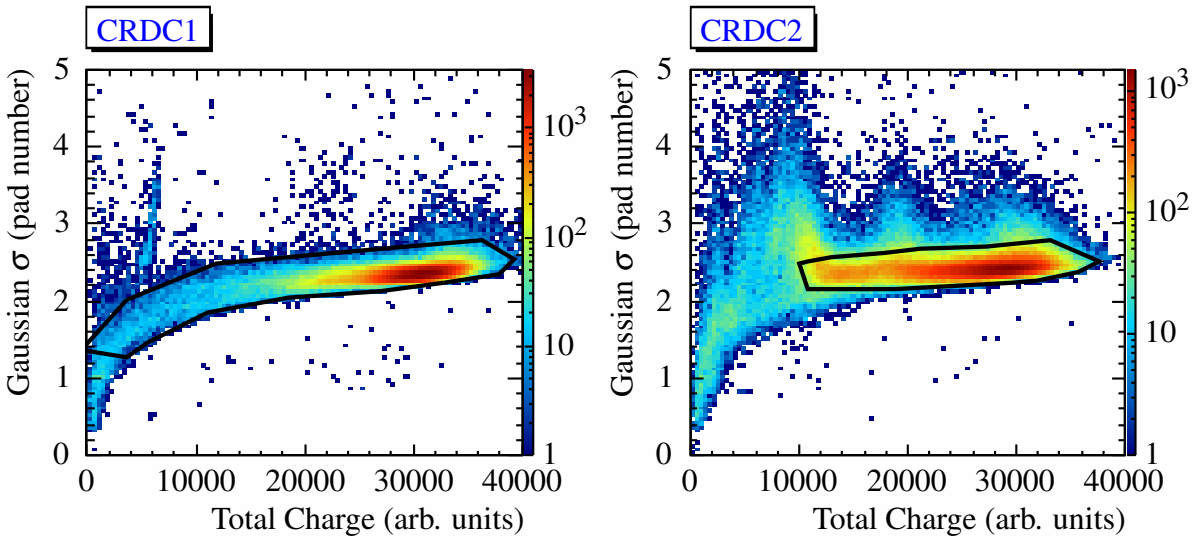

Figure 4.27: CRDC quality gates. Each plot is a histogram of the sigma value of a Gaussian fit to the charge distribution on the pads versus the sum of the charge collected on the pads. The black contours indicate quality gates made on these parameters.

In addition to the ΔE_{Target} versus $\text{ToF}_{\text{A1900}\rightarrow\text{Target}}$ cut, a cut on time of flight from the K1200 cyclotron to the A1900 scintillator versus time of flight from the A1900 scintillator to the target scintillator is used to improve the incoming beam selection. Here the time at the K1200 cyclotron is measured from the cyclotron RF signal. This cut has the effect of removing wedge fragments from the beam, as particles produced from reactions in the aluminum wedge will have a more dramatic change in velocity than those which pass through the wedge unreacted. Thus by selecting only events which are linearly correlated in $\text{ToF}_{\text{RF}\rightarrow\text{A1900}}$ versus $\text{ToF}_{\text{A1900}\rightarrow\text{Target}}$, the presence of wedge fragments is reduced. This cut is indicated in Fig. 4.26.

4.2.2 CRDC Quality Gates

Often a CRDC detector will record an event for which the x position measurement is not reliable. The contribution of such events can be reduced by applying quality gates to each of the focal plane CRDCs. Application of CRDC quality gates will also remove any events that do not pass through the active area of both detectors. Events that have an unreliable x position measurement usually result from a pathological charge distribution on the CRDC pads. They can be identified

event-by-event by considering a plot of the σ value of the Gaussian fitting procedure explained in Section 4.1.1.2 versus the sum of the charge on all CRDC pads; the events for which the x position measurement is not reliable will be anomalous in such a plot. The plots of σ versus total charge are shown for CRDC1 and CRDC2 in Fig. 4.27, with the quality gates indicated in the figure.

4.2.3 Charged Fragment Identification

A major requirement in selecting the events of interest is charged particle separation and identification. This is done in two steps: element selection and isotope selection.

4.2.3.1 Element Selection

Element separation is achieved by measurement of the fragment's energy loss in the ion chamber, as well as its velocity. Energy loss in the ion chamber gas is given by the Bethe-Bloch formula [58]:

$$-\frac{dE}{dx} = 2\pi N_a r_e^2 m_e c^2 \rho \frac{Z}{A}\frac{z^2}{\beta^2}\left[\ln\left(\frac{2m_e\gamma^2 v^2 W_{\max}}{I^2}\right) - 2\beta^2\right], \tag{4.25}$$

with

$2\pi N_a r_e^2 m_e c^2 = 0.1535\ \text{MeVcm}^2/\text{g}$

r_e : classical electron radius = 2.187×10^{-13} cm

m_e : electron mass

N_a : Avagadro's number = 6.022×10^{23} mol^{-1}

I : mean excitation potential

Z : atomic number of absorbing material

A : atomic weight of absorbing material

ρ : density of absorbing material

z : charge of incident particle in units of e

β : v/c of the incident particle

γ : $1/\sqrt{1-\beta^2}$

$W_{\max}$: maximum energy transfer in a single collision.

From Eq. (4.25), it is clear that energy loss is related to the charge number of the incident particle, as well as its velocity:

$$\Delta E \propto \frac{z^2}{\beta^2} \cdot f(\beta). \tag{4.26}$$

Thus elements can be separated by plotting energy loss in the ion chamber versus a parameter which is indicative of fragment velocity. There are two velocity indicator parameters available in the experiment: time of flight through the Sweeper $\left(\mathrm{ToF}_{\mathrm{Target}\rightarrow\mathrm{Thin}}\right)$ and total kinetic energy measured in the thick scintillator. As demonstrated in Figs. 4.28 and 4.29, plotting ion chamber energy loss versus either of these parameters reveals well-separated bands, with each band corresponding to a different element. In both plots, the most intense element is unreacted ^{29}Ne beam $(Z = 10)$. Hence the band directly below this one is composed of the fluorine $(Z = 9)$ events of interest. In the final analysis, the element cuts indicated in Figs. 4.28 and 4.29 are both used.

4.2.3.2 Isotope Selection

The magnetic rigidity of a charged particle is equal to its momentum:charge ratio,[5]

$$B\rho = \frac{p}{q} = \frac{mv}{q}. \tag{4.27}$$

If isotopes of the same element (constant q) and equivalent $B\rho$ are sent through a dipole magnet, then their mass number, A, can be related to their time of flight, t, as follows:

$$v = \frac{B\rho q}{m} \tag{4.28}$$

$$t = A\left(\frac{Lm_u}{B\rho q}\right), \tag{4.29}$$

[5] Ignoring relativity.

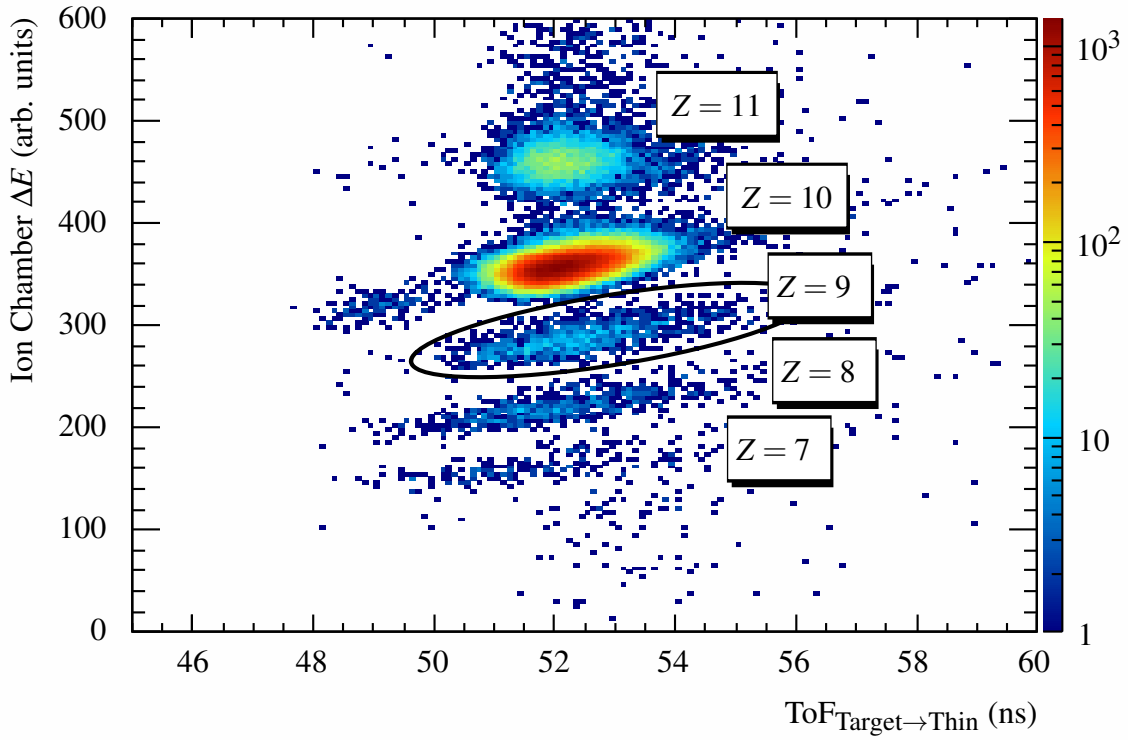

Figure 4.28: Energy loss in the ion chamber versus time of flight through the Sweeper. Each band in the figure is a different isotope, with the most intense band composed primarily of $Z = 10$ unreacted beam. The fluorine $(Z = 9)$ events of interest are circled and labeled in the figure.

where m_u is the average mass of a nucleon in the nucleus and L is the track length. Thus in the case of constant $B\rho$ (constant momentum), isotopes of the same element can be mass-separated simply by considering their time of flight.

In practice, charged particles produced in nuclear reactions have a large spread in momentum. If the magnetic elements used for separation accept a reasonably large range of momenta, then the assumption of Eq. (4.29) that $B\rho$ is constant is no longer valid. Moreover, differing momenta result in variable L, as the track of a charged particle passing through a dipole depends on its rigidity. However, the $B\rho$ and L values of the charged particles are reflected in their emittance (dispersive position and angle) as they exit the device. Magnetic spectrometers, such as the NSCL's S800 [47], can be tuned such that the fragments exiting the device are highly focused in position. In this case, it is possible to see isotopic separation simply by plotting angle at the focal plane versus time of

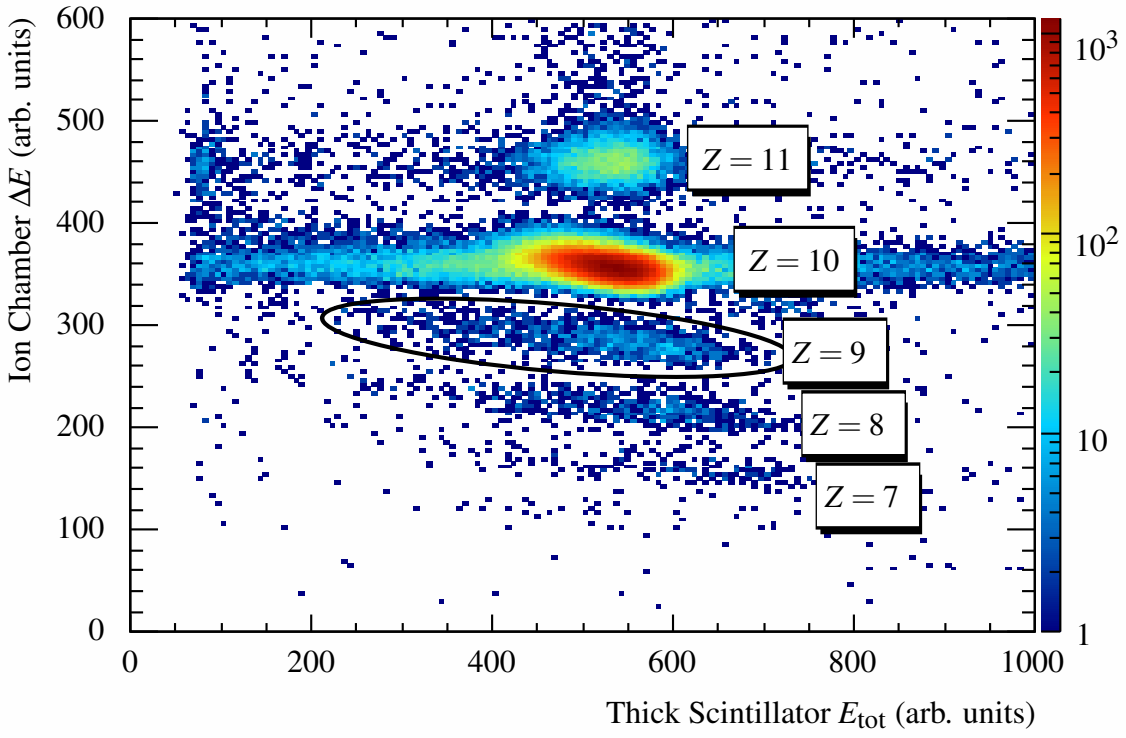

Figure 4.29: Energy loss in the ion chamber versus total kinetic energy measured in the thick scintillator. As in Fig. 4.28, the bands in the figure are composed of different elements, and the most intense band is $Z = 10$. fluorine $(Z = 9)$ events are circled and labeled.

flight. The left panel of Fig. 4.30 is an example of the use of this technique in the S800. The events in the figure are magnesium $(Z = 12)$, and each band is composed of a different isotope [73].

In the case of the Sweeper magnet, the technique outlined above is not sufficient to separate isotopes. This is demonstrated in the right panel of Fig. 4.30, in which a plot of focal plane angle versus time of flight shows no hint of separation. The main reason is that the Sweeper lacks focusing elements; hence angle and position at the focal plane are correlated to a large degree. Furthermore, the magnetic field of the Sweeper is highly nonuniform, due to its large vertical gap of 14 cm. This leads to a significant degree of nonlinearity in the emittance. In the case of the Sweeper, the full correlation between angle, position, and time of flight needs to be considered for isotope separation to be visible. This is demonstrated in Fig. 4.31, which is a three dimensional plot of time of flight versus angle and position, from the present experiment. The events in the plot

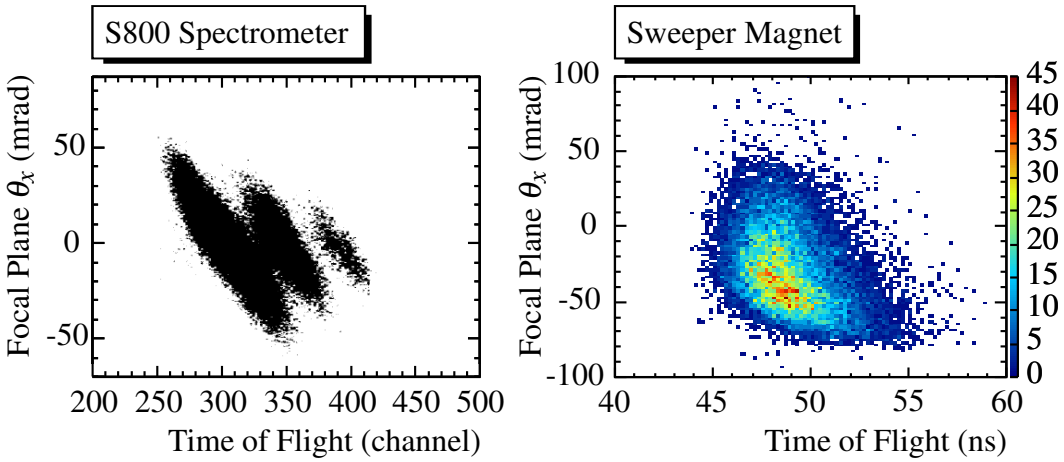

Figure 4.30: Left panel: focal plane dispersive angle vs. time of flight for magnesium isotopes in the S800, taken from Ref. [73]. In this case, isotopes are clearly separated just by considering these two parameters. Right panel: focal plane dispersive angle vs. time of flight for fluorine isotopes in the present experiment. The plot shows no hint of isotope separation, as three dimensional correlations between angle, position and time of flight need to be considered in order to distinguish isotopes.

are fluorine isotopes produced from reactions on the ^{32}Mg beam, and the bands which can be seen in the figure are each composed of a different isotope.

From the picture of Fig. 4.31, a systematic method has been developed to correct the time of flight for angle and position at the focal plane, resulting in a parameter which can be used for isotope selection. The corrections are first determined for fluorine elements from the ^{32}Mg beam, to take advantage of higher statistics. The same corrections can then be used for the isotopes of interest: fluorines produced from the ^{29}Ne beam.

The first step in correcting the time of flight is to construct a single parameter which describes the dispersive-plane emittance, both angle and position. To do this, the three dimensional plot in Fig. 4.31 is profiled in the following way:[6]

1. Slice the x and θ_x axes into a square grid.

2. For the events in each each slice, make a one dimensional projection of the ToF axis.

[6]In practice, this is simply done using the `TH3::Project3DProfile` method of the ROOT [74,75] data analysis package.

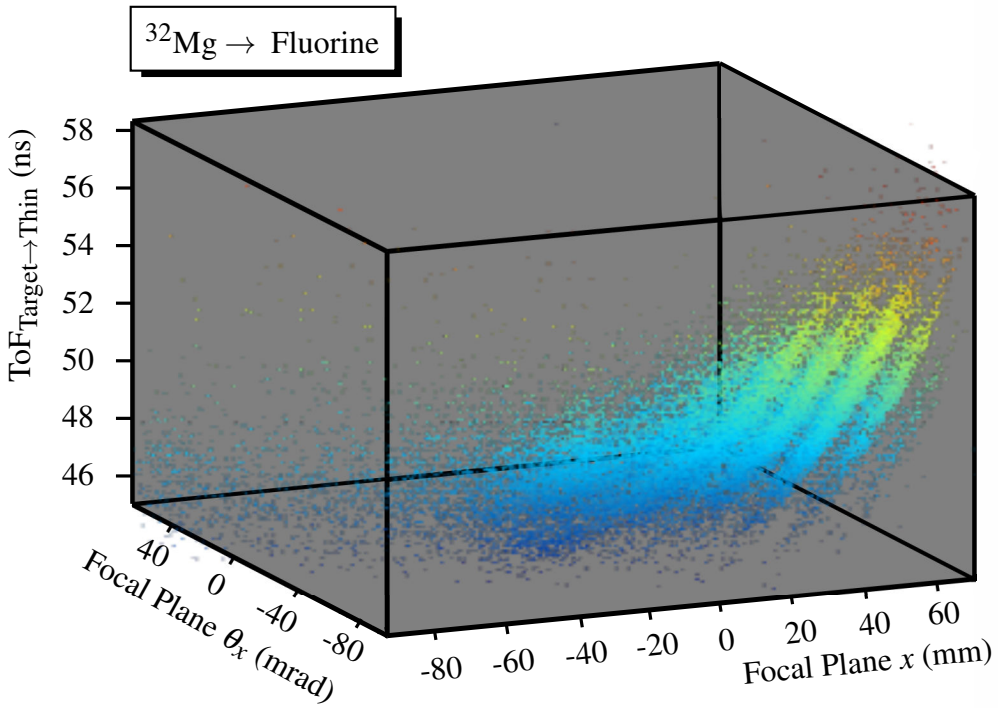

Figure 4.31: Three dimensional plot of time of flight through the Sweeper vs. focal plane angle vs. focal plane position (color is also representative of time of flight). The figure is composed of $Z = 9$ events coming from the ^{32}Mg contaminant beam, and each band in the figure is composed of a different isotope.

3. Find the gravity centroid of the projection of (2).

4. Plot the centroid from (3) versus the central x and θ_x positions of the slice.

The result is shown in Fig. 4.32, with the color axis representing the gravity centroids of the ToF projections. Breaks in color indicate lines of iso-ToF. From here, one determines a function which describes the location of the iso-ToF lines throughout the figure:

$$f(x) = 0.010397 \cdot x^2 + 0.84215 \cdot x + c, \tag{4.30}$$

where c is a constant offset. This function, for a given c, is drawn as the solid black curve in Fig. 4.32. The effect of varying c is to move the curve vertically along the θ_x axis, and an appropriate function will fall on the iso-ToF lines independent of c.

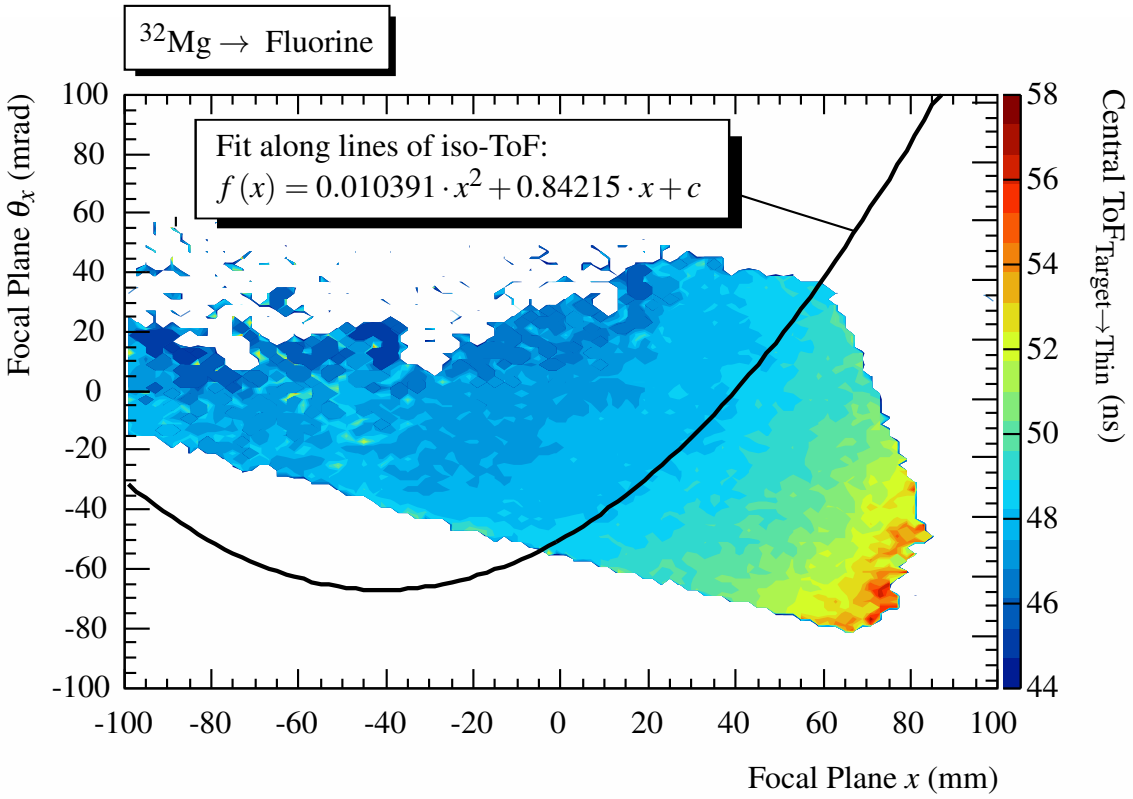

Figure 4.32: Profile of the three dimensional scatter-plot in Fig. 4.31. The solid black curve is a fit to lines of iso-ToF; this fit is used to construct a reduced parameter describing angle and position simultaneously.

From Eq. (4.30), a parameter describing both angle and position is constructed:

$$e(x, \theta_x) = \theta_x - \left(0.010397 \cdot x^2 + 0.84215 \cdot x\right). \tag{4.31}$$

As shown in Fig. 4.33, a plot of the appropriately constructed $e(x, \theta_x)$ versus time of flight demonstrates bands, with each band corresponding to a different isotope.

From the picture of Fig. 4.33, it is possible to improve isotope separation significantly. The first step is to create a corrected time of flight parameter by determining the nominal slope, m, of the bands, represented by the black line in the figure. The time of flight is corrected by simply projecting onto the axis perpendicular to this line:

$$t_{\text{corr}} = t + m^{-1} \cdot e(x, \theta_x). \tag{4.32}$$

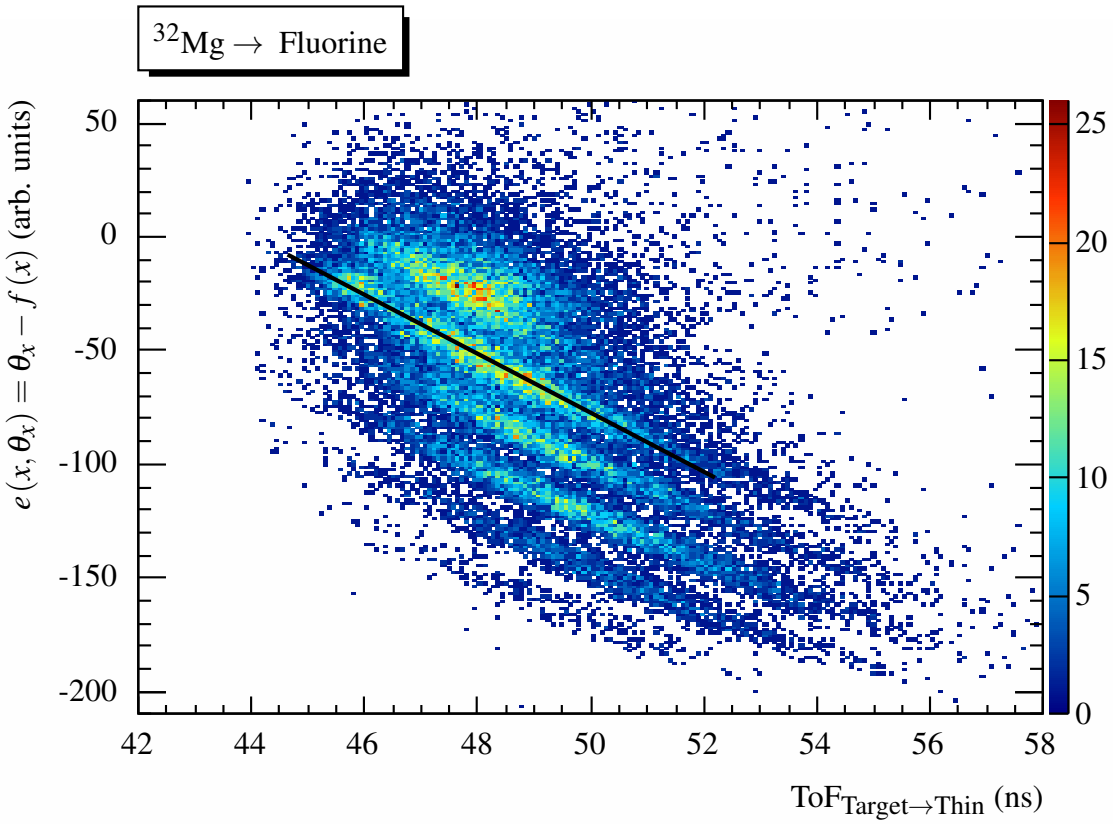

Figure 4.33: Histogram of the emittance parameter, constructed from the fit function in Fig. 4.32, vs. time of flight. The bands in the plot correspond to different isotopes of fluorine. A corrected time of flight parameter can be constructed by projecting onto the axis perpendicular to the line drawn on the figure.

Table 4.6: Final correction factors used for isotope separation. The numbers in the right column are multiplied by the parameter indicated in the left and summed; this sum is then added to ToF$_{\text{Target}\to\text{Thin}}$ to construct the final corrected time of flight.

Parameter	*Correction Factor*		
x	-5.0595×10^{-2}	$x^2\theta_x^2$	1.4×10^{-7}
x^2	-8.97×10^{-4}	y^2	1.0×10^{-3}
x^3	-3.0×10^{-6}	θ_y	-3.0×10^{-3}
θ_x	8.0×10^{-2}	$y_{trgt.}$	4.0×10^{-3}
θ_x^2	-1.0×10^{-5}	E_{thick}	1.3×10^{-3}
θ_x^3	2.0×10^{-6}	$\Delta E_{i.c.}$	4.0×10^{-3}
$x\theta_x$	-1.5×10^{-4}	x_{tcrdc1}	1.7×10^{-2}
$x^2\theta_x$	-2.0×10^{-6}	ToF$_{beam}$	1.0×10^{-1}
$x\theta_x^2$	-6.0×10^{-6}		—

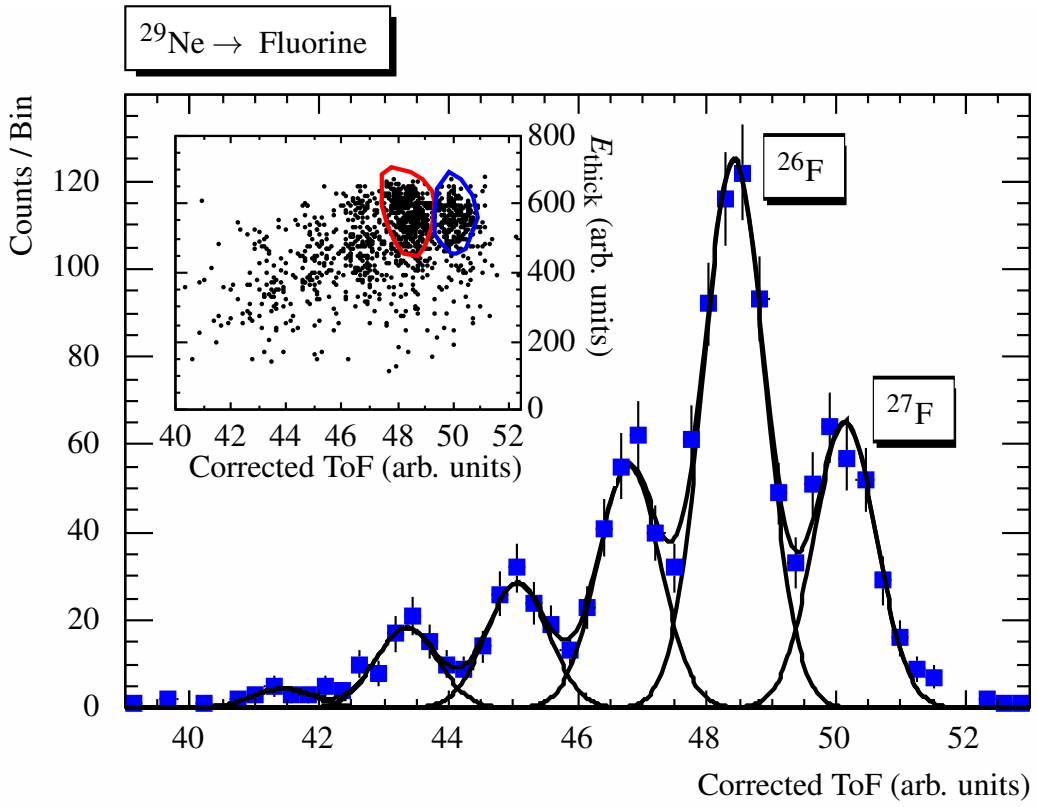

Figure 4.34: Main panel: Corrected time of flight for fluorine isotopes resulting from reactions on the ^{29}Ne beam. The isotopes if interest, ^{26,27}F, are labeled. The black curve in the figure is a fit to the data points with the sum of five Gaussians of equal width. Based on this fit, the cross-contamination between ^{26}F and ^{27}F is approximately 4%. The inset is a scatter-plot of total energy measured in the thick scintillator vs. corrected time of flight. These are the parameters on which ^{26,27}F isotopes are selected in the final analysis, and the cuts for each isotope are drawn in the figure.

The separation is then improved by iteratively plotting corrected time of flight versus angle or position and removing the correlations in a manner similar to that of Eq. (4.32). This is done up to fourth order in x and θ_x, as well as for cross terms $(x^n \cdot \theta_x^n)$. Additionally, correlations between corrected time of flight and any other parameter available in the experiment are searched for and, if present, removed. Table 4.6 lists all of the factors used in constructing the final corrected time of flight. It should be noted that the corrections for non-dispersive angle (θ_y) and dispersive position at TCRDC1 (x_{tcrdc1}) significantly improve the quality of the separation.

The main panel of Fig. 4.34 shows the corrected time of flight, using the factors listed in Table 4.6, for fluorine isotopes produced from ^{29}Ne. As can be seen in the figure, the fluorine

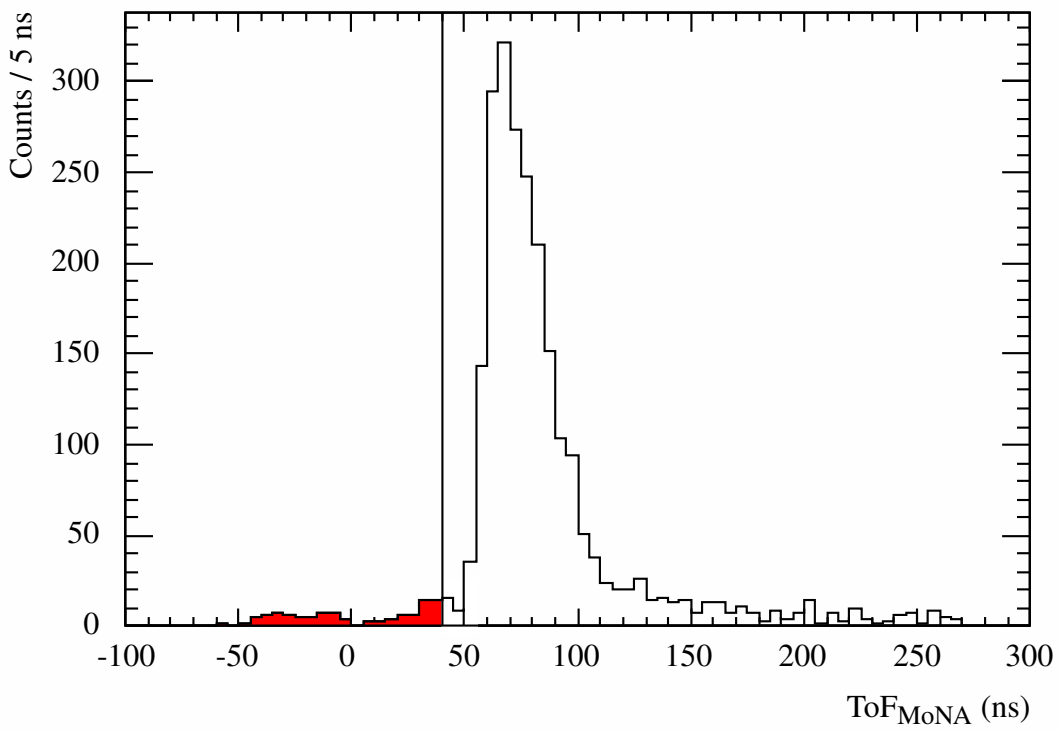

Figure 4.35: Neutron time of flight to MoNA for all reactions products produced from the ^{29}Ne beam. The first time-sorted hit coming to the right of the vertical line at 40 ns is the one used in the analysis.

isotopes are well separated, with a cross contamination between ^{26}F and ^{27}F of approximately 4%. The cross-contamination is determined by fitting the histogram with the sum of five equal-width Gaussians, shown as the solid black curve in the figure, and calculating the overlap between the gate for a given isotope and the Gaussian fit function of its neighbor(s). Fluorine isotopes are identified simply by noting that ^{27}F is the heaviest fluorine species that can be produced from ^{29}Ne. In the final analysis, a two dimensional cut on corrected time of flight and total energy from the thick scintillator is used for isotope selection. A scatter-plot of these two parameters is shown in the inset of Fig. 4.34, along with the gates used in the final analysis.

4.2.4 MoNA Cuts

To avoid biasing the neutron energy measurement, cuts on MoNA parameters are avoided. However, since MoNA often records multiple hits for a given event, it is necessary to decide which hit to use in the final analysis. Hits in MoNA can arise from a number of sources in addition to prompt neutrons: prompt $\gamma-$rays; random background (muons and gammas); and multiple detection of the same event due to scattering of neutrons within the array. Thus a scheme is devised to ensure that the analysis is being performed on the hit which is most likely to be the result of a prompt neutron interacting in MoNA for the first time: hits are time-sorted, and the first hit with time of flight greater than 40 ns is selected. The reason for requiring that the hit come at ToF $>$ 40 ns is that it is not possible for neutrons produced in the target to make it to MoNA any earlier than this. This can be seen in Fig. 4.35, in which the prompt neutron peak begins abruptly at around 50 ns. To avoid cutting any early neutron events, the opening of the neutron window is conservatively placed at 40 ns.

4.2.5 CAESAR Cuts

Fig. 4.36 demonstrates a cut used to reduce the presence of background events in CAESAR. Events which are correlated with the γ decay of a beam nucleus will come at a specific time in CAESAR. Thus by eliminating events which fall outside of a certain time window, the signal to noise ratio is improved. Since CAESAR uses leading edge discriminators for its time measurements, there is significant walk in the time signal. However, by plotting Doppler corrected[7] gamma energy versus time of flight, as in Fig. 4.36, a two dimensional gate can be drawn to select only beam-correlated events. This gate is outlined by the solid black curves drawn in the figure.

[7] The Doppler correction procedure will be presented in Section 4.3.2

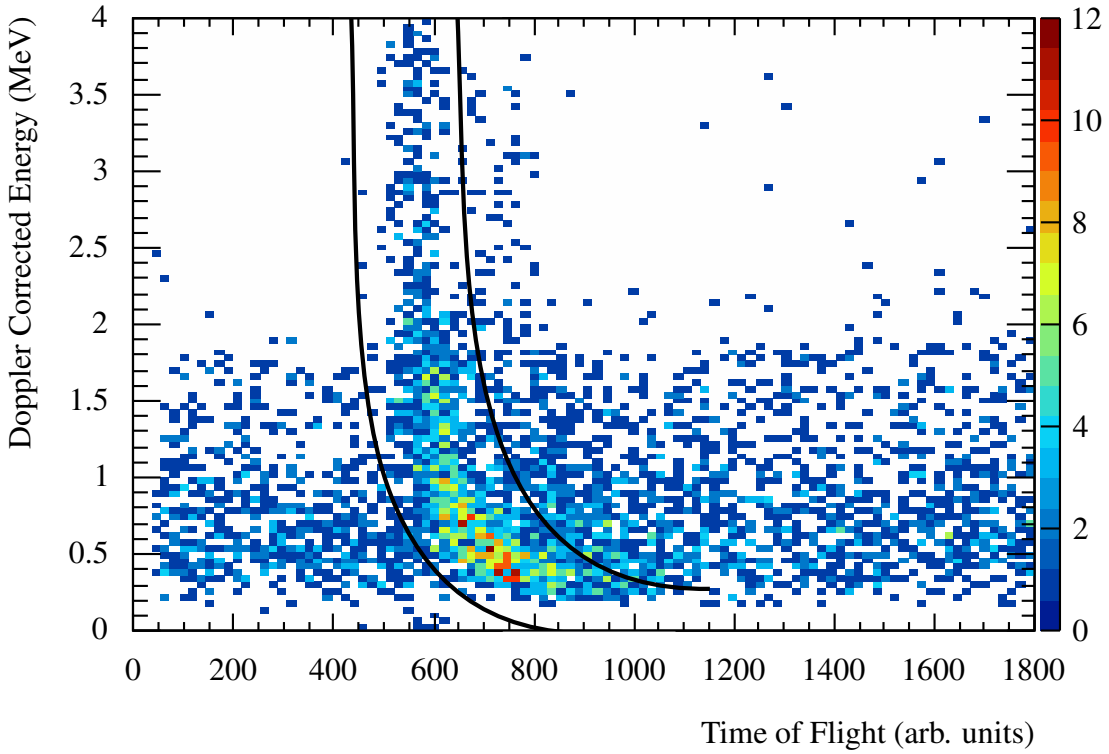

Figure 4.36: Doppler corrected energy vs. time of flight for gammas recorded in CAESAR. To reduce the contribution of background, only those events falling between the solid black curves are analyzed.

4.3 Physics Analysis

The purpose of the present experiment is to measure the decay energy of neutron-unbound states using the invariant mass equation, Eq. (3.7):

$$E_{\text{decay}} = \sqrt{m_f^2 + m_n^2 + 2\left(E_f E_n - p_f p_n \cos\theta\right)} - m_f - m_n.$$

This requires measurement of the kinetic energies and angles at the target of both the neutron, n, and the fragment, f, involved in the breakup of the unbound state. In the case of the neutron, calculation of these quantities is straightforward. The angle is taken from simple ray-tracing between the target location and the interaction point in MoNA, while the kinetic energy is calculated from the time of flight and total distance traveled, using relativistic kinematics:

$$v_n = \frac{\sqrt{x^2+y^2+z^2}}{t} \tag{4.33}$$

$$\gamma_n = 1/\sqrt{1-\left(\frac{v_n}{c}\right)^2} \tag{4.34}$$

$$E_n = \gamma_n m_n. \tag{4.35}$$

In the case of the fragment, calculation of kinetic energy and target angle is more involved. It requires reconstruction of tracks through the Sweeper, as described below.

4.3.1 Inverse Tracking

From knowledge of the Sweeper's magnetic field and ion-optical quantities of a charged particle at the reaction target, it is possible to calculate the ion-optical quantities of the particle as it exits the magnet:

$$\begin{pmatrix} x^{(\mathrm{crdc1})} \\ \theta_x^{(\mathrm{crdc1})} \\ y^{(\mathrm{crdc1})} \\ \theta_y^{(\mathrm{crdc1})} \\ L \end{pmatrix} = \mathscr{M} \begin{pmatrix} x^{(\mathrm{trgt})} \\ \theta_x^{(\mathrm{trgt})} \\ y^{(\mathrm{trgt})} \\ \theta_y^{(\mathrm{trgt})} \\ E^{(\mathrm{trgt})} \end{pmatrix}, \tag{4.36}$$

where L is the track length of the fragment through the Sweeper and $\mathscr{M}$ is a third-order transformation matrix calculated from magnetic field measurements. The transformation matrix is produced using the ion-optical code COSY INFINITY [76]. COSY takes as input the magnetic field of the Sweeper in the central plane—the plane where the only existing vertical components of the field are those perpendicular to the horizontal plane. To measure the central plane field, seven Hall probes were mounted vertically, evenly spaced, on a movable cart and stepped through the magnet. The field in the central plane was constructed from interpolation of the seven Hall probe measurements. More details about the mapping procedure can be found in Ref. [60].

The quantities in Eq. (4.36) which need to be known for invariant mass spectroscopy are $\theta_x^{(\mathrm{trgt})}$, $\theta_y^{(\mathrm{trgt})}$, and $E^{(\mathrm{trgt})}$. As each of these quantities is influenced by the nuclear reaction taking place in the target, none is measured directly. The parameters which are measured, however, are $x^{(\mathrm{crdc1})}$, $\theta_x^{(\mathrm{crdc1})}$, $y^{(\mathrm{crdc1})}$, $\theta_y^{(\mathrm{crdc1})}$, $x^{(\mathrm{trgt})}$, and $y^{(\mathrm{trgt})}$. Thus it is desirable to come up with a transformation which takes as input some combination of the known quantities

$$\left\{x^{(\mathrm{crdc1})},\ \theta_x^{(\mathrm{crdc1})},\ y^{(\mathrm{crdc1})},\ \theta_y^{(\mathrm{crdc1})},\ x^{(\mathrm{trgt})},\ y^{(\mathrm{trgt})}\right\}$$

and gives as output the desired quantities

$$\left\{\theta_x^{(\mathrm{trgt})},\ \theta_y^{(\mathrm{trgt})},\ E^{(\mathrm{trgt})}\right\}.$$

Such a transformation cannot be calculated from direct inversion of $\mathscr{M}$, as the track length L is not known *a priori.* The approach taken by COSY to calculate an inverse matrix is to assume that $x^{(\mathrm{trgt})} = 0$. This allows elimination of the row concerning $x^{(\mathrm{trgt})}$ and the column concerning L, leading to a form of $\mathscr{M}$ that is invertible. Such an approach is valid when the beam is narrowly focused in x, which is *not* the case in the present experiment: the beam spot size is on the order of 2 cm.

To construct an appropriate inverse transformation matrix, a procedure has been developed to perform a partial inversion of $\mathscr{M}$ [77]. The partially inverted matrix, $\mathscr{M}_{pi}$, takes as input the positions and angles at CRDC1 (behind the Sweeper), as well as the x position on the target (measured from the tracking CRDCs[8]). Its output includes all of the desired quantities: $\theta_x^{(\mathrm{trgt})}$, $\theta_y^{(\mathrm{trgt})}$, and $E^{(\mathrm{trgt})}$:

[8] It should be noted that a transformation similar to Eq. (4.36) is used to calculate $x^{(\mathrm{trgt})}$, as the tracking CRDCs are located upstream of the quadrupole triplet. In this case, the E and L terms are ignored, as the dependence of tracks through the triplet on beam energy is negligible.

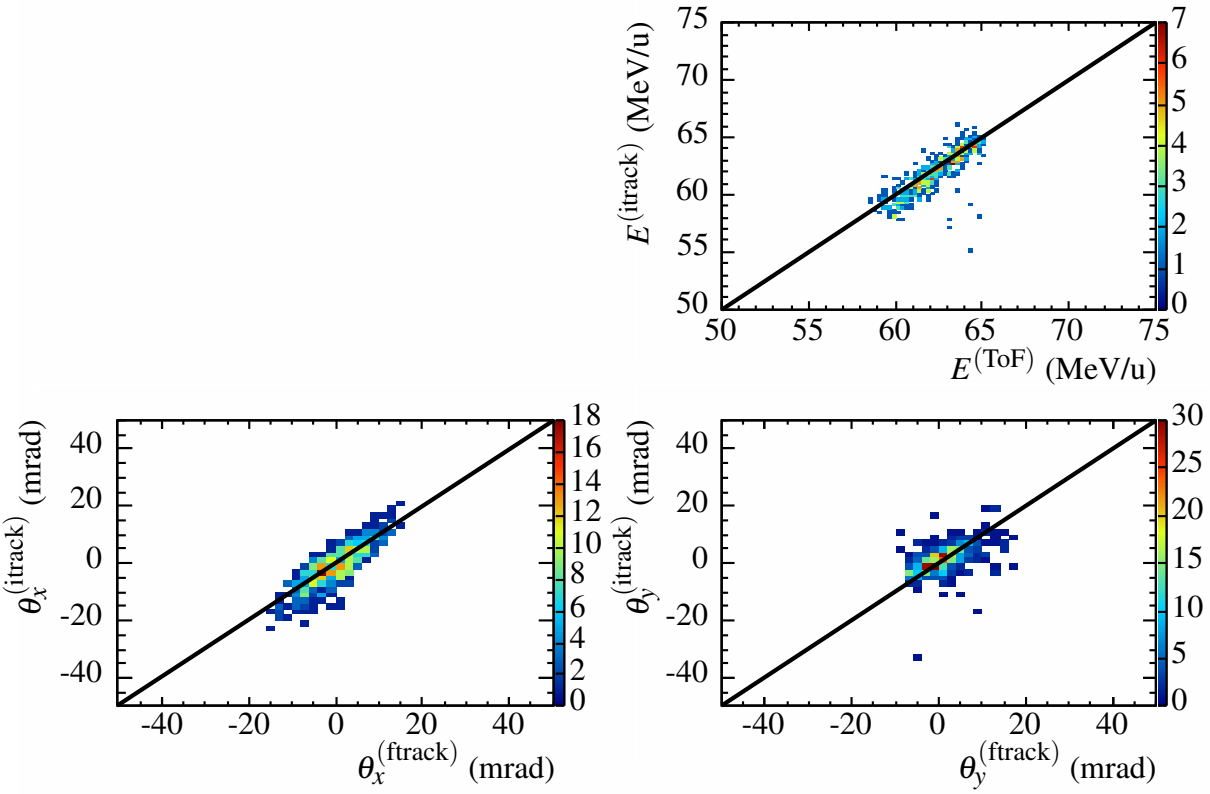

Figure 4.37: Comparison of forward tracked and inverse tracked parameters for unreacted ^{29}Ne beam. The upper right panel is a comparison of kinetic energies, with the x axis being energy calculated from $\mathrm{ToF}_{\mathrm{A1900}\rightarrow\mathrm{Target}}$ and the y axis energy calculated from inverse tracking in the sweeper, c.f. Eq. (4.37). The lower left and lower right panels show a similar comparison for θ_x and θ_y, respectively. In these plots, the x axis is calculated from TCRDC measurements and forward tracking through the quadrupole triplet.

$$\begin{pmatrix} \theta_x^{(\mathrm{trgt})} \\ y^{(\mathrm{trgt})} \\ \theta_y^{(\mathrm{trgt})} \\ L \\ E^{(\mathrm{trgt})} \end{pmatrix} = \mathscr{M}_{pi} \begin{pmatrix} x^{(\mathrm{crdc1})} \\ \theta_x^{(\mathrm{crdc1})} \\ y^{(\mathrm{crdc1})} \\ \theta_y^{(\mathrm{crdc1})} \\ x^{(\mathrm{trgt})} \end{pmatrix}. \tag{4.37}$$

The procedure for calculating the partial inverse transformation matrix $\mathscr{M}_{pi}$ is to perform a series of matrix operations which exchange a coordinate on the right hand side of Eq. (4.36) with one on the left. This is done until the form of Eq. (4.37) is reached. The coordinates to be exchanged

must be entangled to a large degree, i.e. they must share a large first order matrix element in $\mathscr{M}$. The procedure for coordinate-swapping is detailed in Ref. [77].

To check that the inverse mapping procedure gives the correct results, a comparison is made between forward-tracked target parameters and their counterparts calculated with Eq. (4.37), for data taken with the reaction target removed. The comparison was done for a variety of magnet settings, and good agreement was found except when the beam is on the extreme edge of the Sweeper's acceptance. An example comparison, when the beam is near the center of the acceptance, is shown in Fig. 4.37. The reason for disagreement between forward and inverse tracking when the beam is near the edge of the Sweeper's acceptance is that the magnetic field of the Sweeper is poorly understood in this region. However, during production runs the Sweeper is tuned such that the reaction products of interest lie near the center of the acceptance, in a region where there is good agreement between forward and inverse tracking.

4.3.1.1 Mapping Cuts

As mentioned in Section 4.2, some cuts have to be made to ensure that the inverse tracked parameters of Eq. (4.37) are being calculated correctly. The first involves the dispersive plane emittance. As shown in the left panel of Fig. 4.38, when unreacted beam particles are swept across the focal plane, they maintain a positive correlation between angle and position. This is not always the case for reaction products, which are far more dispersed in angle. The right panel of Fig. 4.38 reveals that a significant number of reaction products exit the Sweeper with negative angle and positive position. Such an emittance is the result of the fragments entering the Sweeper with large positive angle, as demonstrated in Fig. 4.39. These large-angle reaction products are off the standard acceptances of the Sweeper, and they are only observed because they take a non-standard path through the magnet. Such paths are not well described by the magnetic field maps of the Sweeper. As such, the target parameters of reaction products falling in this region cannot be faithfully reconstructed. Hence in the final analysis only those fragments which fall within the positively correlated region of θ_x versus x, defined by the sweep run, are included. The cut is indicated by the rectangular

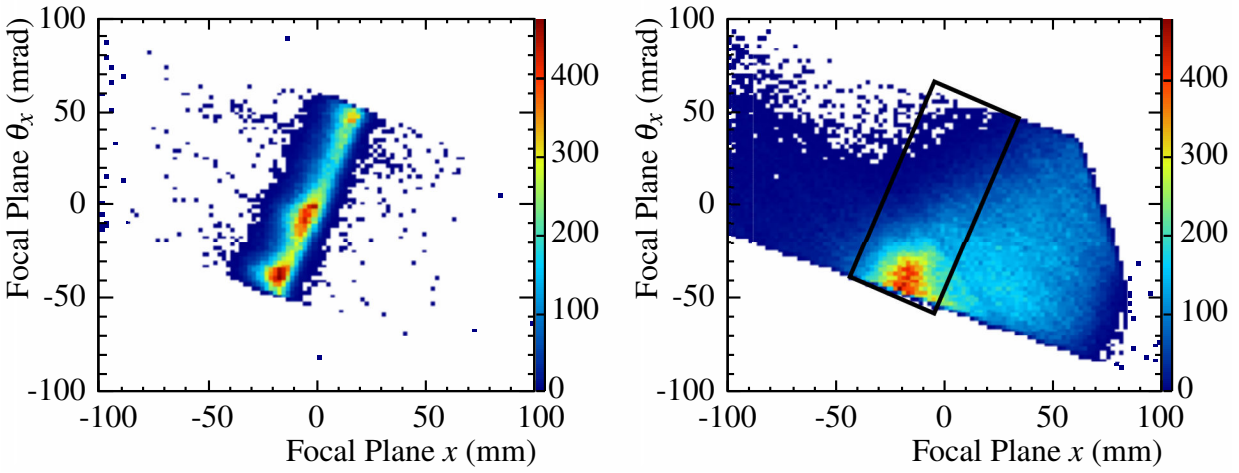

Figure 4.38: Left panel: Focal plane dispersive angle vs. position for unreacted beam particles swept across the focal plane. These events display positive correlation between angle and position, and they define the region of the emittance for which the magnetic field maps of the Sweeper are valid. Right panel: Focal plane dispersive angle vs. position for reaction products produced from the ^{32}Mg beam. A significant portion of these reaction products fall in the region of positive position and negative angle, due to taking a non-standard track through the Sweeper. The rectangular contour drawn on the plot is defined by the "sweep band" of the left panel, and only events falling within this region are used in the final analysis.

contour in the right panel of Fig. 4.38.

The second mapping cut involves position in the non-dispersive plane. As revealed by the left panel of Fig. 4.40, a number of events are reconstructed with a kinetic energy that deviates significantly from the mean. Furthermore, these events do not possess the expected inverse correlation between E_{frag} and $\text{ToF}_{\text{Target}\rightarrow\text{Thin}}$, indicating that the accuracy of the inverse reconstruction may be questionable. Plotting E_{frag} versus y position on CRDC1, as shown in the right panel of Fig. 4.40, reveals that the events with extreme E_{frag} values also hit CRDC1 far from the center. Additionally, the two parameters demonstrate a parabola-like correlation, enhanced at large y position, which is not expected. Most likely, the correlations seen in the figure are not real and are instead a result of deficiencies in the Sweeper field map. COSY only considers field values in the central plane when constructing maps, so it is plausible that the full correlations between energy and non-dispersive parameters are not reproduced. There seems to be no way to improve the situation, at least not while using COSY's central plane method of field map construction. As

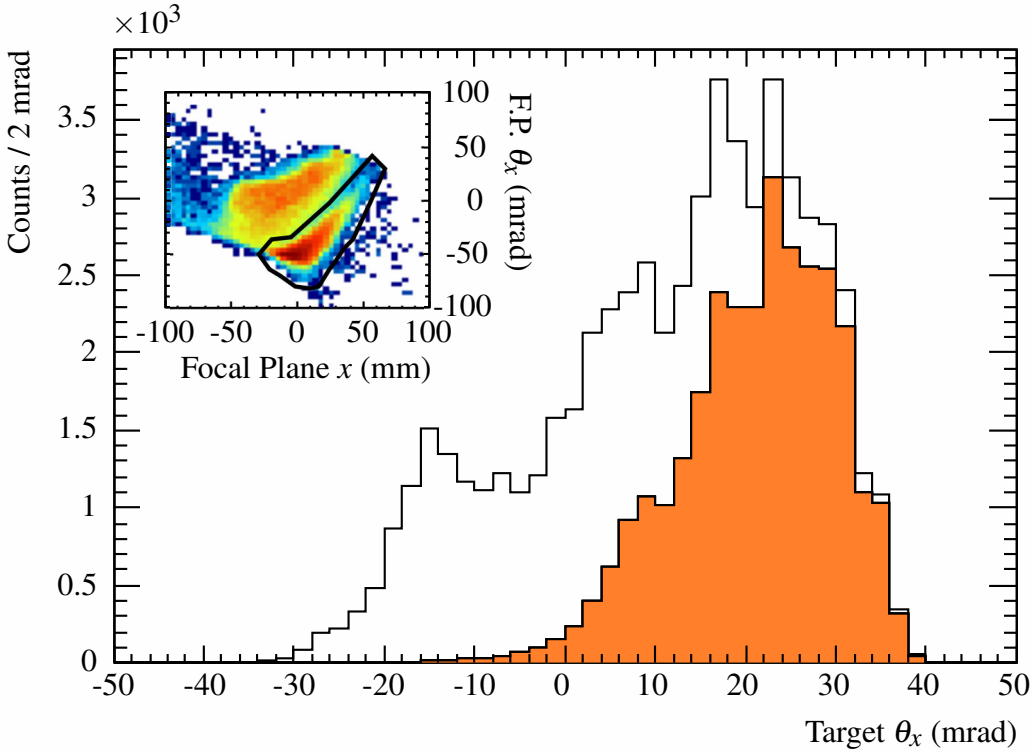

Figure 4.39: Inset: focal plane angle vs. position for unreacted beam particles swept across the focal plane. Unlike the left panel of Fig. 4.38, here the A1900 optics were tuned to give a beam that is highly dispersed in angle. causing the emittance region of negative angle and positive position to be probed. The main panel is a plot of incoming beam angle for all events (unfilled histogram) and events with $+x^{(\mathrm{fp})}$ and $-\theta_x^{(\mathrm{fp})}$ (orange filled histogram). The plot reveals that the $+x^{(\mathrm{fp})}, -\theta_x^{(\mathrm{fp})}$ events have a large positive angle as they enter the Sweeper.

the total number of events impacted is fairly small, those events with absolute value of CRDC1 y greater than 20 mm are excluded from the analysis. The range of ± 20 mm is chosen because it corresponds to the approximate points where E_{frag} begins to correlate significantly with CRDC1 y, as seen in the right panel of Fig. 4.40.

4.3.2 CAESAR

Gamma energies are taken simply from the energy deposited in a crystal, using the calibration procedure of Section 4.1.3. Often a single gamma will interact in multiple crystals due to Compton scattering [78], depositing only a portion of its energy in each. In this case, the gamma energies

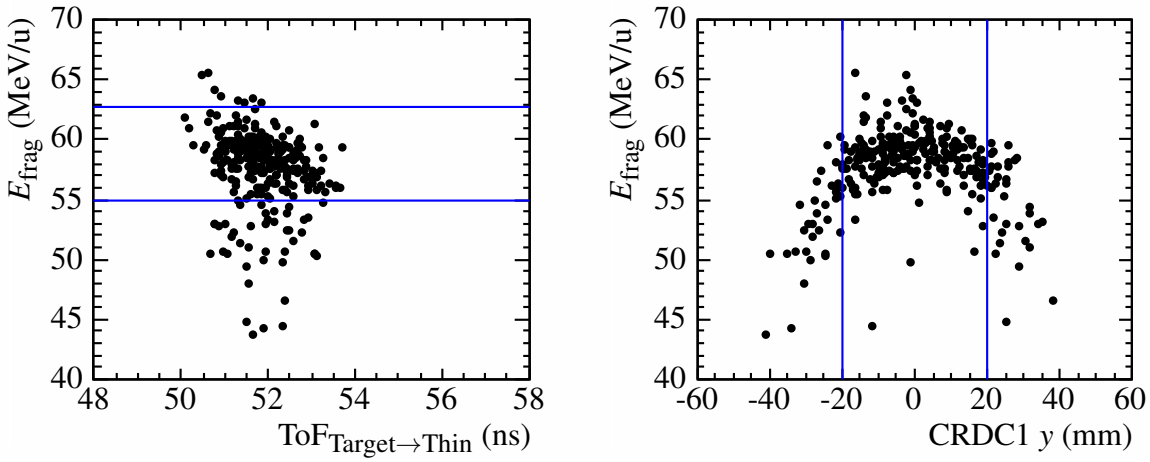

Figure 4.40: Left panel: fragment kinetic energy, calculated from the partial inverse map, vs. time of flight through the Sweeper. The events in the figure are $^{26}\mathrm{F}+n$ coincidences produced from the ^{29}Ne beam. Events with extreme values of E_{frag} also fall outside of the expected region of inverse correlation between E_{frag} and ToF. Right panel: E_{frag} vs. CRDC1 y position. This plot reveals an unexpected correlation between E_{frag} and CRDC1 y, with the extreme E_{frag} events also having a large absolute value of CRDC1 y. This is likely due to limitations of the Sweeper field map, so the events with $\mid y \mid > 20$ mm are excluded from the analysis.

of up to three crystals are summed to calculate the total energy deposition for the event. The summing procedure is only performed when the multiple hits are in neighboring crystals, as hits in non-neighboring detectors are likely to be the result of random coincidences, not multi-scattering.

Gammas resulting from the de-excitation of a beam nucleus are emitted from a source moving at roughly one third the speed of light. As such, their energy measured in the lab frame is significantly Doppler shifted [79]. Thus the gamma energies recorded in CAESAR are Doppler corrected:

$$E_{\mathrm{dop}} = E_{\mathrm{lab}} \frac{1-\beta\cos\theta}{\sqrt{1-\beta^2}}, \tag{4.38}$$

where E_{dop} and E_{lab} are the Doppler corrected and lab frame energies, respectively; β is the relativistic beta-factor, v_{beam}/c; and θ is the angle between the point where the $\gamma-$ray is emitted and the point where it is detected. To calculate θ, the detection point is assumed to be the center of the crystal in which the $\gamma-$ray interacts. In the case of multi-scattering, the center of the first interaction crystal is used. The emission point is assumed to be the center of the reaction target,

and the z position of the target is 7 cm upstream of the center of the array. The z position is verified through comparison with known transitions, as explained in Section 4.4.2.

4.4 Consistency Checks

The present experiment is complicated, both in terms of the physical setup and data analysis. Comparison of present results with those previously published can help to ensure that the present measurement and analysis is performed accurately. In particular, comparison of present results with previous ones is performed for two cases: decay energy reconstruction of $^{23}\mathrm{O}^{*} \rightarrow {}^{22}\mathrm{O} + n$ and gamma transitions in ^{32}Mg and ^{31}Na.

4.4.1 ^{23}O Decay Energy

The unbound first excited state in ^{23}O has been measured to have a decay energy of 45 keV [80–83], feeding the ground state of ^{22}O. In addition to being confirmed multiple times, the transition from $^{23}\mathrm{O}^{*} \rightarrow {}^{22}\mathrm{O} + n$ is narrow, making it a good candidate for a consistency check. The same transition is observed in the present experiment, with relatively high statistics, from fragmentation reactions on the ^{32}Mg beam. These events are analyzed in the same way as the data of interest, with the results presented in Fig. 4.41. The results are consistent with the previous measurements, lending credibility to the analysis.

4.4.2 Singles Gamma-Ray Measurements

To test the Sweeper-MoNA-CAESAR setup, data were taken using a MoNA singles trigger, where a hit in MoNA is not necessary for the event to be recorded. This greatly enhances the collection of de-excitation $\gamma-$rays since a triple coincidence event is no longer required. To reduce experimental dead time, a tungsten beam blocker was inserted in front of CRDC1 to reject the majority of unreacted beam particles.

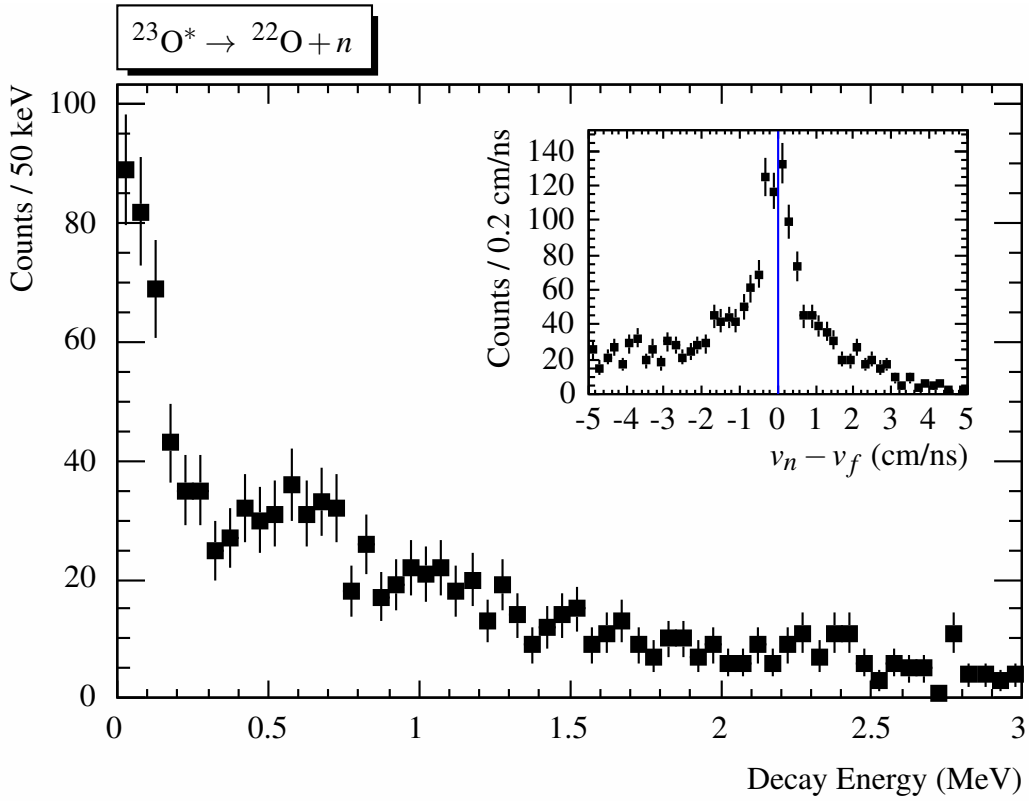

Figure 4.41: Decay energy for $^{23}O^* \rightarrow {}^{22}O + n$ events produced from the ^{32}Mg beam. The spectrum displays a narrow resonance at low decay energy, consistent with previous measurements that place the transition at 45 keV. The inset is a relative velocity $(v_n - v_f)$ histogram for the same events. The narrow peak around $v_{rel} = 0$ is also consistent with the 45 keV decay.

In the singles runs, two previously measured gamma transitions were collected with good statistics. The first is the result of inelastic excitation of the ^{32}Mg beam, populating the first 2^+ excited state at 885 keV [16]. As shown in the left panel of Fig. 4.42, this transition is prominent on top of random background. This well known transition was used to verify the z position of the reaction target, as misplacement of the target in the Doppler correction algorithm will cause the peak to shift and broaden. The peak is narrowest and located at 885 keV when the target location is set at 7 cm upstream of the center of CAESAR.

The other transition prominently observed in the singles data is in ^{31}Na. An excited level at around 370 keV has been observed in three previous measurements [84–86], with the most recent placing the transition at $376(4)$ keV [84]. The same transition is observed in the present

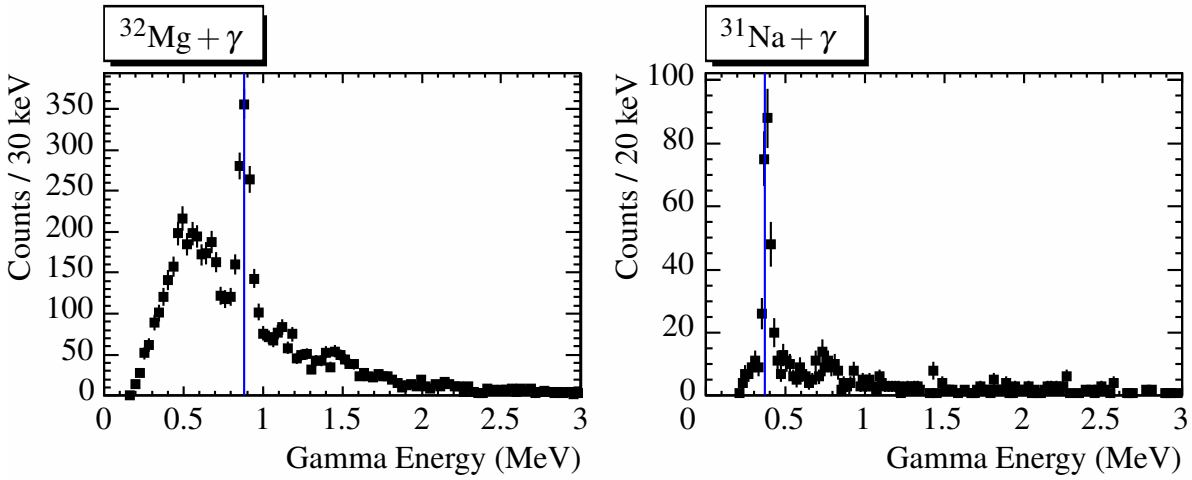

Figure 4.42: Left panel: Doppler corrected gamma energies from inelastic excitation of ^{32}Mg. The blue vertical line indicates the evaluated peak location of 885 keV [16]. Right panel: Doppler corrected gamma energies for ^{31}Na, produced from $1p$ knockout on ^{32}Mg. The most recent published measurement of 376 (4) keV [84] is indicated by the blue vertical line.

experiment, as shown in the right panel of Fig. 4.42.

4.5 Modeling and Simulation

4.5.1 Resonant Decay Modeling

The breakup of an unbound resonant state is a two body process involving a neutron and the residual nucleus. As such, it can be described as a neutron scattering off a nucleus, the neutron impinging with variable energy and angle. The cross section as a function of energy, $\sigma(E)$, of such a scattering process is well described by R-matrix theory [87], with the cross section for resonances given by a Breit-Wigner distribution [88]. The particular form of the Breit-Wigner used in this work has an energy-dependent width:

$$\sigma(E;E_0,\Gamma_0,\ell) = A\frac{\Gamma_\ell(E;\Gamma_0)}{[E_0+\Delta_\ell(E;\Gamma_0)-E]^2+\frac{1}{4}[\Gamma_\ell(E;\Gamma_0)]^2}, \tag{4.39}$$

where A is an amplitude; E_0 is the central resonance energy; Γ_0 parameterizes the resonance width; ℓ is the orbital angular momentum of the resonance; and Γ_ℓ and Δ_ℓ are functions to be

explained. E_0, Γ_0 and ℓ are parameters to be determined from the data (or from theoretical considerations). As mentioned, Eq. (4.39) is derived from R-matrix theory. A summary of the derivation is given here, with the full details available in Ref. [87].

The radial Schrödinger equation for a neutron scattering off a nucleus is:

$$\left[\frac{d}{dr^2} - \frac{\ell(\ell-1)}{r^2} - \frac{2M}{\hbar^2}(V-E)\right] u_\ell(r) = 0. \tag{4.40}$$

R-matrix theory is developed from the solution of Eq. (4.40) at the minimum approach distance before the nuclear interaction becomes important:

$$a = r_0\left(A_n^{1/3} + A_f^{1/3}\right), \tag{4.41}$$

where r_0 parameterizes the nuclear radius (here we use 1.4 fm); and A_n and A_f are the mass number of the neutron and fragment, respectively. Since the nuclear force is effectively absent and the neutron is unaffected by the Coulomb interaction, the potential term, V, in Eq. (4.40) is zero. The solution is then a superposition of incoming and outgoing waves:

$$\begin{aligned} u_\ell^{(\text{in})} &= (G_\ell - iF_\ell) \\ u_\ell^{(\text{out})} &= (G_\ell + iF_\ell), \end{aligned} \tag{4.42}$$

where F_ℓ and G_ℓ are related to $J-$type Bessel functions:

$$\begin{aligned} F_\ell &= (\pi\rho/2)^{1/2} J_{\ell+1/2}(\rho) \\ G_\ell &= (-1)^\ell (\pi\rho/2)^{1/2} J_{-(\ell+1/2)}(\rho). \end{aligned} \tag{4.43}$$

In Eq. (4.43), $\rho = a\sqrt{2ME}/\hbar$, with M the reduced mass of the neutron-fragment system; E the relative energy; and a the boundary distance of Eq. (4.41).

The R-matrix relates the incoming wave function, $u_\ell^{(\text{in})}$, to its derivative at the boundary. For a single resonance, it is given by

$$R = \frac{\hbar^2}{2Ma}\frac{|u_\ell(a)|^2}{E_0 - E} = \frac{\gamma_0^2}{E_0 - E}, \tag{4.44}$$

where E_0 is the resonance energy, and γ_0 is a reduced width representing the wave function at the boundary a :

$$\gamma_0 = \frac{\hbar}{\sqrt{2Ma}} u_\ell(a). \tag{4.45}$$

An outgoing collision matrix, U_ℓ, is related to the R-matrix and the logarithmic derivative of the external wave function, L_ℓ (and its complex conjugate, L_ℓ^*), by a phase factor:

$$U_\ell = \frac{u_\ell^{(\text{in})}}{u_\ell^{(\text{out})}} \frac{1 - L_\ell^* R}{1 - L_\ell R} = e^{2i\delta_\ell}, \tag{4.46}$$

with the logarithmic derivative given by

$$L_\ell = \left. \frac{\rho u_\ell'^{(\text{out})}}{u_\ell^{(\text{out})}} \right|_{r=a} = S_\ell + iP_\ell. \tag{4.47}$$

In Eq. (4.47), S_ℓ and P_ℓ are called the shift and penetrability functions, respectively, and are related to the F_ℓ and G_ℓ of Eq. (4.43) via

$$\begin{aligned} S &= \left[\rho \left(F_\ell F_\ell' + G_\ell G_\ell' \right) / \left(F_\ell^2 + G_\ell^2 \right) \right]_{r=a} \\ P &= \left[\rho / \left(F_\ell^2 + G_\ell^2 \right) \right]_{r=a}. \end{aligned} \tag{4.48}$$

The phase shift, δ_ℓ, is given by:

$$\delta_\ell(E) = \tan^{-1} \left(\frac{\frac{1}{2}\Gamma_\ell(E)}{E_0 + \Delta_\ell(E) - E} \right) - \phi_\ell, \tag{4.49}$$

where ϕ_ℓ is the hard sphere scatter phase shift. Γ_ℓ and Δ_ℓ are the functions presented in Eq. (4.39) and are given by

$$\begin{aligned} \Gamma_\ell(E) &= 2P_\ell(E)\gamma_0^2 \\ \Delta_\ell(E) &= -\left[S_\ell(E) - S_\ell(E_0) \right] \gamma_0^2. \end{aligned} \tag{4.50}$$

The outgoing collision matrix can then be expressed as:

$$U_\ell = \frac{i\Gamma_\ell^{1/2}(E)}{E_0 + \Delta_\ell(E) - E - \frac{i}{2}\Gamma_\ell(E)}. \tag{4.51}$$

This is related to the scattering cross section by

$$\sigma_\ell = \int \sigma(\theta)\, \mathrm{d}x = \frac{\pi}{k^2} \sum_\ell (2\ell + 1) |1 - U_\ell|^2. \tag{4.52}$$

Combining Eq. (4.51) and Eq. (4.52) results in an expression for the cross section, up to a normalization constant:

$$\sigma = A\frac{\Gamma_\ell(E)}{[E_0+\Delta_\ell(E)-E]^2+\frac{1}{4}[\Gamma_\ell(E)]^2}, \tag{4.53}$$

which is the same as Eq. (4.39).

Finally, it should be noted that the reduced width γ_0 is related to the width parameter Γ_0 of Eq. (4.39) by

$$\Gamma_0 = 2\gamma_0^2 P_\ell(E_0). \tag{4.54}$$

4.5.2 Non-Resonant Decay Modeling

In addition to resonances, there may be non-resonant contributions to the data. The non-resonant contribution comes from the decay of highly excited states in ^{28}F, which lie in a region where the level density is large. These states de-excite by neutron emission, and in some cases the emitted neutron is observed in coincidence with the final fragment.

In the case of $^{28}\mathrm{F} \rightarrow {}^{27}\mathrm{F}+n$, the non-resonant contribution is expected to be negligible. The reason is that states in ^{28}F are populated by direct proton knockout from ^{29}Ne. As such, only neutrons which result from the decay of a state in ^{28}F to a bound state in ^{27}F are present in the data. A non-resonant contribution could arise from the decay of continuum states in ^{28}F directly to bound ^{27}F, but the probability of observing such decays is extremely low. The reason is that the decay energy of such a transition would be large (on the order of 5 MeV or greater). As will be explained in Section 4.5.3, the probability to observe a transition with such large decay energy is low, due to geometric acceptances.

It is also plausible that a background contribution to $^{28}\mathrm{F} \rightarrow {}^{27}\mathrm{F}+n$ could arise from neutrons that are removed from the beryllium target nuclei in the knockout reaction. However, observation of such a neutron requires that it exit the target with close to beam velocity and with a transverse momentum direction close to zero degrees. This requires that the proton knocked out of the beam transfer nearly all of its momentum to a single neutron in beryllium in a head-on collision. Such a

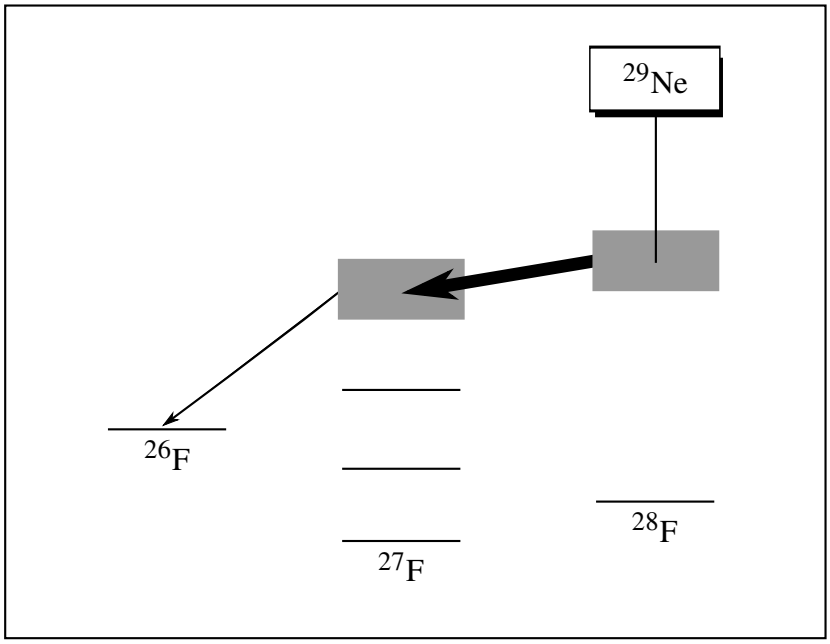

Figure 4.43: Schematic of the process by which non-resonant background is observed in coincidence with ^{26}F. First a highly excited state in ^{28}F is populated from ^{29}Ne. This state then decays to a high excited state in ^{27}F, evaporating a neutron (thick arrow). The excited state in ^{27}F then decays to the ground state of ^{26}F by emitting a high-energy neutron (thin arrow), which is not likely to be observed. The evaporated neutron (thick arrow) has fairly low decay energy and is observed in coincidence with ^{26}F, giving rise to the background.

process is expected to have a small enough cross section that the contribution of target neutrons to the ^{28}F decay spectrum can be neglected in the present work.

In the case of $^{27}\mathrm{F}^* \rightarrow {}^{26}\mathrm{F} + n$, however, a non-resonant contribution is expected. The process through which this background arises is illustrated in Fig. 4.43. A high excited state in ^{28}F is first populated from ^{29}Ne. This state then decays to another highly excited state in ^{27}F, evaporating a neutron. From here, the excited state in ^{27}F can decay to the ground state in ^{26}F by neutron emission, with the ^{26}F observed in the Sweeper. The neutron from the final step is not likely to be observed as the decay energy going from a high excited state in ^{27}F to the ground state of ^{26}F is large; however, the evaporated neutron from the decay of highly excited ^{28}F to highly excited ^{27}F will have relatively low decay energy, allowing it to be observed in coincidence with the ^{26}F.

The decay energy of non-resonant evaporated neutrons can be modeled as a Maxwellian distribution [89, 90]. The arguments for using such a model, as presented in Ref. [89], are summarized

here.

The kinetic energy of the evaporated neutron, relative to the beam, is given by:[9]

$$\varepsilon_n = E_f^* - E_{f\prime}^*, \tag{4.55}$$

where E_f^* is the excitation energy of the original nucleus (in our case ^{28}F), and $E_{f\prime}^*$ is the excitation energy of the daughter (^{27}F). For $\ell \neq 0$, the probability of emitting a neutron with ε_n increases as ε_n becomes larger, due to better penetration of the angular momentum barrier. The distribution of the number of neutrons having energy between ε and $\varepsilon + \mathrm{d}\varepsilon$ is given by

$$G_n(\varepsilon)\,\mathrm{d}\varepsilon = \sum_{\varepsilon < \varepsilon_\beta < \varepsilon + \mathrm{d}\varepsilon} G_C(\beta), \tag{4.56}$$

with $G_C(\beta)$ the probability of decay through a specific channel β:

$$G_C(\beta) = \frac{k_\beta^2 \sigma_C(\beta)}{\sum_\alpha k_\alpha^2 \sigma_C(\alpha)}. \tag{4.57}$$

In Eq. (4.57), the σ_C are the cross sections for decay through a specific channel, and $k = \lambda^{-1}$ is a wave number. The sum in the denominator is over all of the possible decay channels, α. To determine the *relative* intensity distribution of emitted neutron energies, the denominator of Eq. (4.57) is ignored:

$$I_n(\varepsilon)\,\mathrm{d}\varepsilon = c\varepsilon\sigma_C(\varepsilon)\, w_f\left(\varepsilon_f - \varepsilon\right)\mathrm{d}\varepsilon. \tag{4.58}$$

Here the wave number k^2 has been replaced by the factor ε. The function $w_f\left(\varepsilon_f - \varepsilon\right)$ is related to the level density $w(E)$, and its logarithm,

$$S(E) = \ln[w(E)], \tag{4.59}$$

is analogous to the entropy of a thermodynamic system. Expanding S around the maximum decay energy, ε_f, gives

$$S\left(\varepsilon_f - \varepsilon\right) = S\left(\varepsilon_f\right) - \varepsilon\left(\frac{\mathrm{d}S}{\mathrm{d}E}\right)_{E=\varepsilon_f} + \ldots. \tag{4.60}$$

[9] Neglecting the small recoil energy of the fragment.

Using Eq. (4.60) to approximate $w_f\left(\varepsilon_f-\varepsilon\right)$ and absorbing the factor coming from $S\left(\varepsilon_f\right)$ into the constant, one obtains:

$$I_n(\varepsilon)=c\varepsilon\sigma_C(\varepsilon)\exp\left[-\frac{\varepsilon}{\Theta\left(\varepsilon_f\right)}\right]\mathrm{d}\varepsilon. \tag{4.61}$$

The function $\sigma_C(\varepsilon)$ varies extremely slowly and can be absorbed into the leading constant, c. The function Θ is given by

$$\frac{1}{\Theta}=\frac{\mathrm{d}S}{\mathrm{d}E}, \tag{4.62}$$

the expression for the temperature of a thermodynamic system. Thus Θ can be interpreted as the temperature of a thermal neutron source whose relative distribution is dominated by $e^{-\varepsilon/\Theta}$.

The functional form used to model background events differs slightly from that of Eq. (4.61):

$$f(\varepsilon;\Theta)=A\sqrt{\varepsilon/\Theta^3}e^{-\varepsilon/\Theta}, \tag{4.63}$$

with the temperature Θ to be determined from the data. However, the important features, namely the dominant $e^{-\varepsilon/\Theta}$ term, are the same. Minor differences in shape as a result of the leading terms become irrelevant when the effects of experimental resolution are taken into account.

4.5.3 Monte Carlo Simulation

If the decay energy distribution of an unbound state is given by the function $f(E;\vec{\mu})$, where $\vec{\mu}$ are parameters to be determined from the data (E_0, Γ_0, and ℓ), the observed distribution will be smeared by experimental resolution and acceptance:

$$F\left(\tilde{E};\vec{\mu}\right)=\int R\left(E,\tilde{E}\right)f(E;\vec{\mu})\,\mathrm{d}E. \tag{4.64}$$

Here $R\left(E,\tilde{E}\right)$ is the smearing function, and $F\left(\tilde{E};\vec{\mu}\right)$ is what is observed by the experiment. Thus to compare a model to data, the influence of resolution and acceptance must be taken into account.

In the present work, the integral on the right hand side of Eq. (4.64) is not known analytically; hence the influence of resolution and acceptance is introduced using Monte Carlo simulation. First

the breakup of an unbound state is modeled using some function $f(E;\vec{\mu})$. The neutron and fragment are then propagated through their respective experimental systems, and the measurements made in various particle detectors are given appropriate resolutions, as described below. Any event for which a particle falls outside of geometric acceptance limits is tagged appropriately. The result is a simulated data set which is then analyzed in the exact same way as the real experimental data, ignoring events which fail acceptance cuts. The decay energy of the simulated and analyzed data set represents $F\left(\tilde{E};\vec{\mu}\right)$ in Eq. (4.64) and is compared directly to experiment.

The simulation begins with the ^{29}Ne beam impinging on TCRDC1. The properties of the incoming beam (emittance and energy) are free parameters, and they are constrained from comparison with data in which unreacted beam is sent down the focal plane (c.f. Section 4.5.3.1). The x position on TCRDC1 is recorded with a Gaussian spread, $\sigma = 1.3$ mm, to simulate experimental resolution. The σ value is taken from mask runs, comparing the width of recorded events to the actual size of the mask holes.

From TCRDC1, the beam is forward tracked to the reaction target. The proton knockout reaction is treated in the Goldhaber model [91] with the inclusion of a friction term [92] to degrade the beam energy by 0.6%. Inclusion of the friction term is necessary for simulated fragment energies to match those of the data. Following the knockout reaction, the breakup of the unbound state is modeled using one of the functions presented in Sections 4.5.1 and 4.5.2.

After the breakup reaction, the neutron and fragment are treated separately. The neutron is propagated to the front face of MoNA where its measurement is simulated. Time of flight resolution is introduced as a Gaussian spread with $\sigma = 0.3$ ns. Position in the y direction is discretized in the same way as the real measurement: the position is set to be at the center of the bar in which the neutron interacts. In the z direction, only the front wall of MoNA is included in the simulation. The z position discretization is introduced by giving the z position in the simulation a uniform 10 cm spread and analyzing as if the neutron hit at the center of the bar. The x position resolution is given by the convolution of two Laplacians:

$$p_1 \cdot \frac{e^{-|x/\sigma_1|}}{2\sigma_1} + (1-p_1) \cdot \frac{e^{-|x/\sigma_2|}}{2\sigma_2}, \tag{4.65}$$

with $\sigma_1 = 16.2$ cm, $\sigma_2 = 2.33$ cm, and $p_1 = 53.4\%$. Timing and x position resolutions are based on GEANT3 simulations and shadow bar measurements [59].

In addition to resolutions, acceptance cuts concerning the neutron are imposed. There are two points in the beam line where neutron events are lost. The first is the point where the beam pipe intersects the Sweeper magnet gap, 1.06 m downstream of the reaction target. Neutrons passing this point with a radius greater than the internal radius of the pipe, 7.3 cm, are flagged as failing the acceptance cut. The second cut is only in the y direction, coming at the point where neutrons exit the Sweeper vacuum chamber, 1.133 m downstream of the target. Here any neutrons with y position greater than ± 7.3 cm, the gap size, are flagged as being outside the acceptances. The active area of MoNA is included as an acceptance cut in the simulation, but it has no effect as MoNA is entirely shadowed by the beam pipe and vacuum chamber aperture.

Following the breakup, the charged fragment is propagated to CRDC1 using a COSY forward transformation matrix as in Eq. (4.36). From here, the fragment is ray-traced to CRDC2 and the thin scintillator; at each location an acceptance cut is imposed, requiring that the events fall within the active region of the detector (± 150 mm for CRDC2 and ± 200 mm for the thin scintillator). The positions and angles recorded at CRDC1 are given a Gaussian spread to simulate experimental resolution, with $\sigma_{\text{position}} = 1.3$ mm and $\sigma_{\text{angle}} = 0.8$ mrad in both planes. As with TCRDC1, position and angle σ values are taken from CRDC mask runs.

As the x position on the target is used in calculation of decay energy, c.f. Eq. (4.37), an appropriately resolved $x^{(\text{target})}$ must also be simulated. This is accomplished by taking the resolved x position measurement on TCRDC1 and determining a nominal angle, $\vartheta_x^{(\text{tcrdc1})}$, using the method of Section 4.1.1.2. The resolved x position at the target is then calculated by propagating the resolved $x^{(\text{tcrdc1})}$ and $\vartheta_x^{(\text{tcrdc1})}$ through the triplet using a COSY transformation matrix.

Table 4.7: Incoming beam parameters. Each is modeled with a Gaussian, with the widths and centroids listed in the table. Additionally, x and θ_x are given a linear correlation of 0.0741 mrad/mm, and the beam energy is clipped at 1870 MeV.

Parameter	*Centroid*	*Width*
x	0.18 mm	11 mm
θ_x	0 mrad	4 mrad
y	0 mm	9 mm
θ_y	0 mrad	1.1 mrad
E	1800 MeV	50 MeV

4.5.3.1 Verification

As mentioned above, free parameters in the simulation are constrained by comparison with data. The free parameters related to the incoming beam are its emittance in both planes and its kinetic energy. Each of these is modeled as a Gaussian distribution, with the free parameters listed in Table 4.7. The incoming position and angle in the dispersive plane are also given a linear correlation, with a slope of 0.0741 mrad/mm. In the case of incoming energy, the Gaussian distribution is clipped on the high side, with a maximum of 1870 MeV.

The non-dispersive angle and position, as well as the dispersive position, are constrained by TCRDC measurements. Because of the TCRDC2 malfunction (explained in Section 4.1.1.2), the incoming dispersive angle cannot be constrained by the TCRDCs. Instead it is set from comparison with data where unreacted beam is centered in the focal plane. The incoming beam energy is also constrained in the same way. Furthermore, the beam energy was cross-checked against the ion-optics program LISE++ [93] and found to be in reasonable agreement. To verify that the incoming beam parameters are correct, simulated CRDC1 parameters—in the case of unreacted beam centered in the focal plane—are compared to data. These comparisons are shown in Fig. 4.44 and indicate reasonable agreement.

In addition to unreacted beam data, intermediate parameters in the simulation are also verified for the reactions of interest (^{26,27}F in the focal plane). This provides a check of the knockout reaction model used in the simulation and probes a wider region of phase space. In addition to parameters at CRDC1, target parameters, calculated using the inverse mapping procedure of Sec-

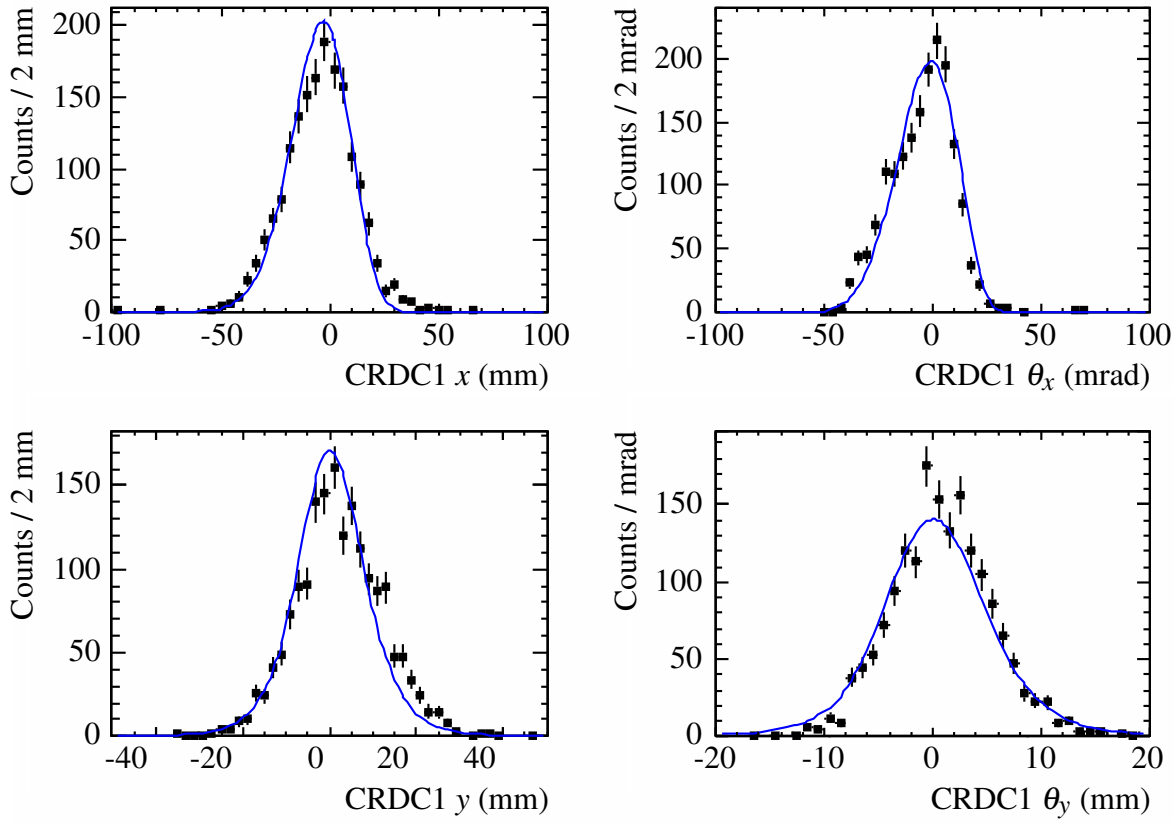

Figure 4.44: Comparison of simulation to data, with unreacted beam sent into the center of the focal plane. The black squares are data points and the solid blue lines are simulation results. It should be noted that the dispersive angle in the focal plane, shown in the upper-right panel, does not match unless the beam energy is clipped at 1870 MeV.

tion 4.3.1, are compared. As shown in Figs. 4.45 and 4.46, the agreement between simulation and data is reasonable. The deviations in non-dispersive angle and position are due to the deficiencies of the field map explained in Section 4.3.1.1.

4.5.4 Maximum Likelihood Fitting

Simulation results are compared to data using an unbinned maximum likelihood technique. Given a resolved decay energy model $F\left(\tilde{E};\vec{\mu}\right)$, the likelihood is constructed by taking the product of F evaluated at each data point:

$$\prod_i F\left(\varepsilon_i;\vec{\mu}\right), \tag{4.66}$$

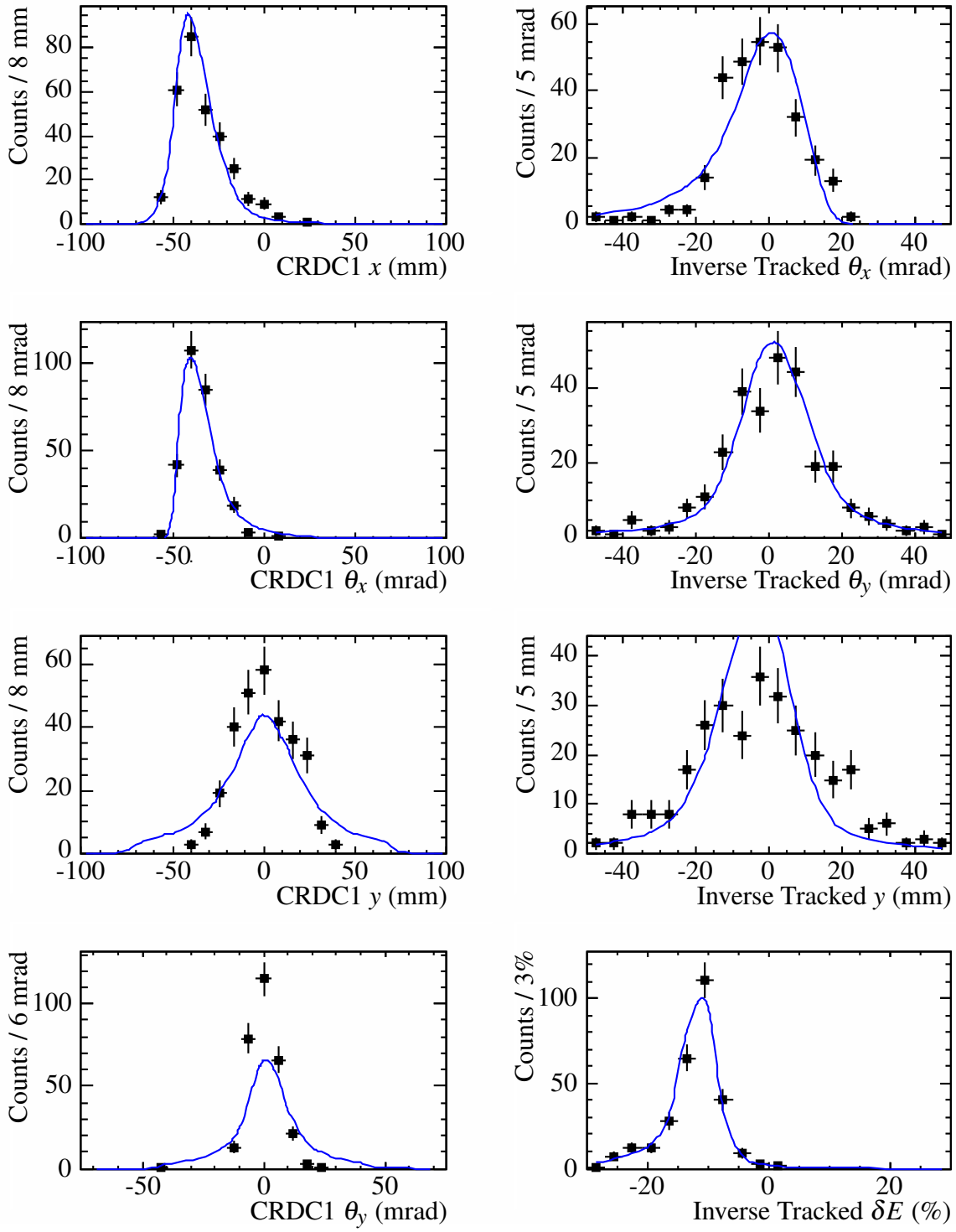

Figure 4.45: Comparison of simulation to data for for ^{26}F reaction products in the focal plane. In each panel, the parameter being compared is indicated by the x axis label. In the lower-right panel, δE refers the the deviation from the central energy of the Sweeper magnet.

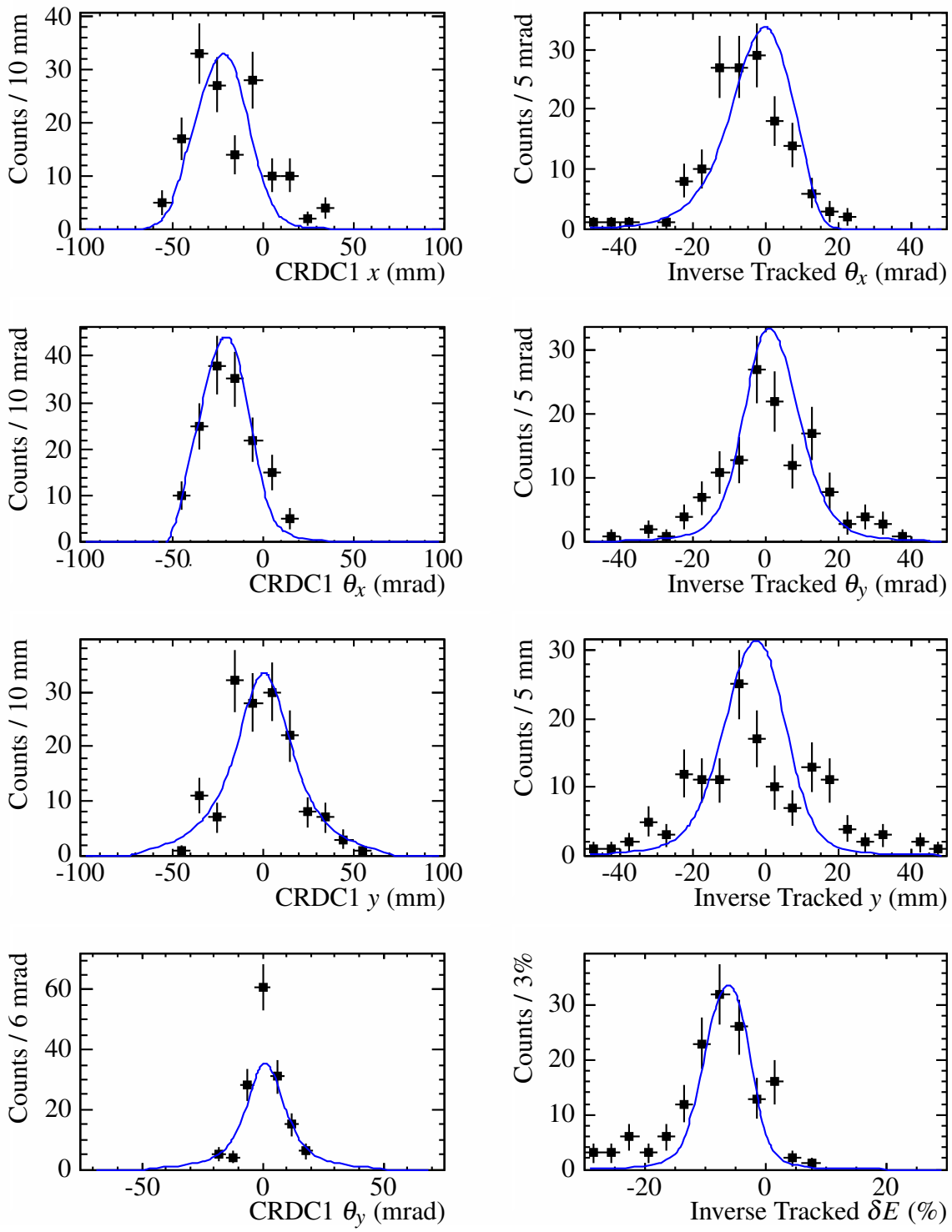

Figure 4.46: Same as Fig. 4.45 but for ^{27}F in the focal plane.

where each ε_i is the decay energy of a recorded event in the experimental data, and the product is over all recorded events. This is translated into a log-likelihood:

$$\ln(L) = \sum_i \ln\left(F\left(\varepsilon_i;\vec{\mu}\right)\right). \tag{4.67}$$

The log-likelihood is then used as a test statistic [94]: the best estimate of the parameters $\vec{\mu}$ is at the point where $\ln(L)$ is maximized, and $n\sigma$ confidence intervals are determined by finding the region of $\vec{\mu}$ where

$$\ln(L)_{\max} - \ln(L) \leq \frac{n^2}{2}. \tag{4.68}$$

In general, Eq. (4.67) requires a continuous form of $F\left(\tilde{E};\vec{\mu}\right)$, which is not the case when $F\left(\tilde{E};\vec{\mu}\right)$ is obtained from Monte Carlo simulation. An appropriate log-likelihood can be constructed, however, by following the prescription of Ref. [95]. The procedure is outlined as follows:

1. Create a simulated data set, for a given set of parameters $\vec{\mu}$, and save the generated decay energy values, E_j (from the unsmeared $f\left(E;\vec{\mu}\right)$), along with the resolution-smeared ones, $\tilde{E}_j$.

2. Form a small volume V_i centered around each experimental data point ε_i.

3. For each ε_i, calculate the total number of events whose *smeared* decay energy, $\tilde{E}_j$, falls within the volume V_i.

4. Divide the sum in (3) by the size of V_i and, for normalization, the total number of generated events.

5. Take the natural log of the quotient in (4) and sum over all of the experimental data points ε_i.

In addition, the sums in Steps 3 and 4 can be over weighted events, with the weights being a function of the *generated* decay energies. By appropriately weighting the points, one can calculate the likelihood using a different decay model, $f\left(E;\vec{\mu}'\right)$, without having to generate a new set of

simulated data. To do this, the appropriate weights are

$$W\left(E_j,\vec{\mu},\vec{\mu}'\right)=\frac{f\left(E,\vec{\mu}'\right)}{f\left(E,\vec{\mu}\right)}. \tag{4.69}$$

Care must be taken to ensure that the weight values are not too large, as statistical errors are determined by the sum of the square of the weights. In particular, generating functions, $f\left(E,\vec{\mu}\right)$, which are too narrow are not a good choice for re-weighting.

The procedure for calculating the log-likelihood from Monte Carlo data can be summarized in a single equation [95]:

$$\ln\left(L\right)=\sum_i \ln\left[\frac{\sum_{\tilde{E}_j\in V_i} W\left(E_j,\vec{\mu},\vec{\mu}'\right)}{V_i\sum_j W\left(E_j,\vec{\mu},\vec{\mu}'\right)}\right]. \tag{4.70}$$

The log-likelihood calculation procedure outlined above can introduce systematic error from two sources: nonlinearity in the smeared function, $F\left(E;\vec{\mu}'\right)$, over the volume size, V_i, and limited Monte Carlo statistics within each V_i. In the present work, the volume size was chosen to be 0.05 MeV. It was demonstrated that this choice of V_i introduces negligible systematic error by performing a likelihood fit to a known (simulated) data set and comparing the fit results to the actual parameter values. To avoid systematic errors of the second type, the total number of generated events is set to be large: approximately three million. This was shown to be sufficient by repeating the fitting procedure using a variety of generator seeds, with the results nearly identical.

Chapter 5

RESULTS

5.1 Resolution and Acceptance

Before presenting the decay energy curves for $^{27}\mathrm{F}^{*} \rightarrow {}^{26}\mathrm{F}+n$ and $^{28}\mathrm{F} \rightarrow {}^{27}\mathrm{F}+n$, a brief discussion of the resolution and acceptance functions of the experimental setup is warranted. Fig. 5.1 is a plot of the simulated acceptance curve for $^{26}\mathrm{F}+n$ coincidences as a function of decay energy (the same plot for $^{27}\mathrm{F}+n$ coincidences is virtually identical). As seen in the figure, the acceptance begins to drop off rather quickly after ~ 400 keV, which is primarily a result of neutrons being shadowed by the beam pipe and Sweeper vacuum chamber box. This shadowing is clearly observed in a plot of the neutron θ_x versus θ_y, shown in the inset of the figure.

As with the acceptance, the resolution of the experimental setup also varies significantly as a function of decay energy. This response function cannot be described analytically (hence the need to perform Monte Carlo simulations), but a general idea of its shape can be obtained by plotting the Gaussian σ of simulated decay energy curves as a function of input decay energy. Such a plot for $^{26}\mathrm{F}+n$ coincidences is shown in the top panel of Fig. 5.2, with the input for each point being a delta function at the indicated relative energy. To give an idea of the actual shape of the resolution function, the main panel of Fig. 5.2 shows the simulated decay energy curves for a variety (0.1 MeV, 0.2 MeV, 0.4 MeV, 0.8 MeV, and 1.5 MeV) of delta function inputs. As with the acceptance curves, the resolution for $^{27}\mathrm{F}+n$ coincidences is virtually identical to that of $^{26}\mathrm{F}+n$.

5.2 ^{27}F Decay Energy

The measured decay energy curve for $^{26}\mathrm{F}+n$ coincidences, resulting from the decay of unbound excited states in ^{27}F, is presented in Fig. 5.3. Comparison with the acceptance curve of Fig. 5.1

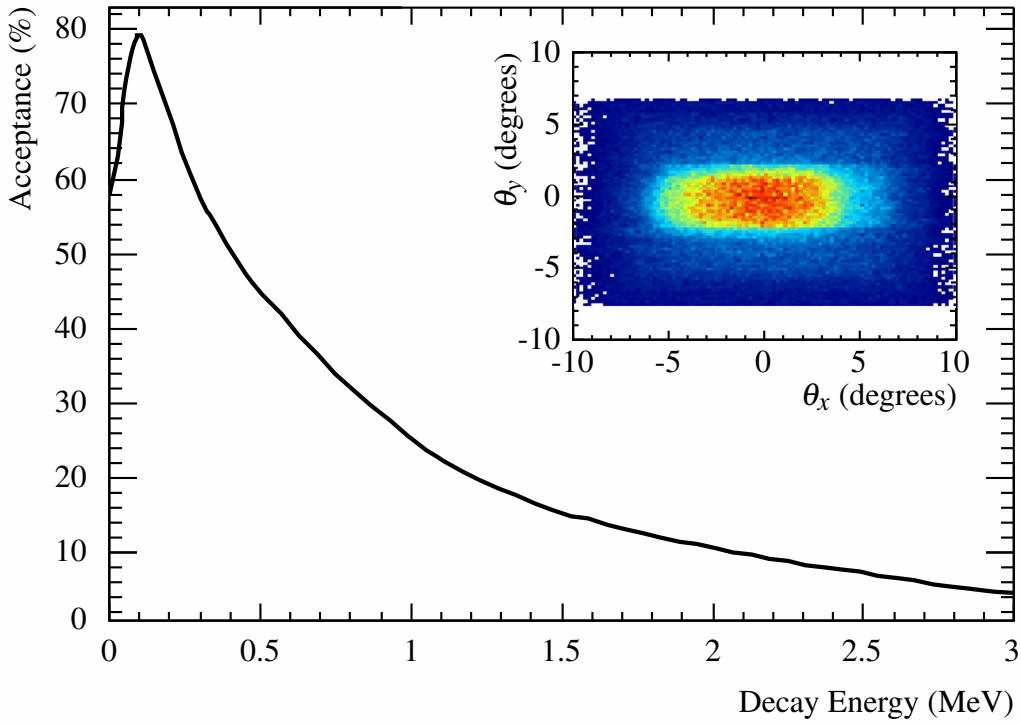

Figure 5.1: Simulated acceptance curve for $^{26}\mathrm{F}+n$ coincidences. The inset is a histogram of measured neutron angles for fragment-neutron coincidences produced from the ^{32}Mg beam, demonstrating the limited neutron acceptance that is a result of neutrons being shadowed by the beam pipe and the vacuum chamber aperture.

reveals a clear enhancement around 400 keV in decay energy. As discussed in Section 4.5, an appropriate model for the decay is that of a Breit-Wigner resonance on top of a non-resonant Maxwellian background. The data are fit by constructing an unbinned log-likelihood test statistic, c.f. Section 4.5.4. The parameters in the fit are the central energy of the Breit-Wigner resonance, E_0; the width of the resonance, Γ_0; the orbital angular momentum, ℓ; the temperature of the non-resonant Maxwellian distribution, Θ; and the relative contribution of the two lineshapes. The width of the measured curve is dominated by experimental resolution and acceptance cuts, and the parameters pertaining to the non-resonant background are not of interest in the present experiment. Hence the only parameter of interest is the central resonance energy, E_0, and all others are treated as nuisance parameters using the profile likelihood method [94]. In this method, $-\ln(L)$ is plotted

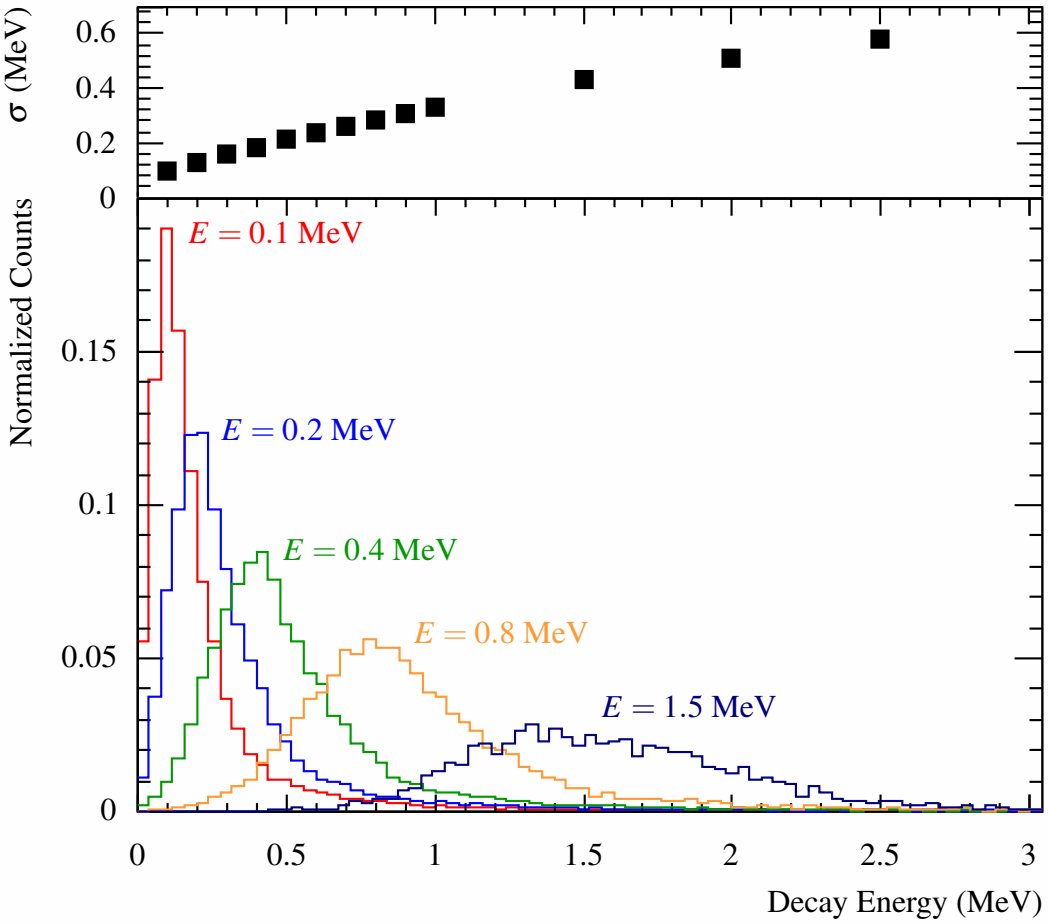

Figure 5.2: Demonstration of the experimental resolution as a function of decay energy for $^{26}\mathrm{F}+n$ coincidences. The bottom panel shows a variety of simulated decay energy curves; in each, the un-resolved decay energy is a delta function, with energies of 0.1 MeV (red), 0.2 MeV (blue), 0.4 MeV (green), 0.8 MeV (orange), and 1.5 MeV (navy). The top panel is a plot of the Gaussian σ of simulated decay energy curves as a function of input energy.

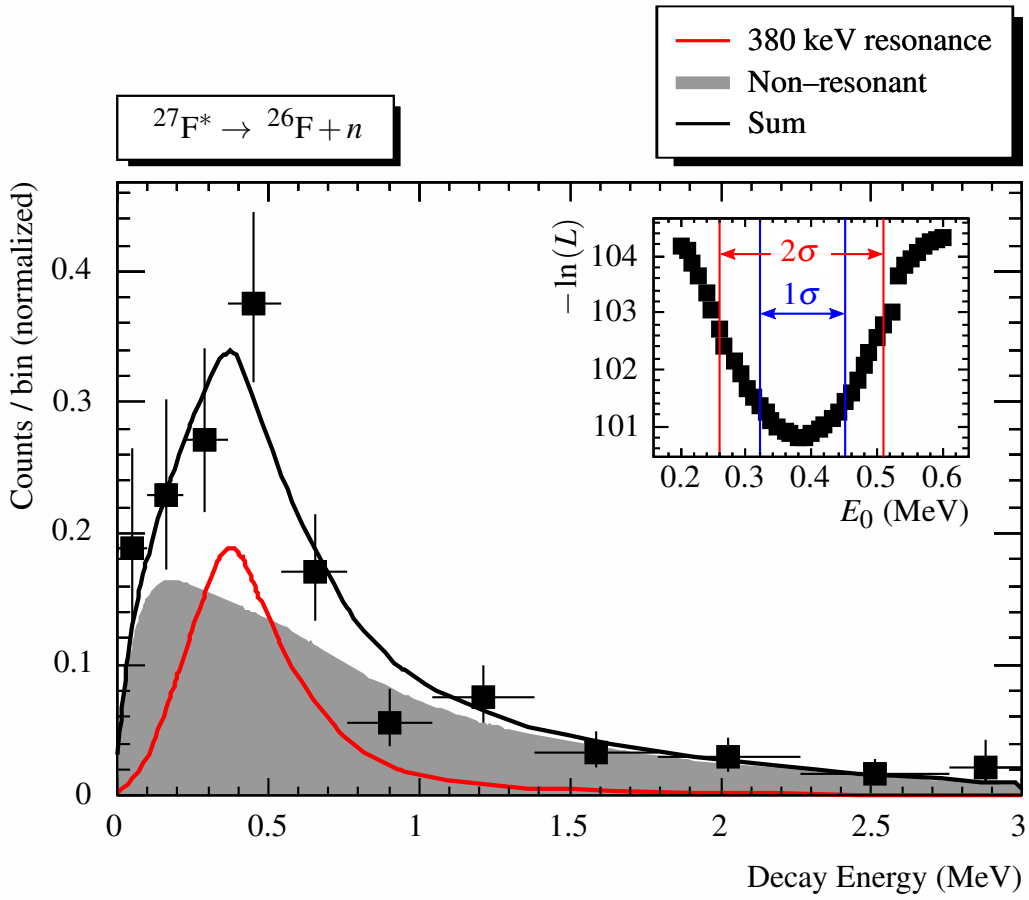

Figure 5.3: Decay energy histogram for $^{26}\mathrm{F}+n$ coincidences. The filled squares are the data points, and the curves display the best fit simulation results. The red curve is a simulated 380 keV Breit-Wigner resonance, while the filled grey curve is a simulated non-resonant Maxwellian distribution with $\Theta = 1.48$ MeV. The black curve is the sum of the two contributions (resonant:total $= 0.33$). The inset is a plot of the negative log of the profile likelihood versus the central resonance energy of the fit. Each point in the plot has been minimized with respect to all other free parameters. The minimum of $-\ln(L)$ vs. E_0 occurs at 380 keV, and the 1σ (68.3% confidence level) and 2σ (95.5% confidence level) limits are indicated on the plot.

as a function of the parameter of interest, with each point on the plot minimized with respect to the nuisance parameters. The orbital angular momentum of the resonance is fixed at $\ell = 2$ from theoretical expectations, assuming the emission of a $0d_{3/2}$ neutron. Although this assumption may be invalid if the state in question has significant p-f shell components, use of the other plausible ℓ values ($\ell = 1$ or $\ell = 3$) to model the decay does not significantly alter the best fit E_0 value.

The inset of Fig. 5.3 displays a plot of the negative log-likelihood of the data versus E_0, with each point on the curve minimized with respect to Γ_0, Θ, and the relative contributions of the resonant and non-resonant models. This constitutes the profile likelihood as mentioned in the previous paragraph. The minimum is located at $E_0 = 380$ keV, and the 1σ (68.3% confidence level) and 2σ (95.5% confidence level) intervals[1] are ± 60 keV and $^{+130}_{-120}$ keV, respectively. At $E_0 = 380$ keV, the nuisance parameters are minimized to $\Gamma_0 = 10$ keV; $\Theta = 1.48$ MeV; and a resonant:total ratio of 33%. The best fit results are plotted as the curves in the main panel of the figure, with the red curve representing the 380 keV resonance; the filled grey curve the non-resonant Maxwellian background; and the black curve their sum.

As mentioned in Section 3.1, the decay energy measurement provides no information to distinguish whether the decays are feeding the ground state or excited states of the daughter nucleus, ^{26}F. To make this determination, one must look at γ-rays recorded in coincidence with ^{26}F and a neutron. A histogram of the Doppler corrected energy of γ-rays recorded in coincidence with $^{26}\mathrm{F} + n$ is shown in Fig. 5.4. Only two triple coincidence events were recorded, which strongly indicates that the presently observed decays feed the ground state of ^{26}F. In the extreme opposite case of a decay which had a 100% branching to a bound excited state in ^{26}F, around 50 counts would be expected in CAESAR assuming 30% efficiency for gamma detection. It is plausible that a small branching fraction to bound excited states in ^{26}F could produce a gamma spectrum that is similar to the one presently observed; however, the presence of multiple decay branches would either manifest itself as multiple resonances in Fig. 5.3 or occur at such a low rate that the

[1] As mentioned in Section 4.5.4, the $n\sigma$ confidence interval is the region in which $\ln(L) - \ln(L)_{\min} \leq n^2/2$.

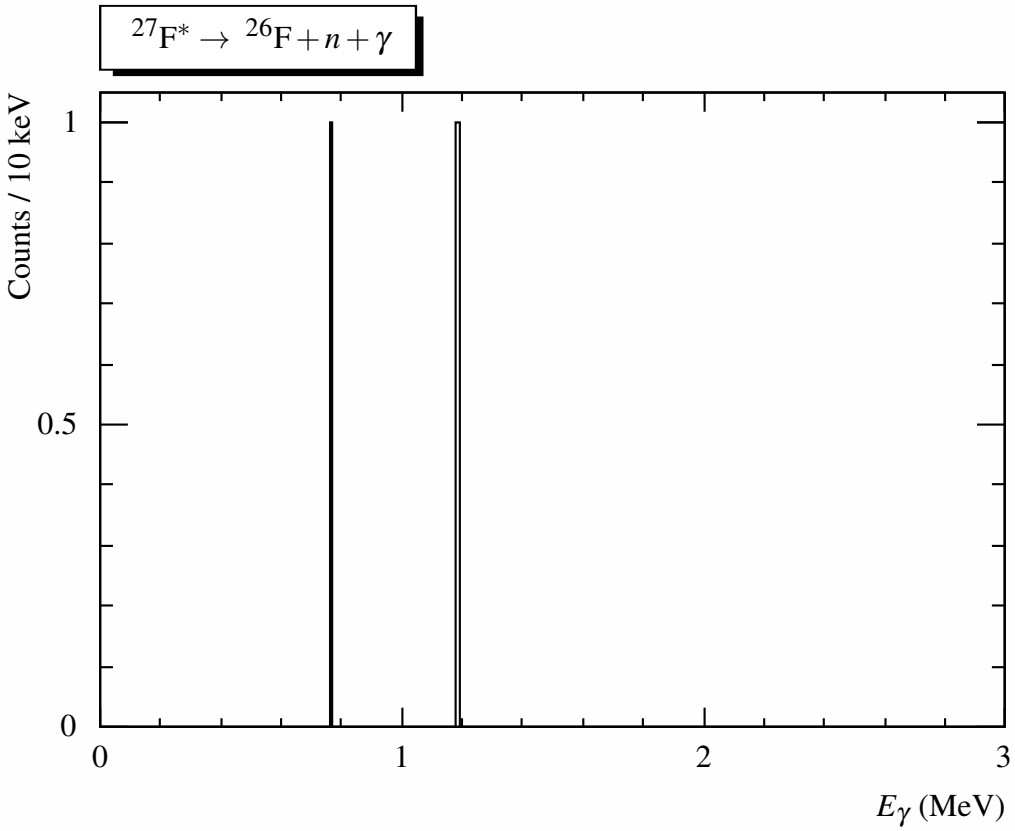

Figure 5.4: Histogram of the Doppler corrected energy of γ-rays recorded in coincidence with ^{26}F and a neutron. Only two CAESAR counts were recorded, giving strong indication that the present decays are populating the ground state of ^{26}F.

contribution of the excited state branch is negligible.

To check that the fit to the data presented in Fig. 5.3 is accurate, it is instructive to compare simulation and data for intermediate parameters used in calculating the decay energy. Fig. 5.5 shows four such comparisons. The parameters being compared in the figure are the opening angle between the neutron and the fragment; the relative velocity (neutron minus fragment) between the two particles; the neutron time of flight to the front layer of MoNA; and the fragment kinetic energy calculated from the inverse mapping procedure of Section 4.3.1. As with Fig. 5.3, red curves represent the 380 keV resonant simulation, filled grey curves the non-resonant background, and black curves their sum. As can be seen in the figure, there is reasonable agreement between simulation and data for each of the four parameters.

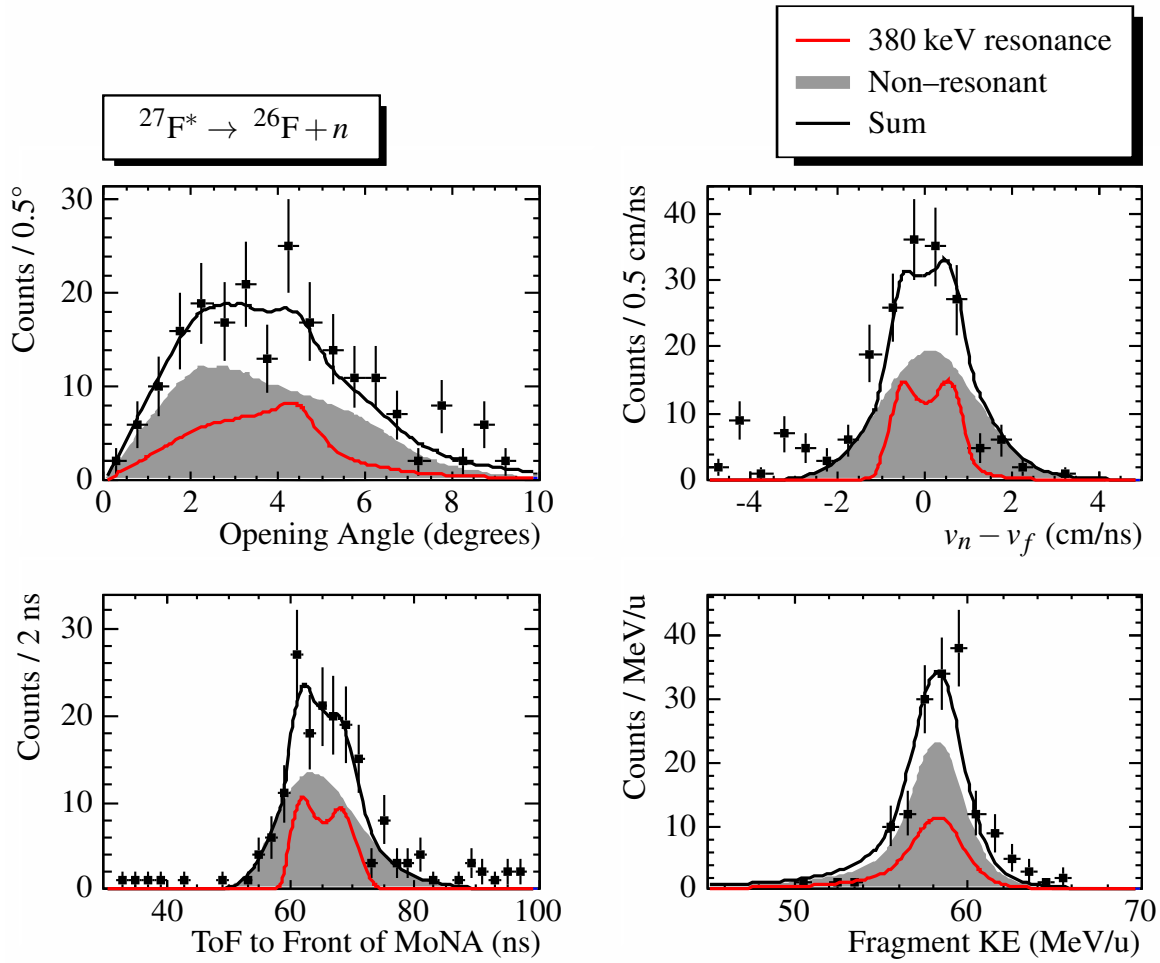

Figure 5.5: Comparison between simulation and data for intermediate parameters (opening angle, relative velocity, neutron ToF, and fragment kinetic energy) used in calculating the decay energy of $^{26}\mathrm{F} + n$ coincidences. The red curves are the result of a 380 keV resonant simulation, and the filled grey curves are the result of the simulation of a non-resonant Maxwellian distribution ($\Theta = 1.48$ MeV). Black curves are the sum of the two contributions (resonant:total = 0.33).

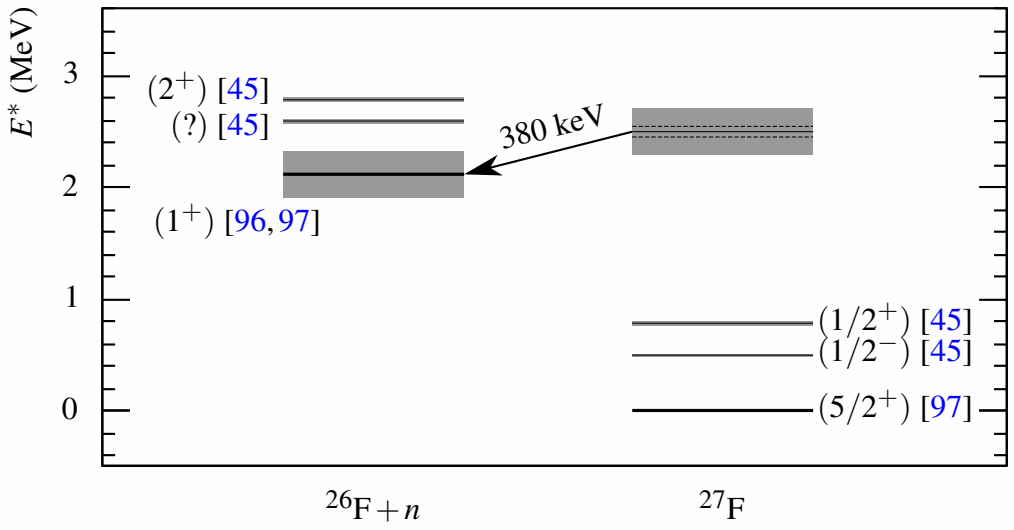

Figure 5.6: Summary of experimentally known levels in ^{26,27}F. The presently measured decay of a resonant excited state in ^{27}F to the ground state of ^{26}F is indicated by the arrow. The grey boxes represent experimental uncertainties in the absolute placement of level energies relative to the ^{27}F ground state. The dashed lines surrounding the present measurement correspond to the $\pm$60 keV uncertainty on the 380 keV decay energy, and the grey error box includes both this 60 keV uncertainty and the 210 keV uncertainty of the ^{26,27}F mass measurements. The bound excited states measured in [45] are placed assuming that all transitions feed the ground state as the authors of [45] do not state conclusively whether their observed γ-rays come in parallel or in cascade.

In order to place the present measurement into a level scheme of ^{27}F, the central resonance energy of 380 keV must be added to the one neutron separation threshold of ^{27}F. The one neutron separation threshold, S_n, of a nucleus with mass number A is the difference in mass[2] between the nucleus and the constituents of its neutron breakup (a lone neutron and the neighboring isotope with mass number $A-1$):

$$S_n = (m_{A-1} + m_n) - m_A. \tag{5.1}$$

Experimental masses are often published in terms of the atomic mass excess, Δ, given by

$$\Delta_A = m_A - Au, \tag{5.2}$$

[2]Atomic mass, including electrons.

where u is the atomic mass unit expressed in the same dimensions as m_A. Thus it is convenient to express S_n in terms of the Δ values of the A and $A-1$ isotopes; combining Eqs. 5.1 and 5.2 results in this expression:

$$\begin{aligned} S_n &= [(A-1)\,u + \Delta_{A-1} + m_n] - (Au + \Delta_A)\,. && (5.3)\\ &= \cancel{Au} - u + \Delta_{A-1} + m_n - \cancel{Au} - \Delta_A && (5.4)\\ &= -\Delta_A + \Delta_{A-1} - u + m_n. && (5.5) \end{aligned}$$

The most recent mass measurements of ^{26,27}F were performed using the time of flight technique at GANIL and are reported in Ref. [96]. These measurements place the atomic mass excesses of ^{27}F and ^{26}F at $\Delta_{27} = 24630 \pm 190$ keV and $\Delta_{26} = 18680 \pm 80$ keV, giving a ^{27}F one neutron separation energy of $S_n = 2120 \pm 210$ keV. Combining this S_n measurement with the present measurement of a 380 ± 60 keV resonant decay from ^{27}F* to the ground state of ^{26}F corresponds to the measurement of a previously unobserved excited state in ^{27}F at 2500 ± 220 keV. It should be noted that despite the relatively large uncertainty of the present measurement, the total uncertainty on the absolute level placement is dominated by that of the ^{27}F one-neutron separation energy. Fig. 5.6 shows the placement of this newly observed excited level in a level scheme summarizing experimentally known levels in ^{27}F and ^{26}F.

5.3 ^{28}F Decay Energy

The decay energy spectrum of ^{28}F is shown in Figs. 5.7 and 5.8. The simulated acceptance curve is identical to that of Fig. 5.1, indicating a resonance in the data with a maximum around 500 keV. As outlined in Section 4.5.2, no background contribution is expected in the decay energy spectrum of ^{28}F; hence an attempt is made to fit the spectrum with a single $\ell = 2$ Breit-Wigner resonance. As with ^{27}F decays, the fit is done by minimizing the unbinned negative log-likelihood. The parameter of interest is the central energy of the resonance, E_0, and the only nuisance parameter, Γ_0, is treated

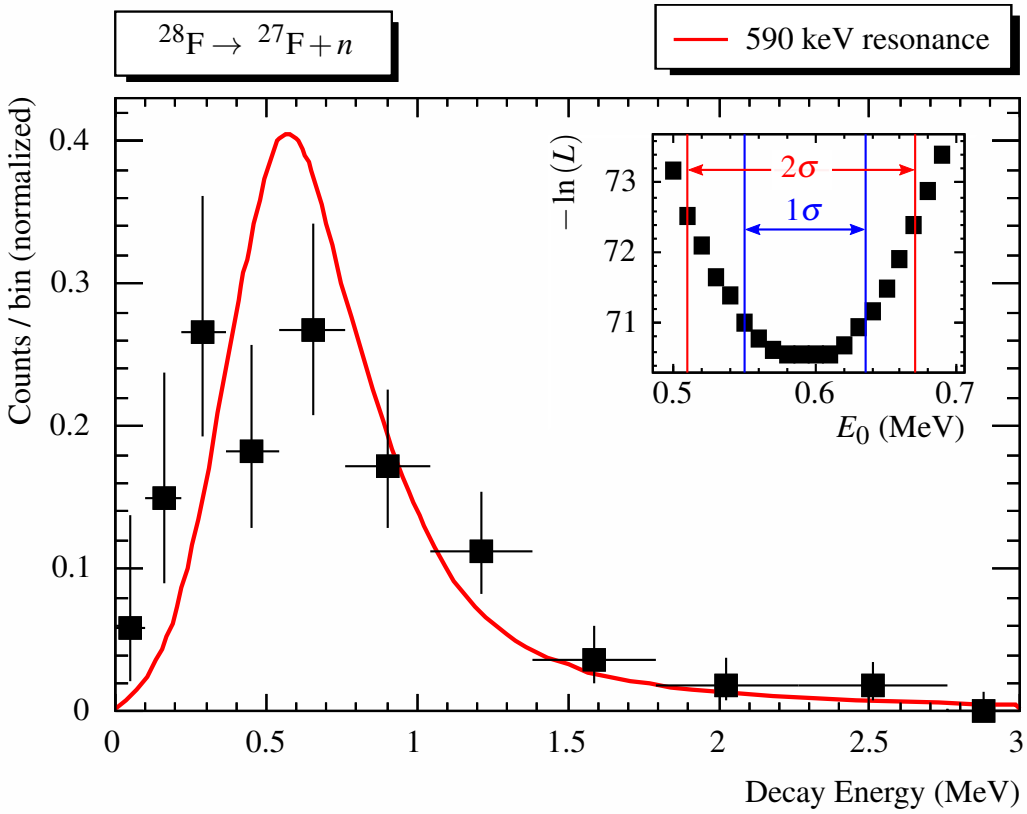

Figure 5.7: Decay energy spectrum of ^{28}F (filled squares with error bars), along with the best single resonance fit (red curve). The inset is a plot of the negative log-likelihood vs. central resonance energy, demonstrating a minimum at 590 keV.

with the profile likelihood method mentioned in Section 5.2. Additionally, Γ_0 is restricted to values ≤ 1 MeV as the simulated lineshape is virtually identical for $\Gamma_0 \geq 1$ MeV.

The result of the single resonance fit is shown in Fig. 5.7. The best fit parameters are $E_0 = 590$ keV and $\Gamma_0 = 1$ MeV. As seen in the figure, the quality of the single resonance fit is rather poor: the fit fails to reproduce the broad shape of the spectrum despite a width value that is over an order of magnitude greater than the single-particle prediction of ~ 60 keV.[3] This suggests that multiple resonances are present in the data and that they should be fit with a superposition of independent resonances.

[3]The single particle prediction for the width is obtained from the solution of the problem of a $0d_{5/2}$ neutron moving in a Woods-Saxon potential, with the potential well depth adjusted until a resonance is found at 590 keV.

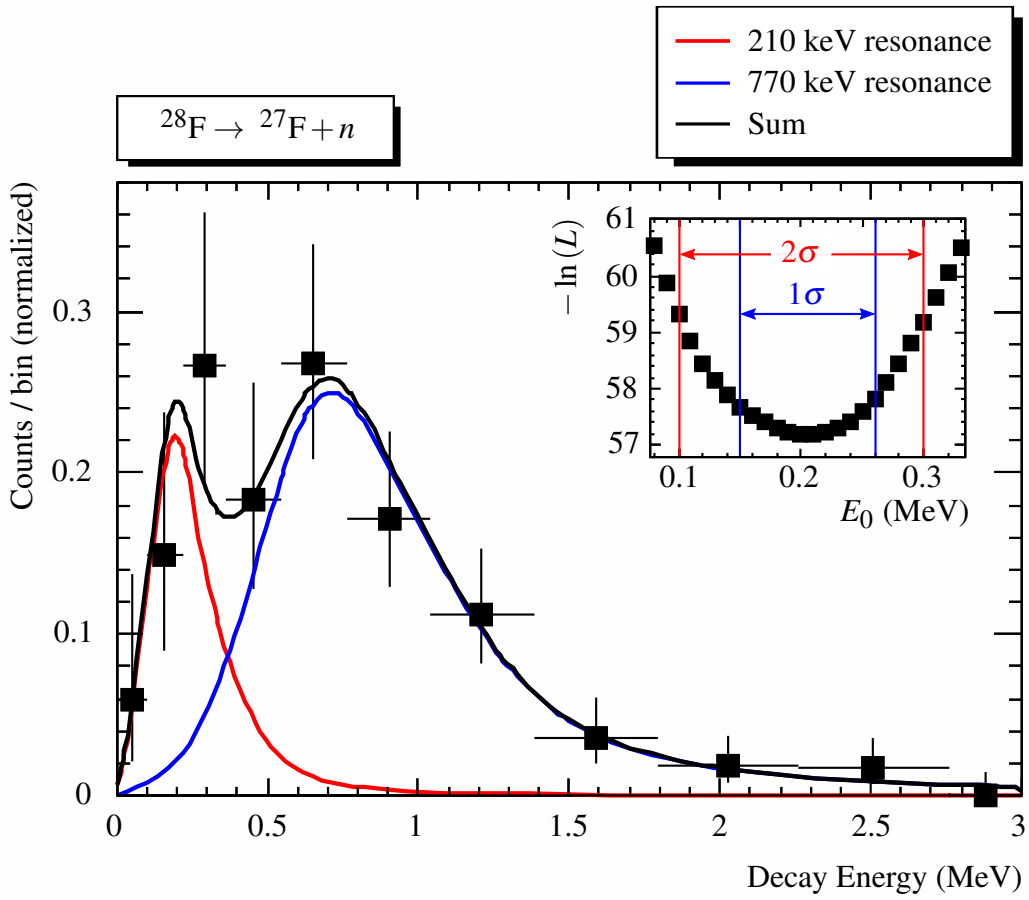

Figure 5.8: Decay energy spectrum for ^{28}F, with the best two resonance fit results superimposed. The filled squares with error bars are the data, and the red and blue curves are the lower resonance ($E_0^{(\mathrm{gs})} = 210$ keV) and upper resonance ($E_0^{(\mathrm{ex})} = 770$ keV) fits, respectively. The black curve is the superposition of the two individual resonances. The inset shows a plot of the negative log-likelihood vs. $E_0^{(\mathrm{gs})}$, demonstrating a minimum at 210 keV and $1,2\sigma$ confidence regions of $^{+50,+90}_{-60,-110}$ keV. Each point on the inset likelihood plot has been minimized with respect to the nuisance parameters $E_0^{(\mathrm{ex})}$, $\Gamma_0^{(\mathrm{ex})}$, and the relative contribution of the two resonances.

Because of coarse resolution and low statistics, it is not possible to precisely resolve the contribution of multiple individual resonances, and the main interest is in determining the location of the ground state. To avoid a solution in which the ground state resonance is made artificially wide, the width of the lower resonance is fixed at $\Gamma_0^{(\mathrm{gs})} = 10$ keV, which is approximately equal to the single-particle prediction for resonances in the expected region of $E_0^{(\mathrm{gs})}$. The width of the upper resonance, $\Gamma_0^{(\mathrm{ex})}$ is allowed to take any value ≤ 1 MeV. The parameter of interest is the central energy of the lower resonance, $E_0^{(\mathrm{gs})}$, and the nuisance parameters—treated with the profile likelihood method—are $E_0^{(\mathrm{ex})}$, $\Gamma_0^{(\mathrm{ex})}$, and the relative contribution of the two resonances. Both resonances in the fit have a fixed orbital angular momentum value of $\ell = 2$.

The result of the two resonance fit is shown in Fig. 5.8. The best fit is found with a lower resonance at $E_0^{(\mathrm{gs})} = 210$ keV and 1σ and 2σ confidence regions of $^{+50}_{-60}$ keV and $^{+90}_{-110}$ keV, respectively. The central energy and width of the upper resonance are $E_0^{(\mathrm{ex})} = 770$ keV and $\Gamma_0^{(\mathrm{ex})} = 1$ MeV, and the ratio of the ground state resonance to the total area is 24.2%. As seen in the figure, the two resonance model gives a reasonable agreement with the data, providing a much better fit than the one resonance hypothesis. The likelihood ratio of the one and two resonance hypotheses, $D = -2\ln(L_1/L_2)$, is equal to 26.7. The two resonance hypothesis has two additional free parameters relative to the one resonance one, so probability distribution of D should be χ^2 with two degrees of freedom [94]. Comparison of D with $\chi^2_{ndf=2}$ critical values indicates that the one resonance hypothesis can be rejected at a confidence level of greater than 4σ.

The large $\Gamma_0^{(\mathrm{ex})}$ of the upper resonance in the fit suggests that more than two resonances might be present in the data, and this interpretation is certainly plausible based on the theoretical level density of ^{28}F below 1 MeV. However, with the present resolution and statistics it is not possible to accurately distinguish the contribution of multiple excited state resonances to the measured decay spectrum. Attempts to fit the data with three independent resonances indicate that the location of the ground state resonance is insensitive to the number of resonances used in the fit: there is no way to match the data points below ~ 300 keV unless the lowest resonance in the sum is placed around 200 keV.

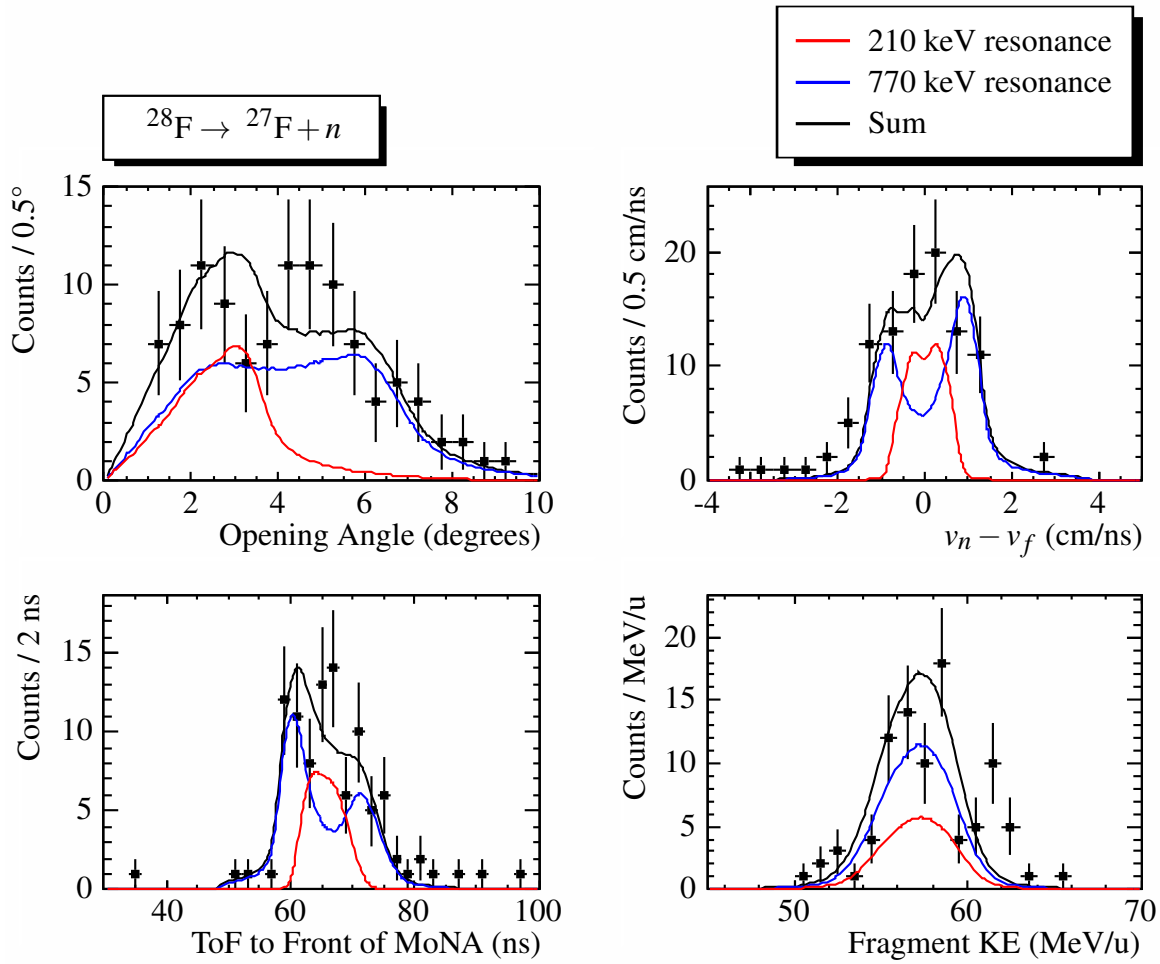

Figure 5.9: Comparison of simulation and data for intermediate parameters used in constructing the decay energy of ^{28}F. The parameters being compared are noted as the x axis labels on the individual panels. The filled circles with error bars are the data, and the red, blue and black curves represent the 210 keV resonance simulation, 770 keV resonance simulation and their sum, respectively.

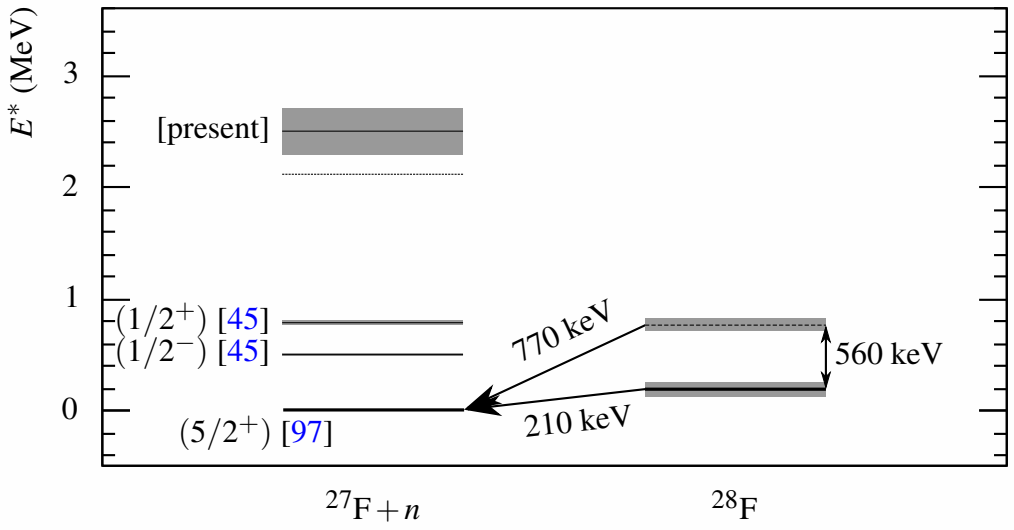

Figure 5.10: Experimental level scheme of ^{28}F and ^{27}F. The black lines represent the nominal placement of states relative to the ground state of ^{27} F, and the grey boxes represent 1σ errors on the measurements. As described in the text, the placement of the 560 keV (770 keV decay energy) excited state in ^{28}F is extremely uncertain, and it is only included in the figure for consistency.

As with ^{27}F decays, it is instructive to compare simulation and data for intermediate parameters that contribute to the calculation of decay energy. This comparison is shown in Fig. 5.9 for decays from ^{28}F. The parameters compared are opening angle between the neutron and the fragment; relative velocity (neutron minus fragment); time of flight to the front and center of MoNA; and the reconstructed fragment energy. As seen in the figure, reasonable agreement is achieved for all parameters when comparing the data to the two resonance fit.

No gamma-rays were recorded in CAESAR in coincidence with ^{28}F + n, indicating that the presently observed decays are feeding the ground state of ^{27}F. This places the ground state binding energy of ^{28}F at $E_{\mathrm{rel}} = 210^{+50}_{-60}$ keV above the ground state of ^{27}F, as shown in the level scheme of Fig. 5.10. The level scheme also displays an excited state in ^{28}F at 560 keV, corresponding to the upper 770 keV resonance of the fit; however, it should be emphasized that the placement of this excited level in ^{28}F is extremely uncertain. As mentioned previously, it is possible to fit

the ^{28}F decay spectrum with more than two resonances, and although the location of the ground state resonance is robust, the placement of excited levels will vary as additional resonances are introduced. Hence the only reliable measurement for ^{28}F is that of its ground state energy relative to ^{27}F.

Using the present measurement and that of the ^{27}F mass, the absolute binding energy of ^{28}F is calculated as

$$B_{28} = B_{27} + E_{\mathrm{rel}}, \tag{5.6}$$

with the binding energy of ^{27}F calculated from its atomic mass measurement via:

$$B_{27} = Zm_p + Nm_n - (\Delta_{27} - Zm_e) - Au, \tag{5.7}$$

where Z, N, and A are the proton, neutron and mass numbers of ^{27}F; m_p, m_n and m_e are the proton, neutron, and electron masses; and, as in Eq. (5.2), u is the atomic mass unit expressed in the same dimensions as the various masses. Using the measurement of $\Delta_{27} = 24630 \pm 190$ keV from Ref. [96], Eq. (5.7) evaluates to $B_{27} = 186.26 \pm 0.19$ MeV. The binding energy of ^{28}F is then calculated from Eq. (5.6) as $B_{28} = 186.47 \pm 0.20$ MeV.

5.4 Cross Sections

In addition to measuring decay energies, it is possible to calculate cross sections for the population of observed states in the reaction ^{9}Be(^{29}Ne, X). The cross section, in millibarns, is given by

$$\sigma = \frac{n_r}{n_t n_b} \times 10^{27}, \tag{5.8}$$

where n_r, n_t, and n_b are the numbers of reactions, target nuclei, and incoming beam particles, respectively. The number of target nuclei is calculated from the target thickness, δ, and the atomic mass of natural beryllium, M_{Be}:

$$n_t = N_A \delta / M_{Be}, \tag{5.9}$$

where N_A is Avagodro's number, 6.02×10^{23} mol^{-1}. Plugging $\delta = 0.288$ g/cm^2 and $M_{Be} = 9.012$ g$\cdot$mol^{-1} into Eq. (5.9), the number of target nuclei evaluates to $n_t = 1.92 \times 10^{22}$. The number of incoming beam particles was recorded by a scaler module connected to the target scintillator

CFD, and to obtain the number of incoming ^{29}Ne beam particles, the total number of scaler counts is divided by the live time of the experimental system and multiplied by the ratio of ^{29}Ne to total beam particles. The ^{29}Ne:total ratio is calculated by comparing the number of events falling within the ^{29}Ne time of flight gate (c.f. Section 4.2.1) to the total number of events recorded in the beam ToF spectrum; this ratio is calculated separately for each production run taken during the experiment.

The number of reactions is given by

$$n_r = f n_c / \varepsilon, \tag{5.10}$$

where n_c is the number of recorded neutron-fragment coincidences; f is the fraction of the total fit area taken up by the decay channel in question; and ε is the total efficiency of the experimental system. The efficiency can be divided up into its constituent parts:

$$\varepsilon = \varepsilon_{geom} \varepsilon_m \bar{\varepsilon}_s. \tag{5.11}$$

In the above equation, ε_{geom} refers to the geometric efficiency of the Sweeper-MoNA system (at the appropriate decay energy) and is obtained from Monte Carlo simulations. ε_m is the detection efficiency of MoNA and is calculated from GEANT4 simulations done with the appropriate incoming neutron energy. $\bar{\varepsilon}_s$ is the intrinsic efficiency of the charged particle detectors. To obtain $\bar{\varepsilon}_s$, a run-by-run intrinsic efficiency is first calculated by comparing the number of fluorine elements that register signals in all charged particle detectors to the total number that trigger the experimental system. This calculation excludes the ion chamber efficiency since the ion chamber is needed to make a fluorine gate. To account for this, the efficiency of the ion chamber for $Z \sim 9$ particles is fist calculated from a target-out run, and this number is multiplied by the run-by-run fluorine efficiency. Drift in the ion chamber efficiency between runs, as well as the difference in efficiency between $Z = 10$ (unreacted beam) and $Z = 9$ is negligible, so the procedure described above is sufficient to obtain a run-by-run charged particle detection efficiency for $Z = 9$ particles. From here, $\bar{\varepsilon}_s$ is calculated by taking a weighted average of the run-by-run charged particle efficiency

values:

$$\bar{\varepsilon}_s = \sum_i w_i \varepsilon_i, \tag{5.12}$$

where the weights w_i are equal to the number of incoming ^{29}Ne beam particles in run i divided by the total number of incoming beam particles, and ε_i is the $Z = 9$ efficiency for run i.

Using the calculation procedure described above, the cross section for the population of the ground state of ^{28}F is calculated to be 0.23 ± 0.06 mb, and the cross section for the population of the 2500 keV excited in ^{27}F is calculated as 1.54 ± 0.68 mb. A detailed summary of the numbers which go into the cross section calculations can be found in Appendix A. It should be noted that there is a significant systematic error on the ^{28}F ground state cross section measurement resulting from uncertainty in the number of excited state resonances to include in the fit to data. The total number of resonances significantly alters the relative contribution of the ground state resonance (f in Eq. (5.10)) which in turn alters the cross section value. Quantifying this systematic error in terms of 1σ confidence intervals is not practical, but to give a sense of its magnitude, the cross section would be calculated as 0.40 ± 0.18 mb ($f = 42.9 \pm 18.3\%$) in the case of three resonances.

Chapter 6

DISCUSSION

res

6.1 Shell Model Calculations

In this chapter, the present experimental results are compared to theoretical predictions in order to place them into a broader physical context. The theoretical predictions are made with large scale shell model calculations, and in this section a brief description of these calculation methods is presented.

As mentioned in Chapter 1, the nuclear shell model is built upon the idea of treating nuclei as a collection of independent particles subjected to a mean field. The most realistic form for the mean field is the Woods-Saxon potential:

$$V(r) = -\frac{V_0}{e^{(r-R)/a}+1}, \tag{6.1}$$

where V_0 is the potential well depth and a represents the surface thickness of the nucleus. R is the nuclear radius, which typically scales as $R = r_0 A^{1/3}$, with the parameter r_0 in the range of 1.2 to 1.4 fm. In addition to the potential well, a strong spin-orbit term is necessary for an accurate description of nuclear properties:

$$V_{so}(r) = -\frac{1}{r}V'(r)\,\vec{\ell}\cdot\vec{s}. \tag{6.2}$$

This spin-orbit term gives rise to the splitting of ℓ orbitals displayed in Fig. 1.1, with the $j = \ell - 1/2$ coupling raised in energy relative to the $j = \ell + 1/2$ coupling.

The simple nuclear potential outlined above, consisting of a mean field and spin orbit term, is only adequate for the description of very basic nuclear properties such as the reproduction of large energy gaps at the "magic numbers" 2, 8, 20, 28, 50, 82, and 126. For a more complete

description of nuclei, the nuclear Hamiltonian, $H = T + V$, must also, at a minimum, take two-body interactions into account. These are typically introduced by splitting the Hamiltonian into two parts:

$$H = H_0 + V_{res}, \tag{6.3}$$

where $H_0 = T + V_0$ includes the kinetic energy T and central potential V_0 and V_{res} is the residual potential given by

$$V_{res} = \sum_{i,j}^{A} V_{ij} - \sum_{i}^{A} V_c(r_i). \tag{6.4}$$

In Eq. (6.4), V_{ij} represent the two-body interactions between nucleons and V_c represents the central potential of Eqs. (6.1) and (6.2).

In principle, one can solve the Schrödinger equation using the potentials described above, with Eq. (6.4) applied to all nucleons in the nucleus. In practice, however, this requires large amounts of computation time for all but the lightest nuclei and is not practical for typical calculations.[1] Instead, the nucleus is divided into an inert core and an active valence space for which the two-body contributions are calculated. Within this model space, the total wavefunction, $|\psi_k\rangle$, for a state with quantum numbers $k = \{n, \ell, j\}$ is given by a sum of basis states:

$$|\psi_k\rangle = \sum_{\alpha} a_{k\alpha} |\psi_\alpha\rangle, \tag{6.5}$$

where the sum is over the orbitals α in the active valence space. The basis states, $|\psi_\alpha\rangle$, are typically defined to have either a definite magnetic quantum number M (referred to as the m-scheme) or a definite total spin quantum number J (the j-scheme).

From the potential of Eqs. (6.3) and (6.4) and the wave function of Eq. (6.5), the time independent Schrödinger equation,

$$H|\psi_k\rangle = E_k|\psi_k\rangle, \tag{6.6}$$

is expressed as

[1] It should be noted that there is presently a great deal of effort being put into the "no core" shell model [98] and other *ab initio* methods that attempt to describe nuclei by starting from first principles and treating all nucleons on an equal footing. However, these calculations are currently only tractable up to $A \sim 20$.

$$(H_0 + V_{res}) \sum_\alpha a_{k\alpha} |\psi_\alpha\rangle = E_k \sum_\alpha a_{k\alpha} |\psi_\alpha\rangle . \tag{6.7}$$

Taking the inner product of both sides of Eq. (6.7) with $\langle\psi_k| = \sum_\beta a_{k\beta} \langle\psi_\beta|$ yields

$$\sum_{\alpha,\beta} a_{k\alpha} a_{k\beta} \langle\psi_\beta| H |\psi_\alpha\rangle = E_k \sum_{\alpha,\beta} a_{k\alpha} a_{k\beta} \delta_{\alpha\beta} . \tag{6.8}$$

The solution of Eq. (6.8) is then equivalent to solving the eigenvalue problem

$$\begin{vmatrix} H_{11} - E_k & H_{12} & \cdots & H_{1n} \\ H_{21} & H_{22} - E_k & \cdots & H_{2n} \\ \vdots & \cdots & \ddots & \vdots \\ H_{n1} & H_{n2} & \cdots & H_{nn} - E_k \end{vmatrix} , \tag{6.9}$$

which determines the energy eigenvalues, E_k, of the system as well as the matrix elements,

$$H_{\beta\alpha} = \langle\psi_\beta| H |\psi_\alpha\rangle \tag{6.10}$$

$$= \langle\psi_\beta| H_0 |\psi_\alpha\rangle + \langle\psi_\beta| V_{res} |\psi_\alpha\rangle . \tag{6.11}$$

The right hand side of Eq. (6.11) is divided into two parts: the single particle energies

$$\langle\psi_\beta| H_0 |\psi_\alpha\rangle = E^{(0)}_{\alpha\beta} \delta_{\alpha\beta} \equiv E^{(0)}_\alpha \tag{6.12}$$

and the two-body matrix elements (TBME)

$$\langle\psi_\beta| V_{res} |\psi_\alpha\rangle \equiv \langle\psi_\beta| V_{12} |\psi_\alpha\rangle . \tag{6.13}$$

From here, one can solve for the $a_{k\alpha}$ coefficients in Eq. (6.7), thus determining the nuclear wavefunctions and allowing calculation of additional spectroscopic properties of the various states as well as their overlap, $\langle\psi_i|\psi_f\rangle$.

In Eq. (6.13), the V_{12} represent the *effective* two-body interactions. In principle these can be derived from the bare nucleon-nucleon interaction, but in practice they are often determined by fitting to experimental data. The fitting procedure begins by choosing a core and valence

space for which the interaction is intended and then by collecting a wide variety of reliable experimental information (typically ground and low-lying excited state energies) on nuclei in the intended region. The TBME are then adjusted until the deviation between experimental data and theoretical predictions is at a minimum, with an approximate theoretical error determined from the Root Mean Square (RMS) deviation between the two. In the present work, shell model calculations are performed using three interactions: USDA and USDB [99], which operate in the *sd* valence space ($\pi 0d_{5/2}\pi 1s_{1/2}\pi 0d_{3/2}\nu 0d_{5/2}\nu 1s_{1/2}\nu 0d_{3/2}$), and the recently developed IOI interaction [100], which operates in a truncated *sd*-*pf* valence space ($\pi 0d_{5/2}\pi 1s_{1/2}\pi 0d_{3/2}$ $\nu 1s_{1/2}\nu 0d_{3/2}\nu 0f_{7/2}\nu 1p_{3/2}\nu 1p_{1/2}$). The calculations are performed using the *j*-scheme code NuShellX@MSU [101, 102].

6.2 ^{27}F Excited State

Fig. 6.1 shows the experimental and theoretical (USDA, USDB, IOI) level schemes of ^{27}F, up to 3.5 MeV. As seen in the figure, all three models predict a fairly high level density in the region of the presently observed resonance at 2500 ± 220 keV. The observation of only a single resonance could indicate selectivity of the reaction mechanism used to populate ^{27}F*, but as the precise reaction mechanism is not known, any attempt to argue for the assignment to a specific state based on reaction cross sections would be highly speculative. Moreover, the ground state structure of the ^{29}Ne beam is somewhat uncertain. Its spin and parity have not been measured experimentally, and there is also discrepancy in shell model predictions. MCSM calculations using the SDPF-M interaction predict the ^{29}Ne ground state to be $3/2^{+}$ with a 100% $2p$-$2h$ configuration [103], while calculations using the IOI interaction and model space predict a $3/2^{-}$ ground state with a configuration that is primarily $1p$-$1h$. The lack of certainty about the ^{29}Ne ground state structure further distorts any clarification that might be gained from consideration of population cross sections.

Further distorting the interpretation of the present observation is the fact that shell model calculations fail to reproduce the bound state measurements of Ref. [45]. Of the calculations presented,

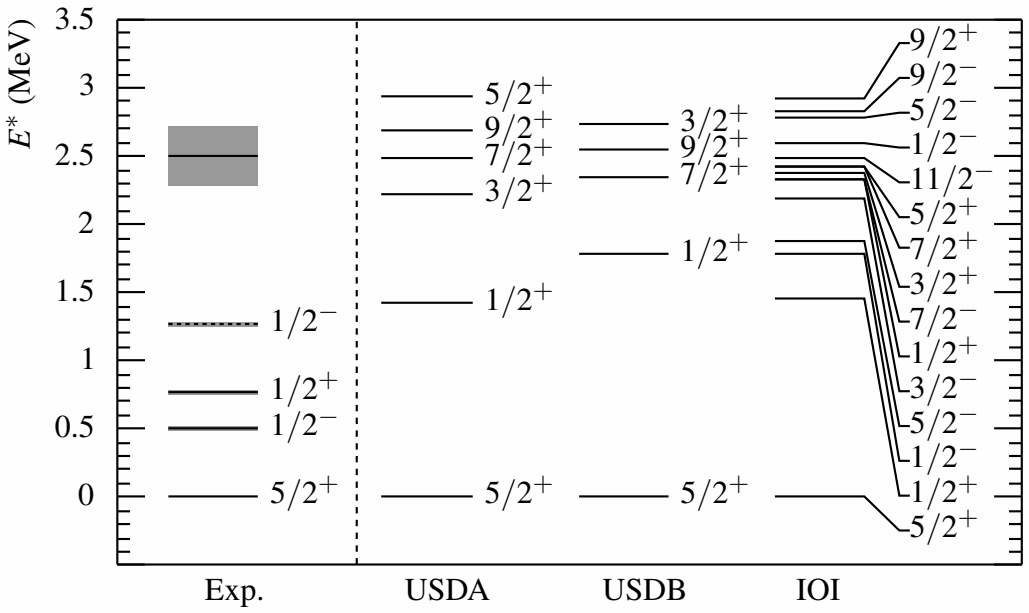

Figure 6.1: Summary of experimental and theoretical (USDA, USDB, IOI) excited levels in ^{27}F. The grey boxes surrounding the experimental values represent the 1σ uncertainties on the measurements. Experimental values are taken from Refs. [97] (ground state J^π), [45] (bound excited states), and the present work. Both possible placements of the 504 keV transition observed in Ref. [45] are included, with the cascade placement shown as the dashed line at 1282 keV.

all overpredict the $1/2^+$ first excited state energy by $\sim$ 700 keV or more, and the IOI calculation overpredicts the $1/2^-$ excited state energy by either $\sim$ 1300 keV or $\sim$ 500 keV depending on whether the experimental observation is placed in parallel or cascade with the $1/2^+$. Additionally, the MCSM/SDPF-M calculations presented in [45] overpredict the $1/2^+$ energy by around 320 keV.

As mentioned in Ref. [45], proton excitations from the *p* shell to the *sd* shell likely play a role in the excited state structure of ^{27}F. This has been explored theoretically in Ref. [104], which deals with excited states in even-*N* fluorine isotopes that involve *p* to *sd* shell proton excitations (or "proton hole" states). The predicted energies of bandhead proton hole states are summarized in Fig. 6.2, taken from the reference. The proton holes are expected to couple to three types of neutron configurations: pure *sd* (resulting in a $1/2^-$ bandhead state), $1p$-$1h$ ($3/2^+$ bandhead state), and

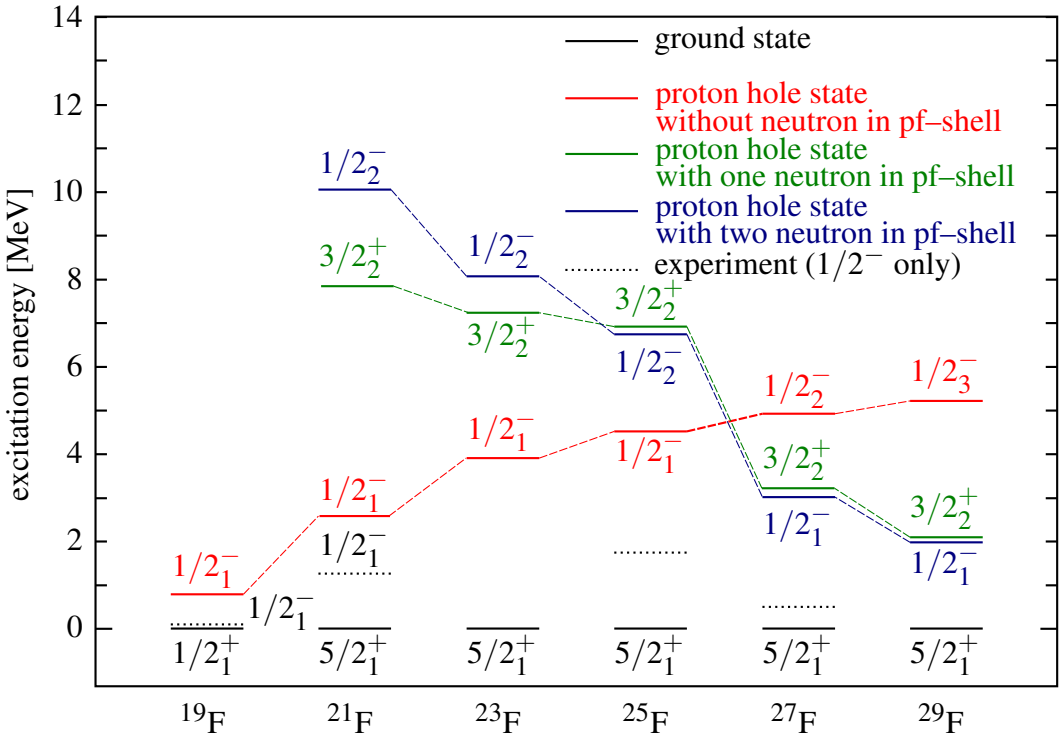

Figure 6.2: Excitation energies of theoretical p shell proton hole states in even-N fluorine isotopes. Adapted from Ref. [104], with the ^{25,27}F $1/2^-$ candidate states of Ref. [45] added, assuming parallel gamma emission.

$2p$-$2h$ ($1/2^-$ bandhead). In the neutron rich fluorine isotopes, the proton hole states coupling to $1p$-$1h$ and $2p$-$2h$ neutron configurations are predicted to be relatively low in excitation energy as a result of the diminished $N = 20$ shell gap, and it is interesting to note that the predicted energies of the $1p$-$1h$ and $2p$-$2h$ states in ^{27}F are both close to the present observation. Regarding p-sd proton excitations, it should also be noted that a new PSDPF interaction has recently been developed [105] to treat configurations in the full p-sd-pf model space, and it would be interesting to compare the predictions of this interaction to the present measurement.

6.3 ^{28}F Binding Energy

As outlined in Chapter 2, it has been well established, both experimentally and theoretically, that there is a region of nuclei in the vicinity of $Z = 11$ and $N = 20$ whose low-lying structures have

significant pf shell "intruder" components, in the form of $\hbar\omega$ excitations of neutrons from the sd shell to the pf shell[2]. This region is often referred to as the "island of inversion," in reference to the inverted filling of single particle levels (pf before sd). The region of inversion was originally thought to encompass only those nuclei directly surrounding ^{32}Na, but in more recent years its boundaries have become an open question. Approaching stability, where nuclei become more experimentally accessible, it is generally agreed that the intruder components fade away for $N \lesssim 18$ and $Z \gtrsim 13$. What is less certain is the importance of intruder configurations as one moves away from stability and towards more neutron rich nuclei, either by adding neutrons or removing protons. It was originally proposed that intruder configurations are significant only for $N \leq 22$ [106], but recent experiments have contradicted this claim, collecting evidence that significant intruder components are present in the ground states of nuclei with higher neutron number. For example, the ^{9}Be(^{38}Si,^{36}Mg)X reaction has been used to establish that there is a significant $2\hbar\omega$ contribution to the ground state of ^{36}Mg, which has 24 neutrons [107].

Going away from stability in the other direction, i.e. removing protons, the contribution of intruder configurations to the ground state structure of nuclei has been largely unexplored, limited to theoretical calculations such as those of Ref. [34], which were introduced in Section 2.4. Experimentally, the fluorine isotopic chain is the only area in which the intruder structure of $Z < 10$, $N \geq 19$ nuclei can be examined in any detail. All lighter elements are unbound past $N = 16$, making experimental investigation of isotopes with $N \geq 19$ extremely difficult since all of these nuclei will decay by the emission of three or more neutrons. The present measurement of the ground state binding energy of ^{28}F is the first experimental investigation into the structure of fluorine nuclei with $N \geq 19$, and in this section its relevance to the intruder structure of ^{28}F will be discussed.

A simple way to check for pf shell intruder components in the ground state of a nucleus is

[2]Here a $n\hbar\omega$ excitation means that n neutrons have been promoted from the sd shell to the pf shell, in contrast to the "normal" filling of orbitals seen near stability. In general, however, it means that a harmonic oscillator gap has been crossed n times: for example $2\hbar\omega$ could mean that either two nucleons were promoted across a single oscillator gap or that a single nucleon was promoted across two oscillator gaps.

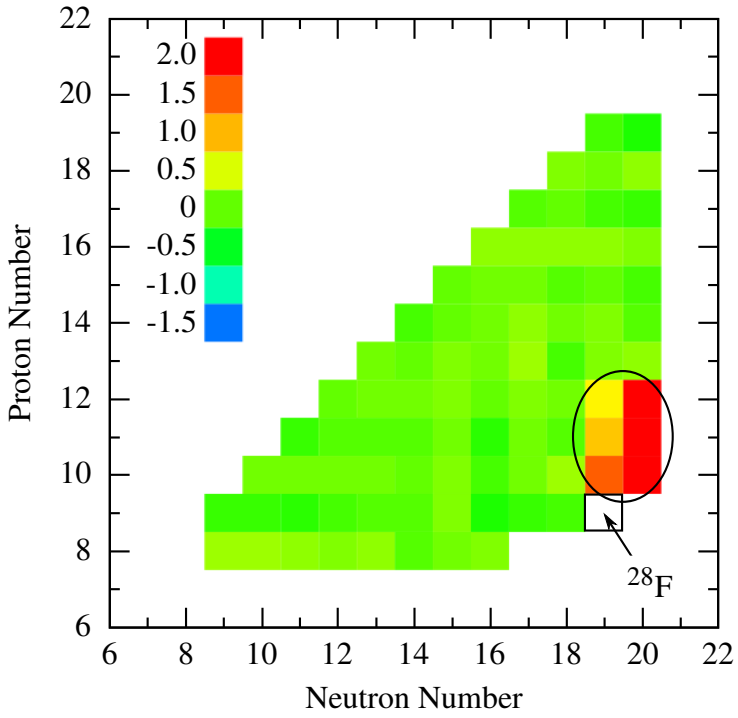

Figure 6.3: Difference between experimental [12, 96] and theoretical (USDB) binding energies for *sd* shell nuclei, with positive values meaning experiment is more bound than theory. Adapted from Ref. [99]

to compare its measured binding energy to the predictions of a shell model which includes only *sd* orbitals in the active valence space. A significant deviation between experiment and theory would likely indicate that configurations which extend outside of the *sd* shell are important to the description of the nucleus in question. Such a comparison is shown in Fig. 6.3, which is a plot of $\mathrm{BE_{exp}} - \mathrm{BE_{th}}$ for *sd* shell nuclei, adapted from Ref. [99]. The theoretical calculations are done in the *sd* valence space using the USDB interaction (the authors of [99] claim similar results using the USDA interaction). The region circled on the plot is composed of traditional island of inversion nuclei, and it is clear that the theoretical predictions deviate significantly from experiment, with experiment more bound than theory by up to 2 MeV. The authors of [99] speculate that ^{28,29}F lie outside of the island of inversion, but at the time of publication the only available experimental binding energies for these nuclei were mass extrapolations, making this claim extremely tenuous.

Another way to examine *pf* shell intruder components theoretically is to use a shell model that

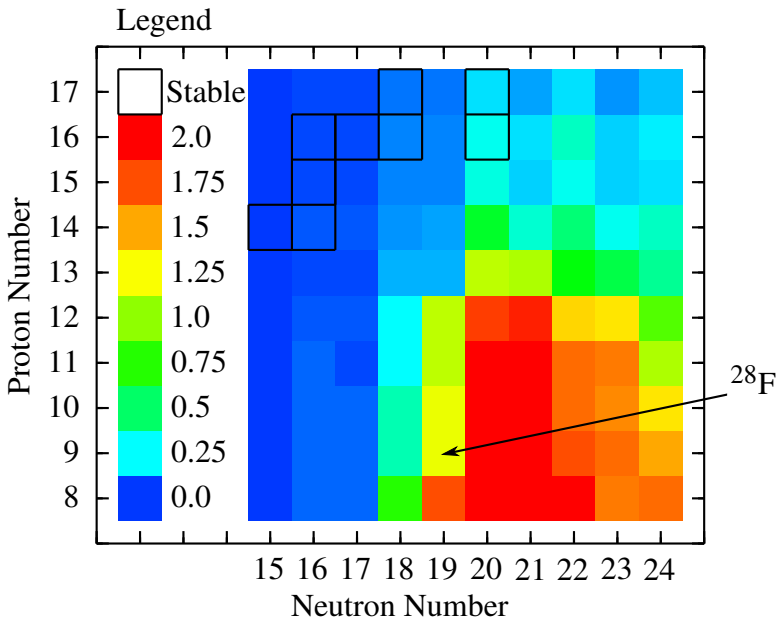

Figure 6.4: Average $\hbar\omega$ excitations in the ground states of nuclei with $8 \leq Z \leq 17$ and $15 \leq N \leq 24$, as calculated in the IOI interaction and truncated $sdpf$ model space. Taken from Ref. [100].

includes the sd and pf shells in its active valence space to calculate the occupation probabilities of pf shell orbitals. Such calculations were recently done for a wide variety of nuclei centered around $N = 20$ [100]. These calculations utilize the IOI interaction and an active valence space composed of the $1s_{1/2}0d_{3/2}0f_{7/2}1p_{3/2}1p_{1/2}$ neutron orbitals. Fig. 6.4 is a plot of the average $\hbar\omega$ excitations in the ground states of nuclei with $8 \leq Z \leq 17$ and $15 \leq N \leq 24$. Nuclei in the traditional island of inversion region are clearly reproduced as having large $\hbar\omega$ contributions to their ground state structure, as are nuclei with $Z \leq 12,\ N \geq 22$. This calculation also predicts all fluorine isotopes with $N \geq 19$ to have an average $\hbar\omega$ excitation of one or greater, placing them within the island of inversion.

The theoretical analyses presented above give differing suggestions as to whether or not ^{28}F is an island of inversion nucleus. To distinguish between the two assertions, it is instructive to compare the predicted ground state binding energies given by the two models. Such a comparison is shown in Fig. 6.5, which is a plot of the predicted binding energies of $N = 19$ isotones in the

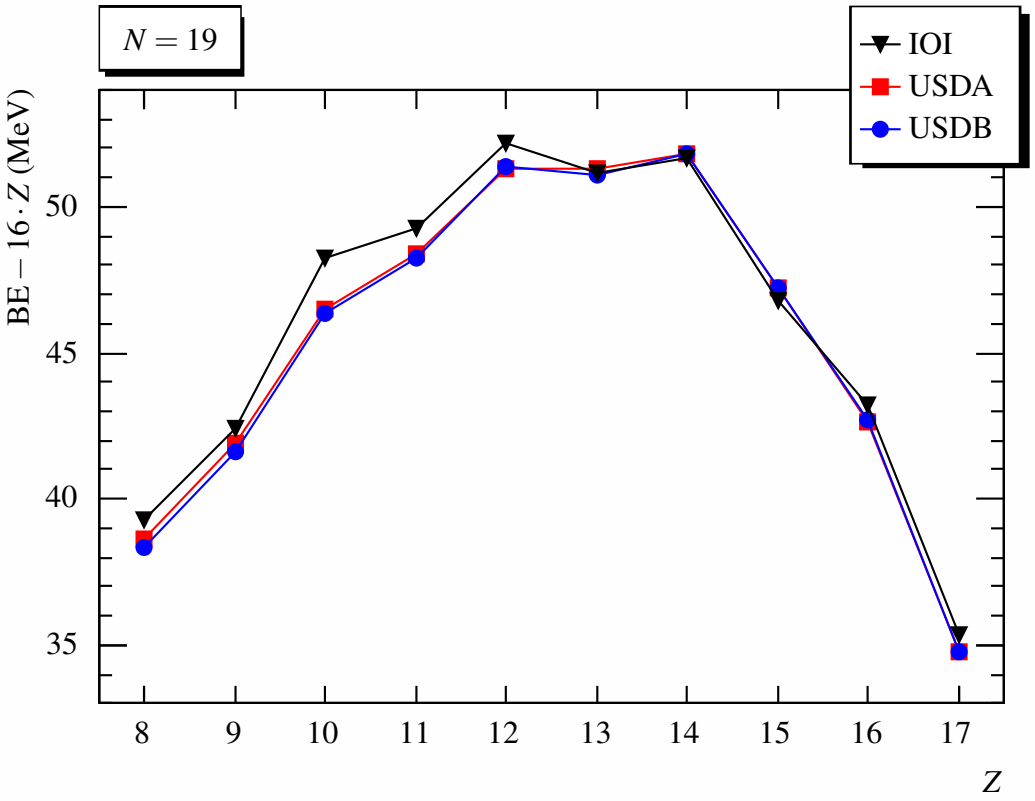

Figure 6.5: Theoretical predictions for the ground state binding energies of $N = 19$ isotones from oxygen $(Z = 8)$ through Chlorine $(Z = 17)$. Calculations are shown for three interactions: IOI (black inverted triangles), USDA (red squares), and USDB (blue circles). To put the binding energies on roughly the same scale, the calculation results have been shifted by subtracting $16 \cdot Z$ from their original values.

IOI, USDA, and USDB shell models (to put the binding energies on roughly the same scale, the calculation results have been shifted by subtracting $16 \cdot Z$ from their original values). For heavier nuclei, which the IOI calculation predicts to have minimal $\hbar\omega$ components, the binding energy predictions are generally in good agreement. As expected, the calculations diverge significantly for $Z = 10,\ 11,\ 12$, with the IOI calculations indicating significantly greater binding. For $Z = 8$ and $Z = 9$, the IOI calculations continue to predict greater binding than UDSA/USDB, albeit to a lesser extent than for $Z = 10,\ 11,\ 12$.

To examine the binding energy systematics of $N = 19$ isotones further, theoretical predictions must be compared to experiment. Fig. 6.6 displays this comparison, plotting the difference in bind-

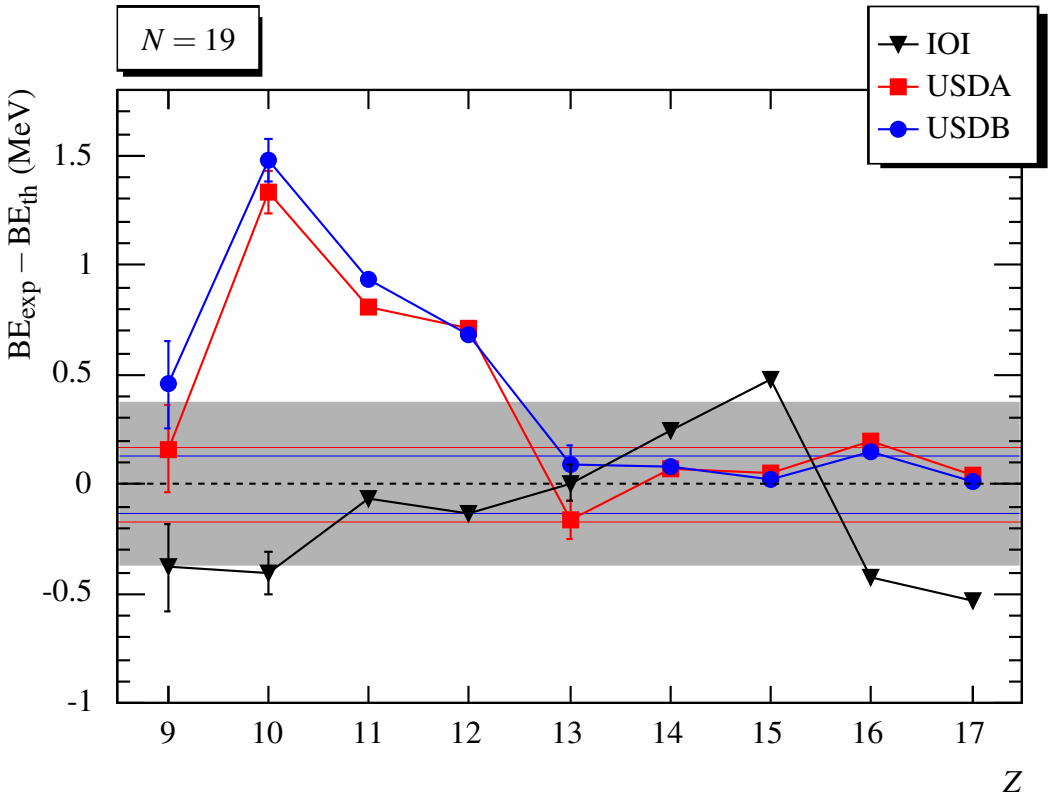

Figure 6.6: Binding energy difference between experiment (Refs. [12, 96] and the present work for $Z = 9$) and theory (IOI, USDA, USDB) for $N = 19$ isotones with $9 \leq Z \leq 17$. As in Fig. 6.3, positive values indicate experiment being more bound than theory. Error bars are from experiment only, and the shaded grey region represents the 370 keV RMS deviation of the IOI interaction, while the horizontal red and blue lines denote the respective 170 keV and 130 keV RMS deviations of USDA and USDB.

ing energy between experiment and theory for $N = 19$ isotones from $Z = 9$ to $Z = 17$. The experimental value for ^{28}F is from the present work, and all others are from Refs. [12,96][3]. As in Fig. 6.5, the theoretical calculations are done using the IOI, USDA, and USDB interactions and their associated model spaces. In this plot the experimental binding energies of isotones with $Z = 10,\ 11,\ 12$ clearly deviate from the USDA/USDB predictions. These nuclei are reasonably well reproduced by the IOI calculations, with the differences between experiment and theory falling within the

[3]Unless otherwise noted, the citation [12,96] means the following: if the mass in question was measured in Ref. [96], the measurement of [96] is used. Otherwise the mass is taken from the 2003 Atomic Mass Evaluation of Ref. [12].

370 keV RMS deviation of the IOI interaction. For ^{28}F, the difference between experiment and USDA/USDB theory drops dramatically, with the USDA calculation giving exact agreement within experimental error bars. Taken alone, this feature strongly suggests that pf shell components are not necessary for a complete description of the ^{28}F ground state. However, this conclusion must be weighed against the IOI calculation results which predict an average $\hbar\omega$ excitation of 1.22 in the ^{28}F ground state. The difference in binding energy between theory (IOI) and experiment is less than the theory's 370 keV RMS deviation; hence the IOI calculation's assertion of a ^{28}F ground with significant ($\geq 1\hbar\omega$) pf shell components cannot be ruled out conclusively. Despite this, the consistency of the present measurement with the USDA/USDB calculations demonstrates that pf shell components are *not* necessary for reproduction of the presently observable properties of the ^{28}F ground state. This is in sharp contrast to the $N = 19$ isotones whose inversion structure is better established—^{29}Ne, ^{30}Na, and ^{31}Mg: the ground state binding energies (and in the case of ^{31}Mg, spin-parity [108]) of these nuclei cannot be reproduced in an *sd*-only calculation.

In addition to the $N = 19$ isotones, it is also instructive to examine the binding energy systematics of the fluorine isotopic chain. Fig. 6.7 plots the experimental (when available) and theoretical (IOI, USDA, USDB) binding energies for fluorine isotopes from $A = 24$ ($N = 15$) to $A = 31$ ($N = 22$), with the top panel showing the difference between experiment and theory for the various models. The lightest two nuclei, ^{24,25}F, are well-reproduced in the USDA/USDB shell models but significantly under-bound by the IOI calculation, likely due to the IOI calculation's exclusion of the $\nu 0d_{5/2}$ orbital from its active valence space [100]. The calculations are in fairly good agreement with data and with each other for ^{26,27}F, but as discussed previously they begin to diverge at ^{28}F, with the IOI model predicting greater binding, and the level of divergence continues to increase for ^{29}F. There is little to compare for the heaviest fluorine nuclei, but the only available experimental information—namely the (non)existence of $^{(30)31}$F—is reproduced by the IOI shell model within its 370 keV RMS deviation.

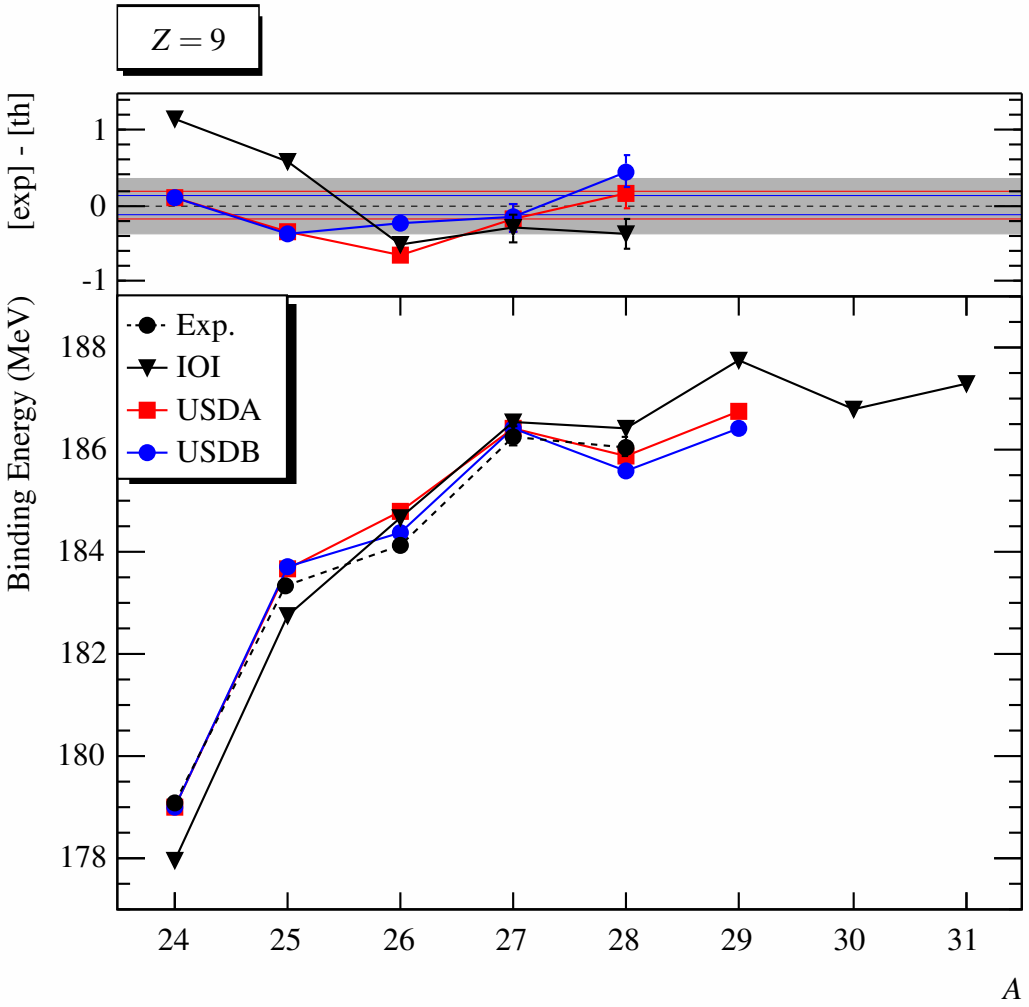

Figure 6.7: Experimental (Refs. [12, 96] and the present work for $A = 28$) and theoretical (IOI, USDA, USDB) binding energy predictions for fluorine isotopes, $24 \leq A \leq 31$. The USDA and USDB calculations end at $A = 29$ $(N = 20)$, as their corresponding model spaces cannot accommodate more than 20 neutrons. The top panel is a plot of binding energy differences (experiment minus theory) for nuclei whose mass has been measured. Error bars in the top panel are from experiment only, and the shaded grey region and red/blue horizontal lines are the same as in Fig. 6.6.

Chapter 7

SUMMARY AND CONCLUSIONS

In this work, the binding energy of ^{28}F and the excitation energy of a neutron-unbound state in ^{27}F have been measured using the technique of invariant mass spectroscopy. The neutron-unbound states were populated by reactions of a 62 MeV/u ^{29}Ne beam impinging on a 288 mg/cm^2 beryllium target, with the radioactive ^{29}Ne beam produced at the NSCL Coupled Cyclotron facility at Michigan State University. Neutrons resulting from the decay of the unbound states were detected in a large area plastic scintillator array (MoNA), and the residual charged fragments were deflected by a dipole magnet and analyzed in a variety of charged particle detectors. Gammas produced in the reaction were also recorded in a CsI(Na) array surrounding the target, allowing for a unique determination of the decay path of the neutron-unbound states. The observed resonances were fit using a Breit-Wigner lineshape with energy dependent width, and the smearing of experimental resolution and acceptance was accounted for in a Monte Carlo simulation of the experiment.

In ^{27}F, a resonant state was observed with 380 ± 60 keV decay energy, feeding the ground state of ^{26}F. In addition to this resonant state, a non-resonant background was observed in the data; this background is expected to arise from the neutron evaporation of high-lying states in ^{28}F, and it is well described by a Maxwellian distribution of thermalized beam velocity neutrons. Combined with the one neutron separation energy of ^{27}F, measured in Ref. [96] to be 2120 ± 210 keV, the presently observed resonance corresponds to an excited level in ^{27}F at 2500 ± 220 keV.

In ^{28}F, the ground state was observed to decay to the ground state of ^{27}F with a relative energy of 210^{+50}_{-60} keV, corresponding to a ^{28}F binding energy of 186.47 ± 0.20 MeV. In addition to the ground state, the inclusion of at least one additional higher-lying resonance was necessary to describe the data, with the location of the ground state peak insensitive to the number of additional resonances included in the fit.

To interpret the present measurements, they are compared to shell model predictions. For ^{27}F,

shell model calculations in both the *sd* and truncated *sd-pf* model spaces predict a fairly high level density in the neighborhood of 2500 keV in excitation energy, making it impossible to assign the present observation to a specific state based on energies alone. Assignments based on calculated cross sections are also not possible as the specific mechanism by which the observed excited state was populated is not certain. Excited states with *p* shell proton hole structure are also predicted in this energy region, making them plausible candidates as well. Either an improvement in the predictive power of theoretical calculations or the collection of additional experimental data will be needed before it is possible to assign the presently observed 2500 keV state in ^{27}F to a specific level.

The measurement of the ^{28}F ground state energy is particularly interesting when interpreted in terms of ground state mass systematics and the boundaries of the island of inversion. Until now, there was no experimental data available to indicate whether the island of inversion extends to lower element number than its traditional boundary of $Z = 10$. The present measurement of the ^{28}F binding energy lies between the predictions of the IOI (truncated *sd-pf* model space) and USDA/USDB (*sd* model space) shell models and is consistent with both calculations within their RMS values. The merging of the USDA/USDB and IOI calculations—in contrast to ^{29}Ne, ^{30}Na, and ^{31}Mg—suggests the presence of a "southern shore" of the island of inversion at ^{28}F, and this is confirmed by the binding energy measurement of the present work.

The present results also suggest a number of additional studies which could be useful in clarifying the structure of fluorine nuclei in the vicinity of $N = 20$. Perhaps the most pertinent for determining the bottom edge of the island of inversion is a mass measurement of ^{29}F. As shown in Fig. 6.7, the deviation between USDA/USDB and IOI calculations for the ground state binding of ^{29}Ne is large, so an experimental test of these predictions would provide significant insight into the situation. Furthermore, a measurement of the first excited state energy in ^{29}F would provide much needed information about the size of the $N = 20$ shell gap for fluorine isotopes. It is unlikely that ^{29}F has bound excited states (though a measurement would also be necessary to confirm this assumption); hence measuring its first excited state would require neutron decay spectroscopy

involving two neutron emission.

There are also a few possibilities to expand upon the present measurement of unbound states in ^{27}F and ^{28}F. Since the presently observed resonances have been shown to decay to the ground state of their respective daughter nuclei, one possibility would be to repeat the present measurement without the CAESAR array. The main advantage would be an increase in statistics: removing CAESAR would allow the reaction target to be moved forward, significantly decreasing the neutron shadowing demonstrated in Fig. 5.1 and increasing the detection efficiency for high decay energies. Additionally, inclusion of the recently commissioned Large multi-Institutional Scintillator Array (LISA) [109] in the setup would allow for neutron detection at larger angles, further increasing efficiency at high decay energy. Removal of CAESAR would also allow the Sweeper magnet to be run at higher rigidity as the Sweeper's field was limited in the present experiment to allow the CAESAR PMTs to operate properly. In turn, this allows the incoming beam energy to be optimized for maximum ^{29}Ne production, increasing overall statistics. Finally, it may be possible to populate unbound states in either ^{27}F or ^{28}F by other reaction mechanisms, such as $^{27}\mathrm{F}(d,p)^{28}\mathrm{F}^{(*)}$, $^{27}\mathrm{F}(p,p')^{27}\mathrm{F}^{*}$, $2p$ knockout, $1n$ knockout to ^{28}F, or fragmentation of an intense secondary beam. Depending on specific cross sections and beam rates, each of these reaction mechanisms has the potential to increase overall population rates for the states of interest. Additionally, using (d,p), (p,p'), or $2p$ knockout to populate unbound states could increase the selectivity of the reaction, making it possible to assign observed resonances to specific levels in ^{27}F or ^{28}F.

APPENDIX

Appendix A

CROSS SECTION CALCULATIONS

A.1 ^{27}F Excited State

Table A.1: Average values used in calculating the cross section to $^{27}F^{*}$.

Number of Recorded Reactions:	157 ± 12.5
Ion Chamber Efficiency:	98.93%
Number of Target Nuclei:	1.92×10^{22}
Geometric Acceptence:	$11.66 \pm 0.77\%$
MoNA Efficiency:	77%
Fit Fraction:	$32.93 \pm 14.00\%$
Average Sweeper Efficiency:	$58.32 \pm 0.37\%$
Actual Number of Reactions:	987.37 ± 432.10
Cross Section (mb):	1.54 ± 0.68

Table A.2: Run-by-run values used in calculating the cross section to $^{27}F^{*}$.

Run	Target Scint. Scaler	Live Time	Sweeper Efficiency	^{29}Ne Counted	^{29}Ne Actual
1089	3001020 ± 1732	91.7%	$39.9 \pm 9.9\%$	200 ± 14.1	31317.9 ± 2225.2
1090	4040444 ± 2010	91.6%	$44.3 \pm 8.1\%$	271 ± 16.5	42209.7 ± 2576.4
1091	189262 ± 435	96.9%	$49.5 \pm 60.6\%$	6 ± 2.4	1975.8 ± 810.7
1093	25275536 ± 5027	91.1%	$41.7 \pm 3.3\%$	1575 ± 39.7	242605.4 ± 6139.9
1094	24541327 ± 4953	91.6%	$46.9 \pm 3.6\%$	1582 ± 39.8	244373.5 ± 6172.1
1095	22791135 ± 4774	92.0%	$51.1 \pm 4.2\%$	1392 ± 37.3	212834.0 ± 5729.2
1096	21890982 ± 4678	91.9%	$47.7 \pm 3.9\%$	1304 ± 36.1	200507.3 ± 5576.0
1097	20407576 ± 4517	92.4%	$48.4 \pm 3.9\%$	1297 ± 36.0	195929.6 ± 5464.6
1105	19950460 ± 4466	92.7%	$54.8 \pm 4.4\%$	1225 ± 35.0	184233.9 ± 5286.5
1106	12628284 ± 3553	93.8%	$56.0 \pm 5.4\%$	834 ± 28.9	124168.9 ± 4319.5
1108	17691674 ± 4206	93.2%	$57.3 \pm 4.9\%$	1407 ± 37.5	199581.8 ± 5348.9
1109	17867137 ± 4226	93.8%	$55.2 \pm 4.5\%$	1369 ± 37.0	193730.4 ± 5262.7
1110	17716754 ± 4209	93.7%	$62.7 \pm 5.0\%$	1286 ± 35.9	186514.1 ± 5226.8
1111	16059746 ± 4007	94.3%	$60.1 \pm 4.8\%$	1260 ± 35.5	180875.0 ± 5122.8
1113	4750703 ± 2179	95.0%	$59.1 \pm 8.3\%$	354 ± 18.8	49556.5 ± 2647.0
1114	25168982 ± 5016	90.7%	$52.0 \pm 3.9\%$	1836 ± 42.8	277433.6 ± 6507.3
1115	25160236 ± 5015	90.9%	$60.4 \pm 4.3\%$	1689 ± 41.1	257524.3 ± 6295.5

Table A.2 (cont'd)

1116	15548067 ± 3943	91.6%	54.0 ± 5.1%	926 ± 30.4	145404.8 ± 4798.9
1117	24027531 ± 4901	91.4%	59.3 ± 4.2%	1575 ± 39.7	237691.9 ± 6016.5
1118	21661193 ± 4654	92.8%	58.7 ± 4.3%	1479 ± 38.5	216643.1 ± 5659.6
1119	17135263 ± 4139	94.1%	54.5 ± 4.6%	1214 ± 34.8	173626.0 ± 5007.1
1120	17113386 ± 4136	93.7%	55.7 ± 4.8%	1182 ± 34.4	171097.1 ± 5000.0
1121	14095999 ± 3754	93.9%	54.0 ± 5.0%	1013 ± 31.8	144142.2 ± 4550.7
1122	17641234 ± 4200	92.9%	54.8 ± 4.7%	1292 ± 35.9	187542.4 ± 5243.5
1123	19223693 ± 4384	92.9%	55.8 ± 4.6%	1366 ± 37.0	195480.7 ± 5314.2
1124	22330606 ± 4725	91.8%	59.1 ± 4.1%	1522 ± 39.0	226377.7 ± 5829.8
1125	18688958 ± 4323	92.9%	54.8 ± 4.3%	1417 ± 37.6	203755.2 ± 5440.4
1126	15837226 ± 3979	92.3%	50.4 ± 4.5%	1176 ± 34.3	171328.9 ± 5021.1
1127	19985301 ± 4470	93.0%	51.9 ± 4.1%	1416 ± 37.6	204460.7 ± 5459.5
1128	18085021 ± 4252	93.2%	55.1 ± 4.4%	1420 ± 37.7	197721.8 ± 5273.9
1129	15951827 ± 3993	94.3%	57.9 ± 4.7%	1273 ± 35.7	172301.6 ± 4853.9
1130	2492166 ± 1578	95.0%	38.6 ± 9.5%	171 ± 13.1	24404.5 ± 1875.0
1140	16757226 ± 4093	87.6%	53.1 ± 4.6%	1205 ± 34.7	193735.1 ± 5609.4
1141	13926658 ± 3731	88.3%	56.2 ± 5.2%	1040 ± 32.2	161555.7 ± 5035.4
1143	21910209 ± 4680	84.2%	54.5 ± 4.4%	1485 ± 38.5	237811.5 ± 6199.5
1144	23719230 ± 4870	84.3%	54.8 ± 4.1%	1533 ± 39.2	266120.7 ± 6829.1
1145	21989507 ± 4689	85.1%	51.5 ± 4.0%	1445 ± 38.0	245730.8 ± 6495.2
1146	20372770 ± 4513	85.9%	54.7 ± 4.4%	1400 ± 37.4	235622.1 ± 6328.7
1147	21596655 ± 4647	85.5%	55.8 ± 4.3%	1526 ± 39.1	261159.3 ± 6720.1
1148	15650741 ± 3956	83.4%	53.1 ± 5.0%	1091 ± 33.0	192036.5 ± 5843.8
1149	5868992 ± 2422	84.2%	57.8 ± 8.8%	440 ± 21.0	77004.9 ± 3691.4
1150	24269714 ± 4926	83.8%	60.5 ± 4.3%	1775 ± 42.1	302168.8 ± 7209.8
1151	19513034 ± 4417	85.0%	57.1 ± 4.7%	1552 ± 39.4	254968.9 ± 6508.1
1152	22430111 ± 4736	84.6%	60.0 ± 4.4%	1694 ± 41.2	283908.0 ± 6935.1
1153	19863414 ± 4456	85.2%	63.7 ± 5.0%	1524 ± 39.0	253086.4 ± 6518.3
1154	19033532 ± 4362	86.2%	60.9 ± 4.8%	1431 ± 37.8	235644.5 ± 6262.6
1155	20794627 ± 4560	85.1%	63.5 ± 5.0%	1500 ± 38.7	250472.7 ± 6500.5
1156	22451595 ± 4738	84.3%	63.1 ± 4.7%	1586 ± 39.8	269563.8 ± 6803.2
1157	20948687 ± 4576	84.8%	57.7 ± 4.4%	1477 ± 38.4	251494.4 ± 6577.4
1158	21333904 ± 4618	84.5%	64.5 ± 4.8%	1563 ± 39.5	266312.9 ± 6771.8
1159	20446442 ± 4521	85.7%	66.1 ± 5.3%	1444 ± 38.0	242834.8 ± 6423.0
1160	11803820 ± 3435	87.3%	56.8 ± 5.7%	835 ± 28.9	135507.9 ± 4713.0
1161	20873358 ± 4568	85.9%	63.7 ± 4.9%	1535 ± 39.2	254828.4 ± 6538.4
1162	16189705 ± 4023	87.1%	63.3 ± 5.2%	1213 ± 34.8	194190.1 ± 5604.9
1163	20564885 ± 4534	85.5%	60.1 ± 4.6%	1497 ± 38.7	246009.6 ± 6391.0
1164	7878480 ± 2806	85.9%	60.8 ± 7.0%	602 ± 24.5	97552.5 ± 3997.2
1178	19672213 ± 4435	92.2%	57.5 ± 4.4%	1733 ± 41.6	214828.0 ± 5186.6
1179	17834673 ± 4223	92.6%	59.0 ± 4.6%	1556 ± 39.4	193200.4 ± 4922.5
1180	19197414 ± 4381	92.6%	64.8 ± 4.8%	1807 ± 42.5	216209.7 ± 5112.9
1181	19140691 ± 4375	92.4%	57.5 ± 4.1%	1818 ± 42.6	217485.0 ± 5127.7
1182	20354920 ± 4511	92.1%	60.9 ± 4.4%	1923 ± 43.9	232113.8 ± 5321.1

Table A.2 (cont'd)

1183	22614066 ± 4755	90.9%	59.1 ± 4.2%	2018 ± 44.9	253296.9 ± 5667.5
1184	20477828 ± 4525	91.3%	62.5 ± 4.6%	1824 ± 42.7	228056.2 ± 5367.2
1185	20578329 ± 4536	91.5%	55.0 ± 4.1%	1772 ± 42.1	222769.6 ± 5318.4
1186	19386935 ± 4403	92.0%	55.5 ± 4.3%	1608 ± 40.1	199332.9 ± 4994.6
1187	19010744 ± 4360	92.6%	58.4 ± 4.4%	1569 ± 39.6	194731.2 ± 4939.6
1188	15234289 ± 3903	93.7%	62.4 ± 4.8%	1247 ± 35.3	152597.1 ± 4341.7
1189	2945693 ± 1716	94.5%	68.1 ± 11.1%	232 ± 15.2	29491.2 ± 1945.4
1190	20949406 ± 4577	89.9%	57.5 ± 4.2%	1657 ± 40.7	221344.2 ± 5463.6
1191	25329980 ± 5032	89.7%	57.2 ± 3.9%	2029 ± 45.0	269480.7 ± 6011.3
1192	25537387 ± 5053	89.8%	56.0 ± 3.8%	2016 ± 44.9	265923.2 ± 5950.4
1193	18188870 ± 4264	90.1%	55.0 ± 4.5%	1505 ± 38.8	196188.1 ± 5081.8
1200	23858454 ± 4884	90.7%	59.8 ± 4.3%	2088 ± 45.7	269477.9 ± 5927.8
1201	21881779 ± 4677	90.7%	61.1 ± 4.3%	1998 ± 44.7	258741.0 ± 5819.7
1202	21276721 ± 4612	91.1%	59.6 ± 4.3%	1833 ± 42.8	235270.5 ± 5523.1
1203	20828044 ± 4563	91.6%	60.6 ± 4.2%	1636 ± 40.4	213453.6 ± 5302.2
1204	20387850 ± 4515	91.9%	60.6 ± 4.3%	1655 ± 40.7	213027.4 ± 5261.7
1205	19828325 ± 4452	91.9%	62.6 ± 4.7%	1665 ± 40.8	212022.4 ± 5221.8
1206	21125139 ± 4596	91.8%	59.4 ± 4.4%	1762 ± 42.0	224502.0 ± 5374.6
1207	22280195 ± 4720	91.9%	62.7 ± 4.5%	1768 ± 42.0	226144.2 ± 5403.5
1208	26351043 ± 5133	90.5%	57.2 ± 3.7%	2000 ± 44.7	265713.6 ± 5968.8
1209	23918837 ± 4890	90.7%	58.0 ± 4.1%	1797 ± 42.4	239095.2 ± 5665.9
1210	6372790 ± 2524	91.1%	61.7 ± 8.5%	507 ± 22.5	67020.7 ± 2990.8
1211	17853055 ± 4225	90.4%	57.3 ± 4.8%	1387 ± 37.2	186370.3 ± 5028.0
1212	20277572 ± 4503	91.4%	60.0 ± 4.6%	1531 ± 39.1	206020.4 ± 5289.9
1213	21140403 ± 4597	91.5%	57.3 ± 4.3%	1597 ± 40.0	208358.9 ± 5237.5
1214	22781767 ± 4773	91.3%	58.6 ± 4.2%	1882 ± 43.4	243934.9 ± 5650.6
1215	20588488 ± 4537	91.8%	62.0 ± 4.3%	1730 ± 41.6	220717.1 ± 5332.8
1216	20042146 ± 4476	92.8%	61.0 ± 4.6%	1556 ± 39.4	196403.2 ± 5001.8
1220	22596837 ± 4753	90.5%	58.8 ± 4.2%	2415 ± 49.1	289448.9 ± 5924.3
1221	16165191 ± 4020	92.9%	59.8 ± 4.8%	1761 ± 42.0	198652.3 ± 4761.0
1222	19070486 ± 4366	92.3%	60.5 ± 4.5%	2207 ± 47.0	249994.3 ± 5353.8
1223	19325690 ± 4396	91.4%	60.1 ± 4.3%	1848 ± 43.0	220047.3 ± 5145.6
1225	20909552 ± 4572	91.3%	63.0 ± 4.5%	1502 ± 38.8	261405.1 ± 6783.6
1233	18187898 ± 4264	92.9%	61.6 ± 4.7%	1706 ± 41.3	199869.8 ± 4863.9
1234	21761008 ± 4664	91.8%	61.8 ± 4.4%	1961 ± 44.3	239931.8 ± 5445.7
1235	23146474 ± 4811	90.8%	58.6 ± 4.1%	1957 ± 44.2	249185.6 ± 5660.5
1236	13516906 ± 3676	90.8%	61.1 ± 5.7%	1157 ± 34.0	149798.1 ± 4426.2
1237	21490463 ± 4635	91.2%	54.9 ± 4.0%	1844 ± 42.9	231587.1 ± 5419.7
1238	19105536 ± 4370	91.1%	57.3 ± 4.4%	1652 ± 40.6	207406.0 ± 5128.3
1239	23556654 ± 4853	90.3%	56.6 ± 4.0%	1891 ± 43.5	244735.4 ± 5654.5
1240	22511285 ± 4744	90.7%	59.4 ± 4.1%	1859 ± 43.1	238712.5 ± 5563.3
1241	21297564 ± 4614	91.5%	59.0 ± 4.3%	1756 ± 41.9	222533.5 ± 5336.0
1242	19179082 ± 4379	92.2%	57.6 ± 4.4%	1559 ± 39.5	194173.4 ± 4940.9
1243	24268564 ± 4926	90.9%	57.7 ± 3.9%	1862 ± 43.2	244984.7 ± 5703.6

Table A.2 (cont'd)

1244	24539032 ± 4953	90.5%	55.1 ± 3.8%	1906 ± 43.7	251699.7 ± 5792.2
1245	20324635 ± 4508	92.0%	59.8 ± 4.4%	1580 ± 39.7	203183.3 ± 5135.3
1246	19032078 ± 4362	92.4%	58.0 ± 4.3%	1525 ± 39.1	193178.2 ± 4970.1
1247	8933724 ± 2988	94.0%	55.9 ± 5.9%	719 ± 26.8	88158.2 ± 3303.1
1248	19970394 ± 4468	92.1%	56.7 ± 4.2%	1515 ± 38.9	195149.8 ± 5036.4
1249	19232613 ± 4385	92.4%	53.5 ± 4.1%	1480 ± 38.5	187825.3 ± 4904.5
1250	18142414 ± 4259	92.7%	57.2 ± 4.4%	1400 ± 37.4	176389.5 ± 4735.6
1251	10099094 ± 3177	93.4%	54.2 ± 5.6%	717 ± 26.8	89891.9 ± 3371.1
1258	28323971 ± 5322	90.4%	58.9 ± 3.8%	2346 ± 48.4	299106.6 ± 6205.0
1259	28388250 ± 5328	90.2%	57.9 ± 3.7%	2250 ± 47.4	288505.4 ± 6110.3
1260	22416359 ± 4734	90.6%	59.3 ± 4.2%	1851 ± 43.0	236018.4 ± 5512.2
1261	8040483 ± 2835	90.7%	57.9 ± 6.9%	650 ± 25.5	82188.5 ± 3238.7
1262	24326748 ± 4932	91.5%	58.2 ± 4.0%	1968 ± 44.4	255008.2 ± 5776.1
1263	19628230 ± 4430	92.0%	59.5 ± 4.4%	1694 ± 41.2	209904.9 ± 5125.2
1264	22249854 ± 4716	92.4%	62.6 ± 4.3%	1893 ± 43.5	229400.7 ± 5297.8
1265	18994505 ± 4358	92.9%	55.8 ± 4.2%	1655 ± 40.7	199158.9 ± 4919.5
1266	21764049 ± 4665	91.7%	57.7 ± 4.4%	1919 ± 43.8	237714.7 ± 5453.8
1267	22692282 ± 4763	91.7%	58.2 ± 4.0%	1882 ± 43.4	236056.2 ± 5467.5
1268	19894163 ± 4460	92.7%	56.5 ± 4.3%	1624 ± 40.3	200924.2 ± 5009.3
1269	17044353 ± 4128	93.0%	58.7 ± 4.5%	1368 ± 37.0	167024.0 ± 4536.5
1270	1332497 ± 1154	92.7%	55.4 ± 18.5%	102 ± 10.1	13346.9 ± 1327.7
1271	19664923 ± 4434	91.8%	57.5 ± 4.3%	1622 ± 40.3	203356.0 ± 5073.4
1272	19760737 ± 4445	92.4%	60.6 ± 4.5%	1607 ± 40.1	198574.9 ± 4976.7
1273	10796136 ± 3285	93.5%	65.7 ± 6.4%	924 ± 30.4	111120.8 ± 3673.3
1301	22137675 ± 4705	91.1%	58.2 ± 4.3%	1651 ± 40.6	213825.3 ± 5285.7
1302	20878220 ± 4569	92.0%	59.5 ± 4.3%	1639 ± 40.5	208679.3 ± 5178.4
1303	24360464 ± 4935	91.9%	61.4 ± 4.1%	1997 ± 44.7	255136.1 ± 5736.9
1304	24321781 ± 4931	91.1%	60.7 ± 4.1%	1759 ± 41.9	231993.1 ± 5555.7
1305	7182742 ± 2680	91.7%	67.5 ± 7.7%	568 ± 23.8	75912.5 ± 3200.7
1306	26656131 ± 5162	92.2%	60.6 ± 3.8%	1993 ± 44.6	255867.0 ± 5756.9
1307	25245755 ± 5024	91.8%	58.5 ± 3.9%	1974 ± 44.4	253918.1 ± 5741.6
1308	24413198 ± 4940	91.9%	56.0 ± 3.8%	1870 ± 43.2	240004.4 ± 5575.3
1309	16203154 ± 4025	92.5%	60.1 ± 5.2%	6217 ± 78.8	795445.3 ± 10316.8
1310	28670090 ± 5354	91.8%	62.5 ± 3.9%	2021 ± 45.0	275219.7 ± 6149.2
1311	22870406 ± 4782	91.8%	60.5 ± 4.2%	1570 ± 39.6	211037.6 ± 5348.8
1322	19534132 ± 4419	92.0%	61.8 ± 4.3%	1651 ± 40.6	205993.0 ± 5094.4
1323	20906242 ± 4572	91.5%	61.7 ± 4.2%	1828 ± 42.8	230675.9 ± 5422.7
1324	19428946 ± 4407	92.0%	63.0 ± 4.3%	1619 ± 40.2	202705.8 ± 5062.1
1325	28672792 ± 5354	89.6%	60.2 ± 3.5%	2362 ± 48.6	312490.6 ± 6461.4
1326	25794283 ± 5078	90.0%	57.8 ± 3.8%	2150 ± 46.4	289287.6 ± 6270.6
1327	26064005 ± 5105	90.5%	58.7 ± 3.9%	2111 ± 45.9	279468.3 ± 6112.3
1328	23805045 ± 4879	90.6%	59.9 ± 4.1%	1914 ± 43.7	253670.2 ± 5826.4
1329	11224701 ± 3350	90.6%	59.4 ± 5.8%	869 ± 29.5	116825.2 ± 3981.8
1331	23538523 ± 4851	92.2%	61.0 ± 4.1%	1846 ± 43.0	237044.3 ± 5542.9

Table A.2 (cont'd)

1332	25622670 ± 5061	91.5%	62.0 ± 3.7%	1979 ± 44.5	256977.1 ± 5803.3
1333	25451103 ± 5044	91.3%	58.5 ± 3.9%	2022 ± 45.0	259075.6 ± 5788.5
1334	22669137 ± 4761	91.4%	55.4 ± 3.8%	1809 ± 42.5	231646.2 ± 5471.9
1335	24981509 ± 4998	91.5%	58.9 ± 3.8%	1910 ± 43.7	245197.8 ± 5635.8
1336	23463093 ± 4843	92.0%	58.7 ± 4.0%	1827 ± 42.7	228916.5 ± 5379.8
1337	22452005 ± 4738	91.7%	58.6 ± 4.2%	1836 ± 42.8	231477.4 ± 5427.9
1338	22038360 ± 4694	91.9%	57.0 ± 4.3%	1816 ± 42.6	228725.5 ± 5393.1
1339	21424663 ± 4628	92.1%	58.0 ± 4.4%	1717 ± 41.4	214529.1 ± 5201.3
1340	18608744 ± 4313	92.3%	59.9 ± 4.4%	1501 ± 38.7	187062.9 ± 4850.9

A.2 ^{28}F Ground State

Table A.3: Average values used in calculating the cross section to ^{28}F.

Number of Recorded Reactions:	90 ± 9.5
Ion Chamber Efficiency:	98.93%
Number of Target Nuclei:	1.92×10^{22}
Geometric Acceptence:	33.39 ± 2.41%
MoNA Efficiency:	77%
Fit Fraction:	24.17 ± 6.10%
Average Sweeper Efficiency:	58.32 ± 0.37%
Actual Number of Reactions:	145.08 ± 41.05
Cross Section (mb):	0.23 ± 0.06

Table A.4: Run-by-run values used in calculating the cross section to ^{28}F.

Run	Target Scint. Scaler	Live Time	Sweeper Efficiency	^{29}Ne Counted	^{29}Ne Actual
1089	3001020 ± 1732	91.7%	39.9 ± 9.9%	200 ± 14.1	31317.9 ± 2225.2
1090	4040444 ± 2010	91.6%	44.3 ± 8.1%	271 ± 16.5	42209.7 ± 2576.4
1091	189262 ± 435	96.9%	49.5 ± 60.6%	6 ± 2.4	1975.8 ± 810.7
1093	25275536 ± 5027	91.1%	41.7 ± 3.3%	1575 ± 39.7	242605.4 ± 6139.9
1094	24541327 ± 4953	91.6%	46.9 ± 3.6%	1582 ± 39.8	244373.5 ± 6172.1
1095	22791135 ± 4774	92.0%	51.1 ± 4.2%	1392 ± 37.3	212834.0 ± 5729.2
1096	21890982 ± 4678	91.9%	47.7 ± 3.9%	1304 ± 36.1	200507.3 ± 5576.0
1097	20407576 ± 4517	92.4%	48.4 ± 3.9%	1297 ± 36.0	195929.6 ± 5464.6
1105	19950460 ± 4466	92.7%	54.8 ± 4.4%	1225 ± 35.0	184233.9 ± 5286.5
1106	12628284 ± 3553	93.8%	56.0 ± 5.4%	834 ± 28.9	124168.9 ± 4319.5
1108	17691674 ± 4206	93.2%	57.3 ± 4.9%	1407 ± 37.5	199581.8 ± 5348.9

Table A.4 (cont'd)

1109	17867137 ± 4226	93.8%	55.2 ± 4.5%	1369 ± 37.0	193730.4 ± 5262.7
1110	17716754 ± 4209	93.7%	62.7 ± 5.0%	1286 ± 35.9	186514.1 ± 5226.8
1111	16059746 ± 4007	94.3%	60.1 ± 4.8%	1260 ± 35.5	180875.0 ± 5122.8
1113	4750703 ± 2179	95.0%	59.1 ± 8.3%	354 ± 18.8	49556.5 ± 2647.0
1114	25168982 ± 5016	90.7%	52.0 ± 3.9%	1836 ± 42.8	277433.6 ± 6507.3
1115	25160236 ± 5015	90.9%	60.4 ± 4.3%	1689 ± 41.1	257524.3 ± 6295.5
1116	15548067 ± 3943	91.6%	54.0 ± 5.1%	926 ± 30.4	145404.8 ± 4798.9
1117	24027531 ± 4901	91.4%	59.3 ± 4.2%	1575 ± 39.7	237691.9 ± 6016.5
1118	21661193 ± 4654	92.8%	58.7 ± 4.3%	1479 ± 38.5	216643.1 ± 5659.6
1119	17135263 ± 4139	94.1%	54.5 ± 4.6%	1214 ± 34.8	173626.0 ± 5007.1
1120	17113386 ± 4136	93.7%	55.7 ± 4.8%	1182 ± 34.4	171097.1 ± 5000.0
1121	14095999 ± 3754	93.9%	54.0 ± 5.0%	1013 ± 31.8	144142.2 ± 4550.7
1122	17641234 ± 4200	92.9%	54.8 ± 4.7%	1292 ± 35.9	187542.4 ± 5243.5
1123	19223693 ± 4384	92.9%	55.8 ± 4.6%	1366 ± 37.0	195480.7 ± 5314.2
1124	22330606 ± 4725	91.8%	59.1 ± 4.1%	1522 ± 39.0	226377.7 ± 5829.8
1125	18688958 ± 4323	92.9%	54.8 ± 4.3%	1417 ± 37.6	203755.2 ± 5440.4
1126	15837226 ± 3979	92.3%	50.4 ± 4.5%	1176 ± 34.3	171328.9 ± 5021.1
1127	19985301 ± 4470	93.0%	51.9 ± 4.1%	1416 ± 37.6	204460.7 ± 5459.5
1128	18085021 ± 4252	93.2%	55.1 ± 4.4%	1420 ± 37.7	197721.8 ± 5273.9
1129	15951827 ± 3993	94.3%	57.9 ± 4.7%	1273 ± 35.7	172301.6 ± 4853.9
1130	2492166 ± 1578	95.0%	38.6 ± 9.5%	171 ± 13.1	24404.5 ± 1875.0
1140	16757226 ± 4093	87.6%	53.1 ± 4.6%	1205 ± 34.7	193735.1 ± 5609.4
1141	13926658 ± 3731	88.3%	56.2 ± 5.2%	1040 ± 32.2	161555.7 ± 5035.4
1143	21910209 ± 4680	84.2%	54.5 ± 4.4%	1485 ± 38.5	237811.5 ± 6199.5
1144	23719230 ± 4870	84.3%	54.8 ± 4.1%	1533 ± 39.2	266120.7 ± 6829.1
1145	21989507 ± 4689	85.1%	51.5 ± 4.0%	1445 ± 38.0	245730.8 ± 6495.2
1146	20372770 ± 4513	85.9%	54.7 ± 4.4%	1400 ± 37.4	235622.1 ± 6328.7
1147	21596655 ± 4647	85.5%	55.8 ± 4.3%	1526 ± 39.1	261159.3 ± 6720.1
1148	15650741 ± 3956	83.4%	53.1 ± 5.0%	1091 ± 33.0	192036.5 ± 5843.8
1149	5868992 ± 2422	84.2%	57.8 ± 8.8%	440 ± 21.0	77004.9 ± 3691.4
1150	24269714 ± 4926	83.8%	60.5 ± 4.3%	1775 ± 42.1	302168.8 ± 7209.8
1151	19513034 ± 4417	85.0%	57.1 ± 4.7%	1552 ± 39.4	254968.9 ± 6508.1
1152	22430111 ± 4736	84.6%	60.0 ± 4.4%	1694 ± 41.2	283908.0 ± 6935.1
1153	19863414 ± 4456	85.2%	63.7 ± 5.0%	1524 ± 39.0	253086.4 ± 6518.3
1154	19033532 ± 4362	86.2%	60.9 ± 4.8%	1431 ± 37.8	235644.5 ± 6262.6
1155	20794627 ± 4560	85.1%	63.5 ± 5.0%	1500 ± 38.7	250472.7 ± 6500.5
1156	22451595 ± 4738	84.3%	63.1 ± 4.7%	1586 ± 39.8	269563.8 ± 6803.2
1157	20948687 ± 4576	84.8%	57.7 ± 4.4%	1477 ± 38.4	251494.4 ± 6577.4
1158	21333904 ± 4618	84.5%	64.5 ± 4.8%	1563 ± 39.5	266312.9 ± 6771.8
1159	20446442 ± 4521	85.7%	66.1 ± 5.3%	1444 ± 38.0	242834.8 ± 6423.0
1160	11803820 ± 3435	87.3%	56.8 ± 5.7%	835 ± 28.9	135507.9 ± 4713.0
1161	20873358 ± 4568	85.9%	63.7 ± 4.9%	1535 ± 39.2	254828.4 ± 6538.4
1162	16189705 ± 4023	87.1%	63.3 ± 5.2%	1213 ± 34.8	194190.1 ± 5604.9
1163	20564885 ± 4534	85.5%	60.1 ± 4.6%	1497 ± 38.7	246009.6 ± 6391.0

Table A.4 (cont'd)

1164	7878480 ± 2806	85.9%	60.8 ± 7.0%	602 ± 24.5	97552.5 ± 3997.2
1178	19672213 ± 4435	92.2%	57.5 ± 4.4%	1733 ± 41.6	214828.0 ± 5186.6
1179	17834673 ± 4223	92.6%	59.0 ± 4.6%	1556 ± 39.4	193200.4 ± 4922.5
1180	19197414 ± 4381	92.6%	64.8 ± 4.8%	1807 ± 42.5	216209.7 ± 5112.9
1181	19140691 ± 4375	92.4%	57.5 ± 4.1%	1818 ± 42.6	217485.0 ± 5127.7
1182	20354920 ± 4511	92.1%	60.9 ± 4.4%	1923 ± 43.9	232113.8 ± 5321.1
1183	22614066 ± 4755	90.9%	59.1 ± 4.2%	2018 ± 44.9	253296.9 ± 5667.5
1184	20477828 ± 4525	91.3%	62.5 ± 4.6%	1824 ± 42.7	228056.2 ± 5367.2
1185	20578329 ± 4536	91.5%	55.0 ± 4.1%	1772 ± 42.1	222769.6 ± 5318.4
1186	19386935 ± 4403	92.0%	55.5 ± 4.3%	1608 ± 40.1	199332.9 ± 4994.6
1187	19010744 ± 4360	92.6%	58.4 ± 4.4%	1569 ± 39.6	194731.2 ± 4939.6
1188	15234289 ± 3903	93.7%	62.4 ± 4.8%	1247 ± 35.3	152597.1 ± 4341.7
1189	2945693 ± 1716	94.5%	68.1 ± 11.1%	232 ± 15.2	29491.2 ± 1945.4
1190	20949406 ± 4577	89.9%	57.5 ± 4.2%	1657 ± 40.7	221344.2 ± 5463.6
1191	25329980 ± 5032	89.7%	57.2 ± 3.9%	2029 ± 45.0	269480.7 ± 6011.3
1192	25537387 ± 5053	89.8%	56.0 ± 3.8%	2016 ± 44.9	265923.2 ± 5950.4
1193	18188870 ± 4264	90.1%	55.0 ± 4.5%	1505 ± 38.8	196188.1 ± 5081.8
1200	23858454 ± 4884	90.7%	59.8 ± 4.3%	2088 ± 45.7	269477.9 ± 5927.8
1201	21881779 ± 4677	90.7%	61.1 ± 4.3%	1998 ± 44.7	258741.0 ± 5819.7
1202	21276721 ± 4612	91.1%	59.6 ± 4.3%	1833 ± 42.8	235270.5 ± 5523.1
1203	20828044 ± 4563	91.6%	60.6 ± 4.2%	1636 ± 40.4	213453.6 ± 5302.2
1204	20387850 ± 4515	91.9%	60.6 ± 4.3%	1655 ± 40.7	213027.4 ± 5261.7
1205	19828325 ± 4452	91.9%	62.6 ± 4.7%	1665 ± 40.8	212022.4 ± 5221.8
1206	21125139 ± 4596	91.8%	59.4 ± 4.4%	1762 ± 42.0	224502.0 ± 5374.6
1207	22280195 ± 4720	91.9%	62.7 ± 4.5%	1768 ± 42.0	226144.2 ± 5403.5
1208	26351043 ± 5133	90.5%	57.2 ± 3.7%	2000 ± 44.7	265713.6 ± 5968.8
1209	23918837 ± 4890	90.7%	58.0 ± 4.1%	1797 ± 42.4	239095.2 ± 5665.9
1210	6372790 ± 2524	91.1%	61.7 ± 8.5%	507 ± 22.5	67020.7 ± 2990.8
1211	17853055 ± 4225	90.4%	57.3 ± 4.8%	1387 ± 37.2	186370.3 ± 5028.0
1212	20277572 ± 4503	91.4%	60.0 ± 4.6%	1531 ± 39.1	206020.4 ± 5289.9
1213	21140403 ± 4597	91.5%	57.3 ± 4.3%	1597 ± 40.0	208358.9 ± 5237.5
1214	22781767 ± 4773	91.3%	58.6 ± 4.2%	1882 ± 43.4	243934.9 ± 5650.6
1215	20588488 ± 4537	91.8%	62.0 ± 4.3%	1730 ± 41.6	220717.1 ± 5332.8
1216	20042146 ± 4476	92.8%	61.0 ± 4.6%	1556 ± 39.4	196403.2 ± 5001.8
1220	22596837 ± 4753	90.5%	58.8 ± 4.2%	2415 ± 49.1	289448.9 ± 5924.3
1221	16165191 ± 4020	92.9%	59.8 ± 4.8%	1761 ± 42.0	198652.3 ± 4761.0
1222	19070486 ± 4366	92.3%	60.5 ± 4.5%	2207 ± 47.0	249994.3 ± 5353.8
1223	19325690 ± 4396	91.4%	60.1 ± 4.3%	1848 ± 43.0	220047.3 ± 5145.6
1225	20909552 ± 4572	91.3%	63.0 ± 4.5%	1502 ± 38.8	261405.1 ± 6783.6
1233	18187898 ± 4264	92.9%	61.6 ± 4.7%	1706 ± 41.3	199869.8 ± 4863.9
1234	21761008 ± 4664	91.8%	61.8 ± 4.4%	1961 ± 44.3	239931.8 ± 5445.7
1235	23146474 ± 4811	90.8%	58.6 ± 4.1%	1957 ± 44.2	249185.6 ± 5660.5
1236	13516906 ± 3676	90.8%	61.1 ± 5.7%	1157 ± 34.0	149798.1 ± 4426.2
1237	21490463 ± 4635	91.2%	54.9 ± 4.0%	1844 ± 42.9	231587.1 ± 5419.7

Table A.4 (cont'd)

1238	19105536 ± 4370	91.1%	57.3 ± 4.4%	1652 ± 40.6	207406.0 ± 5128.3
1239	23556654 ± 4853	90.3%	56.6 ± 4.0%	1891 ± 43.5	244735.4 ± 5654.5
1240	22511285 ± 4744	90.7%	59.4 ± 4.1%	1859 ± 43.1	238712.5 ± 5563.3
1241	21297564 ± 4614	91.5%	59.0 ± 4.3%	1756 ± 41.9	222533.5 ± 5336.0
1242	19179082 ± 4379	92.2%	57.6 ± 4.4%	1559 ± 39.5	194173.4 ± 4940.9
1243	24268564 ± 4926	90.9%	57.7 ± 3.9%	1862 ± 43.2	244984.7 ± 5703.6
1244	24539032 ± 4953	90.5%	55.1 ± 3.8%	1906 ± 43.7	251699.7 ± 5792.2
1245	20324635 ± 4508	92.0%	59.8 ± 4.4%	1580 ± 39.7	203183.3 ± 5135.3
1246	19032078 ± 4362	92.4%	58.0 ± 4.3%	1525 ± 39.1	193178.2 ± 4970.1
1247	8933724 ± 2988	94.0%	55.9 ± 5.9%	719 ± 26.8	88158.2 ± 3303.1
1248	19970394 ± 4468	92.1%	56.7 ± 4.2%	1515 ± 38.9	195149.8 ± 5036.4
1249	19232613 ± 4385	92.4%	53.5 ± 4.1%	1480 ± 38.5	187825.3 ± 4904.5
1250	18142414 ± 4259	92.7%	57.2 ± 4.4%	1400 ± 37.4	176389.5 ± 4735.6
1251	10099094 ± 3177	93.4%	54.2 ± 5.6%	717 ± 26.8	89891.9 ± 3371.1
1258	28323971 ± 5322	90.4%	58.9 ± 3.8%	2346 ± 48.4	299106.6 ± 6205.0
1259	28388250 ± 5328	90.2%	57.9 ± 3.7%	2250 ± 47.4	288505.4 ± 6110.3
1260	22416359 ± 4734	90.6%	59.3 ± 4.2%	1851 ± 43.0	236018.4 ± 5512.2
1261	8040483 ± 2835	90.7%	57.9 ± 6.9%	650 ± 25.5	82188.5 ± 3238.7
1262	24326748 ± 4932	91.5%	58.2 ± 4.0%	1968 ± 44.4	255008.2 ± 5776.1
1263	19628230 ± 4430	92.0%	59.5 ± 4.4%	1694 ± 41.2	209904.9 ± 5125.2
1264	22249854 ± 4716	92.4%	62.6 ± 4.3%	1893 ± 43.5	229400.7 ± 5297.8
1265	18994505 ± 4358	92.9%	55.8 ± 4.2%	1655 ± 40.7	199158.9 ± 4919.5
1266	21764049 ± 4665	91.7%	57.7 ± 4.4%	1919 ± 43.8	237714.7 ± 5453.8
1267	22692282 ± 4763	91.7%	58.2 ± 4.0%	1882 ± 43.4	236056.2 ± 5467.5
1268	19894163 ± 4460	92.7%	56.5 ± 4.3%	1624 ± 40.3	200924.2 ± 5009.3
1269	17044353 ± 4128	93.0%	58.7 ± 4.5%	1368 ± 37.0	167024.0 ± 4536.5
1270	1332497 ± 1154	92.7%	55.4 ± 18.5%	102 ± 10.1	13346.9 ± 1327.7
1271	19664923 ± 4434	91.8%	57.5 ± 4.3%	1622 ± 40.3	203356.0 ± 5073.4
1272	19760737 ± 4445	92.4%	60.6 ± 4.5%	1607 ± 40.1	198574.9 ± 4976.7
1273	10796136 ± 3285	93.5%	65.7 ± 6.4%	924 ± 30.4	111120.8 ± 3673.3
1301	22137675 ± 4705	91.1%	58.2 ± 4.3%	1651 ± 40.6	213825.3 ± 5285.7
1302	20878220 ± 4569	92.0%	59.5 ± 4.3%	1639 ± 40.5	208679.3 ± 5178.4
1303	24360464 ± 4935	91.9%	61.4 ± 4.1%	1997 ± 44.7	255136.1 ± 5736.9
1304	24321781 ± 4931	91.1%	60.7 ± 4.1%	1759 ± 41.9	231993.1 ± 5555.7
1305	7182742 ± 2680	91.7%	67.5 ± 7.7%	568 ± 23.8	75912.5 ± 3200.7
1306	26656131 ± 5162	92.2%	60.6 ± 3.8%	1993 ± 44.6	255867.0 ± 5756.9
1307	25245755 ± 5024	91.8%	58.5 ± 3.9%	1974 ± 44.4	253918.1 ± 5741.6
1308	24413198 ± 4940	91.9%	56.0 ± 3.8%	1870 ± 43.2	240004.4 ± 5575.3
1309	16203154 ± 4025	92.5%	60.1 ± 5.2%	6217 ± 78.8	795445.3 ± 10316.8
1310	28670090 ± 5354	91.8%	62.5 ± 3.9%	2021 ± 45.0	275219.7 ± 6149.2
1311	22870406 ± 4782	91.8%	60.5 ± 4.2%	1570 ± 39.6	211037.6 ± 5348.8
1322	19534132 ± 4419	92.0%	61.8 ± 4.3%	1651 ± 40.6	205993.0 ± 5094.4
1323	20906242 ± 4572	91.5%	61.7 ± 4.2%	1828 ± 42.8	230675.9 ± 5422.7
1324	19428946 ± 4407	92.0%	63.0 ± 4.3%	1619 ± 40.2	202705.8 ± 5062.1

Table A.4 (cont'd)

1325	28672792 ± 5354	89.6%	60.2 ± 3.5%	2362 ± 48.6	312490.6 ± 6461.4
1326	25794283 ± 5078	90.0%	57.8 ± 3.8%	2150 ± 46.4	289287.6 ± 6270.6
1327	26064005 ± 5105	90.5%	58.7 ± 3.9%	2111 ± 45.9	279468.3 ± 6112.3
1328	23805045 ± 4879	90.6%	59.9 ± 4.1%	1914 ± 43.7	253670.2 ± 5826.4
1329	11224701 ± 3350	90.6%	59.4 ± 5.8%	869 ± 29.5	116825.2 ± 3981.8
1331	23538523 ± 4851	92.2%	61.0 ± 4.1%	1846 ± 43.0	237044.3 ± 5542.9
1332	25622670 ± 5061	91.5%	62.0 ± 3.7%	1979 ± 44.5	256977.1 ± 5803.3
1333	25451103 ± 5044	91.3%	58.5 ± 3.9%	2022 ± 45.0	259075.6 ± 5788.5
1334	22669137 ± 4761	91.4%	55.4 ± 3.8%	1809 ± 42.5	231646.2 ± 5471.9
1335	24981509 ± 4998	91.5%	58.9 ± 3.8%	1910 ± 43.7	245197.8 ± 5635.8
1336	23463093 ± 4843	92.0%	58.7 ± 4.0%	1827 ± 42.7	228916.5 ± 5379.8
1337	22452005 ± 4738	91.7%	58.6 ± 4.2%	1836 ± 42.8	231477.4 ± 5427.9
1338	22038360 ± 4694	91.9%	57.0 ± 4.3%	1816 ± 42.6	228725.5 ± 5393.1
1339	21424663 ± 4628	92.1%	58.0 ± 4.4%	1717 ± 41.4	214529.1 ± 5201.3
1340	18608744 ± 4313	92.3%	59.9 ± 4.4%	1501 ± 38.7	187062.9 ± 4850.9

REFERENCES

REFERENCES

[1] Maria Goeppert-Mayer. *The shell model* (1963). Nobel Lectures, Physics 1963–1970. http://tinyurl.com/nobel-lectures/mayer-lecture.pdf

[2] Elsasser, W. M. *Sur le principe de Pauli dans les noyaux*. J. Phys. Radium, **4**, no. 10 (1933), 549. http://dx.doi.org/10.1051/jphysrad:01933004010054900

[3] O. Sorlin and M.-G. Porquet. *Nuclear magic numbers: New features far from stability*. Progress in Particle and Nuclear Physics, **61**, no. 2 (2008), 602 . ISSN 0146-6410. http://dx.doi.org/10.1016/j.ppnp.2008.05.001

[4] Maria Goeppert-Mayer. *On closed shells in nuclei*. Phys. Rev., **74**, no. 3 (1948), 235. http://dx.doi.org/10.1103/PhysRev.74.235

[5] Maria Goeppert-Mayer. *On closed shells in nuclei. II*. Phys. Rev., **75**, no. 12 (1949), 1969. http://dx.doi.org/10.1103/PhysRev.75.1969

[6] Otto Haxel, J. Hans D. Jensen, and Hans E. Suess. *On the "magic numbers" in nuclear structure*. Phys. Rev., **75**, no. 11 (1949), 1766. http://dx.doi.org/10.1103/PhysRev.75.1766.2

[7] Roger D. Woods and David S. Saxon. *Diffuse surface optical model for nucleon–nuclei scattering*. Phys. Rev., **95**, no. 2 (1954), 577. http://dx.doi.org/10.1103/PhysRev.95.577

[8] C. Thibault, R. Klapisch, C. Rigaud, A. M. Poskanzer, R. Prieels, L. Lessard, and W. Reisdorf. *Direct measurement of the masses of ^{11}Li and $^{26-32}$Na with an on-line mass spectrometer*. Phys. Rev. C, **12**, no. 2 (1975), 644. http://dx.doi.org/10.1103/PhysRevC.12.644

[9] G. Huber, F. Touchard, S. Büttgenbach, C. Thibault, R. Klapisch, H. T. Duong, S. Liberman, J. Pinard, J. L. Vialle, P. Juncar, and P. Jacquinot. *Spins, magnetic moments, and isotope shifts of $^{21-31}$Na by high resolution laser spectroscopy of the atomic D_1 line*. Phys. Rev. C, **18**, no. 5 (1978), 2342. http://dx.doi.org/10.1103/PhysRevC.18.2342

[10] C. Détraz, D. Guillemaud, G. Huber, R. Klapisch, M. Langevin, F. Naulin, C. Thibault, L. C. Carraz, and F. Touchard. *Beta decay of $^{27-32}$Na and their descendants*. Phys. Rev. C, **19**, no. 1 (1979), 164. http://dx.doi.org/10.1103/PhysRevC.19.164

[11] D. Guillemaud-Mueller, C. Detraz, M. Langevin, F. Naulin, M. de Saint-Simon, C. Thibault, F. Touchard, and M. Epherre. *$\beta-$decay schemes of very neutron–rich sodium isotopes and their descendants*. Nuclear Physics A, **426**, no. 1 (1984), 37 . ISSN 0375-9474. http://dx.doi.org/10.1016/0375-9474(84)90064-2

[12] G. Audi, A. H. Wapstra, and C. Thibault. *The 2003 atomic mass evaluation: (II). Tables, graphs and references*. Nuclear Physics A, **729**, no. 1 (2003), 337 . ISSN 0375-9474. The 2003 NUBASE and Atomic Mass Evaluations.
http://dx.doi.org/10.1016/j.nuclphysa.2003.11.003

[13] R. Klapisch, J. Chaumont, C. Philippe, I. Amarel, R. Fergeau, M. Salome, and R. Bernas. *Spectrometre de masse en ligne pour l'etude d'isotopes de tres courtes periodes produits par reactions nucleaires*. Nuclear Instruments and Methods, **53** (1967), 216 . ISSN 0029-554X.
http://dx.doi.org/10.1016/0029-554X(67)91358-4

[14] P. Fallon, E. Rodriguez-Vieitez, A. O. Macchiavelli, A. Gade, J. A. Tostevin, P. Adrich, D. Bazin, M. Bowen, C. M. Campbell, R. M. Clark, J. M. Cook, M. Cromaz, D. C. Dinca, T. Glasmacher, I. Y. Lee, S. McDaniel, W. F. Mueller, S. G. Prussin, A. Ratkiewicz, K. Siwek, J. R. Terry, D. Weisshaar, M. Wiedeking, K. Yoneda, B. A. Brown, T. Otsuka, and Y. Utsuno. *Two-proton knockout from ^{32}Mg: Intruder amplitudes in ^{30}Ne and implications for the binding of $^{29,31}F$*. Phys. Rev. C, **81**, no. 4 (2010), 041302.
http://dx.doi.org/10.1103/PhysRevC.81.041302

[15] Y Yanagisawa, M Notani, H Sakurai, M Kunibu, H Akiyoshi, N Aoi, H Baba, K Demichi, N Fukuda, H Hasegawa, Y Higurashi, M Ishihara, N Iwasa, H Iwasaki, T Gomi, S Kanno, M Kurokawa, Y.U Matsuyama, S Michimasa, T Minemura, T Mizoi, T Nakamura, A Saito, M Serata, S Shimoura, T Sugimoto, E Takeshita, S Takeuchi, K Ue, K Yamada, K Yoneda, and T Motobayashi. *The first excited state of ^{30}Ne studied by proton inelastic scattering in reversed kinematics*. Physics Letters B, **566**, no. 1-2 (2003), 84 . ISSN 0370-2693.
http://dx.doi.org/10.1016/S0370-2693(03)00802-5

[16] P. M. Endt. *Supplement to energy levels of A = 21-44 nuclei (VII)*. Nuclear Physics A, **633**, no. 1 (1998), 1 . ISSN 0375-9474.
http://dx.doi.org/10.1016/S0375-9474(97)00613-1

[17] John A. Cameron and Balraj Singh. *Nuclear data sheets for A = 38*. Nuclear Data Sheets, **109**, no. 1 (2008), 1 . ISSN 0090-3752.
http://dx.doi.org/10.1016/j.nds.2007.12.001

[18] John A. Cameron and Balraj Singh. *Nuclear data sheets for A = 40*. Nuclear Data Sheets, **102**, no. 2 (2004), 293 . ISSN 0090-3752.
http://dx.doi.org/10.1016/j.nds.2004.06.001

[19] Anonymous. *Cumulated index to A–chains*. Nuclear Data Sheets, **112**, no. 6 (2011), ii . ISSN 0090-3752.
http://dx.doi.org/10.1016/S0090-3752(11)00050-0

[20] Magdalena Kowalska. *Ground state properties of neutron–rich Mg isotopes—the "island of inversion" studied with laser and β–NMR spectroscopy*. Ph.D. thesis, Johannes Gutenberg Universität, Mainz, Germany (2006).
http://cdsweb.cern.ch/record/983758/files/

[21] Takaharu Otsuka. *The euroschool lectures on physics with exotic beams*, volume III, chapter 1. Springer-Verlag, Heidelberg (2009), pages 19–25.
http://dx.doi.org/10.1007/978-3-540-85839-3

[22] Yutaka Utsuno, Takaharu Otsuka, Takahiro Mizusaki, and Michio Honma. *Varying shell gap and deformation in $N \sim 20$ unstable nuclei studied by the Monte Carlo shell model*. Phys. Rev. C, **60**, no. 5 (1999), 054315.
http://dx.doi.org/10.1103/PhysRevC.60.054315

[23] B A Brown and B H Wildenthal. *Status of the nuclear shell model*. Annual Review of Nuclear and Particle Science, **38**, no. 1 (1988), 29.
http://dx.doi.org/10.1146/annurev.ns.38.120188.000333

[24] T. T. S. Kuo and G. E. Brown. *Reaction matrix elements for the $0f$–$1p$ shell nuclei*. Nuclear Physics A, **114**, no. 2 (1968), 241 . ISSN 0375-9474.
http://dx.doi.org/10.1016/0375-9474(68)90353-9

[25] E. K. Warburton, D. E. Alburger, J. A. Becker, B. A. Brown, and S. Raman. *Probe of the shell crossing at $A = 40$ via beta decay: Experiment and theory*. Phys. Rev. C, **34**, no. 3 (1986), 1031.
http://dx.doi.org/10.1103/PhysRevC.34.1031

[26] D.J. Millener and D. Kurath. *The particle-hole interaction and the beta decay of ^{14}B*. Nuclear Physics A, **255**, no. 2 (1975), 315 . ISSN 0375-9474.
http://dx.doi.org/10.1016/0375-9474(75)90683-1

[27] Takaharu Otsuka, Toshio Suzuki, Rintaro Fujimoto, Hubert Grawe, and Yoshinori Akaishi. *Evolution of nuclear shells due to the tensor force*. Phys. Rev. Lett., **95**, no. 23 (2005), 232502.
http://dx.doi.org/10.1103/PhysRevLett.95.232502

[28] Takaharu Otsuka, Rintaro Fujimoto, Yutaka Utsuno, B. Alex Brown, Michio Honma, and Takahiro Mizusaki. *Magic numbers in exotic nuclei and spin-isospin properties of the NN interaction*. Phys. Rev. Lett., **87**, no. 8 (2001), 082502.
http://dx.doi.org/10.1103/PhysRevLett.87.082502

[29] Takaharu Otsuka, Toshiaki Matsuo, and Daisuke Abe. *Mean field with tensor force and shell structure of exotic nuclei*. Phys. Rev. Lett., **97**, no. 16 (2006), 162501.
http://dx.doi.org/10.1103/PhysRevLett.97.162501

[30] Yutaka Utsuno, Takaharu Otsuka, Thomas Glasmacher, Takahiro Mizusaki, and Michio Honma. *Onset of intruder ground state in exotic Na isotopes and evolution of the $N = 20$ shell gap*. Phys. Rev. C, **70**, no. 4 (2004), 044307.
http://dx.doi.org/10.1103/PhysRevC.70.044307

[31] A. Poves and J. Retamosa. *The onset of deformation at the $N = 20$ neutron shell closure far from stability*. Physics Letters B, **184**, no. 4 (1987), 311 . ISSN 0370-2693.
http://dx.doi.org/10.1016/0370-2693(87)90171-7

[32] E. Caurier, F. Nowacki, and A. Poves. *Large-scale shell model calculations for exotic nuclei*. The European Physical Journal A - Hadrons and Nuclei, **15** (2002), 145. ISSN 1434-6001. 10.1140/epja/i2001-10243-7.
http://dx.doi.org/10.1140/epja/i2001-10243-7

[33] F. Sarazin, H. Savajols, W. Mittig, F. Nowacki, N. A. Orr, Z. Ren, P. Roussel-Chomaz, G. Auger, D. Baiborodin, A. V. Belozyorov, C. Borcea, E. Caurier, Z. Dlouhý, A. Gillibert, A. S. Lalleman, M. Lewitowicz, S. M. Lukyanov, F. de Oliveira, Y. E. Penionzhkevich, D. Ridikas, H. Sakuraï, O. Tarasov, and A. de Vismes. *Shape coexistence and the $N = 28$ shell closure far from stability*. Phys. Rev. Lett., **84**, no. 22 (2000), 5062.
http://dx.doi.org/10.1103/PhysRevLett.84.5062

[34] Yutaka Utsuno, Takaharu Otsuka, Takahiro Mizusaki, and Michio Honma. *Extreme location of F drip line and disappearance of the $N = 20$ magic structure*. Phys. Rev. C, **64**, no. 1 (2001), 011301.
http://dx.doi.org/10.1103/PhysRevC.64.011301

[35] T. Baumann, A. M. Amthor, D. Bazin, B. A. Brown, C. M. Folden III, A. Gade, T. N. Ginter, M. Hausmann, M. Matos, D. J. Morrissey, M. Portillo, A. Schiller, B. M. Sherrill, A. Stolz, O. B. Tarasov, and M. Thoennessen. *Discovery of ^{40}Mg and ^{42}Al suggests neutron drip-line slant towards heavier isotopes*. Nature, **449** (2007), 1022 .
http://dx.doi.org/10.1038/nature06213

[36] T. Otsuka, M. Honma, T. Mizusaki, N. Shimizu, and Y. Utsuno. *Monte carlo shell model for atomic nuclei*. Progress in Particle and Nuclear Physics, **47**, no. 1 (2001), 319 . ISSN 0146-6410.
http://dx.doi.org/10.1016/S0146-6410(01)00157-0

[37] H. Sakurai, S. M. Lukyanov, M. Notani, N. Aoi, D. Beaumel, N. Fukuda, M. Hirai, E. Ideguchi, N. Imai, M. Ishihara, H. Iwasaki, T. Kubo, K. Kusaka, H. Kumagai, T. Nakamura, H. Ogawa, Yu. E. Penionzhkevich, T. Teranishi, Y. X. Watanabe, K. Yoneda, and A. Yoshida. *Evidence for particle stability of ^{31}F and particle instability of ^{25}N and ^{28}O*. Physics Letters B, **448**, no. 3-4 (1999), 180 . ISSN 0370-2693.
http://dx.doi.org/10.1016/S0370-2693(99)00015-5

[38] O. Tarasov, R. Allatt, J. C. Angélique, R. Anne, C. Borcea, Z. Dlouhý, C. Donzaud, S. Grévy, D. Guillemaud-Mueller, M. Lewitowicz, S. Lukyanov, A. C. Mueller, F. Nowacki, Yu. Oganessian, N. A. Orr, A. N. Ostrowski, R. D. Page, Yu. Penionzhkevich, F. Pougheon, A. Reed, M. G. Saint-Laurent, W. Schwab, E. Sokol, O. Sorlin, W. Trinder, and J. S. Winfield. *Search for ^{28}O and study of neutron-rich nuclei near the N = 20 shell closure*. Physics Letters B, **409**, no. 1-4 (1997), 64 . ISSN 0370-2693.
http://dx.doi.org/10.1016/S0370-2693(97)00901-5

[39] M. Langevin, E. Quiniou, M. Bernas, J. Galin, J. C. Jacmart, F. Naulin, F. Pougheon, R. Anne, C. Détraz, D. Guerreau, D. Guillemaud-Mueller, and A. C. Mueller. *Production of neutron-rich nuclei at the limits of particles stability by fragmentation of 44 MeV/u ^{40}Ar projectiles*. Physics Letters B, **150**, no. 1-3 (1985), 71 . ISSN 0370-2693.
http://dx.doi.org/10.1016/0370-2693(85)90140-6

[40] D. Guillemaud-Mueller, J. C. Jacmart, E. Kashy, A. Latimier, A. C. Mueller, F. Pougheon, A. Richard, Yu. E. Penionzhkevich, A. G. Artuhk, A. V. Belozyorov, S. M. Lukyanov, R. Anne, P. Bricault, C. Détraz, M. Lewitowicz, Y. Zhang, Yu. S. Lyutostansky, M. V. Zverev, D. Bazin, and W. D. Schmidt-Ott. *Particle stability of the isotopes ^{26}O and ^{32}Ne in the reaction 44 MeV/nucleon $^{48}Ca+Ta$.* Phys. Rev. C, **41**, no. 3 (1990), 937.
http://dx.doi.org/10.1103/PhysRevC.41.937

[41] M. Fauerbach, D. J. Morrissey, W. Benenson, B. A. Brown, M. Hellström, J. H. Kelley, R. A. Kryger, R. Pfaff, C. F. Powell, and B. M. Sherrill. *New search for ^{26}O.* Phys. Rev. C, **53**, no. 2 (1996), 647.
http://dx.doi.org/10.1103/PhysRevC.53.647

[42] Z Dlouhý, Yu Penionzhkevich, R Anne, D Baiborodin, C Borcea, A Fomichev, D Guillemaud Mueller, R Kalpakchieva, M Lewitowicz, S Lukyanov, A C Mueller, Yu Oganessian, R D Page, A Reed, M G Saint-Laurent, E Sokol, N Skobelev, O Sorlin, O Tarasov, V Toneev, and W Trinder. *Dripline nuclei produced by quasi–fragmentation of the $^{32,34,36}S$ primary beams*. Journal of Physics G: Nuclear and Particle Physics, **25**, no. 4 (1999), 859.
http://stacks.iop.org/0954-3899/25/i=4/a=055

[43] S. Lukyanov and Yu. Penionzhkevich. *The neutron drip line in the region of $N = 20$ and $N = 28$ closures*. Physics of Atomic Nuclei, **67** (2004), 1627. ISSN 1063-7788. 10.1134/1.1802348.
http://dx.doi.org/10.1134/1.1802348

[44] T. Kubo, M. Ishihara, N. Inabe, H. Kumagai, I. Tanihata, K. Yoshida, T. Nakamura, H. Okuno, S. Shimoura, and K. Asahi. *The RIKEN radioactive beam facility*. Nuclear Instruments and Methods in Physics Research Section B: Beam Interactions with Materials and Atoms, **70**, no. 1-4 (1992), 309 . ISSN 0168-583X.
http://dx.doi.org/10.1016/0168-583X(92)95947-P

[45] Z. Elekes, Zs. Dombrádi, A. Saito, N. Aoi, H. Baba, K. Demichi, Zs. Fülöp, J. Gibelin, T. Gomi, H. Hasegawa, N. Imai, M. Ishihara, H. Iwasaki, S. Kanno, S. Kawai, T. Kishida, T. Kubo, K. Kurita, Y. Matsuyama, S. Michimasa, T. Minemura, T. Motobayashi, M. Notani, T. Ohnishi, H.J. Ong, S. Ota, A. Ozawa, H.K. Sakai, H. Sakurai, S. Shimoura, E. Takeshita, S. Takeuchi, M. Tamaki, Y. Togano, K. Yamada, Y. Yanagisawa, and K. Yoneda. *Bound excited states in ^{27}F.* Physics Letters B, **599**, no. 1-2 (2004), 17 . ISSN 0370-2693.
http://dx.doi.org/10.1016/j.physletb.2004.08.028

[46] N. Frank, D. Albertson, J. Bailey, T. Baumann, D. Bazin, B. A. Brown, J. Brown, P.A. DeYoung, J.E. Finck, A. Gade, J. Hinnefeld, R. Howes, M. Kasperczyk, J-L. Lecouey, B. Luther, W. A. Peters, H. Scheit, A. Schiller, A. Smith, M. Thoennessen, and J. Tostevin. *Neutron unbound states in $^{25,26}F$* (2011). Submitted for publication in Phys. Rev. C.

[47] D. Bazin, J. A. Caggiano, B. M. Sherrill, J. Yurkon, and A. Zeller. *The S800 spectrograph*. Nuclear Instruments and Methods in Physics Research Section B: Beam Interactions with Materials and Atoms, **204** (2003), 629 . ISSN 0168-583X. 14th International Conference on Electromagnetic Isotope Separators and Techniques Related to their Applications.
http://dx.doi.org/10.1016/S0168-583X(02)02142-0

[48] J. R. Terry, B. A. Brown, C. M. Campbell, J. M. Cook, A. D. Davies, D.-C. Dinca, A. Gade, T. Glasmacher, P. G. Hansen, B. M. Sherrill, H. Zwahlen, D. Bazin, K. Yoneda, J. A. Tostevin, T. Otsuka, Y. Utsuno, and B. Pritychenko. *Single–neutron knockout from intermediate energy beams of $^{30,32}Mg$: Mapping the transition into the "island of inversion"*. Phys. Rev. C, **77**, no. 1 (2008), 014316.
http://dx.doi.org/10.1103/PhysRevC.77.014316

[49] Vandana Tripathi, S. L. Tabor, C. R. Hoffman, M. Wiedeking, A. Volya, P. F. Mantica, A. D. Davies, S. N. Liddick, W. F. Mueller, A. Stolz, B. E. Tomlin, T. Otsuka, and Y. Utsuno. *β-delayed γ spectroscopy of neutron rich $^{27,28,29}Na$*. Phys. Rev. C, **73**, no. 5 (2006), 054303.
http://dx.doi.org/10.1103/PhysRevC.73.054303

[50] Isao Tanihata. *Radioactive beam facilities and their physics program*. Nuclear Physics A, **553** (1993), 361 . ISSN 0375-9474.
http://dx.doi.org/10.1016/0375-9474(93)90636-C

[51] F. Marti, P. Miller, D. Poe, M. Steiner, J. Stetson, and X. Y. Wu. *Commissioning of the coupled cyclotron system at NSCL*. AIP Conference Proceedings, **600**, no. 1 (2001), 64.
http://dx.doi.org/10.1063/1.1435199

[52] D. J. Morrissey, B. M. Sherrill, M. Steiner, A. Stolz, and I. Wiedenhoever. *Commissioning the A1900 projectile fragment separator*. Nuclear Instruments and Methods in Physics Research Section B: Beam Interactions with Materials and Atoms, **204** (2003), 90 . ISSN 0168-583X. 14th International Conference on Electromagnetic Isotope Separators and Techniques Related to their Applications.
http://dx.doi.org/10.1016/S0168-583X(02)01895-5

[53] D. Weisshaar, A. Gade, T. Glasmacher, G.F. Grinyer, D. Bazin, P. Adrich, T. Baugher, J.M. Cook, C.Aa. Diget, S. McDaniel, A. Ratkiewicz, K.P. Siwek, and K.A. Walsh. *CAESAR–a high-efficiency CsI(Na) scintillator array for in-beam $\gamma-$ray spectroscopy with fast rare-isotope beams*. Nuclear Instruments and Methods in Physics Research Section A: Accelerators, Spectrometers, Detectors and Associated Equipment, **624**, no. 3 (2010), 615 . ISSN 0168-9002.
http://dx.doi.org/10.1016/j.nima.2010.09.148

[54] B. Luther, T. Baumann, M. Thoennessen, J. Brown, P. DeYoung, J. Finck, J. Hinnefeld, R. Howes, K. Kemper, P. Pancella, G. Peaslee, W. Rogers, and S. Tabor. *MoNA–the Modular Neutron Array*. Nuclear Instruments and Methods in Physics Research Section A: Accelerators, Spectrometers, Detectors and Associated Equipment, **505**, no. 1-2 (2003), 33 . ISSN 0168-9002. Proceedings of the tenth Symposium on Radiation Measurements and Applications.
http://dx.doi.org/10.1016/S0168-9002(03)01014-3

[55] T. Baumann, J. Boike, J. Brown, M. Bullinger, J.P. Bychoswki, S. Clark, K. Daum, P.A. DeYoung, J.V. Evans, J. Finck, N. Frank, A. Grant, J. Hinnefeld, G.W. Hitt, R.H. Howes, B. Isselhardt, K.W. Kemper, J. Longacre, Y. Lu, B. Luther, S.T. Marley, D. McCollum, E. McDonald, U. Onwuemene, P.V. Pancella, G.F. Peaslee, W.A. Peters, M. Rajabali,

J. Robertson, W.F. Rogers, S.L. Tabor, M. Thoennessen, E. Tryggestad, R.E. Turner, P.J. VanWylen, and N. Walker. *Construction of a modular large-area neutron detector for the NSCL*. Nuclear Instruments and Methods in Physics Research Section A: Accelerators, Spectrometers, Detectors and Associated Equipment, **543**, no. 2-3 (2005), 517 . ISSN 0168-9002.
http://dx.doi.org/10.1016/j.nima.2004.12.020

[56] M.D. Bird, S.J. Kenney, J. Toth, H.W. Weijers, J.C. DeKamp, M. Thoennessen, and A.F. Zeller. *System testing and installation of the NHMFL/NSCL sweeper magnet*. IEEE Transactions on Applied Superconductivity, **15**, no. 2 (2005), 1252 . ISSN 1051-8223.
http://dx.doi.org/10.1109/TASC.2005.849553

[57] Saint-Gobain Crystals. *BC-400, BC-404, BC-408, BC-412, BC-416 premium plastic scintillators* (2005).
http://www.detectors.saint-gobain.com

[58] W.R Leo. *Techniques for nuclear and particle physics experiments: A how to approach*. Springer-Verlag, New York, NY, 2nd edition (1994).

[59] Bill Peters. *Study of neutron unbound states using the Modular Neutron Array (MoNA)*. Ph.D. thesis, Michigan State University, East Lansing, Michigan (2007).
http://gradworks.umi.com/32/82/3282185.html

[60] Nathan Frank. *Spectroscopy of neutron unbound states in neutron rich oxygen isotopes*. Ph.D. thesis, Michigan State University, East Lansing, Michigan (2006).
http://tinyurl.com/nscltheses/Frank2006_217.pdf

[61] Calem R. Hoffman. *Investigation of the neutron–rich oxygen isotopes at the drip line*. Ph.D. thesis, Florida State University, Tallahassee, Florida (2009).
http://tinyurl.com/nscltheses/Hoffman2009_255.pdf

[62] M. Galassi, J. Davies, J. Theiler, B. Gough, G. Jungman, M. Booth, and F. Rossi. *GNU Scientific Library reference manual*. Technical report, GNU (2007).
http://www.gnu.org/software/gsl/manual/htmlnode/

[63] K. Levenberg. *A method for the solution of certain non-linear problems in least squares*. Quarterly Journal of Applied Mathematics, **II**, no. 2 (1944), 164.

[64] Donald W. Marquardt. *An algorithm for least-squares estimation of nonlinear parameters*. Journal of the Society for Industrial and Applied Mathematics, **11**, no. 2 (1963), pp. 431. ISSN 03684245.
http://www.jstor.org/stable/2098941

[65] L. Heilbronn, Y. Iwata, and H. Iwase. *Off-line correction for excessive constant-fraction-discriminator walk in neutron time-of-flight experiments*. Nuclear Instruments and Methods in Physics Research Section A: Accelerators, Spectrometers, Detectors and Associated Equipment, **522**, no. 3 (2004), 495 . ISSN 0168-9002.
http://dx.doi.org/10.1016/j.nima.2003.11.398

[66] T. Kobayashi and T. Sugitate. *Test of prototypes for a highly-segmented TOF hodoscope*. Nuclear Instruments and Methods in Physics Research Section A: Accelerators, Spectrometers, Detectors and Associated Equipment, **287**, no. 3 (1990), 389 . ISSN 0168-9002. http://dx.doi.org/10.1016/0168-9002(90)91552-M

[67] Technical Report W5013. *GEANT CERN library long writeup*. Technical report, CERN (1994). http://wwwasdoc.web.cern.ch/wwwasdoc/geant/geantall.html

[68] R.B. Firestone. *Nuclear data sheets for A = 22*. Nuclear Data Sheets, **106**, no. 1 (2005), 1 . ISSN 0090-3752. http://dx.doi.org/10.1016/j.nds.2005.10.003

[69] Huo Junde. *Nuclear data sheets for A = 56*. Nuclear Data Sheets, **86**, no. 2 (1999), 315 . ISSN 0090-3752. http://dx.doi.org/10.1006/ndsh.1999.0004

[70] G. Mukherjee and A.A. Sonzogni. *Nuclear data sheets for A = 88*. Nuclear Data Sheets, **105**, no. 2 (2005), 419 . ISSN 0090-3752. http://dx.doi.org/10.1016/j.nds.2005.06.001

[71] Yu. Khazov, A. Rodionov, and F.G. Kondev. *Nuclear data sheets for A = 133*. Nuclear Data Sheets, **112**, no. 4 (2011), 855 . ISSN 0090-3752. http://dx.doi.org/10.1016/j.nds.2011.03.001

[72] E. Browne and J.K. Tuli. *Nuclear data sheets for A = 137*. Nuclear Data Sheets, **108**, no. 10 (2007), 2173 . ISSN 0090-3752. http://dx.doi.org/10.1016/j.nds.2007.09.002

[73] Heather Zwahlen. *Angular distributions of gamma rays with intermediate-energy beams and spectroscopy of* ^{32}Mg. Ph.D. thesis, Michigan State University, East Lansing, Michigan (2005). http://tinyurl.com/nscltheses/Zwahlen2005_210.pdf

[74] I. Antcheva, M. Ballintijn, B. Bellenot, M. Biskup, R. Brun, N. Buncic, Ph. Canal, D. Casadei, O. Couet, V. Fine, L. Franco, G. Ganis, A. Gheata, D. Gonzalez Maline, M. Goto, J. Iwaszkiewicz, A. Kreshuk, D. Marcos Segura, R. Maunder, L. Moneta, A. Naumann, E. Offermann, V. Onuchin, S. Panacek, F. Rademakers, P. Russo, and M. Tadel. *ROOT – A C++ framework for petabyte data storage, statistical analysis and visualization*. Computer Physics Communications, **180**, no. 12 (2009), 2499 . ISSN 0010-4655. 40 YEARS OF CPC: A celebratory issue focused on quality software for high performance, grid and novel computing architectures. http://dx.doi.org/10.1016/j.cpc.2009.08.005

[75] Rene Brun and Fons Rademakers. *ROOT – An object oriented data analysis framework*. Nuclear Instruments and Methods in Physics Research Section A: Accelerators, Spectrometers, Detectors and Associated Equipment, **389**, no. 1-2 (1997), 81 . ISSN 0168-9002. New Computing Techniques in Physics Research V. http://dx.doi.org/10.1016/S0168-9002(97)00048-X

[76] Kyoko Makino and Martin Berz. *COSY INFINITY version 9*. Nuclear Instruments and Methods in Physics Research Section A: Accelerators, Spectrometers, Detectors and Associated Equipment, **558**, no. 1 (2006), 346 . ISSN 0168-9002. Proceedings of the 8th International Computational Accelerator Physics Conference - ICAP 2004.
http://dx.doi.org/10.1016/j.nima.2005.11.109

[77] N. Frank, A. Schiller, D. Bazin, W.A. Peters, and M. Thoennessen. *Reconstruction of nuclear charged fragment trajectories from a large-gap sweeper magnet*. Nuclear Instruments and Methods in Physics Research Section A: Accelerators, Spectrometers, Detectors and Associated Equipment, **580**, no. 3 (2007), 1478 . ISSN 0168-9002.
http://dx.doi.org/10.1016/j.nima.2007.07.008

[78] Arthur H. Compton. *A quantum theory of the scattering of x-rays by light elements*. Phys. Rev., **21**, no. 5 (1923), 483.
http://dx.doi.org/10.1103/PhysRev.21.483

[79] A. Einstein. *Zur elektrodynamik bewegter körper*. Annalen der Physik, **322**, no. 10 (1905), 891. ISSN 1521-3889.
http://dx.doi.org/10.1002/andp.19053221004

[80] A. Schiller, N. Frank, T. Baumann, D. Bazin, B. A. Brown, J. Brown, P. A. DeYoung, J. E. Finck, A. Gade, J. Hinnefeld, R. Howes, J.-L. Lecouey, B. Luther, W. A. Peters, H. Scheit, M. Thoennessen, and J. A. Tostevin. *Selective population and neutron decay of an excited state of* ^{23}O. Phys. Rev. Lett., **99**, no. 11 (2007), 112501.
http://dx.doi.org/10.1103/PhysRevLett.99.112501

[81] N. Frank, T. Baumann, D. Bazin, B.A. Brown, J. Brown, P.A. DeYoung, J.E. Finck, A. Gade, J. Hinnefeld, R. Howes, J.-L. Lecouey, B. Luther, W.A. Peters, H. Scheit, A. Schiller, M. Thoennessen, and J. Tostevin. *Neutron decay spectroscopy of neutron-rich oxygen isotopes*. Nuclear Physics A, **813**, no. 3-4 (2008), 199 . ISSN 0375-9474.
http://dx.doi.org/10.1016/j.nuclphysa.2008.09.009

[82] G. Christian, W.A. Peters, D. Absalon, D. Albertson, T. Baumann, D. Bazin, E. Breitbach, J. Brown, P.L. Cole, D. Denby, P.A. DeYoung, J.E. Finck, N. Frank, A. Fritsch, C. Hall, A.M. Hayes, J. Hinnefeld, C.R. Hoffman, R. Howes, B. Luther, E. Mosby, S. Mosby, D. Padilla, P.V. Pancella, G. Peaslee, W.F. Rogers, A. Schiller, M.J. Strongman, M. Thoennessen, and L.O. Wagner. *Production of nuclei in neutron unbound states via primary fragmentation of* ^{48}Ca. Nuclear Physics A, **801**, no. 3-4 (2008), 101 . ISSN 0375-9474.
http://dx.doi.org/10.1016/j.nuclphysa.2008.01.004

[83] C. R. Hoffman, T. Baumann, J. Brown, P. A. DeYoung, J. E. Finck, N. Frank, J. D. Hinnefeld, S. Mosby, W. A. Peters, W. F. Rogers, A. Schiller, J. Snyder, A. Spyrou, S. L. Tabor, and M. Thoennessen. *Observation of a two-neutron cascade from a resonance in* ^{24}O. Phys. Rev. C, **83**, no. 3 (2011), 031303.
http://dx.doi.org/10.1103/PhysRevC.83.031303

[84] P. Doornenbal, H. Scheit, N. Kobayashi, N. Aoi, S. Takeuchi, K. Li, E. Takeshita, Y. Togano, H. Wang, S. Deguchi, Y. Kawada, Y. Kondo, T. Motobayashi, T. Nakamura, Y. Satou, K. N.

Tanaka, and H. Sakurai. *Exploring the "island of inversion" by in-beam γ-ray spectroscopy of the neutron-rich sodium isotopes* $^{31,32,33}Na$. Phys. Rev. C, **81**, no. 4 (2010), 041305. http://dx.doi.org/10.1103/PhysRevC.81.041305

[85] Z. Elekes, Zs. Dombrádi, A. Saito, N. Aoi, H. Baba, K. Demichi, Zs. Fülöp, J. Gibelin, T. Gomi, H. Hasegawa, N. Imai, M. Ishihara, H. Iwasaki, S. Kanno, S. Kawai, T. Kishida, T. Kubo, K. Kurita, Y. Matsuyama, S. Michimasa, T. Minemura, T. Motobayashi, M. Notani, T. Ohnishi, H. J. Ong, S. Ota, A. Ozawa, H. K. Sakai, H. Sakurai, S. Shimoura, E. Takeshita, S. Takeuchi, M. Tamaki, Y. Togano, K. Yamada, Y. Yanagisawa, and K. Yoneda. *Proton inelastic scattering studies at the borders of the "island of inversion": The* $^{30,31}Na$ *and* $^{33,34}Mg$ *case*. Phys. Rev. C, **73**, no. 4 (2006), 044314. http://dx.doi.org/10.1103/PhysRevC.73.044314

[86] B. V. Pritychenko, T. Glasmacher, B. A. Brown, P. D. Cottle, R. W. Ibbotson, K. W. Kemper, L. A. Riley, and H. Scheit. *First observation of an excited state in the neutron-rich nucleus* ^{31}Na. Phys. Rev. C, **63**, no. 1 (2000), 011305. http://dx.doi.org/10.1103/PhysRevC.63.011305

[87] A. M. Lane and R. G. Thomas. *R-matrix theory of nuclear reactions*. Rev. Mod. Phys., **30**, no. 2 (1958), 257. http://dx.doi.org/10.1103/RevModPhys.30.257

[88] G. Breit and E. Wigner. *Capture of slow neutrons*. Phys. Rev., **49**, no. 7 (1936), 519. http://dx.doi.org/10.1103/PhysRev.49.519

[89] John M. Blatt and Victor F. Weisskopf. *Theoretical Nuclear Physics*. Springer-Verlag, New York, NY, 2nd edition (1979).

[90] K. J. Le Couteur and D. W. Lang. *Neutron evaporation and level densities in excited nuclei*. Nuclear Physics, **13**, no. 1 (1959), 32 . ISSN 0029-5582. http://dx.doi.org/10.1016/0029-5582(59)90136-1

[91] A.S. Goldhaber. *Statistical models of fragmentation processes*. Physics Letters B, **53**, no. 4 (1974), 306 . ISSN 0370-2693. http://dx.doi.org/10.1016/0370-2693(74)90388-8

[92] O. Tarasov. *Analysis of momentum distributions of projectile fragmentation products*. Nuclear Physics A, **734** (2004), 536 . ISSN 0375-9474. http://dx.doi.org/10.1016/j.nuclphysa.2004.01.099

[93] O.B. Tarasov and D. Bazin. *LISE++: Radioactive beam production with in-flight separators*. Nuclear Instruments and Methods in Physics Research Section B: Beam Interactions with Materials and Atoms, **266**, no. 19-20 (2008), 4657 . ISSN 0168-583X. Proceedings of the XVth International Conference on Electromagnetic Isotope Separators and Techniques Related to their Applications. http://dx.doi.org/10.1016/j.nimb.2008.05.110

[94] W.T. Eadie, D. Drijard, F.E. James, M. Roos, and B. Sadoulet. *Statistical Methods in Experimental Physics*. North-Holland Publishing Company, Amsterdam, 1st edition (1971).

[95] D.M. Schmidt, R.J. Morrison, and M.S. Witherell. *A general method of estimating physical parameters from a distribution with acceptance and smearing effects*. Nuclear Instruments and Methods in Physics Research Section A: Accelerators, Spectrometers, Detectors and Associated Equipment, **328**, no. 3 (1993), 547 . ISSN 0168-9002.
http://dx.doi.org/10.1016/0168-9002(93)90674-7

[96] B. Jurado, H. Savajols, W. Mittig, N.A. Orr, P. Roussel-Chomaz, D. Baiborodin, W.N. Catford, M. Chartier, C.E. Demonchy, Z. Dlouhý, A. Gillibert, L. Giot, A. Khouaja, A. Lépine-Szily, S. Lukyanov, J. Mrazek, Y.E. Penionzhkevich, S. Pita, M. Rousseau, and A.C. Villari. *Mass measurements of neutron–rich nuclei near the $N = 20$ and 28 shell closures*. Physics Letters B, **649**, no. 1 (2007), 43 . ISSN 0370-2693.
http://dx.doi.org/10.1016/j.physletb.2007.04.006

[97] G. Audi, O. Bersillon, J. Blachot, and A. H. Wapstra. *The $N\mathcal{UBASE}$ evaluation of nuclear and decay properties*. Nuclear Physics A, **624**, no. 1 (1997), 1 . ISSN 0375-9474.
http://dx.doi.org/10.1016/S0375-9474(97)00482-X

[98] Petr Navrátil, Sofia Quaglioni, Ionel Stetcu, and Bruce R Barrett. *Recent developments in no-core shell-model calculations*. Journal of Physics G: Nuclear and Particle Physics, **36**, no. 8 (2009), 083101. (and references therein).
http://dx.doi.org/10.1088/0954-3899/36/8/083101

[99] B. Alex Brown and W. A. Richter. *New "USD" hamiltonians for the sd shell*. Phys. Rev. C, **74**, no. 3 (2006), 034315.
http://dx.doi.org/10.1103/PhysRevC.74.034315

[100] Angelo Signoracci. *Effective interactions for nuclear structure calculations*. Ph.D. thesis, Michigan State University, East Lansing, Michigan (2011).
http://tinyurl.com/nscltheses/Signoracci2011_284.pdf

[101] B. Alex Brown. *Nuclear structure resources*.
http://www.nscl.msu.edu/~brown/resources/resources.html

[102] W.D.M. Rae. *NuShell and NuShellX*.
http://knollhouse.eu/NuShellX.aspx

[103] Elena Rodriguez-Vieitez. *Structure and cross section data of neutron–rich $N \sim 20$ nuclei produced in fragmentation and few–nucleon knockout reactions*. Ph.D. thesis, University of California, Berkeley, Berkeley, California (2007).
http://gradworks.umi.com/33/23/3323512.html

[104] M. Kimura and N. Furutachi. *Molecule–like structure with covalent neutrons of F isotopes toward the neutron drip line*. Phys. Rev. C, **83**, no. 4 (2011), 044304.
http://dx.doi.org/10.1103/PhysRevC.83.044304

[105] M. Bouhelal, F. Haas, E. Caurier, F. Nowacki, and A. Bouldjedri. *A PSDPF interaction to describe the $1\hbar\omega$ intruder states in sd shell nuclei*. Nuclear Physics A, **864**, no. 1 (2011), 113 . ISSN 0375-9474.
http://dx.doi.org/10.1016/j.nuclphysa.2011.06.026

[106] E. K. Warburton, J. A. Becker, and B. A. Brown. *Mass systematics for A = 29–44 nuclei: The deformed A ∼ 32 region*. Phys. Rev. C, **41**, no. 3 (1990), 1147.
http://dx.doi.org/10.1103/PhysRevC.41.1147

[107] A. Gade, P. Adrich, D. Bazin, M. D. Bowen, B. A. Brown, C. M. Campbell, J. M. Cook, S. Ettenauer, T. Glasmacher, K. W. Kemper, S. McDaniel, A. Obertelli, T. Otsuka, A. Ratkiewicz, K. Siwek, J. R. Terry, J. A. Tostevin, Y. Utsuno, and D. Weisshaar. *Spectroscopy of ^{36}Mg: Interplay of normal and intruder configurations at the neutron–rich boundary of the "island of inversion"*. Phys. Rev. Lett., **99**, no. 7 (2007), 072502.
http://dx.doi.org/10.1103/PhysRevLett.99.072502

[108] G. Neyens, M. Kowalska, D. Yordanov, K. Blaum, P. Himpe, P. Lievens, S. Mallion, R. Neugart, N. Vermeulen, Y. Utsuno, and T. Otsuka. *Measurement of the spin and magnetic moment of ^{31}Mg: Evidence for a strongly deformed intruder ground state*. Phys. Rev. Lett., **94**, no. 2 (2005), 022501.
http://dx.doi.org/10.1103/PhysRevLett.94.022501

[109] W. Rogers. *Construction and testing of the Large multi–Institutional Scintillator Array (LISA)—a model of collaborative undergraduate research*. APS Meeting Abstracts (2011), 13004.
http://adsabs.harvard.edu/abs/2011APS..APRB13004R